Behavioral EMI Models of Switched Power Converters

Hemant Bishnoi

Dissertation submitted to the Faculty of the Virginia Polytechnic Institute and State University in partial fulfillment of the requirements for the degree of

Doctor of Philosophy

in

Electrical Engineering

Dushan Boroyevich, Chair

Paolo Mattavelli

Khai D. T. Ngo

Gary S. Brown

Traian Iliescu

September 24, 2013

Blacksburg, Virginia

Keywords: Common Mode (CM), Differential Mode (DM), Electro-magnetic Interference (EMI), High frequency modeling, Terminal model

© 2013, Hemant Bishnoi

Behavioral EMI Models of Switched Power Converters

by

Hemant Bishnoi

Dushan Boroyevich, Chair

Electrical Engineering

ABSTRACT

Measurement-based behavioral electromagnetic interference (EMI) models have been shown earlier to accurately capture the EMI behavior of switched power converters. These models are compact, linear, and run in frequency domain, enabling faster and more stable simulations compared to the detailed lumped-circuit models. So far, the behavioral EMI modeling techniques are developed and applied to the converter's input side only. The resulting models are therefore referred to as "*terminated EMI models*". Under the condition that the output side of the converter remains fixed, these models can predict the input side EMI for any change in the impedance of the input side network. However, any change at the output side would require re-extraction of the behavioral model. Thus the terminated EMI models are incapable of predicting the change in the input side EMI due to changes at the output side of the converter or vice versa.

The above mentioned limitation has been overcome by an "*un-terminated EMI model*" proposed in this dissertation. Un-terminated EMI models are developed here to predict both the common-mode (CM) and the differential (DM) noise currents at the input and the output sides of a motor-drive system. The modeling procedure itself has been simplified and now requires fewer measurements and results in less noise in the identified model parameters. Both CM and DM models are then combined to predict the total noise in the motor-drive system. All models are validated by experiments and their limitations identified.

A significant portion of this dissertation is then devoted to the application of behavioral EMI models in the design of EMI filters. Comprehensive design procedures are developed for both DM and CM filters in a motor-drive system. The filters designed using the proposed methods are experimentally shown to satisfy the DO-160 conducted emissions standards.

The dissertation ends with a summary of contributions, limitations, and some future research directions.

ACKNOWLEDGEMENTS

I would like to extend my greatest thanks to my advisor, Dr. Dushan Boroyevich, for his guidance during my education, be it research or course work. I especially want to thank him for his support and motivation during the ups and downs of my graduate life. His clarity of thinking on research matters and logistics kept the ball rolling even during the most difficult times. In the end, I felt he always showed confidence in me and gave me responsibilities that helped tremendously in my personal development.

This research work has been significantly influenced by Dr. Paolo Mattavelli. He is one my committee members and his technical guidance has been of immense help to me. Most importantly, he effectively closed all the gaps when Dr. Boroyevich was not available due to his busy schedules and his commitments during the time he served as the president of PELS, IEEE. I would like to thank my other committee members, Dr. Khai Ngo, Dr. Gary Brown and Dr. Traian Iliescu for sharing their precious time in evaluating my research work and being available for guidance whenever I needed. I would also like to thank Dr. Rolando Burgos for his support during the last few months of this research.

Amongst my colleagues, I would especially like to thank Andrew C. Baisden, not only for convincing me to pursue PhD in CPES but also for his guidance in the project work. I would also like to thank Igor Cvetkovic for his help in building the EMI test fixture that turned out to be instrumental in all experimental results covered in this dissertation. My colleagues, especially Dong, Fang Luo, Ruxi Wang, Chanwit Prasantanakorn, Wei Zhang, Remi Robutel, Avinash Doorgah and Xuning Zhang have helped me in several technical matters that came during the course of this research. Last but not the least, David Reusch, Douglas Sterk, Henry (Zheng) Chen, Marko Jakšić, Bo Wen, Sara Ahmed, Milisav Danilovic, Fabien Dubois, Fran E. Gonzalez, David Gilham, Mudassar Kahtib, Kevin Loudier and Gandharava Kumar were always a pleasure to interact with. I would like to thank Teresa Shaw, Linda Long, Marianne Hawthorne and Teresa (Trish) Rose for their help in the administrative matters. In the end, I would also like to thank Nicolas Gazel, Houmam, Moussa and Regis Meuret from Hispano-Suiza (SAFRAN Group) for their generous support to this research.

I am honored to have spent my crucial years amongst such talented group of people. I am sure that they have all influenced me in a way that will always reflect in my professional life.

This research work has been funded by Hispano-Suiza (SAFRAN Group), France. On the behalf of CPES, I would like to thank them for their continued support and commitment towards research and education. With their help, several exchanges of talented students and ideas from French universities have taken place and these exchanges have positively influenced our research work.

To my parents

Muni Raj & Renu Singh

For their support and encouragement

During these long years of education

TABLE OF CONTENTS

LIST OF FIGURES

1 INTRODUCTION

1.1 BACKGROUND

Power electronics has revolutionized the way we process power to meet the growing energy need of our society. The introduction of fast switching power semiconductor devices has greatly improved the dynamic response (controllability), efficiency and power density of the power converters. This class of converters are collectively known as switched power converters or switched mode power supplies (SMPS). However, the fast voltage (or current) switching action of semiconductor devices leads to greater electromagnetic interference (EMI) in the system. Devices can now switch 600V to1200V in a matter of only a couple of hundred nano-seconds. The device manufacturers are steadily moving towards developing faster devices enabling an increase in the switching frequency of the power converters [1]. A higher switching frequency means a smaller size EMI filter, which in turn means less total volume or larger power density [1] but it also means greater EMI. The issue of EMI is challenging because it is one of the most significant factors deciding the time-to-market of the product. EMI testing usually starts when a prototype of the power converter is ready. At this stage, poor EMI performance would most often mean using a larger EMI filter to meet the EMI standards, since making changes in the design could turn out to be a lengthy and costly process [2]. Large EMI filters can definitely solve the problem of noise, however they lead to a non-optimal design from the volume and weight point of view. Thus research in EMI in power electronics is mainly focused on developing methods of estimating the EMI performance of power converters at early stages of design and EMI filter optimization.

A major boost to EMI research is now coming from the aerospace industry. The current efforts in airplane design are focused on more-electric aircraft (MEA). The cost of maintaining the hydraulic, pneumatic and mechanical power systems is too high as it takes time to repair them and a grounded airplane only adds more loss to the airline operators. The concept of MEA has been questioned for several decades since World War II but the recent breakthroughs in the field of power electronics made MEA look more feasible [3]. The MEA concept can help in optimization of aircraft power systems leading to a reduction in the cost of operation and lesser weight [3]. With the first flight of *Boeing 787 Dreamliner*, the MEA is now a reality. In this

aircraft almost all pneumatic systems are replaced by electrical systems [4]. It also introduces an electronic brake actuator (EBA) system which removed the complex and costly hydraulic break system [4]. In the new Airbus A380 as well, the hydraulic thrust reverser has been replaced by the electronic-thrust-reverser-actuator-system or ETRAS® developed by Hispano-Suiza, SAFRAN power [5]. This integration of large amount of power electronics has now made the issue of EMI even more concerning for the aircraft manufacturers [6] and provides the general motivation for the research work here.

This chapter gives the motivation and the outline of the dissertation. Section 1.2 introduces the basics of conducted emissions and commonly used terminologies. This is followed by a review of the latest research in the modeling of conducted EMI in power electronics in section 1.3. Based on the literature review, motivation and outline of the dissertation is developed in the section 1.4.

1.2 CONDUCTED EMISSIONS

1.2.1 Definition

The work presented in this dissertation is limited to *conducted emissions* only and hence a brief discussion is provided to introduce the terminology which will be used quite often in the rest of the dissertation. Conducted emissions are the EMI noise that circulates between the concerned system (power converter in this case) and the external network via the physical connections between them. Fig. 1.1 illustrates this phenomena [7]. The arrows shown in Fig 1.1 indicate the direction of noise propagation only and not the direction of current. The entire system can be divided into three parts, the noise source which is causing EMI, the receiver that is being affected by EMI and the electrical connections that form the coupling paths.

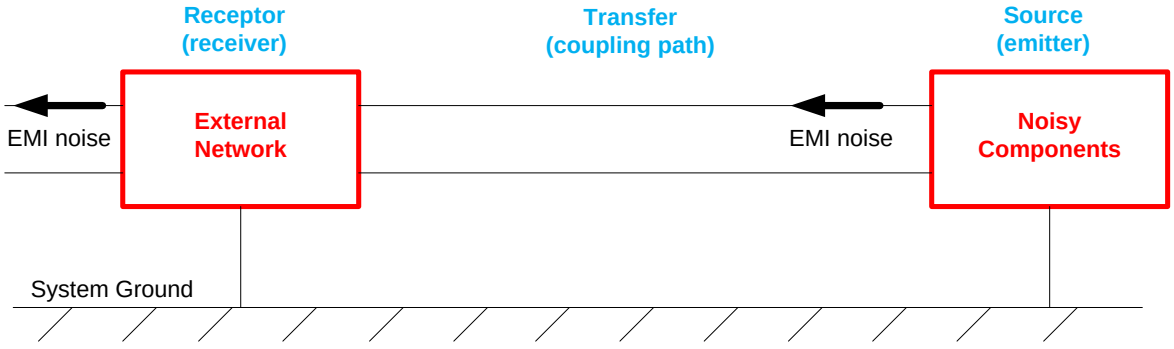

Fig. 1.1: Conducted emissions propagation

1.2.2 Measurements

Fig. 1.2 describes a standard conducted emissions set-up. The set-up shows a switched power converter (noise source) connected to an artificial external network. The artificial network is called the *line-impedance-stabilization-network* (LISN) and is required as per all conducted emissions standards. Since the user may have different external networks depending on their application, a fixed network is defined by the standards which must be used for evaluating the EMC compliance of the electronic products. LISN is a kind of line-filter that has a 50Ω input impedance looking from the *device-under-test* (DUT) side. It isolates the dc/ac mains from the DUT and hence enables accurate measurement of noise from DUT only [2]. The termination is chosen to be 50Ω in order to match the 50Ω port of a spectrum analyzer (or an EMC receiver) which is used for measuring the EMI noise.

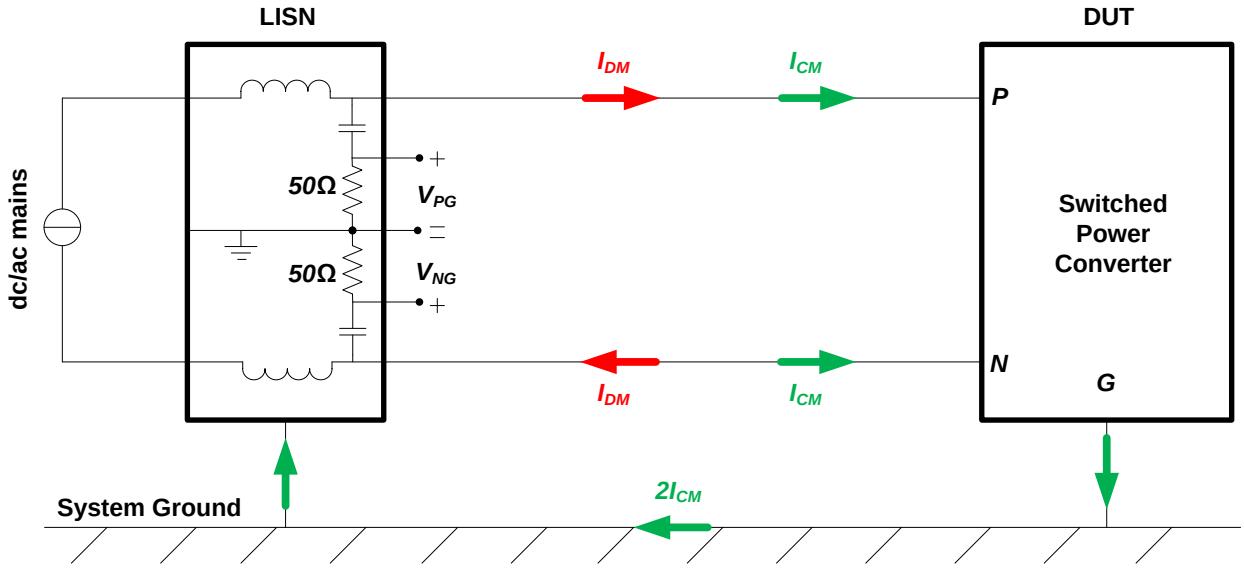

Fig. 1.2: Conducted emissions measurement set-up

There are two main types of conducted emissions, *common-mode* (CM) and *differential mode* (DM). The DM noise (I_{DM}) flows in the opposite direction between the LISN and the DUT. This is the intended signal path in the system that carries the functional currents. The CM noise (I_{CM}) flows in same direction and then returns via a ground connection. This is the un-intentional

propagation path in the system. From Fig 1.2, the noise voltage developed across the LISN is given by

$$V_{PG} = 50(I_{DM} + I_{CM}) \tag{1}$$

$$V_{NG} = 50(-I_{DM} + I_{CM}) \tag{2}$$

Thus the measured noise voltage across the LISN (V_{PG} and V_{NG}) will have both CM and DM noise. From (1) and (2), the CM and DM noise can be calculated by:

$$V_{DM} = 50I_{DM} = \frac{V_{PG} - V_{NG}}{2} \tag{3}$$

$$V_{CM} = 50I_{CM} = \frac{V_{PG} + V_{NG}}{2} \tag{4}$$

Equation (3) gives the DM noise measured on one side of the LISN but (4) gives the total CM noise in the system. The total DM noise equals to $2V_{DM}$ (or equal to V_P-V_N). Some standards are based on noise currents instead of the noise voltage. The noise currents in the wires are given by:

$$I_P = I_{DM} + I_{CM} \tag{5}$$

$$I_N = -I_{DM} + I_{CM} \tag{6}$$

The measured of positive and negative side currents can be used to calculate the CM and DM noise by:

$$I_{DM} = \frac{I_P - I_N}{2} \tag{7}$$

$$I_{CM} = \frac{I_P + I_N}{2} \tag{8}$$

There is also a third classification of noise, called the *mixed-mode* noise [8, 9]. It is possible to represent the two-port network of the DUT in Fig. 1.2 (Port-P and Port-N with respect to Ground-G) as an equivalent network with CM and DM being the two-ports and ground being the reference [10]. Then the transfer parameters of such a network give rise to mixed-mode noise. In other words, mixed-mode noise is the noise resulting from the coupling between the CM and DM part of the system.

It should be noted that all quantities in the above equations are vectors and hence both magnitude and phase are necessary to separate the noise. To measure CM and DM noise directly, a noise separator can be used [11]. The other way is to measure V_{PG} and V_{NG} (or I_P and I_N) simultaneously in time domain using an oscilloscope and then use Fast Fourier Transform (FFT)

to convert measured signals into frequency domain. In this way both phase and magnitude can be extracted.

It is worthwhile to mention that the CM noise is mostly responsible for producing radiated emissions from the system [7]. This is illustrated in Fig. 1.3. The fields generated by two wires is in opposite directions in the case of DM currents and hence the net field is smaller, whereas in the case of the CM noise current, the field generated is in the same direction and hence the resultant field is larger. Thus containing CM noise is crucial to the EMI design of a power supply.

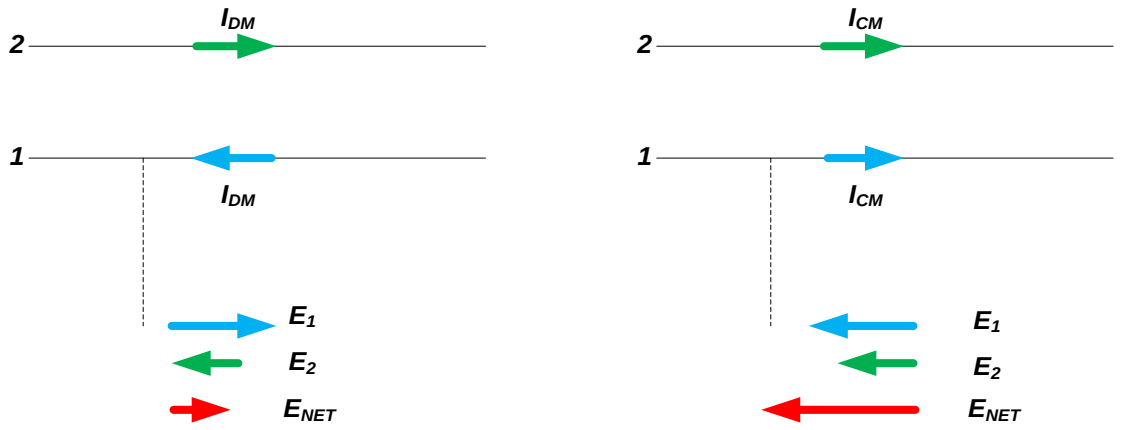

Fig. 1.3: Radiated emissions due to DM and CM currents

1.2.3 EMI Standards

Several international standards are in place to control the EMI pollution in the power systems and in the environment [2]. The standards are usually of two types, electromagnetic emissions and electromagnetic susceptibility (or immunity) standards and both are further divided into conducted and radiated emission standards. The idea is to ensure that every product that is launched in the market is electromagnetic compatible (EMC). The standards can be different depending on the country. For example in United States of America, ANSI (American national standards institute) and FCC (Federal communications commission) standards are used. In Europe the European Union (EU) has come up with several standards ranging from general (EN 61000-6-3) to product specific (EN 55022 for Information Technology Equipment) standards. Some standards are internationally accepted like IEC (International electrotechnical commission)

and CISPR (Comité International Spécial des Perturbations Radioélectriques) standards [12]. The standards are always environment specific like commercial electronics (FCC/CISPR, class A), industrial electronics (FCC/CISPR, class B), military (MIL-STD-461) [13], aerospace (DO-160) [14] etc. These standards detail the test set-up, noise measurement method and the noise limits (usually in frequency domain) which must be adhered to for the EMC certification of the final product. As an example, the DO-160 standards for conducted emissions in aerospace applications are shown in Fig 1.4. It is based on the total noise current in one wire, in other words the EMI noise measured in one wire must not exceed the given limits within 150 kHz to 30 MHz.

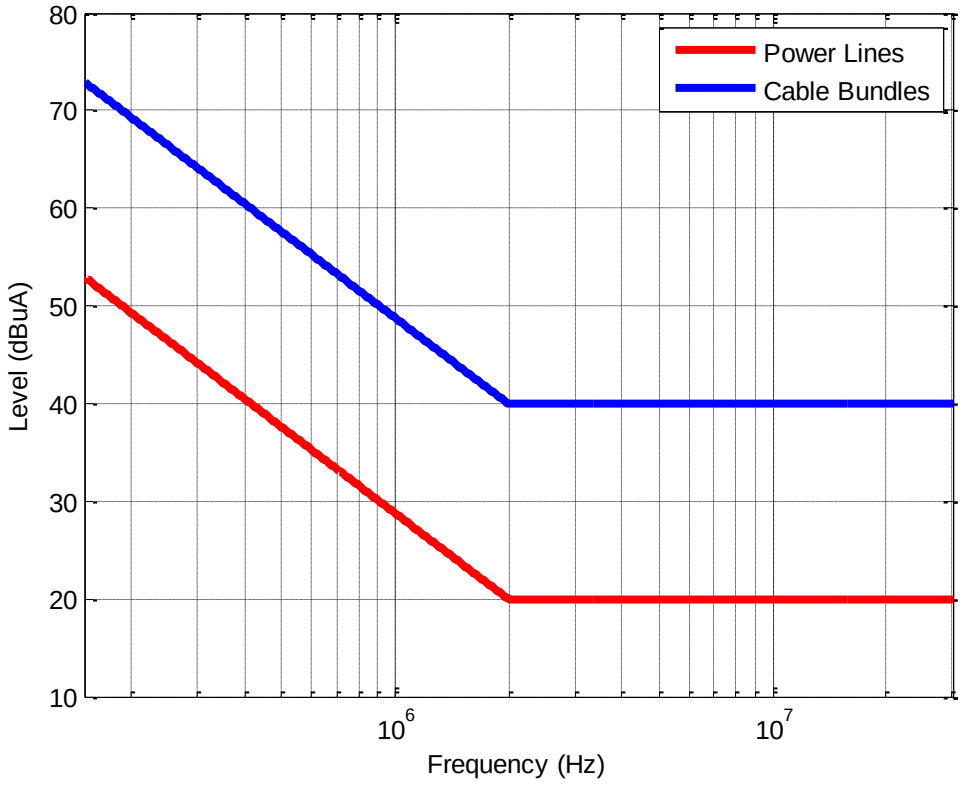

Fig. 1.4: Conducted emission limits in DO-160E (Section 21) for L, M &H categories

1.3 LITERATURE REVIEW

The design for EMI mitigation is the key to making a power converter electromagnetically compatible and EMI filters are most often used for this purpose. Design of EMI filters, in

principle, should start with a good simulation model of the power converter that is accurate in the EMI frequency range and can be used for predicting EMI under different input/output conditions. However extracting such models is not a trivial task as the measured noise levels are sensitive to the geometry of the design and the final geometry will not take shape until at least one prototype of the converter is laid down. Thus design of EMI filters for power converters has been traditionally done using trial-and-error methods. Over the last few decades however, several modeling methodologies have been published for extracting EMI models of power converters. They can be classified into two broad categories. Detailed lumped-circuit modeling and behavioral modeling. The best technique is the one which is most easy to implement and gives satisfactory accuracy in the interested range of frequencies.

1.3.1 Detailed Modeling Approach

The detailed lumped circuit modeling approach is based on the physics of the circuit and is the classical way to model any electronic circuit. The interconnects like wires and printed circuit board (PCB) traces are modeled using passive RLC equivalents. Other passive components like resistors, capacitors and inductors can be directly measured for their impedance using an impedance analyzer. The equivalent circuit models for the PCBs are usually extracted by electromagnetic numerical tools like Q3D®, and finite element method (FEM) tools like Ansoft® Maxwell. Other tools based on partial element equivalent circuit (PEEC) like InCa® can also be used in cases where RL equivalents are sufficient to model the interconnects [15]. The switches in power converters are modeled using semiconductor device models. These device models are non-linear and are based on a higher order differential equation.

For simple converters, such a model may be suitable [16] and could provide the most versatile solutions for EMI predictions. The main benefits of lumped circuit models are adaptability and scalability as everything is based on physics. The gate drive, control, power stage etc. can be modeled separately and then included in the final time domain simulation model of the power converter. Parametric analysis is very easy as the effects of using different devices or components can be easily evaluated by simply replacing their models in the simulation with new ones.

The lumped circuit models however get very complex with the increase in the number of semiconductor devices and the highest frequency of interest. Even with all the details, the model

may not work as the simulator can have convergence issues. The accuracy of such models for complicated topologies has been found to be good only up to around 10 MHz [17, 18]. Thus in theory, detailed lumped circuit models provide the most versatile solution to EMI modeling but in practice its use is limited. The development time is long and needs a lot of experience. The device models themselves may not be easily available. Sometimes manufactures provide them but they could be encrypted or otherwise they have to be developed separately.

In order to simplify the models extraction processes and increase model robustness, engineers started using reduced order models. In such models the devices are replaced by voltage or current sources. Since the devices are used as switches, the voltage across them has an approximately squared shape. However it has been shown that [19] such an approximation is not accurate and finite rise/fall time must be included for the better representation of the switched voltage (or current) [20-24]. The robustness of such models has been demonstrated in handling complex systems [25-28] however it is seen that the accuracy is only good up to several MHz. In [19] it was shown that approximation of the voltage (or current) switching characteristics with a trapezoidal waveform may not be very accurate either. Attempts have been made to use piece wise linear approximation of the voltage and current though the devices [29]. However, this kind of modeling then becomes specific to the device in use and the accuracy was not seen to be any better than the previous models. Simplified models of IGBT for EMI analysis has also been developed in [30, 31]. Here the IGBT is modeled with an ideal switch, an ON resistance and a few capacitances. The accuracy of results was found to be good up to only several MHz, most likely because of the limitations of other lumped circuit models that were used to model the system.

The problem of the accurate reproduction of the switching slope (of voltage and/or current) can be solved by directly measuring the voltage across the switches and then representing them as a noise sources in the EMI model [32-34]. This method has shown to be more accurate than assuming the switched voltages to have a trapezoidal state [33, 34]. These methods do not take-off the burden of extracting the complete lumped circuit model of the converter and their advantage lies in simplifying the complexity semiconductor device models only.

1.3.2 Behavioral Modeling Approach

The discussion of lumped circuit models points to an important limitation in the technique itself. It is not suitable for doing system level EMI simulations. Simulating several converters with detailed lumped circuit equivalents would require large computational resources and time, not to mention that the chances of convergence gets severely diminished. Moreover in the design of power distribution networks inside aircrafts, power converters supplied by several different manufacturers are required to be integrated. These manufactures seldom provide any internal information of their products as its proprietary. In such cases the lumped circuit modeling technique cannot be used since no details of the layout and devices is available. In order to tackle this dual problem of system level EMI simulations and lack of layout information, researchers started to develop black-box modeling techniques also called the behavioral modeling techniques.

These techniques model the power converters using a one-port or a two-port network with independent sources [35, 36]. A one-port network with an independent source is nothing but a Thevenin (or Norton) equivalent of the circuit. Extension of the Thevenin theorem to multi-terminal networks is also possible [37, 38]. The impedances of multi-terminal Thevenin-equivalents can be easily represented as multi-port networks with independent sources, so there is no fundamental difference between the two. In time domain, the existence of Thevenin (or Norton) equivalents is not restricted by linearity or time-variance [39, 40], that is the Thevenin models exist even for the non-linear and time-variant circuit. However they are restricted in the frequency domain by linearity and time-variance. This is because the 'impedances' are defined only for linear and time-invariant circuits. Thus Thevenin (or Norton) models in frequency domain require the circuit to be approximately linear and time-invariant.

In [41], a simplified two-terminal model is developed for a motor-drive system using Thevenin-equivalent. Both the noise source (Thevenin source) and the noise impedance (Thevenin impendence) were measured directly. The accuracy was not good mostly due to the inaccuracy of the noise source itself. The DM noise source was directly measured across the DC-link capacitor and the CM noise was measured by disconnecting the ground wire. In [42, 43], the CM noise in the motor-drive is directly measured and modeled as voltage sources. The parts of the motor-drive that are passive like cable (harnesses), motor, LISN etc. are modeled as two-port networks. The main limitation of this method is the over-simplification of the motor-drive

model. Only one noise source is used to describe the CM equivalent of the motor-drive and the impedance of the motor-drive is modeled with only one capacitor to ground. This leads to inaccuracy beyond a few MHz, however the technique is fairly easy to implement and the model can even be run in a math tool as the system is modeled with two-port networks which facilitates calculations by using only the network equations.

Another class of behavior modeling technique indirectly calculates the noise source and noise impedances using two or more conditions and then simultaneous solving of network equations [44-64]. This technique uses more generic models of noise sources rather than assuming a particular topology for a given topology. Thus the models are more complete in the sense of minimum required number of voltage/current source and the number of impedances necessary for a complete description a multi-terminal network [37]. The earliest attempt on EMI modeling of power converters using this technique was seen in [44]. The technique however had limitations regarding identification of noise-source impedance. A resonant method was used to estimate the input impedance of the converter in which a known external impedance was tuned to resonate with the input impedance of the converter. This technique is not easy to use as tuning the impedance is not easy and at higher frequencies the input impedance may have several resonances within the same decade so very precise tuning is needed.

Qian Liu et. al published several paper [19, 45, 47, 48, 50, 52, 53] on extraction of three-terminal model of a phase-leg, called the Modular-Terminal-Behavioral (MTB) model. A phase-leg is one of the most redundant topology within switched power converters and forms a basic switching cell. The idea was to obtain an EMI model of one phase-leg and then use as many instances depending on the type of converter to predict the total EMI from the power supply. Fig. 1.4 shows the MTB model and the chopper-circuit that was used for the model extraction by Qian. Although the idea was novel, it was difficult to extract such a model in practice. The model itself had an issue since it had only two impedance although three is required for description of a minimum size model of a three-terminal network [37]. Another issue was that the model was validated in condition that was very close to the ones used during model extraction or in other words no understanding was developed regarding the boundary where the model starts to fail. The cross talk between the phase-leg was not considered either. The best results for EMI prediction were obtained when only one phase-leg is used [50] but with the addition of another phase-leg [52] and with ac operations [53] the accuracy of the prediction

was shown to get worse. Other limitations with the MTB model was in the understanding of the model itself, it was claimed that the extracted model was of the phase-leg but no observations that could possibly support that contention were provided. Very little discussion was provided with regards to the model impedances. The extracted model impedances seemed to be changing with the operating point [19], which is un-natural and hence deserved more explanation.

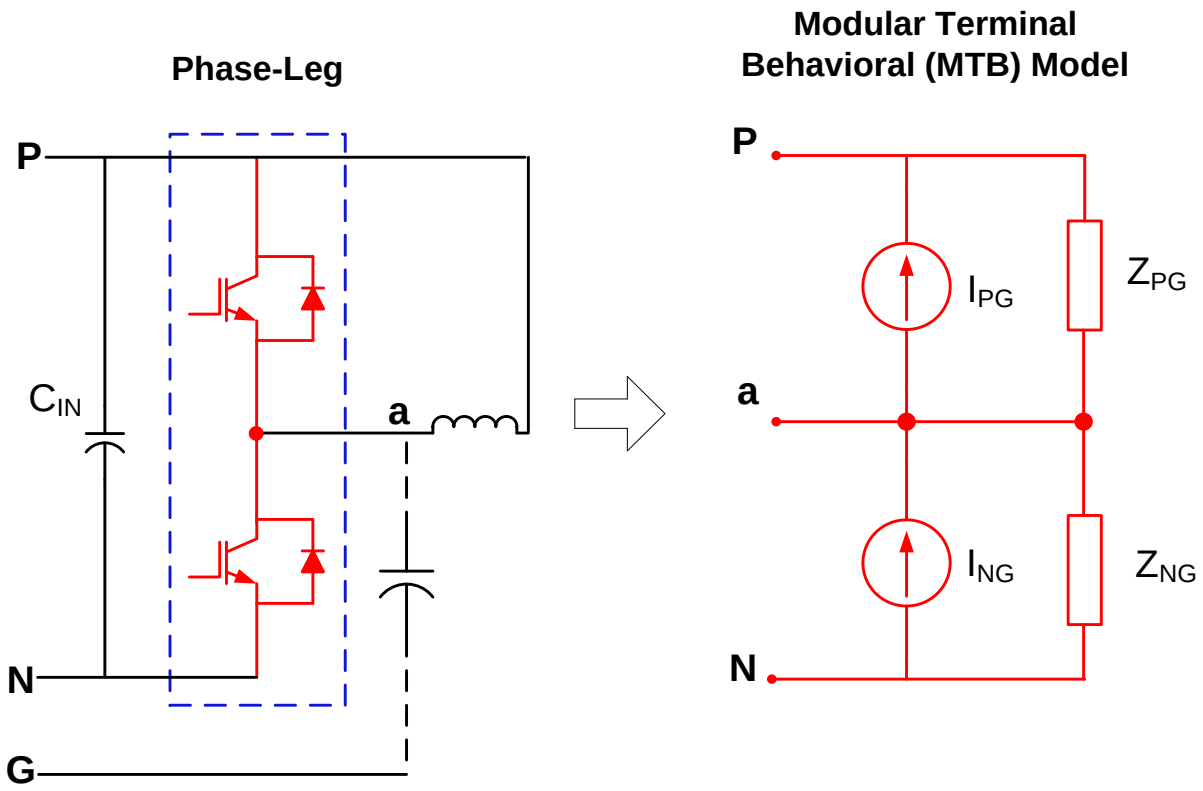

Fig. 1.5: Qian's Modular-terminal-behavioral (MTB) model

Andrew C. Baisden et. al made several improvements over the Qian's MTB model with his generalized-terminal-model (GTM). The major difference is that the entire converter is modeled as a black-box with a three-terminal Norton equivalent and not just a phase-leg. This is shown in Fig. 1.6. Another important contribution was on selection of external network impedances (or conditions) for accurate extraction noise sources and noise impedances [55, 59]. This helped in establishing boundaries on the maximum and minimum impedance at the terminals of the model for it to produce accurate results. From Fig. 1.5 and Fig 1.6, it can be seen that the MTB model was modified and three impedances in delta connection were used instead of two to describe a

three-terminal network. The model was validated for a 400W boost converter [60] only, however it was experimentally shown to have accuracy up to almost 100 MHz which is beyond the upper frequency of 30 MHz prescribed in conducted emission standards. These results established the advantages of behavioral models over lumped-circuit models. The three-terminal Norton model was also reported in [57]. In [63] the three-terminal Norton-equivalent was used to predict the net EMI for two boost converters connected in parallel (on the same dc bus).

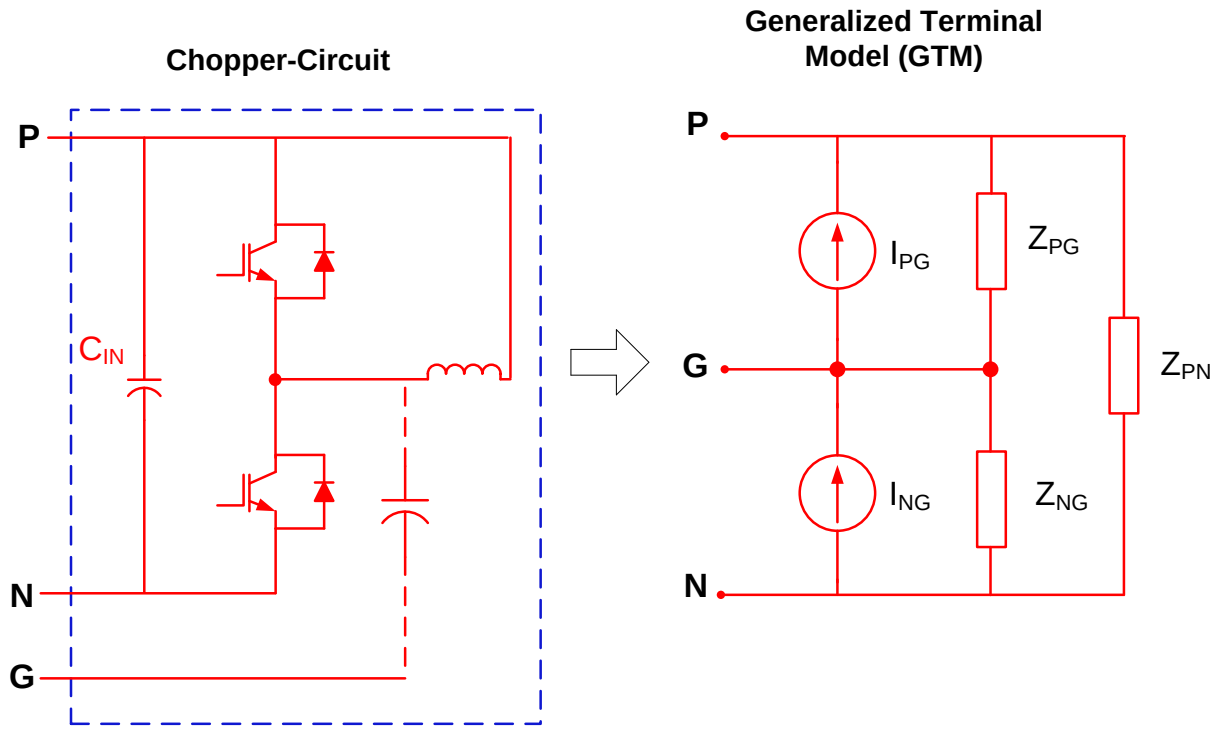

Fig. 1.6: Andrew's Generalized Terminal Model (GTM)

Apart from these major attempts several others have published similar ideas over the last decade. In [46, 49] a three-terminal Thevenin equivalent is used for modeling an ac-dc converter. Instead of two sources the model here has three sources which are characterized in two different setups. The accuracy was found to be reasonable. In [51, 54], a three-terminal Thevenin equivalent is used to model an electronic equipment. The model impedances are extracted by first measuring the complete two-port S-parameters of system using a vector-network-analyzer (VNA), while it's in operation. This is a limitation as such measurements are not possible for high power applications. In [56, 58], a similar model was developed without using the VNA.

Some other works that are based on indirect calculation of noise source impedance are also in publication [8, 65-71]. These works are dedicated to the estimation of the input impedance of power converters only.

1.4 EMI FILTERS

The estimation of input impedance can help in the design and optimization of EMI filters [72-76]. The EMI filters are basically impedance mismatching networks and thus require an accurate estimation of the impedances that are expected to be seen at their input and output side. Both behavioral models and impedance estimation techniques provide the input impedance of the converter directly. The advantage of using behavioral EMI models is that it also provides the noise-sources. In [72], it was shown conclusively that the use of input impedance of the converter can help in reducing the size of the EMI filter. Thus the techniques and assumptions used in [77-79] lead to an un-optimal design of the EMI filter. The focus of research on EMI filters is also on the automation of the design procedure [34]. This involves using an EMI model along with the knowledge of filter design and magnetics to achieve the smallest possible filter.

There are several papers that address the issue of EMI filter design, but there are very few who give the actual design steps. The ones that do give use assumed values of the load and source impedances leading to an un-optimal design. Thus, there is a need to come up with a methodology to design EMI filters that clearly take into consideration the input/output impedance. Behavioral models can provide an excellent platform [80] for design and optimization of EMI filters and to help in avoiding the traditional trial-and-error type practices.

1.5 MOTIVATION AND OBJECTIVES

From the literature review it was observed that the area of behavioral modeling is the most promising for design of EMI filters and system level EMI analysis. The behavioral models provide very high accuracy in the entire EMI frequency range along with the advantage of hassle-free simulations. This class of models are much easier to simulate owing to their simple topology.

This dissertation expands the knowledge gained from the generalized terminal model (GTM) [55, 59, 60] developed by Andrew. The model was shown to work well for a boost converter but more work is needed to validate its generality for other topologies. At the same time a limitation

was identified with the GTM and the other behavioral models, all of them model the system from the input side only. These models are referred as *terminated* models in this dissertation as the load side of the converter is required to be fixed for the model to produce accurate EMI predictions. For systems like motor-drives, both input and output side EMI needs to addressed, especially for Aerospace applications [14]. Thus there is a need of an *un-terminated* behavioral EMI model that can predict the changes in EMI at the input side of the converter due to change at the load side and vice versa. Another direction that needs to be looked at is the use of behavioral models to design EMI filters. It is important to evaluate the utility of behavioral models not just for EMI analysis/prediction but also for EMI design.

The extracted model impedances in the previous literature were found to be extremely noisy and many times without any physical sense and hence there is a scope of improvement in the model impedance identification as well as in further simplifying the entire modeling procedure itself. Lastly the validity of the method needs to be explored in order to find out the necessary conditions required for application of such linear and time-invariant models to power converters that are fundamentally non-linear and time-variant.

Based on the above mentioned limitations and unexplored directions, the following goals have been identified for this dissertation:

1. The GTM modeling technique will be validated for converters with buck type input including both dc-dc and ac power converters.
2. The noise in the extracted model impedances will be investigated and the modeling technique shall be modified to minimize this noise.
3. The behavioral EMI modeling technique will be tested for their applicability to time-variant systems.
4. An un-terminated behavioral EMI model will be developed to address both input and output side EMI of a power converter.
5. A procedure will be developed using the behavioral EMI models for automated design of both input and output side EMI filters.

2 SWITCHED IMPEDANCE

Switched power converters are inherently nonlinear and time-variant circuits. Behavioral EMI modeling attempts to model these converters using linear and time-invariant (LTI) models. However the reason behind validity of such an approximation has been overlooked in most publications. This chapter attempts to explore the applicability of such behavioral modeling techniques to power converters. Specifically it is important to understand that the behavioral modeling techniques are black-box techniques and hence the network inside the box could very well be nonlinear and time-variant. In such cases, the outcome of applying LTI models needs to be investigated. We start this investigation by looking into networks that present switched impedance at their terminals.

Switched impedance by itself is an ill-defined phenomena as impedance is a frequency domain concept and gives the equivalent resistance that the passives (R, L and C) components offer to the flow of ac current. However, impedance transformations (a result of applying Laplace transformation on time-domain network equations) assume that these passive components are linear and time-invariant. In fact $Z(\omega)$ is a very familiar notation in electrical engineering texts but $Z(t)$ is something that is never seen. It will be interesting to know if applying LTI theory to switched circuits can lead to at least a mathematical (numerical) model, which may not have any physical meaning but can still be usable from an EMI prediction point of view.

We will only look at a switched resistance case here and not switched impedance. Hence it is not possible to generalize the conclusions at the end, however, we should be able to have a fair assessment on what for certain is not possible and under what circumstances one should be careful while applying the behavioral modeling techniques.

2.1 BEHAVIORAL MODELING APPROACH

Let's start with the basics of behavioral modeling approach. Although in literature several variations of this approach can be found, the basic idea is still the same. External impedances are changed to create a change in the measured voltage/current at the terminals of the network and then by solving network equations, parameters of pre-decided noise model are calculated. These pre-decided noise models could be Thevenin/Norton models or any other combination of sources

and impedances that can accurately capture the EMI behavior of the network at its terminals. We will stick to Thevenin and Norton models for our discussion owing to their generality.

Fig. 2.1 shows an arbitrary network that we wish to model using a Thevenin or Norton equivalent. Under the condition that short-circuit conditions and/or open-circuit conditions are not possible (like in the case of power converters), we adopt a different strategy to determine the Thevenin/Norton equivalent of the network. A known resistance (R_S) is inserted between the terminals 'a' and 'b' as shown in Fig 2.2 (a). For a Thevenin model, the voltage drop across R_S is given by

$$v = V_{TH} \frac{R_S}{R_S + Z_{TH}} \tag{1}$$

For a Norton model, the voltage drop will be given by

$$v = I_N \frac{R_S Z_N}{R_S + Z_N} \tag{2}$$

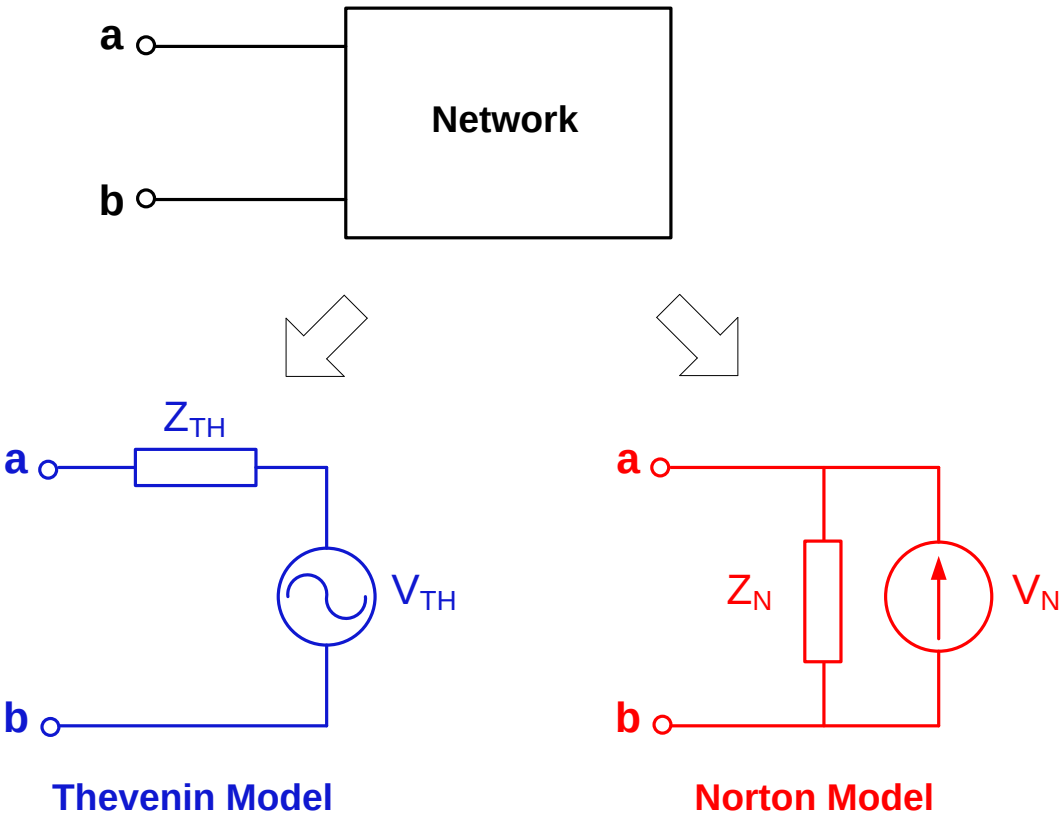

Fig. 2.1: An arbitrary network and its Thevenin and Norton models

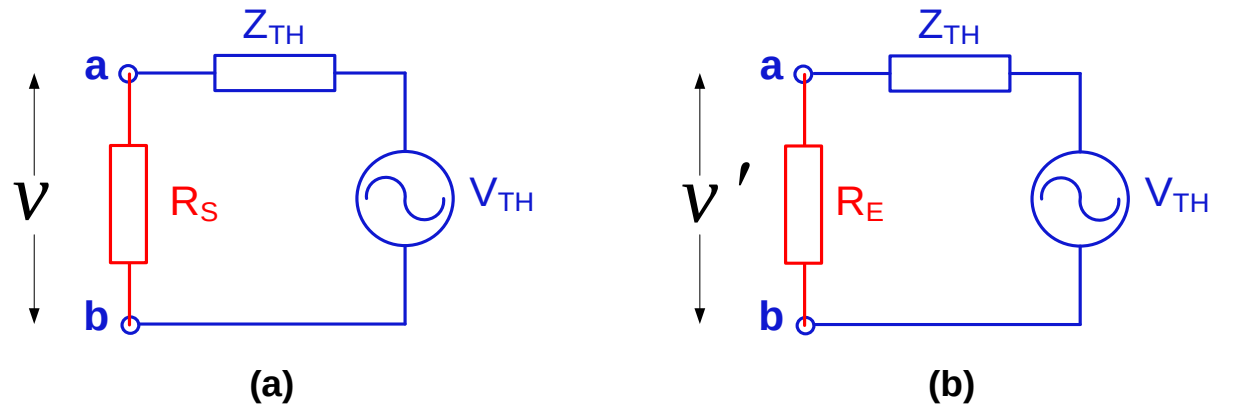

Fig. 2.2: Extraction of Thevenin model (a) condition 1 (b) condition 2

All quantities in (1) and (2) are in frequency domain. The voltage (v) developed at the terminals is recorded in time-domain and converted into frequency-domain by using FFT. The resistance R_S is then replaced by another resistance R_E as shown in Fig. 2.2 (b). This will result in change in the measured terminal voltage across 'a' and 'b'. The terminal voltage for Thevenin model of Fig. 2.2 (b) is given by

$$v' = V_{TH} \frac{R_E}{R_E + Z_{TH}} \tag{3}$$

and for a Norton model, the terminal voltage is given by

$$v' = I_N \frac{R_E Z_{TH}}{R_E + Z_N} \tag{4}$$

These equations can be now solved simultaneously to obtain the equivalent-source and equivalent-impedance. From (1) and (3), the equivalent voltage-source and impedance for Thevenin model can be calculated as

$$V_{TH} = vv' \frac{R_E - R_S}{R_S v + R_S v'} \tag{5}$$

$$Z_{TH} = -R_E R_S \frac{v - v'}{R_E v + R_S v'} \tag{6}$$

Similarly from (2) and (4), the equivalent voltage-source and impedance for the Norton model can be calculated as

$$I_N = -vv' \frac{R_E - R_S}{R_E R_S (v - v')} \tag{7}$$

$$Z_N = -R_E R_S \frac{v - v'}{R_E v + R_S v'} \tag{8}$$

It can be seen from (6) and (8) that the calculated impedance in both cases is same which is as expected.

2.2 SWITCHED RESISTANCE CIRCUITS

Let us use the equations to extract Thevenin/Norton models of some switched-resistance circuits using circuit simulations. It is possible to come-up with hundreds of (if not countless) different switched-resistance topologies and hence it becomes necessary to categorize them in some way. We divided them into two categories that are discussed next.

2.2.1 Switched Norton and Constant Thevenin Source

Fig. 2.3 shows an example network in this category. Here the open-circuit voltage (Thevenin source) is dc but the short-circuit current (Norton-source) is switched. It should be noted that in spite of being nonlinear and time-variant, this network has a Thevenin equivalent. The Thevenin impedance is nothing but a switched resistance between 10.001 kΩ and 11 kΩ and the Thevenin source is a dc voltage of 100V. Thus in time-domain a Thevenin model does exists for the network of Fig.2.3. The question is whether it exists in frequency-domain or not, because behavioral EMI models of power converters are based on frequency-domain equivalents that aids fast computation of EMI spectra and better convergence in circuit simulators.

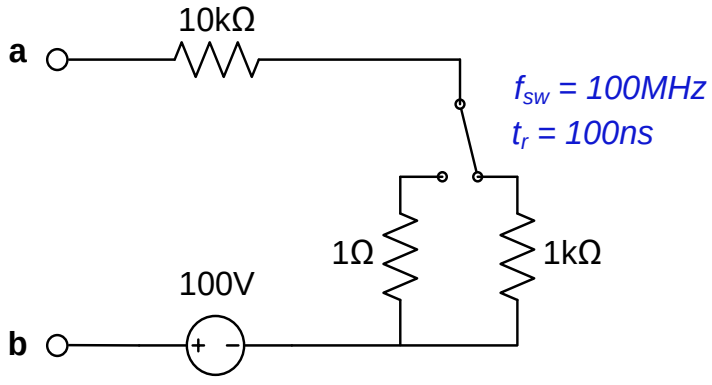

Fig. 2.3: An example of switched Norton Source and dc Thevenin source network

In case of power converters, switches are used to manipulate energy from a dc source, thus the extraction of a Thevenin or Norton model would result in approximating a network having constant sources and switched impedance with an equivalent network that has constant impedance and switched source. We use two external resistance R_S = 50 Ω and R_E = 5 Ω for extracting the Thevenin and Norton equivalent. All results are obtained from simulations in Saber®. Fig. 2.4 (a) shows the Thevenin and Norton source and Fig. 2.4 (b) shows the Thevenin and Norton Impedances.

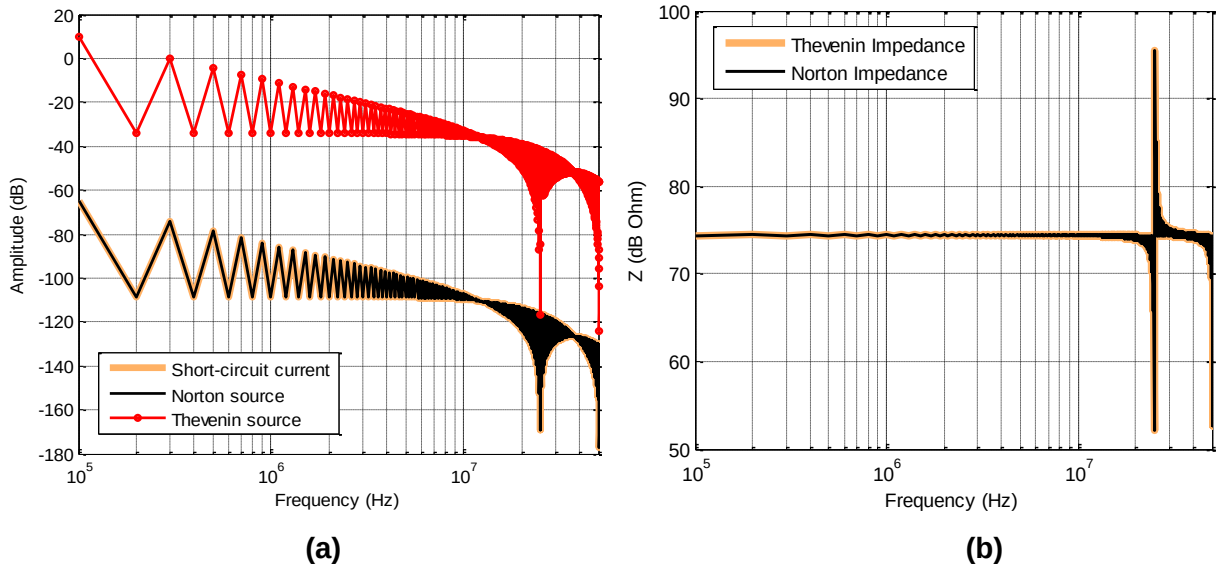

Fig. 2.4: (a) Calculated Thevenin and Norton sources (b) Calculated Thevenin and Norton impedances

Let us compare the model with our expectations. The calculated Norton source matched the simulated short-circuit current, however the Thevenin source did not because it is expected to be just dc. Thus it can be seen that the Thevenin source in this network has no mapping from time-domain to frequency-domain but the Norton source has physical meaning in both domains. From Fig. 2.4 (b), the impedance is seen to be identical but does not make any physical sense as we do not know what a switched resistance is supposed to look like in frequency-domain. Nevertheless, let's assume that the calculated impedance is useful. We now try to use the model to predict the terminal voltage for two different cases. In one case the network is terminated with 25 Ω resistance and in the other it is terminated with 50 kΩ resistance. Fig. 2.5 (a) and Fig. 2.5 (b) show these results. It can be seen that the models predict for 25 Ω but the error is higher in

case of 50 kΩ. Thus there is no unique Thevenin or Norton equivalent that completely describes the terminal behavior of the network. The reason for the mismatch in case of 50 kΩ resistance can be explained as follows. For the network of Fig. 2.3, as the resistance between the terminals increase ($\rightarrow \infty$), the voltage will start to decrease at all frequencies except at dc and this is because the open circuit voltage is just a 100 V dc source. However the Thevenin equivalent of the network has a constant switched voltage source with constant impedance, so the terminal voltage is seen to increase with the increase in the resistance at all frequencies, which is obvious. This is the contradiction. We see an opposite trend in the predicted terminal voltage from what we would see in a reality.

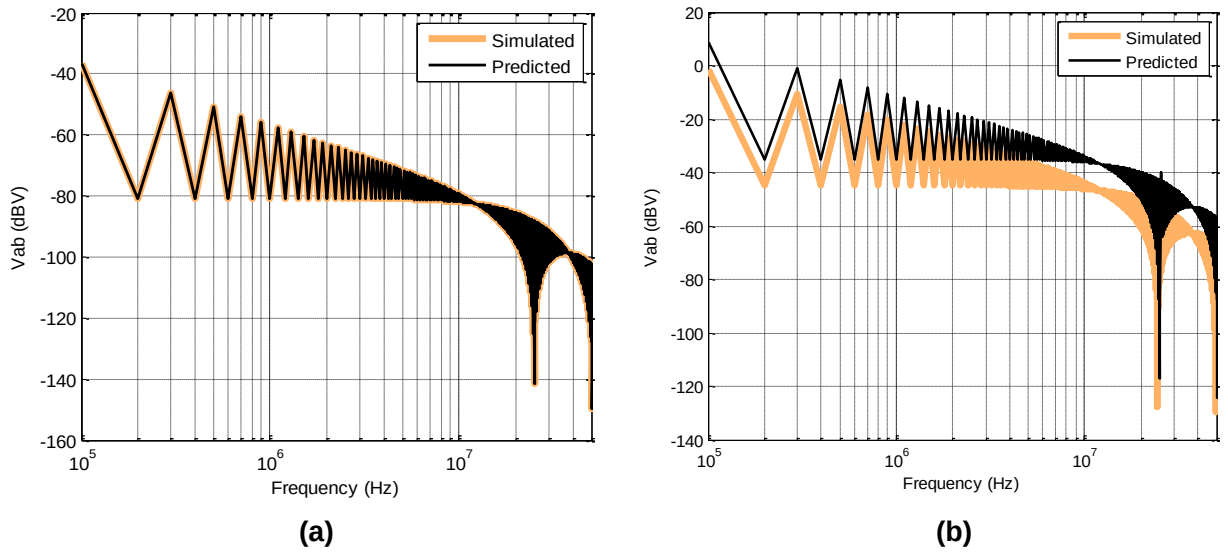

Fig. 2.5: Predicted terminal voltages for (a) 25 Ω (b) 50 kΩ

Stated another way the prediction results will be accurate only when the Thevenin/Norton impedance becomes irrelevant in comparison with the resistance at the terminals of the network. This will happen when the terminating resistance is much smaller than the equivalent Thevenin/Norton impedance. In other words, if the terminating resistance is R_T then from the Norton equivalent the voltage drop across it is given by

$$v_{R_T} = I_N \frac{R_T Z_N}{R_T + Z_N} = I_N R_T \left(\frac{1}{\frac{R_T}{Z_N} + 1} \right) \tag{9}$$

When $R_T << Z_N$, we can approximate the terminal voltage as

$$v_{R_T} \approx I_N R_T \tag{10}$$

This leads to another important conclusion that the calculated equivalent impedance of the network is wrong and is only adding errors into the prediction of terminal voltages.

2.2.2 Switched Thevenin and Constant Norton Source

As the name suggests, this type of network is in fact the dual of the network in Fig. 2.3 and an example is shown in Fig. 2.6. The conclusions from the simulations of this network are also similar to the ones obtained before. Let's choose R_S = 25 kΩ and R_E = 30 kΩ. Then using equation sets (5)-(6) and (7)-(8), the model is derived and is shown in Fig. 2.7. Again it can be seen that the impedance does not make any physical sense. For the equivalent sources the Thevenin source does match the simulated open-circuit voltage but the Norton source will never match the expected short-circuit current as it is dc in this case. With these models, prediction is attempted for terminating resistance of R_T = 500 Ω and R_T = 50 kΩ. The results are shown in Fig. 2.8. It can be seen that the model correctly predicts for resistances larger than the maximum switched resistance of 11 kΩ but for smaller resistance the prediction results are not so accurate.

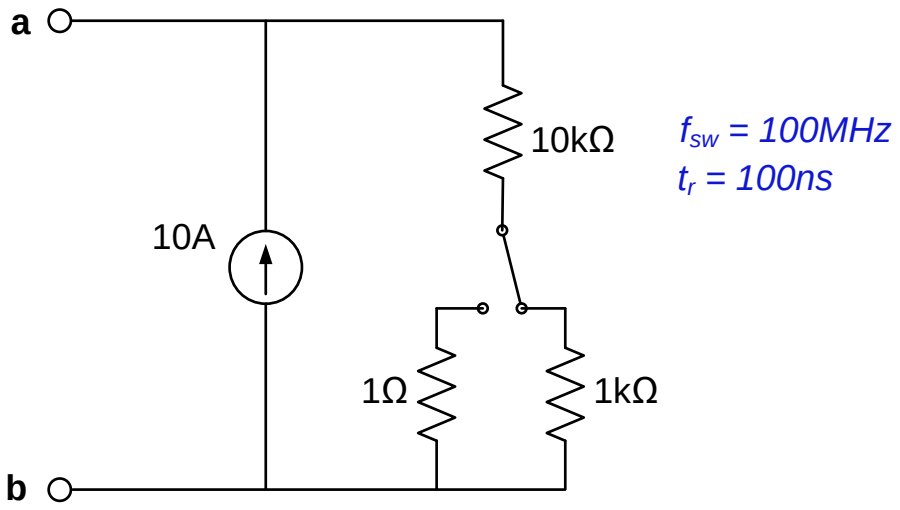

Fig. 2.6: An example of switched Thevenin Source and dc Norton source network

Again like before, the observation here suggests that the predictions come out right only when the identified equivalent impedance of the network is insignificant in comparison to the

resistance applied at the terminals of the network. Thus the observations are also dual of the ones we saw before in the case of switched Norton and constant Thevenin sources.

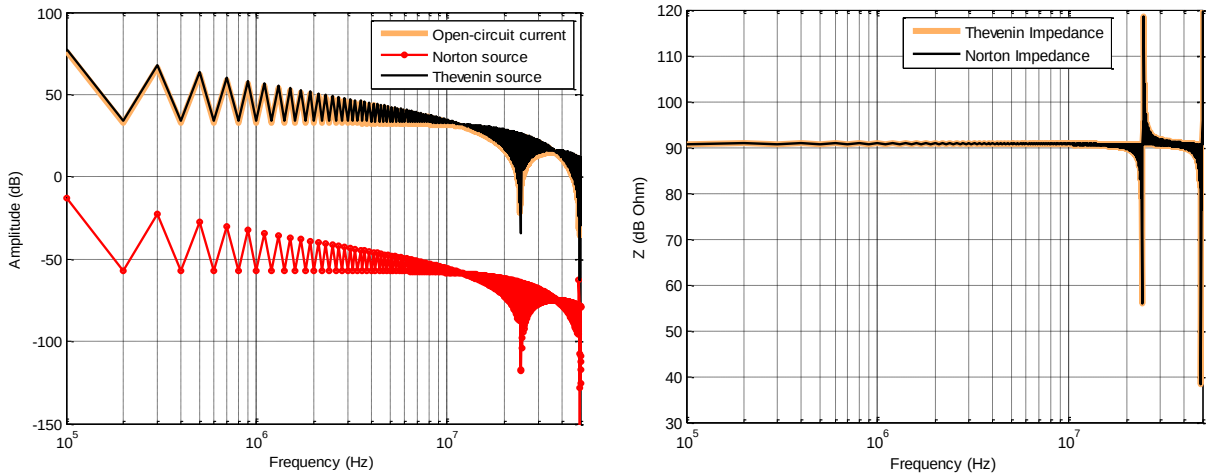

(a) **(b)**

Fig. 2.7: Calculated Thevenin and Norton sources (b) Calculated Thevenin and Norton impedances

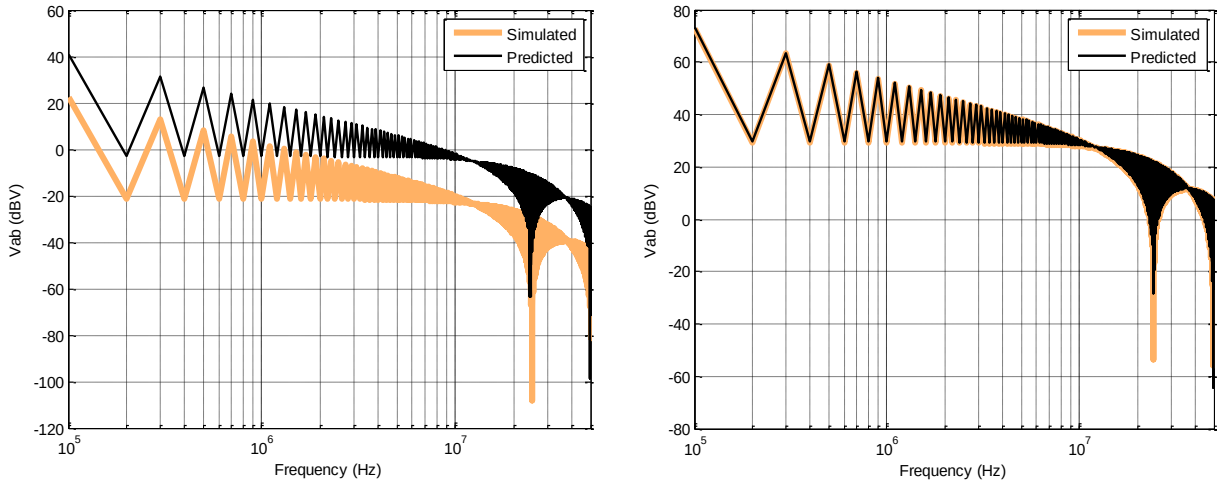

(a) **(b)**

Fig. 2.8: Predicted terminal voltages for (a) 50 Ω (b) 50 kΩ

2.3 CONCLUSIONS

We saw from the previous discussion that applying the behavioral modeling technique to a nonlinear and time-variant network leads to only a fictitious model that has no physical meaning.

Its range of prediction is also limited by the relative value of impedance applied to its terminals to the derived equivalent impedance. Thus the behavioral modeling technique in general is not applicable to nonlinear and time-variant networks. This raises an important question, under what conditions could it be applicable? We know that most power converters have either an inductor (like in boost converter) or a capacitor (like in buck converter) at their inputs. These elements provide dominant impedance at the input terminals of the converter thus masking the nonlinear part of the converter which has semiconductor switches and diodes. Thus looking in from the terminals, the system does not appear time-variant at all. Even for the case shown in Fig. 2.3, it is seen that the 10 kΩ resistance is masking the time-variant part of the network. As long as the external impedance is smaller than 10 kΩ, the fact that the system is non-linear and time-variant will not matter and the extracted terminal model will give good prediction results. However, if the external resistance becomes comparable (or greater) to the masking impedance (10 kΩ) the model will start to fall apart.

Another important question is under what conditions use of constant linear sources is justified. Intuitively such an approximation is only possible when the application of external impedances to the terminals of the network do not disturb the switching waveforms (voltage and current) across the devices. For a buck converter, the input capacitor not only provides the essential masking impedance but also provides the much needed switching energy for the devices, thus eliminating the influence on the switching performance on the external network. For a boost converter it is the input inductor and the output capacitor that provides the masking impedance. In [58], a similar reason is cited.

The question of what is the minimum masking impedance for this technique to work is not a trivial one. Some attempt has been made in [74] but the results are questionable due to the analysis of a nonlinear network using superposition. The reason being is that the masking impedance has a dual job of masking the non-linear part of the circuit and also reducing the influence of the external network on the switching waveform. Satisfying only of these criterions does not serve the purpose. More-over the time varying impedance of the switches when they are changing their state (at the switching instant and in between the two states) is extremely hard to model and therefore it is not easy to determine the exact minimum impedance for masking.

3 TERMINATED EMI-BEHAVIORAL-MODELS

The previous chapters detailed the work that has been in the field of EMI-behavioral-modeling and some fundamental limitations of the technique itself. Let's start now with the discussion of *terminated EMI-behavioral-models*. From the literature review, this is the only type of modeling that has been attempted so far. Extensive work has been done in the development of the technique, principally by Qian Liu [19, 45, 47, 50, 52, 53] and Andrew C. Baisden [55, 59-61] along with few others. The work presented in this dissertation uses Andrew's results as the basis and then build-on from there. The experiments that will be covered in this chapter complements his research.

To have a meaningful start, let's attempt modeling a Half-Bridge inverter using the conventional physics based modeling technique. This discussion should set the motivation behind the alternate EMI modeling techniques in the right path.

3.1 PHYSICS BASED MODELING

3.1.1 Half-Bridge Inverter

Fig. 3.1 shows the circuit for a half-bridge inverter connected to LISN and Fig. 3.2 shows the picture of a half-bridge test set-up. The half-bridge inverter operates as an open-loop control dc-ac converter with 100 V dc input and 100Hz, 70 V peak-to-peak ac output across a 50 Ω load (R_L). The switching frequency (f_S) is 100 kHz. The input bulk capacitors (C_{IN}) are 47 µF electrolytic capacitors. The diodes in the phase-leg are 600V/10A silicon carbide diodes (C3D10060A) from Cree® and the IGBTs (HGTG12N60A4) are 600V/12A N-channel IGBTs from Fairchild®.

3.1.2 IGBT Model

Insulated gate bipolar transistors (IGBT) HGTG12N60A4 were selected for this study. These IGBTs are 600V/12A N-channel IGBTs and are manufactured by Fairchild®. Fairchild® also has a physics based model available for this device on their website. This model has been used without any modification. Modeling of a semiconductor device is not in the scope of this study.

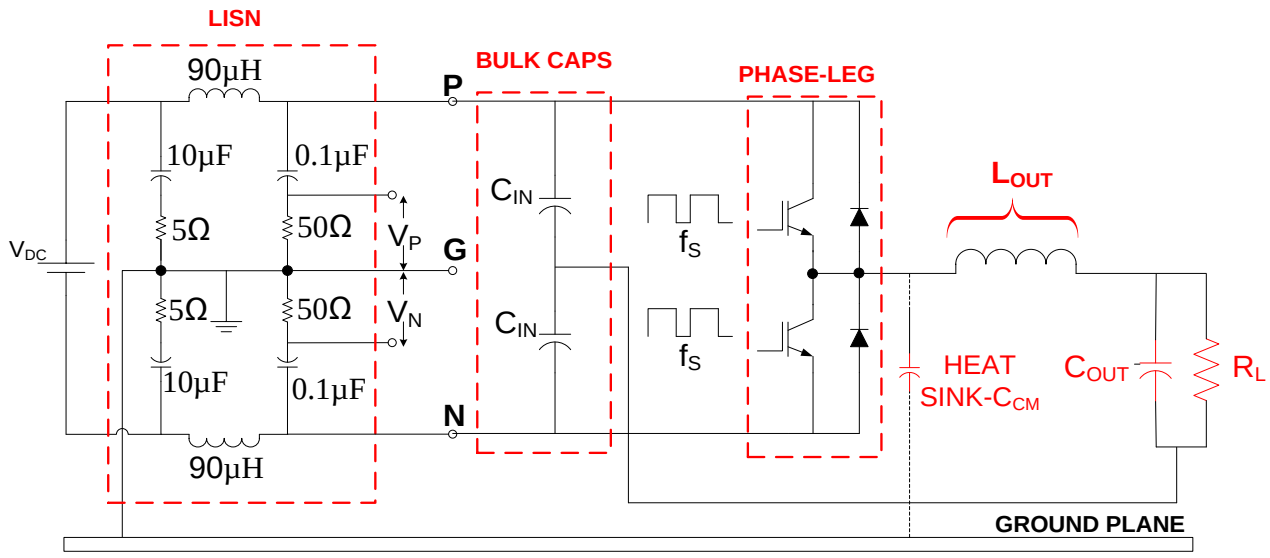

Fig. 3.1: Schematic of half-bridge inverter set-up

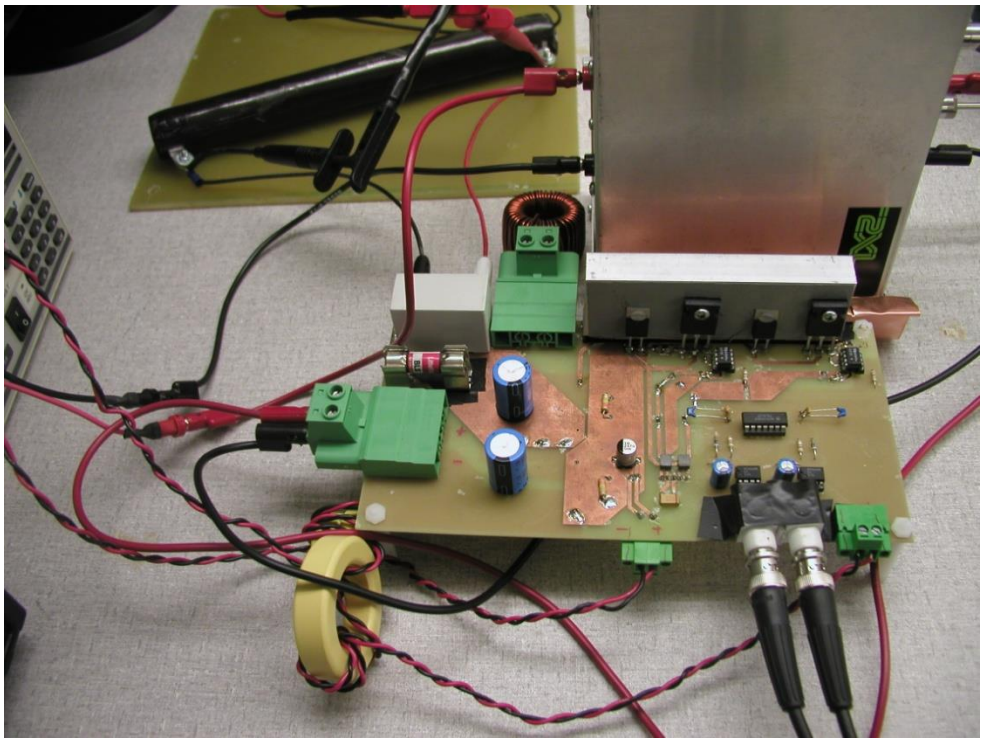

Fig. 3.2: Half-bridge inverter laboratory set-up

3.1.3 Diode Model

CREE 600V/10A silicon carbide (SiC) diodes C3D10060A were selected for the free-wheeling operation. Again the physics-based model of these devices was obtained from

manufacturer. The model available was a SPICE model which was converted into a SABER® model. To do that, an ideal diode was chosen from the SABER® parts library and its model parameters were changed on the basis of SPICE model file. Default values were used for parameters not specified in SPICE model.

3.1.4 Printed Circuit Board Model

A lumped-circuit model of the printed circuit board (PCB) was developed using Q3D extractor®. This tool can be used to extract parasitic circuit elements in irregular and arbitrary geometries and generate inductance/capacitance matrices for multi-conductor interconnects. The Altium Designer® was used to design the PCB and a snapshot of the completed PCB is shown in Fig. 3.3.

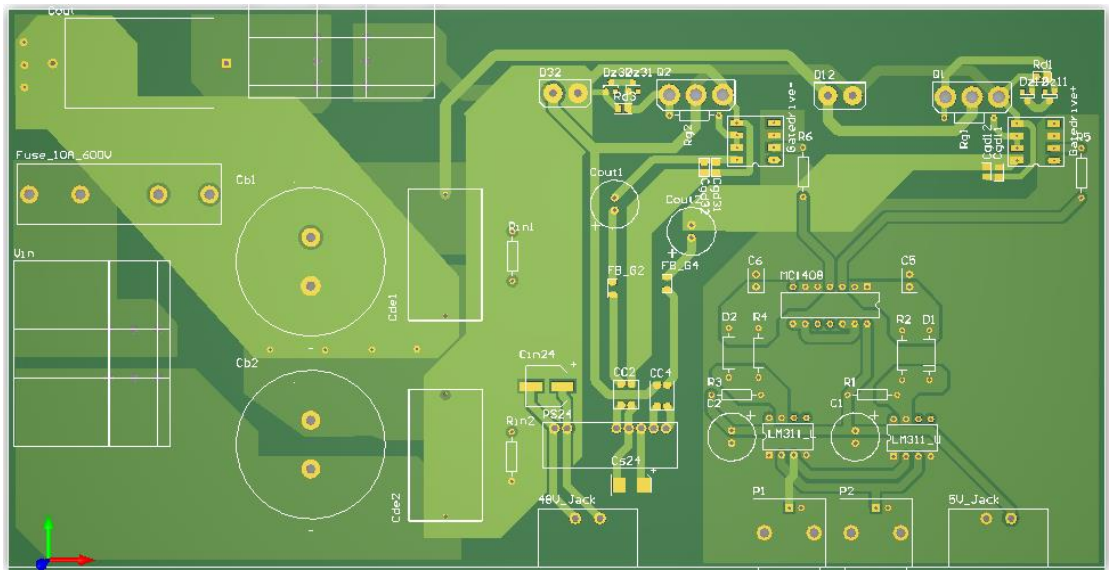

Fig. 3.3: PCB for half-bridge inverter in Altium Designer®

The PBC file was first exported from Altium Designer® into AutoCAD format, and then imported into Q3D extractor®. Fig. 3.4 shows the view of the PCB in Q3D extractor® window. EMI from power stage usually dominates the emission spectrum and hence only the power stage of the PCB was modeled. Each trace was modeled separately to find its parasitic inductance. Mutual capacitances between traces were neglected except for some regions where it was expected to be significant.

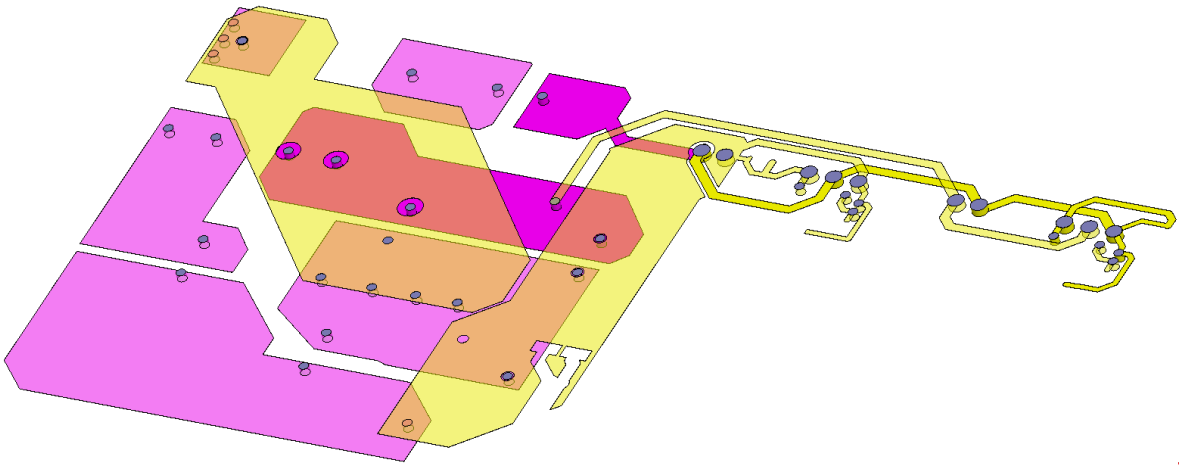

Fig. 3.4: PCB for half-bridge inverter in Q3D extractor®

3.1.5 Component Models

Other components like the bulk capacitors and, output inductor etc. were modeled by directly using measurements with an impedance analyzer. Simple RLC models were then fitted to these measured impedances. Fig 3.5 shows the comparison for the measured and fitted impedance for the output capacitor (C_{OUT}). The equivalent circuit model of C_{OUT} is also shown in Fig 3.5. All models were made to fit until 100 MHz. The model of the inductor can be found in [59].

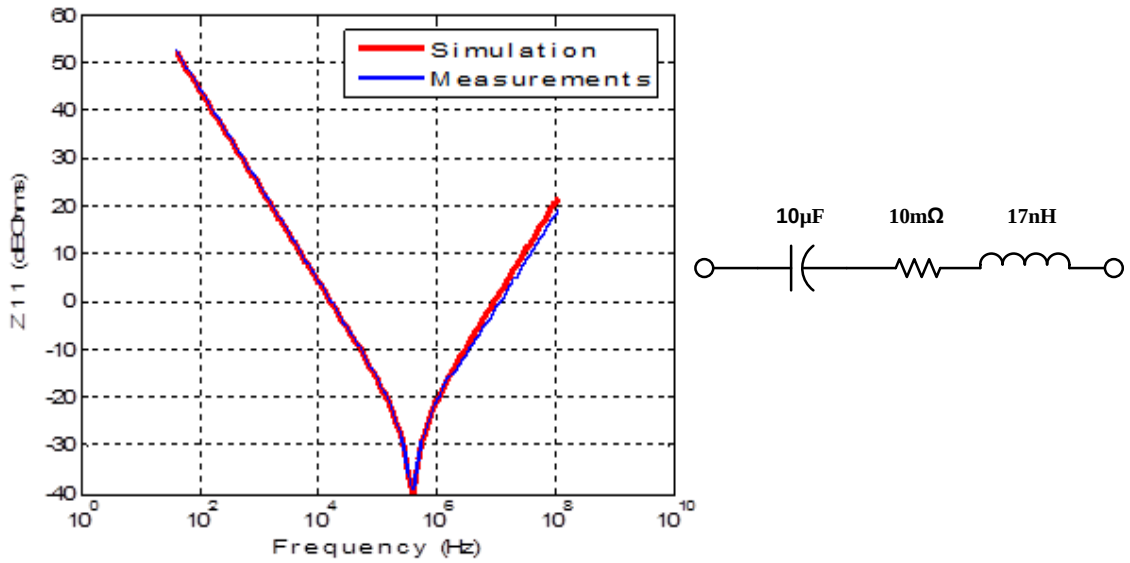

Fig. 3.5: Lumped circuit model of output capacitor

3.1.6 Model of Ground Plane

The CM impedance or the impedance of the ground connection between the converter and the LISN was measured directly. The CM capacitances from the device to the heat-sink were measured directly and the ground plane inductance was measured and tuned. There was a slight issue with tuning the ground plane inductance as the plane was constructed by a copper foil rather than a solid copper sheet thus lacking mechanical stability. If the foil was bent or moved the inductance was found to change slightly. Fig. 3.6 shows the final model that was used in the simulation for the CM path impedance. Here Q1 and Q2 are the collectors of the IGBTs and D1 and D2 are the cathodes of the anti-parallel diodes.

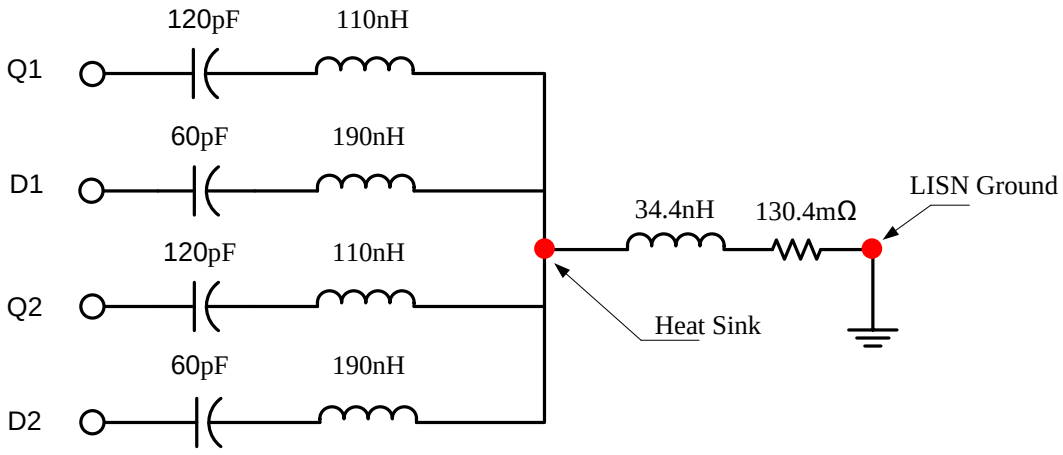

Fig. 3.6: CM path impedance model

3.1.7 Full Lumped Circuit Model

We can now combine all the models in SABER® to form the full lumped-circuit model of half-bridge inverter. Fig. 3.7 shows this SABER® model. The observed rise time and fall time in hardware were replicated in the gate driver constructed in SABER®. The gate driver input was modeled using Q_3D® as well. Thus all possible efforts were made to make the model as accurate and realistic at possible. Any further detailing of models would be too complicated and time consuming. As mentioned before, an expected source of error was the modeling of ground connection formed by the copper foil. The inductance of the copper foil (34.4nH) along with parasitic capacitance between the devices and the heat-sink (120 pF) resonates at around 80MHz.

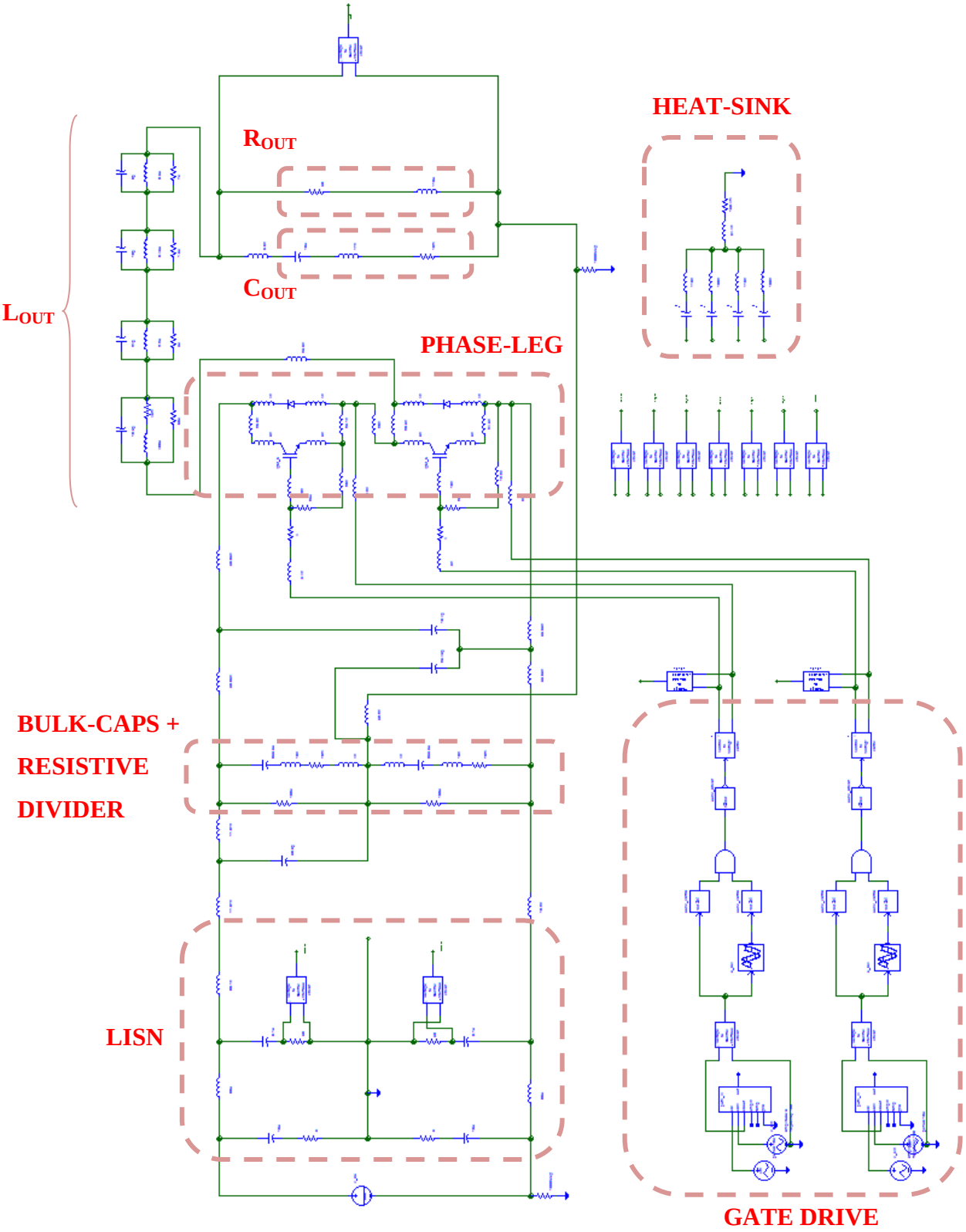

Fig. 3.7: Lumped Circuit Equivalent model of half-bridge inverter

Any movement of setup or change in shape of the copper file resulted in the shift of the resonance frequency. Thus matching this resonance was found to be a problem. It led to an obvious conclusion that the fixture has an influence electromagnetic fields and thus must be mechanically stable to ensure repeatability of EMI experiments

3.1.8 Simulation Results

The circuit was simulated for one full-line cycle of 100Hz with a time step of 2nsec. This is required to get the necessary detail in the waveforms for frequencies up-to 100MHz. The comparison of the output voltage across R_{OUT} between the simulations and the measurements is shown in Fig 3.8. In the background (in rainbow colors), we have the waveform as observed on the oscilloscope in the fast acquisition mode and overlapped (in blue) on top of it inside the red box is the waveform obtained from the SABER® simulations. The results were found to match well with the measurements. The EMI spikes riding on the output waveform are evident in both simulations and measurements. As the operating point moves up the average spike size increases and the SABER® model were able to replicate this. Off course the random nature of spike size cannot be captured by simulations.

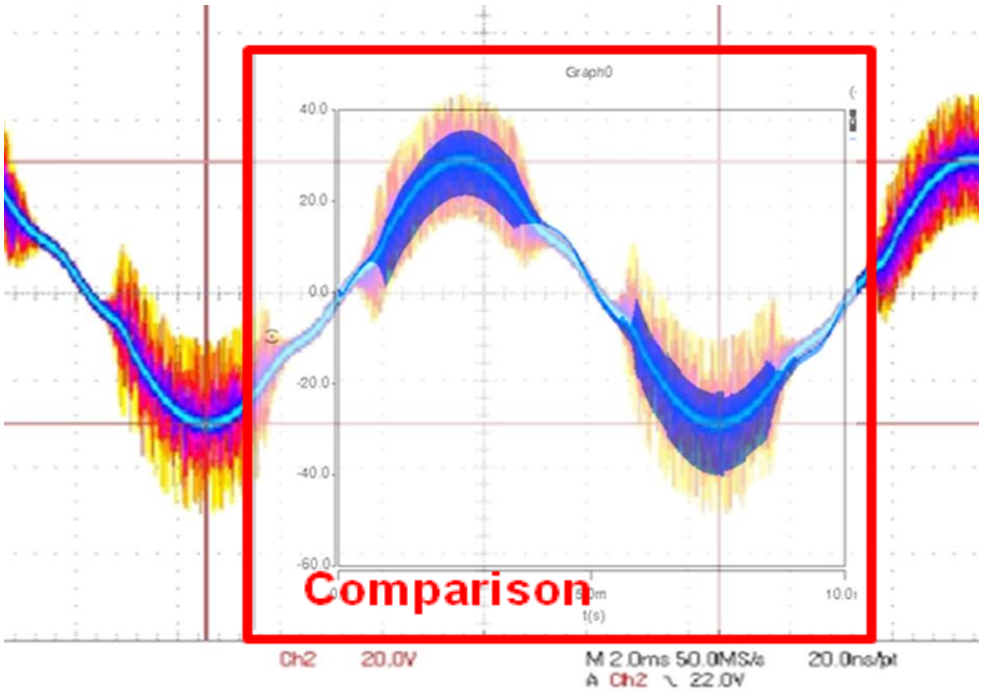

Fig. 3.8: Comparison of measured and simulated waveforms from lumped circuit model in SABER®

3.1.9 EMI Noise Simulations For A Buck Converter

It is confirmed from the above results that "functionally" the SABER® simulation model is good and can be used for EMI analysis. To compare the EMI results the half-bridge inverter was made to work in the buck mode by short circuiting the bottom capacitors and adjusting the drive signals. Changes were made in simulation accordingly.

A comparison of the simulated and measurement noise on the LISN was made and is shown in Fig. 3.9. As a first experiment the ground plane was removed and hence the noise received on the LISN was dominated by the DM. The ground plane model (Fig. 3.6) was disconnected to simulate this condition. Fig. 3.9 (a) shows the frequency domain comparison of measured and simulated noise on the positive side of the LISN and Fig. 3.9 (b) shows the time domain noise comparison of simulated and measured noise. It can be seen that the simulated results compare well with the measured ones at most frequencies up to at least 30 MHz, which is the limit of conducted emissions as per most commonly used standards.

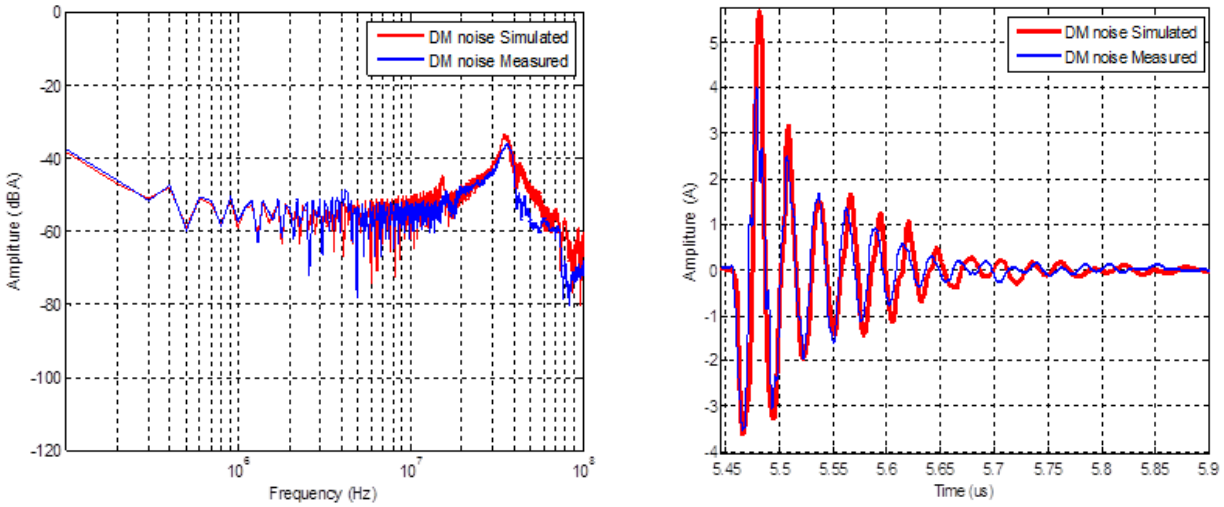

Fig. 3.9: Comparison of measured and simulated DM noise on the LISN

The ground plane was then connected and comparisons were made between the simulated and measured conducted noise at the LISN. To simulate this case the CM model (Fig. 3.6) was in the simulations. Fig 3.10 shows the CM and DM noise comparison of simulated and measured

results. As expected, a mismatch at 80 MHz is seen because of the inaccurate model of the ground plane. If the copper foil is bent slightly, this resonance in the measurement was seen to shift. The plot in green shows the error in the simulated results. The error increases as the frequency increases, but in general the match was found to be fairly good.

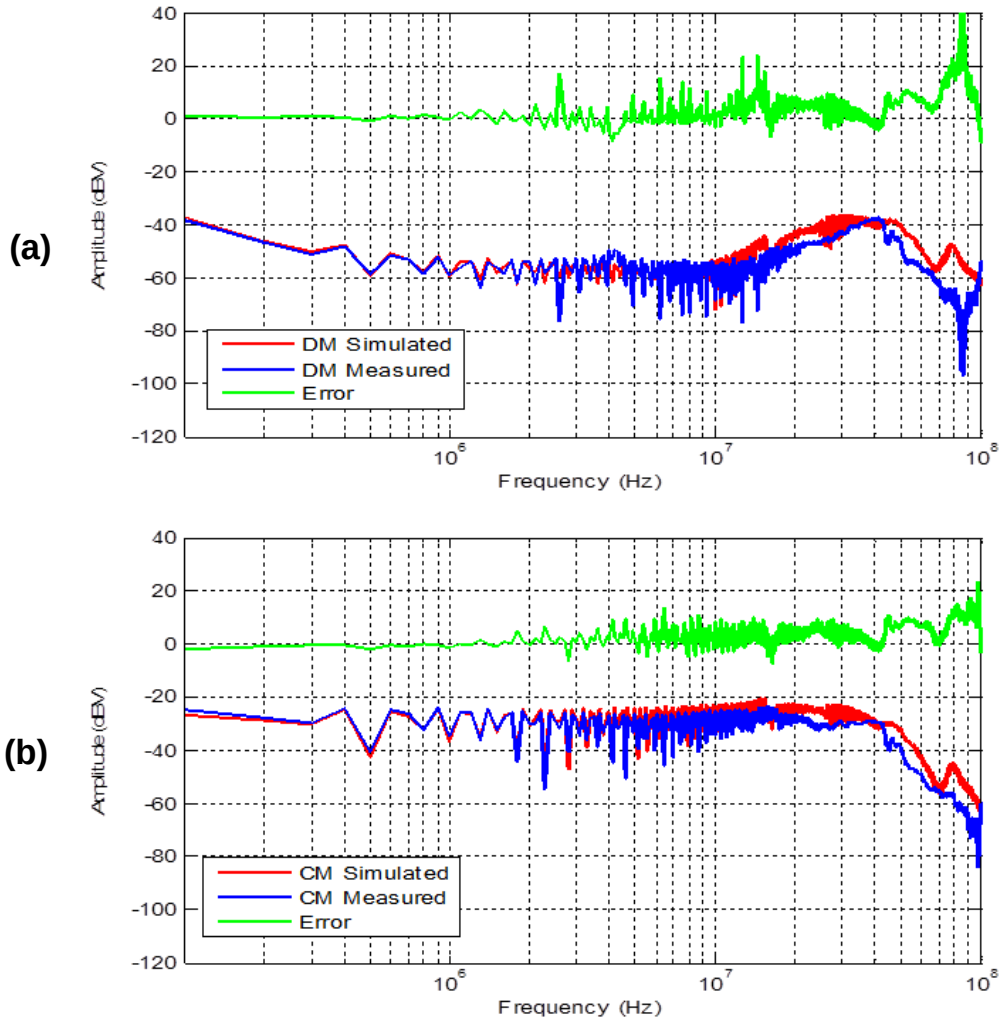

Fig. 3.10: Comparison of simulated and measured CM and DM noise on the LISN

3.1.10 Advantages and Limitations

The above experiments show that physics based lumped circuit models are useful and can facilitate EMI troubleshooting. In fact these types of models are the most versatile as well. Say we want to see the performance of a different set of devices than the ones we used. All that needs

to be done is to replace the current device models with the new ones. Thus lumped circuit model are easily modifiable and are modular in structure. They are very useful in conducting parametric analysis for the converter.

The problem with the lumped circuit modeling technique is the time and effort that goes into making them work. It took about 45 days to make the model for a half-bridge inverter and achieve a successful run in the SABER® simulator. The model was found to be moderately robust. Even small changes in the parasitic make the simulation crash. To run it again, the simulator parameters had to be adjusted and this often involved quite a bit of trial-and-error. Every simulation takes about 20 minutes mainly because of the presence of large inductances in the LISN which results in very long time constants. It should be noticed that all this trouble had to be taken for a power converter that has only one phase-leg. It is understandable that such models for a multi-phase converter would only take longer to develop and would only cause more problems with simulations.

Another important limitation is that the lumped circuit modeling required intimate details of the circuit's geometry. If the details regarding the devices, components and PCB are not available, it is impossible to develop such an accurate model of the converter. Moreover, looking at the difficulty in simulating such models, it's quite evident that they are not suited for system level EMI analysis. In system engineering like aircraft manufacturing, the engineers may need to integrate converters from several different manufactures into the power distribution network of the aircraft. These manufactures most often do not provide internal details of their converters as its propriety information. Thus alternate EMI modeling techniques are needed to address these problems.

This is the motivation behind the research work done in behavioral modeling techniques. These techniques are aimed at developing black-box models of the power converters. The models can then be used for system level EMI study and since they are black-box, there is no need for any internal details of the converter. Also since these models are reduced order, meaning they have only a few sources and impedances, they can be simulated without any significant convergence problems with the simulator.

The limitation of black-box modeling is that, the internal details of the system are lost and hence parametric analysis due to changes in devices or other components cannot be investigated. Thus both kinds of EMI models are important and it only depends on who is using it and what is

the purpose. For the manufactures of the converter, lumped circuit modeling is more useful but once their design is ready they can extract a black-box model using behavioral modeling techniques and give it to their customers (system engineers). In this way their design information is protected. The lumped circuit modeling technique has been around for several decades but the solutions for system level black-box models are very limited and still needs investigation on their extraction procedure and utility.

3.2 BUCK CONVERTER

As discussed in the previous section, to address the problems of system level EMI issues there was a need of an EMI modeling technique that is simple to simulate and yet accurate in the entire conducted emissions band. This led to development of behavioral EMI modeling techniques. The GTM [60] is a terminated EMI modeling technique and has been shown to predict EMI from a boost converter at most frequencies up to 100 MHz with really good accuracy. The next thing is to extend this technique in modeling EMI from a buck converter. We start by first giving the model definition of a three-terminal Norton equivalent that will be used to model EMI noise from a buck converter.

3.2.1 Model Definition

This section reviews the generalized behavioral modeling procedure. Fig. 3.11 shows a buck converter and its equivalent three-terminal EMI model. C_{CM} denotes the parasitic capacitance of the converter to the ground. The model has two current sources and three equivalent impedances. This model is a generic three-terminal Norton equivalent of a linear network. In Fig. 3.11, terminals positive (P), negative (N) and ground (G) are matched to the input terminals of the buck converter. The goal is to model the entire buck converter at these input terminals using the three-terminal model.

In the measurements of conducted emissions, it is required to isolate the device under test (DUT) from the power source with a line impedance stabilization network (LISN). For modeling purposes, the LISN is replaced with its output impedances ($Z_{LISN\text{-}P}$ and $Z_{LISN\text{-}N}$), as shown in Fig. 3.12. The modeling procedure assumes that the converter appears to be linear and time-invariant at its input terminals. This assumption however should be verified for every converter

before behavioral EMI modeling in carried out. The following loop equations can be derived from Fig. 3.12:

$$V_{PG} = \left(I_{PG} - \frac{V_{PG} - V_{NG}}{Z_{PN}} \right) \cdot Z_{PG} \parallel Z_{LISN-P} \tag{1}$$

$$V_{NG} = \left(-I_{NG} + \frac{V_{PG} - V_{NG}}{Z_{PN}} \right) \cdot Z_{NG} \parallel Z_{LISN-N} \tag{2}$$

The case shown in Fig. 3.12 is referred to as the nominal case. In order to solve for five model parameters, other equations can be developed by adding shunt impedance(s) between P and G, between N and G, or both. These configurations are referred to as attenuated cases. Fig. 3.13 shows the attenuated case when the shunt impedance is applied to the positive side of the LISN. Equations (3) and (4) are derived from Fig. 3. Similarly, (5) and (6) are derived for the case when the shunt impedance is applied on the negative side of the LISN. Note that when the shunt is applied, the EMI noise voltages at the LISN change. Thus voltage terms in all of the following equations are different for each case.

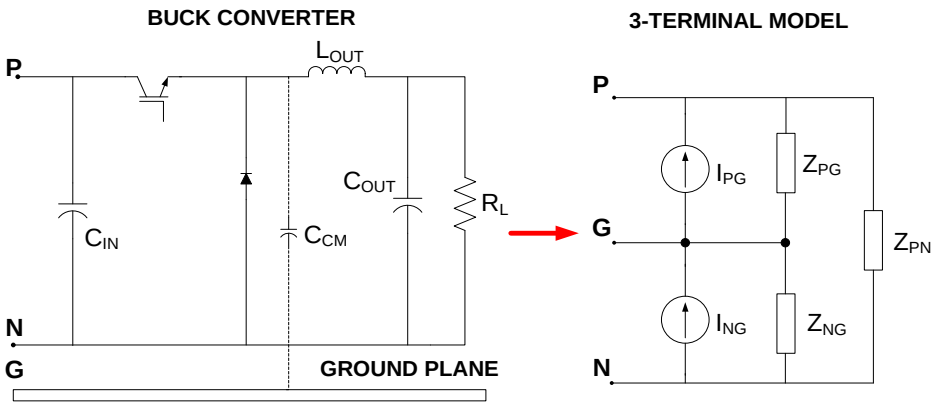

Fig. 3.11: Generalized three-terminal model of buck-converter based on Norton equivalent.

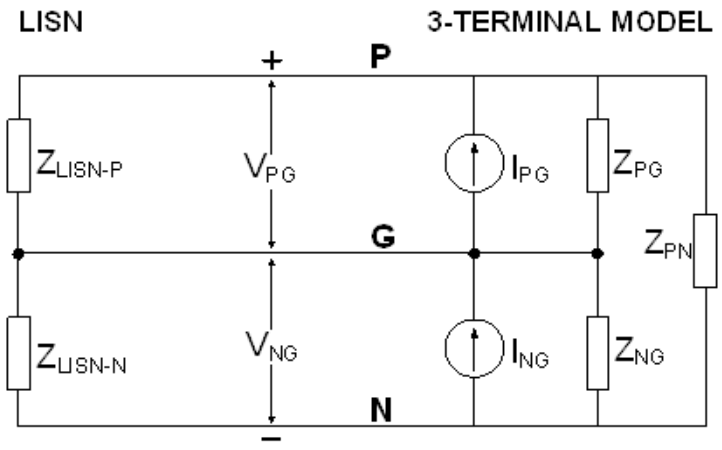

Fig. 3.12: Nominal case for model extraction.

$$V'_{PG} = \left(I_{PG} - \frac{V'_{PG} - V'_{NG}}{Z_{PN}} \right) \cdot Z_{PG} \parallel Z_{LISN-P} \parallel Z_{SHUNT-P} \tag{3}$$

$$V'_{NG} = \left(-I_{NG} + \frac{V'_{PG} - V'_{NG}}{Z_{PN}} \right) \cdot Z_{NG} \parallel Z_{LISN-N} \tag{4}$$

$$V''_{PG} = \left(I_{PG} - \frac{V''_{PG} - V''_{NG}}{Z_{PN}} \right) \cdot Z_{PG} \parallel Z_{LISN-P} \tag{5}$$

$$V''_{NG} = \left(-I_{NG} + \frac{V''_{PG} - V''_{NG}}{Z_{PN}} \right) \cdot Z_{NG} \parallel Z_{LISN-N} \parallel Z_{SHUNT-N} \tag{6}$$

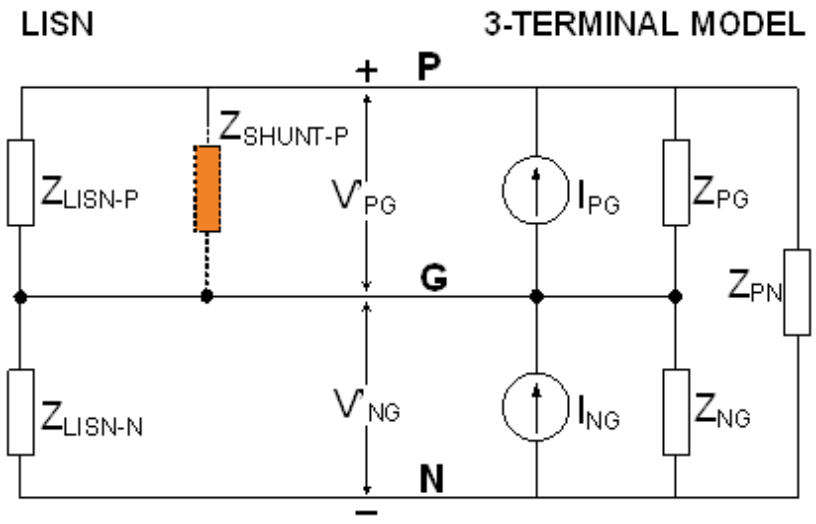

Fig. 3.13: Attenuated case for model extraction.

Equations (1) - (4) and (6) can be now solved for I_{PG}, I_{NG}, Z_{PG}, Z_{NG} and Z_{PN}. The final closed-form solutions are complicated; hence, they are not shown here for the sake of simplicity [59]. This procedure, although shown here for a buck converter, in general is the same for any power converter with three-terminals at its input. It should be noted that the model is always extracted at one operating point and hence cannot be used over a wide range of operating conditions. However, since the model is develop only for EMI, separate models for one or a few worst-case operating conditions should be enough to address all EMI issues.

The model shown in Fig. 3.11 is just one of the possible topologies that can be used for system identification at EMI frequencies. As mentioned before, a Thevenin model can also be used. In fact, a mixed current and voltage source model such as the one shown in Fig. 3.14 is also possible. Here V_{CM} represents the common mode voltage with respect to ground and the current source I_{DM} is the differential mode currents drawn by the power supply. It should be noted that the model is extracted in an in-circuit test according to EMI standards and therefore the mixed mode noise effect is captured automatically in the two sources. In other words, the noise sources shown in Fig. 3.14 do not represent pure CM or pure DM noise. Though various topologies are possible, there was no significant difference seen in their accuracy. Therefore in the rest of the chapter we use the model given in Fig.3.14

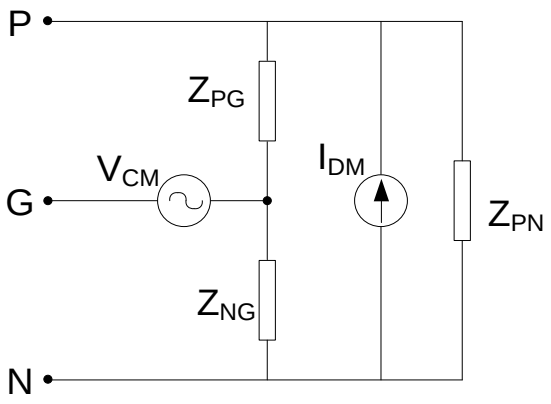

Fig. 3.14: Generalized three-terminal model with voltage and current sources.

3.2.2 Experimental Set-up

3.2.2.1 Buck Converter

The experimental setup is shown in Fig. 3.15. As mentioned earlier, the half-bridge inverter discussed in previous sections is used here in the dc-dc mode. The buck converter operates with 200 V dc input, and 100 V dc output across a 50 Ω load. The switching frequency (f_S) is 100 kHz. The input capacitor (C_{IN}) is a 47 µF electrolytic capacitor. The diode is a 600V/10A silicon carbide (SiC) diode (C3D10060A) from CREE and the IGBT (HGTG12N60A4) is a 600V/12A N-channel IGBT from Fairchild. Fig. 3.16 gives the picture of the laboratory set-up.

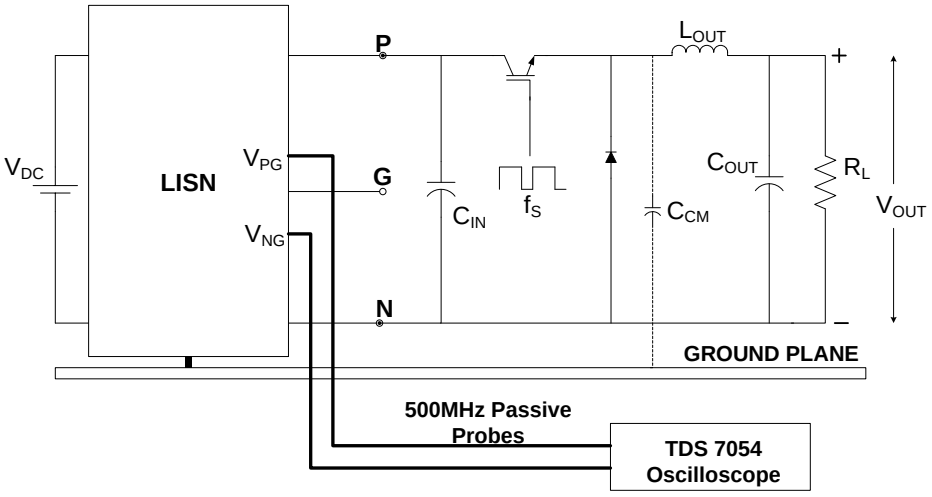

Fig. 3.15: Experimental setup for extraction of three-terminal model of a buck converter.

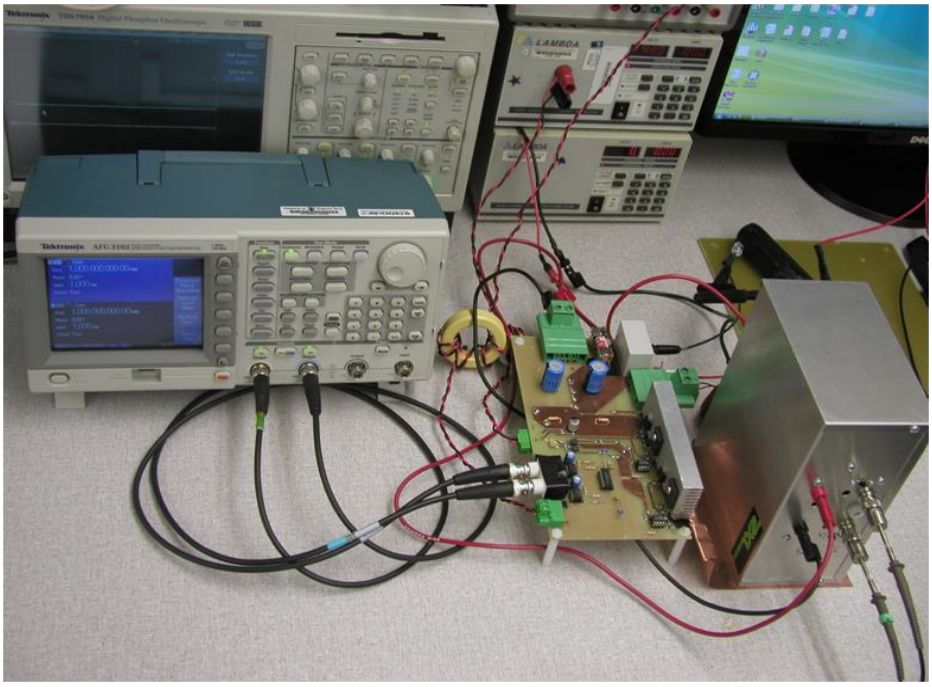

Fig. 3.16: Laboratory set-up for terminal model extraction of a buck converter

To attain better accuracy at high frequencies, the output impedances of the LISN (Z_{LISN-P} and Z_{LISN-N}) and the shunt impedances ($Z_{SHUNT-P}$ and $Z_{SHUNT-N}$) were characterized with an Agilent 4294A impedance analyzer. The scope was set to capture one switching cycle of the converter. It is assumed that all switching cycles are fairly identical unless there is any change in the operating point of the converter. Averaging was used to remove the random noise and the data was recorded with a sampling time of 200 ps/point.

3.2.2.2 Selection of External Impedances

The LISN used for experiments was modified to validate the terminal model under different source impedance conditions. A linear model should be independent of the external network in the desired frequency range and operating conditions. Thus, in order to validate the developed models, two different LISN impedances; 50 Ω and 1 kΩ, were chosen. The modified LISN is shown in Fig. 3.17. Selection switches were added to switch between 50 Ω and 1 kΩ output impedance. A well-conditioned model should be able to predict terminal voltages (V_{PG} and V_{NG}) for both the 50 Ω and 1 kΩ LISN.

An option for including the shunt impedances was also built into the LISN itself. This was done to minimize the effects of parasitic and obtain reproducible results. The shunt impedance used here is a series combination of a 2 µF capacitor and a 1 Ω resistor.

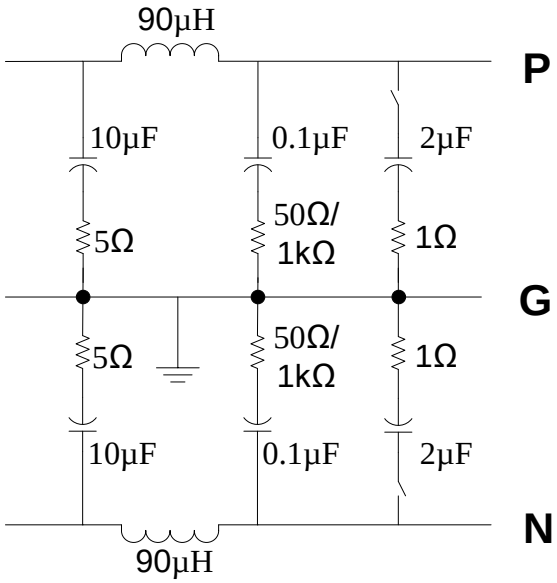

Fig. 3.17: Line impedance stabilization network (LISN).

3.2.2.3 Applicability of the Method

The behavioral modeling method uses linear time-invariant circuits for approximating the EMI behavior of power converters. It is worthwhile to understand the conditions that allow the use of linear time-invariant theory for modeling a power converter which by nature is a non-linear and time-variant network. The discussions here are based on the buck converter described earlier in the experimental set-up but they should apply to any converter that has a buck type input.

The issue of time-variance can be understood by considering the variation in the input impedance of the buck-converter while it is in operation. Fig. 3.18 shows measurements of the DM impedance with an impedance analyzer (Agilent 4294A) for two extreme cases and an under zero dc bias condition. In the first measurement, the devices were physically removed and in the second measurement the devices were short circuited. For a buck converter, these conditions will normally not exist but are chosen here only to show the worst case situations under all operating conditions. It can be seen from Fig. 3.18 that there is no significant difference in the input

impedance in the conducted emissions range (150 kHz to 30 MHz) and even up to 100 MHz. At lower frequencies some difference is seen, however the impedance here is very small. The measurements show that the LISN does not see any significant change in the input impedance of the buck converter under all operating conditions, even during the time when the commutation takes place. The impedance seen in Fig. 3.18 is inductive after 100 kHz and comes from the parasitic inductances of the input dc-bus (L_{BUS}) as shown in Fig. 3.19. These parasitic inductances provide constant and dominant impedance that masks the time varying behavior of the switches. Thus looking from the dc-input side, the buck converted used here can be approximated as a time-invariant network. In a similar way, the CM input impedance can be shown to be constant as well.

The three-terminal model uses two constant and linear current sources to capture the switching noise from the converter. In the case of a buck converter, such an approximation is possible with the presence of an input capacitor (C_{IN}). A properly chosen value of C_{IN} will ensure that the switching waveforms (voltage across the device and the current through the device) remain largely unaffected by any changes in the impedance that converters see into the dc network (LISN). The input capacitor must provide effective decoupling between the dc-bus. The ideas is to keep the impedance of the capacitive branch lower than the impedance of the dc-bus ($Z_{LISN} + Z_{Lbus}$) in the entire frequency range to ensure that the switching energy is derived from the capacitor and not the dc-source.

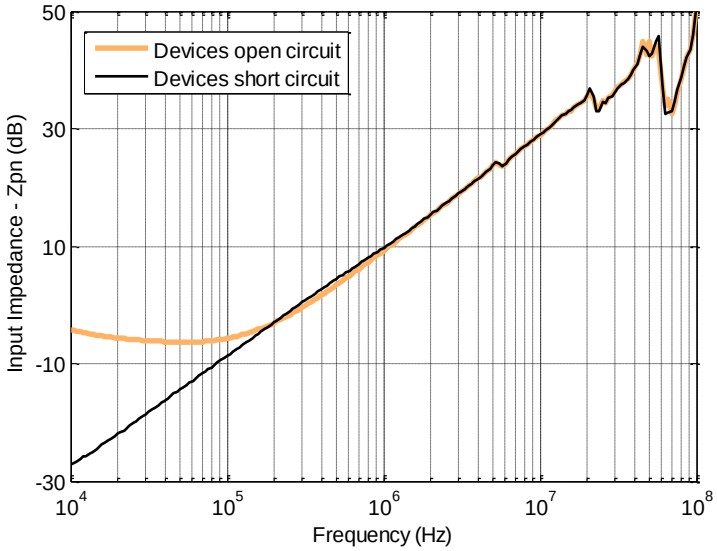

Fig. 3.18: Comparison of input DM impedance with the devices open and short circuited.

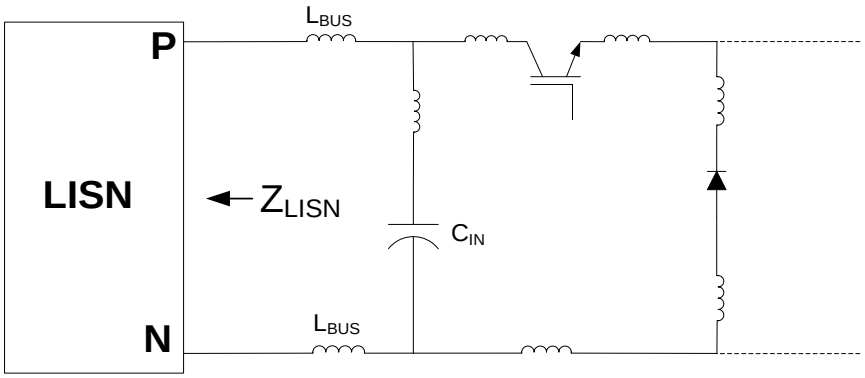

Fig. 3.19: Location of parasitic inductances in the input side of a buck converter.

The basic inference from the above discussion is that as long as the switching waveforms remain preserved from changes in the external network (LISN) and the converter appears time-invariant at its input terminals, the behavioral modeling method can be applied for approximating the EMI behavior of the power converter. The results shown here cannot be assumed for all power converters, especially the low power ones. Depending on the size and geometry of the converter, one should verify if these conditions hold or not. For most medium to high power applications, these conditions are likely to hold true.

3.2.3 Model Results

A three-terminal model was developed for each LISN impedance (50 Ω and 1 kΩ) using the procedure described in section 3.2. It is worth noting that the models of an arbitrary three-terminal LTI circuit created from 50 Ω and 1 kΩ LISN will be identical to each other with respect to the extracted model parameters. This is because in principle a LTI circuit can always be represented by its Norton or Thevenin equivalent, regardless of the external configuration.

Fig. 3.20 shows the comparison of I_{PG} and I_{NG} for the models created from the 50 Ω and 1 kΩ LISN. It is clear that the extracted frequency domain current sources do not show any significant difference when extracted from 50 Ω or 1 kΩ at most frequencies.

Fig. 3.21 (a) shows the comparison of extracted model impedances Z_{PG}, Z_{NG} and Z_{PN}. Z_{PN} is almost the same for both models as this impedance is dominated by the inductance of the input bus and the 47 µF input capacitors between P and N terminals. From Z_{PG} and Z_{NG}, the CM capacitive coupling path is evident. Capacitive behavior can be seen in frequency range from

1 MHz to 10 MHz. Above 10 MHz, several spikes can be seen in the identified model impedances. However, due to better signal to noise (S/N) ratio the spikes in the impedances extracted from 1 kΩ LISN are much lesser. Fig. 3.21 (b) shows the comparison of measured voltage on the positive side of the 1 kΩ and the 50 Ω LISN for the nominal case. It can be seen that at most frequencies the measured voltage in the case of 1 kΩ LISN is about 10dB higher than that of the 50 Ω LISN indicating better S/N ratio. The smaller amplitude, especially at higher frequencies may also cause numerical ill-conditioning of the system of equations. To show this effect the data measured on 50 Ω LISN was re-sampled at 2ns/point resolution and the model impedances were extracted like before. Fig. 3.21 (c) shows the comparison of identified Z_{NG} from the original data-set (200 ps/point) and the re-sampled one. At around 5 MHz and at higher frequencies, where the amplitude of the measured voltage was low (Fig. 3.21 (b)), some new spikes can be observed now. The 1 kΩ LISN was however found to be immune to changes in sampling frequency. Thus in all 1 kΩ LISN is suited better for extraction of model parameters as it provides better S/N ratio.

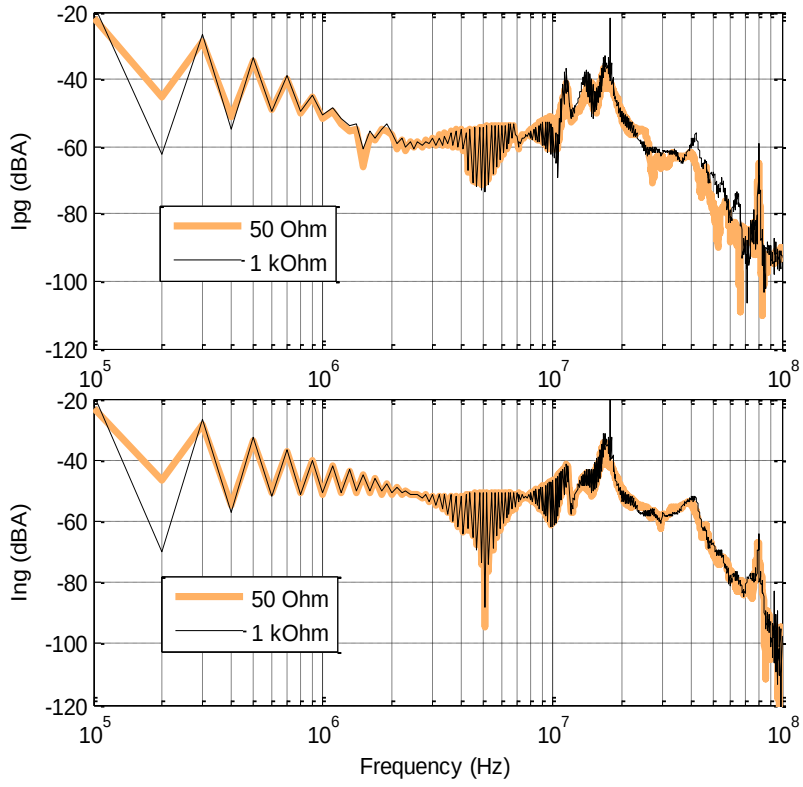

Fig. 3.20: Extracted Noise sources I_{PG} and I_{NG} of the three-terminal model.

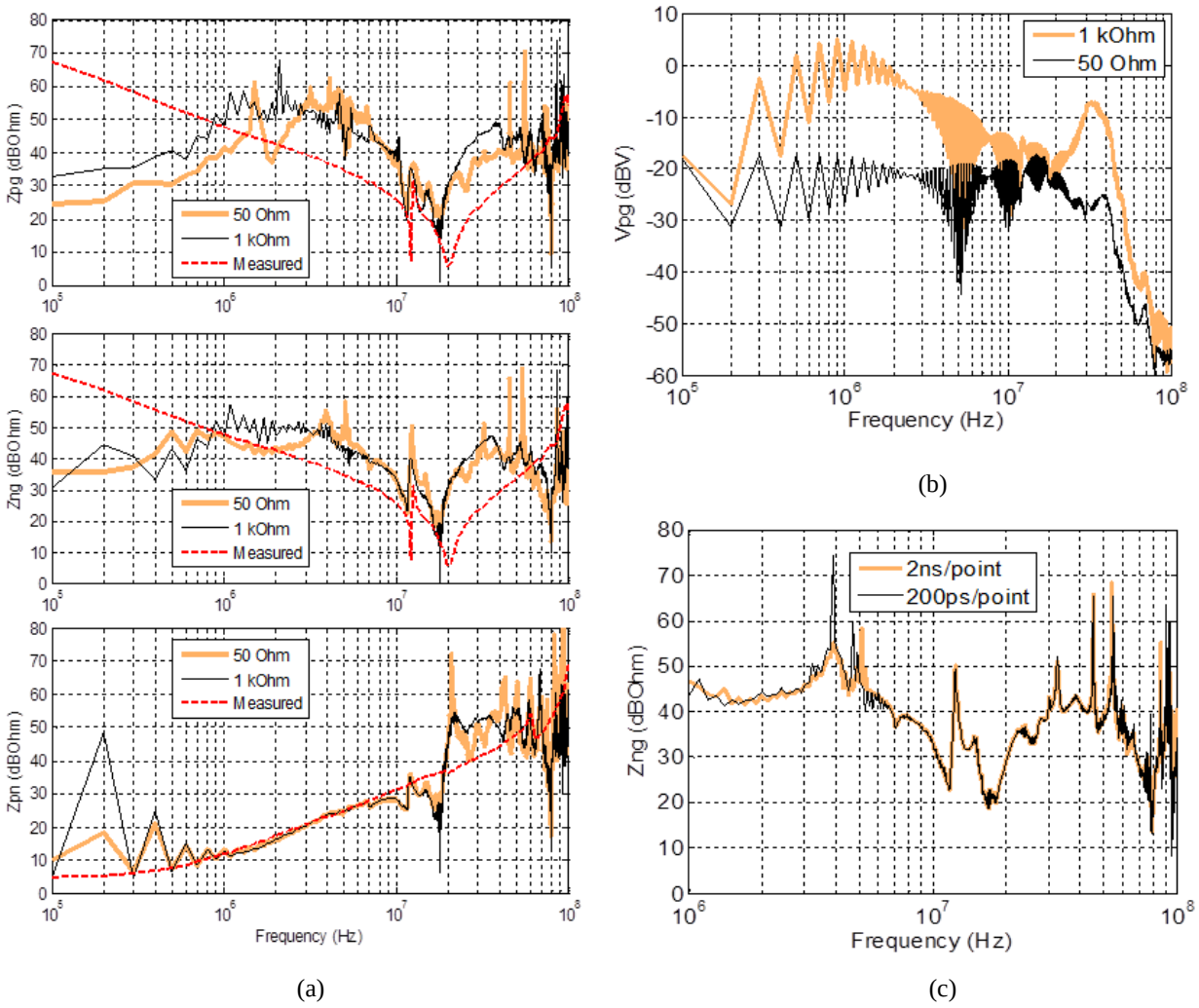

Fig. 3.21: (a) Extracted impedances Z_{PG}, Z_{NG} and Z_{PN} of the three-terminal model. (b) Comparison of measured voltage on 1 kΩ LISN and 50 Ω LISN for the nominal case. (c) Effect of sampling frequency on extracted model impedances from the 50 Ω LISN.

Fig. 3.21 (a) also shows direct measurements of input impedances. These measurements were performed using an impedance analyzer (Agilent 4294A) when the converter was under zero dc bias (converter was switched off) condition. The DM impedance (Z_{PN}) was measured between terminals P and N with the converter isolated from the ground. Direct measurements of Z_{PG} and Z_{NG} were obtained by assuming them to be equal to one-half of the measured CM impedance between P-N short circuited and the ground. It can be observed that the extracted CM impedances (Z_{PG} and Z_{NG}) are asymmetric in the capacitive region. The real topological variation of the CM impedances, which may be different due to the geometry of the converter can be observed here. The CM impedances are also quite different from the ones obtained by direct

measurements. The reason for this difference is that, under zero dc bias conditions the IGBT's impedance is much smaller than the CM impedances. The IGBT output capacitance under zero bias is very large (nF range) compared to parasitic capacitance between the converter and the heat sink (pF range). Thus all parasitic CM capacitances to heat sink appear in parallel. This is evident from Fig. 3.21 (a) as the measured CM capacitance is larger than the ones extracted by the behavioral modeling approach. The extracted DM impedance on the other hand was a good match with the measured DM impedance except at high frequencies. Thus the behavioral modeling technique is useful in estimating model impedances in real operating conditions. Unlike the extracted model impedances, the measurements from impedance analyzer do not show any spikes. Moreover, above 10 MHz there is a mismatch between the extracted Z_{PN} and the measured Z_{PN} from the impedance analyzer. This is because the impedance analyzer uses an internal sweep-frequency source that keeps constant and adequately large amplitude over the entire frequency range, thus producing good S/N ratio at all frequencies.

The behavioral modeling procedure on the other hand uses the switching noise from the converter to extract model impedances indirectly. The amplitude of this noise drops at higher frequency as seen in Fig. 3.21 (b) leading to degradation in S/N ratio and error in estimation of impedances.

3.2.4 Model Errors

3.2.4.1 Effect of LISN impedance

The extracted CM impedances (Z_{PG} and Z_{NG}) seem to be inductive below 1 MHz. This is unrealistic because at lower frequencies CM impedance must be capacitive. It was shown earlier [60] and [55] that in order to correctly identify the model impedances, the LISN impedance must be within an order of magnitude of the unknown impedance. To get an intuitional understanding of the mathematical derivation in [60] and [55], let us consider the example shown in Fig. 3.22. Here an arbitrary two-terminal Norton equivalent network is attached to a LISN.

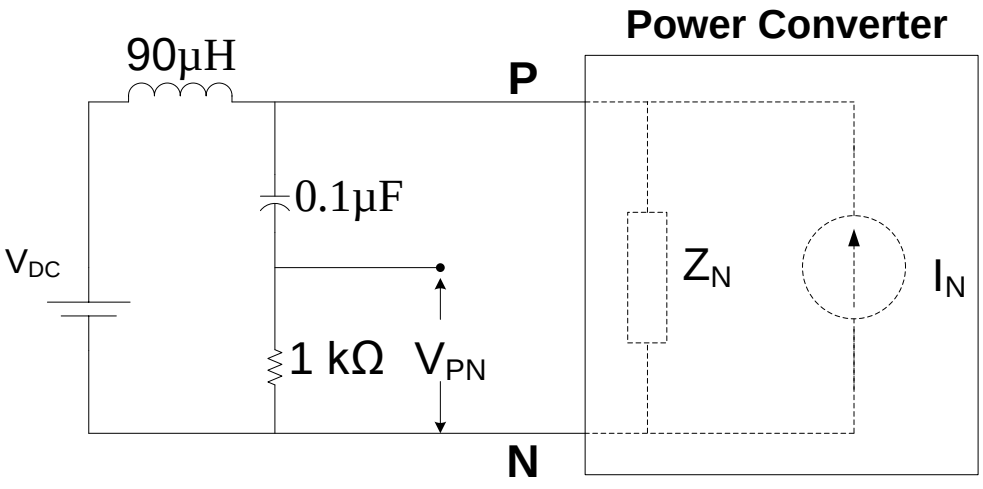

Fig. 3.22: Two-terminal network connected to a LISN

It can be seen that if all measurements are performed across 1 kΩ resistor then the inductor of the LISN is in parallel with Z_N. If Z_N is a small capacitor (100-300 pF) then at lower frequencies the impedance of the LISN inductor is much smaller than Z_N. Thus voltage measurements at lower frequencies are dominated by the LISN inductor and identification of Z_N becomes difficult. On the other hand, the DM impedance (Z_{PN}) can be correctly identified with this LISN as it is well below the LISN impedances at lower frequencies. The above mentioned problem can be avoided by using a series insertion method as reported in [49] or by estimating the low frequency CM impedance assuming capacitive behavior and extrapolating its value from the higher frequency measurements. Since all experiments shown here use the same LISN, no such corrections were found necessary.

3.2.4.2 Identifying Real Parts of Model Impedances

An issue that has never been reported before is that the behavioral modeling technique can result in impedances Z_{PG}, Z_{NG} and Z_{PN} that have negative real parts at certain frequencies. As an example, the real parts of Z_{NG} are plotted in Fig. 3.23. The negative real parts do not have any physical significance. Two reasons were identified for this kind of model error.

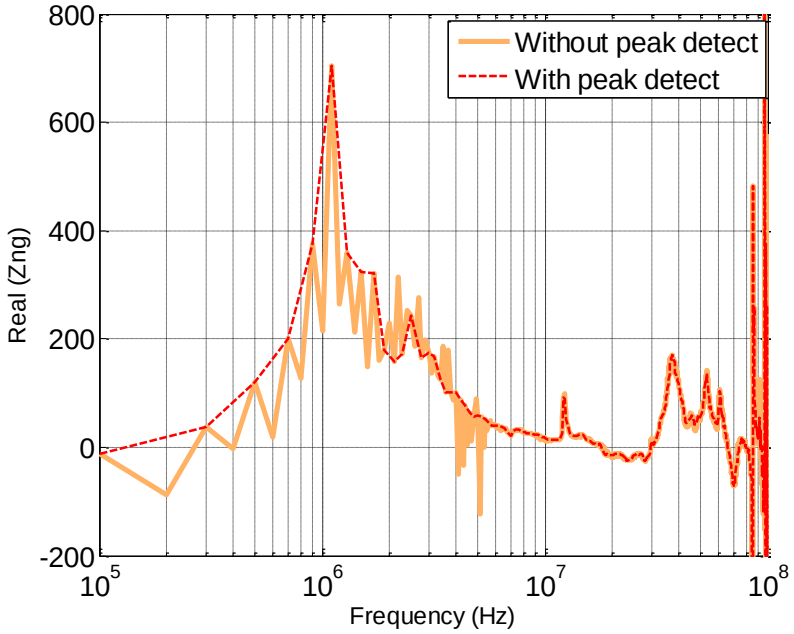

Fig. 3.23: Real parts of extracted common mode impedance Z_{NG}

The first reason is that the amplitude of measured voltages at certain frequencies may be very small and hence the system of equations can get numerically ill-conditioned at those frequency points. A simple peak detect algorithm was used to eliminate them. Frequency points where the amplitude of the measured voltages was found to be smaller than the adjacent frequency points were removed. The model was then extracted using the modified frequency domain data and the real parts of the resulting Z_{NG} are plotted in Fig. 3.23 as well. It can be seen that at frequencies (for ex. 200 kHz), where the measured voltage was found to be low, the real part became negative but with peak detection this frequency point was eliminated. In Fig. 3.20 and 3.21 (a), a spike at 200 kHz can be observed for the same reason.

The second reason is that the real part of the impedance may be very small compared to its imaginary part. In Fig. 3.21 a spike at around 1 MHz can be observed. This occurs at the parallel resonance between the common mode capacitor and the LISN inductor (see Z_{PG} and Z_{NG} in Fig. 3.21 (a)). The real part here should approach 1kΩ (LISN resistance). It can be seen from Fig. 3.23 that the identification of the real part starts to improve as they become significantly large in comparison to the imaginary part. However, even after peak detection some frequency points (for ex. at 100 kHz and around 20 to 30 MHz) are still negative because the real part here is very small compared to the imaginary part. At these frequencies the real part of the

impedances can be set to positive or to zero without loss of accuracy as their contribution is anyway negligible.

3.2.5 Model Validation

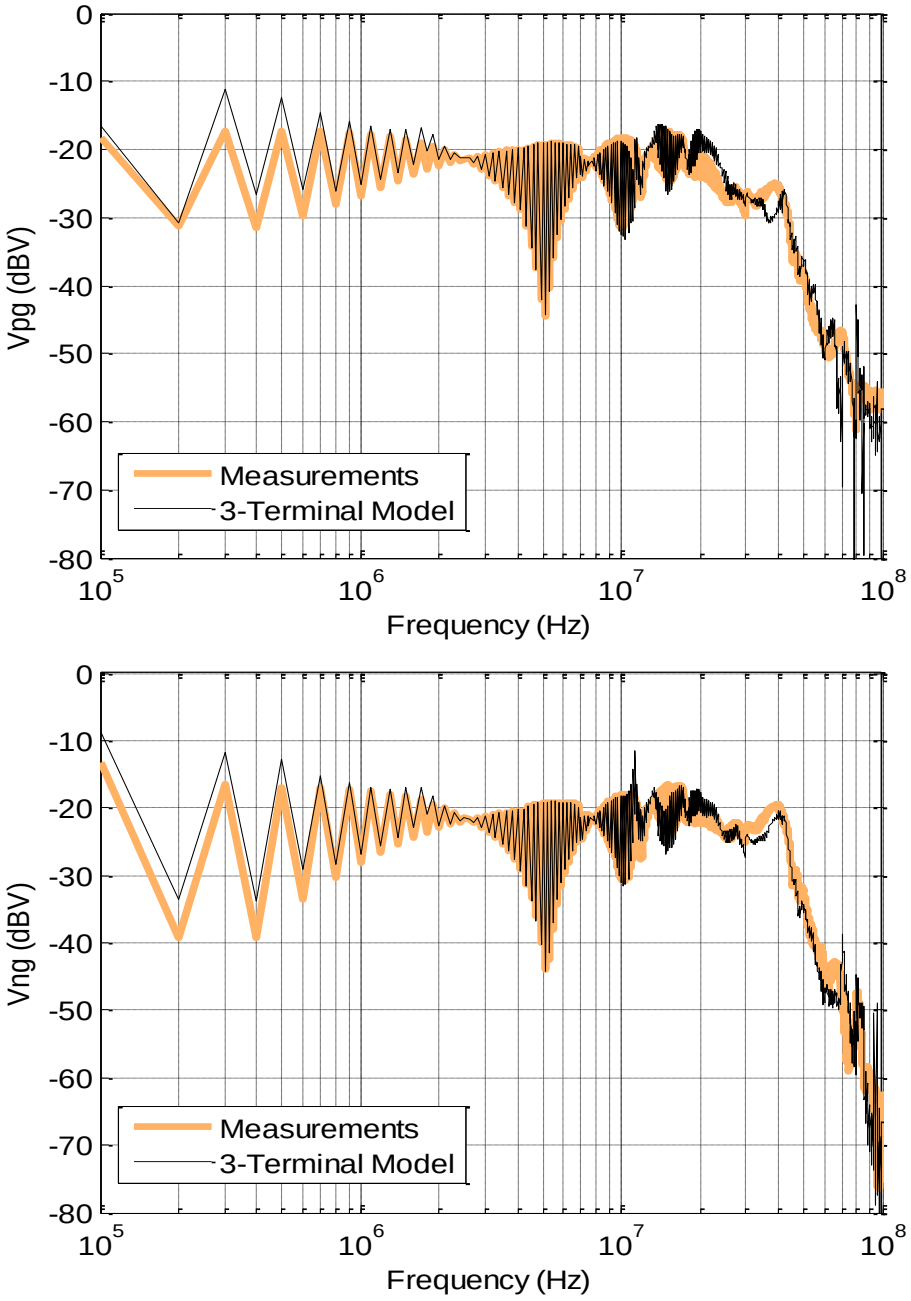

Fig. 3.24: Comparison of measured and predicted conducted emissions at the positive and the negative terminal (V_{PG} & V_{NG}) of 50 Ω LISN by a model created from 1 kΩ LISN

Two modes were created as mentioned before, one with 1 kΩ LISN and the other with a 50 kΩ LISN. First, the model created from the 1 kΩ LISN was used to predict conducted emissions for the 50 Ω LISN. Fig. 3.24 shows the comparison of predicted conducted emissions with the actual measurements of conducted emissions on a 50 Ω LISN. The predictions made by the three-terminal model match well with the measurements from 100 kHz, which is the switching frequency of the buck converter, up to 100 MHz at almost all frequencies. The error is less than 6dB up to 70 MHz. These predictions are computed in a math tool and show results for all frequency points including the ones that have a negative real part of model impedances.

Fig. 3.25 again gives the prediction results (only for the positive side of the LISN) by a model created with a 1 kΩ LISN for a 50 Ω LISN. However, here all the negative real parts of the model impedances were set to positive. As explained earlier, if the real part of the impedance is not significant compared to its imaginary part, this manipulation should not affect the EMI prediction results. Compared to prediction of V_{PG} in Fig. 3.25, no significant difference is observed in prediction accuracy. In fact, with the impedances now having a physical meaning, the model can now be made to run on circuit simulation software. Lumped circuit equivalent models of any external networks like cables, EMI filters etc. can now be simulated with the terminal model of the converter to evaluate their effects on conducted emissions. The noise impedances can now be used for designing and optimizing EMI filters as well.

The model created with the 50 Ω LISN was then used to estimate conducted emissions for the 1 kΩ LISN. The results obtained were compared with measured conducted emissions values on the 1 kΩ LISN in Fig. 3.26. Again prediction for only the positive side of the LISN is shown here. Negative side results were found to be similar. It can be seen that the model created from the 50 Ω LISN failed to predict conducted emissions at both low and high frequencies.

The reason for poor prediction at higher frequencies can be due to a lower impedance of the 50 Ω LISN compared to the DM impedance of the system. This error is similar to the one explained in section 3.4. The signal to noise ratio of measured voltages on a 50 Ω LISN is also worse compared to voltages measured on a 1 kΩ LISN (Fig. 3.21 (b)). At lower frequencies as well, the predictions are not good enough. Thus even though in principle there should not be any difference between models extracted from 50 Ω and 1 kΩ LISN, due to measurement related errors one of them may be more accurate than the other.

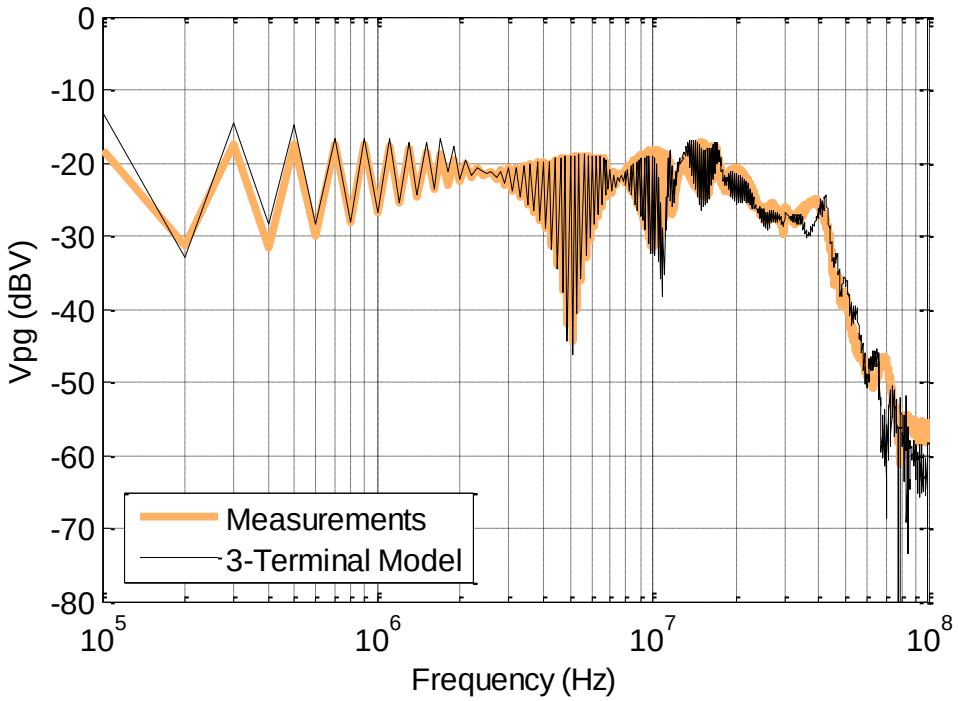

Fig. 3.25: Comparison of measured and predicted conducted emissions at the positive terminal (V_{PG}) of 50 Ω LISN by a model created from 1 kΩ LISN with all negative real parts of model impedances manually changed to positive

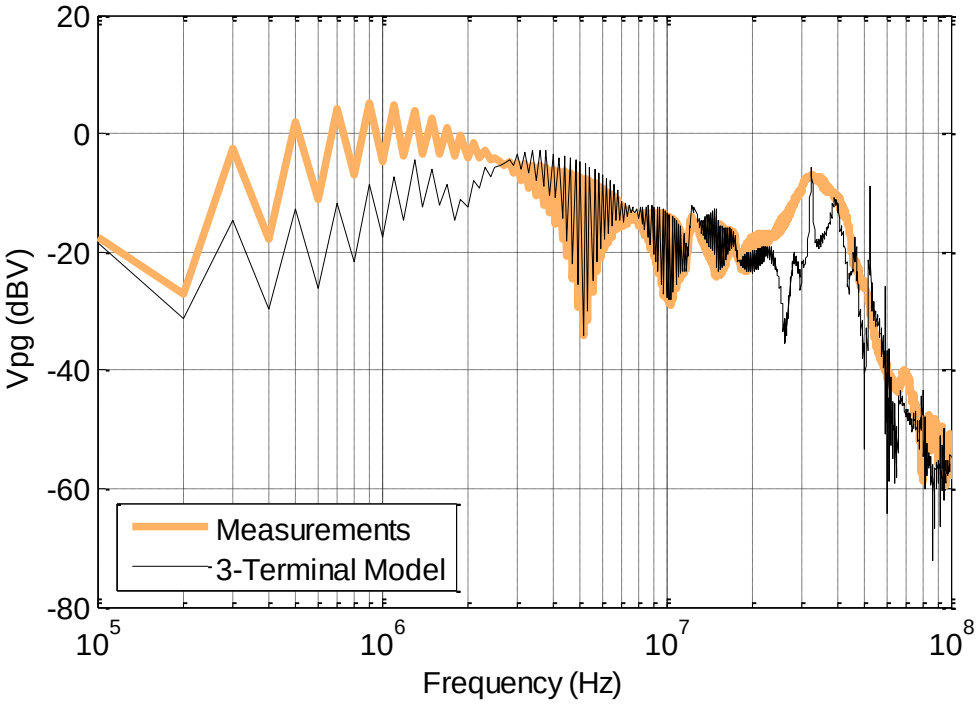

Fig. 3.26: Comparison of measured and predicted conducted emissions at the positive terminal (V_{PG}) of 1 kΩ LISN by a model created from 50 Ω LISN

The previous discussion has demonstrated that the behavioral modeling method is applicable to buck converters as well. However, both boost and buck converters are dc-dc converter. The applicability of the method to ac systems still needs to be investigated. To demonstrate the applicability of the method to ac systems two converters will be modeled using the behavioral modeling technique. One of them is a half-bridge inverter and the other is a three-phase inverter.

3.3 HALF-BRIDGE INVERTER

The hardware used for modeling purpose is the same that was used to demonstrate lumped circuit equivalent and the details were provided in subsection 3.1.1. The fundamental difference in the operation of the half-bridge inverter is that the operating point of the converter changes over the line cycle as was shown earlier in Fig. 3.8. Thus in order to capture the EMI resulting from the variation of the operating point of the system, the EMI during the entire line cycle needs to be captured. Time domain waveforms with very high resolution and longer time duration leads to large data sets. Some work regarding reduction of data-sets has been done earlier [59]. However, here we use the full data set to demonstrate the accuracy of behavioral modeling methods. If reduced data sets are used then accuracy only degrades.

Fig. 3.27 shows the screen shot of the oscilloscope with three waveforms. The blue and the yellow ones are the EMI waveforms received on the LISN ports. The green waveform shows a complete line-cycle of the output voltage. It can be seen here that the EMI received changes as the operating point of the system changes. Also another thing to notice here is that the positive and negative half-cycles are not symmetric and consequently the EMI recorded in the positive and negative half-cycles is not symmetric either. Hence the data reduction techniques in [59] that exploit the symmetry of the converter's operation will give larger errors. Thus the entire data set as seen in Fig. 3.47 will be used to extract the EMI model. This should be enough to demonstrate the concept and the power of behavioral modeling techniques in general.

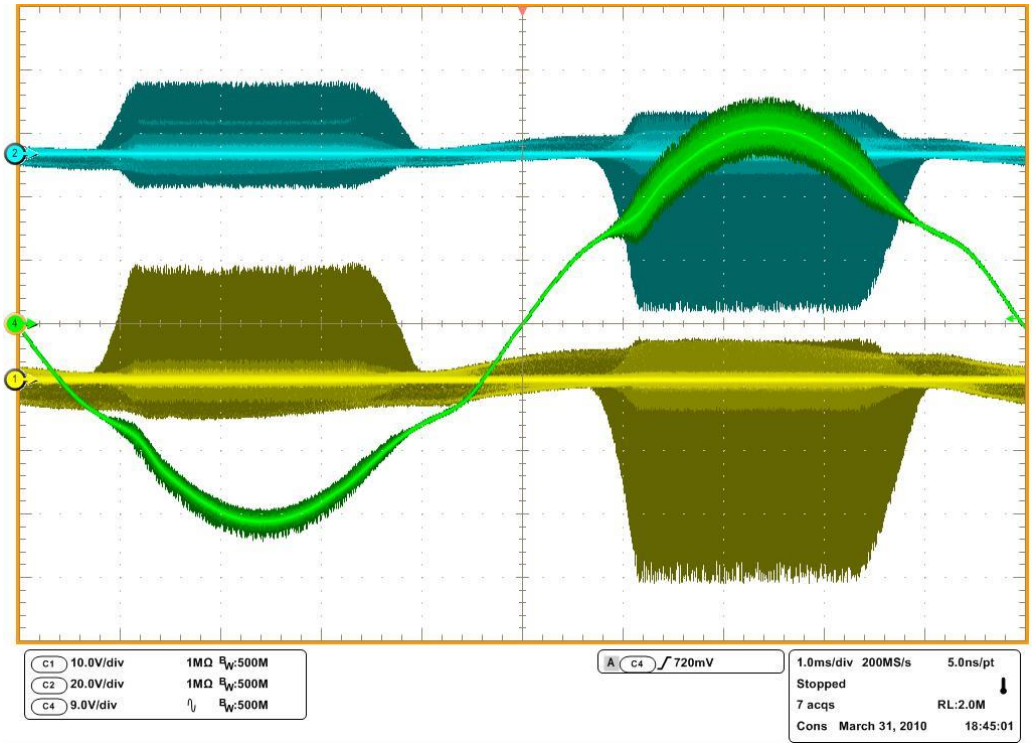

Fig. 3.27: Oscilloscope screen shot of the EMI received on the LISN during the entire line cycle of the half-bridge inverter

3.3.1 Model Results

A three-terminal model was developed for both 50 Ω and 1 kΩ LISN impedances. Fig. 3.28 shows the comparison of I_{PG} and I_{NG} for the models created with 50 Ω and 1 kΩ LISNs. It is clear that the extracted frequency domain current sources do not show any significant difference except at low frequencies. Fig. 3.29 shows the comparison of extracted model impedances from a 50 Ω LISN and a 1 kΩ LISN. From Z_{PG} and Z_{NG}, the capacitive coupling path is evident. Capacitive behavior can be seen in the frequency range from 1 MHz to 10 MHz. However, again at low frequencies a consistent difference of 10 dB or more can be observed for all model impedances. This indicates that the LISN is seeing significant nonlinearity and time-variant behavior between the terminals near the switching frequency of the inverter (100 kHz). Again, it was found that in this case the model created from the 1 kΩ LISN was more accurate in terms of linearity over the entire frequency range than the model created from the 50 Ω LISN.

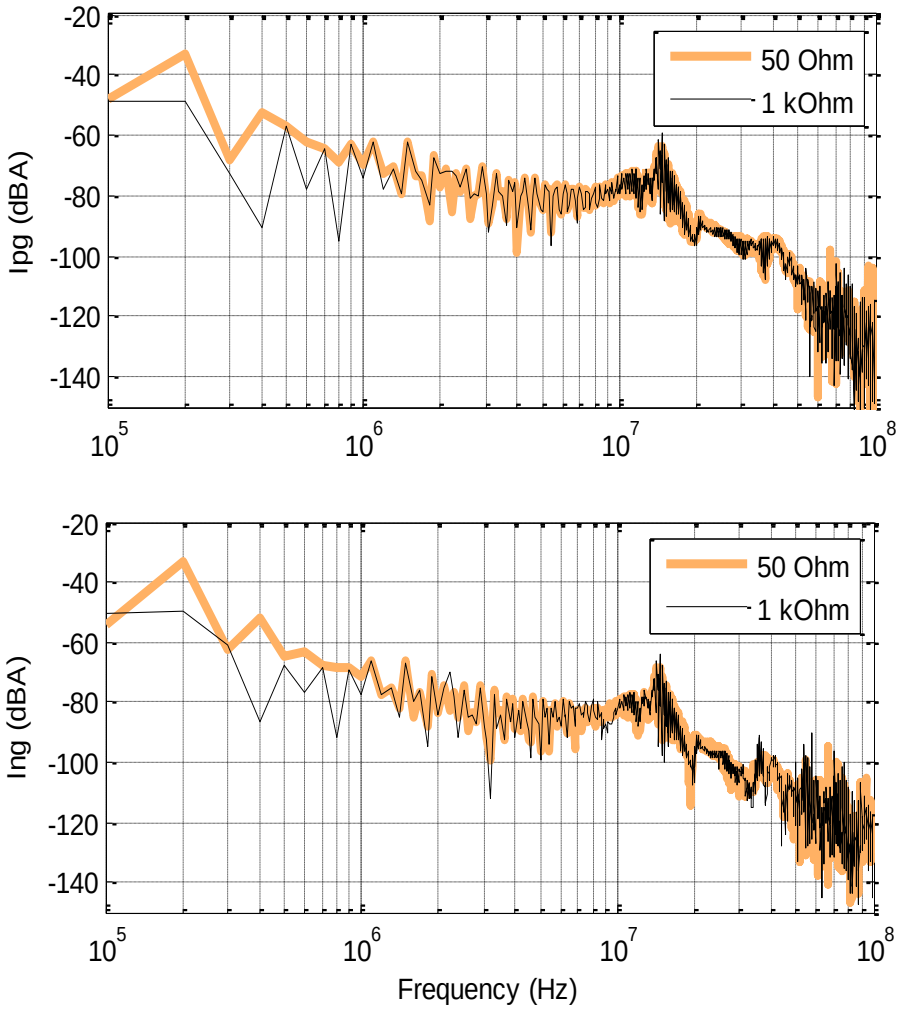

Fig. 3.28: Extracted current sources for a three-terminal model

3.3.2 Model Validation

The model created from 1 kΩ LISN was used in simulations to predict conducted emissions for the 50 Ω LISN. Fig. 3.30 and Fig. 3.11 show the comparison of predicted conducted emissions with the actual measurements of conducted emissions on the 50 Ω LISN.

The predictions made by the three-terminal model match with the measurements within 6 dB of error up to 30 MHz. From 30 MHz to 100 MHz, the trend of predicted results for conducted emissions generally matches well with the measurements. From Fig. 3.30 and Fig. 3.11, one can see that the model extracted from 1 kΩ LISN was able to predict the EMI received on the 50 Ω LISN, indicating its good linearity and time-invariance properties.

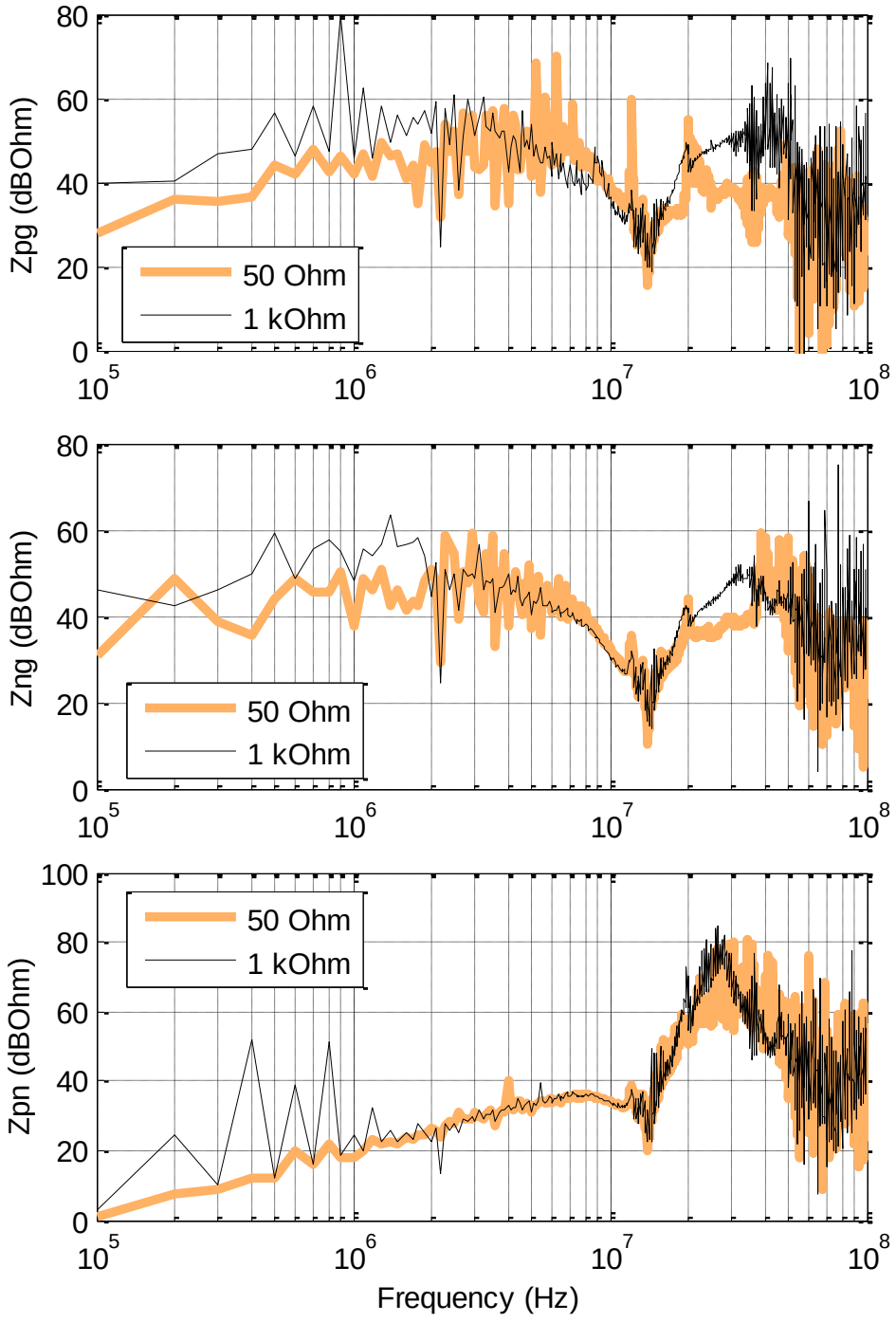

Fig. 3.29: Extracted terminal impedances for a three-terminal model

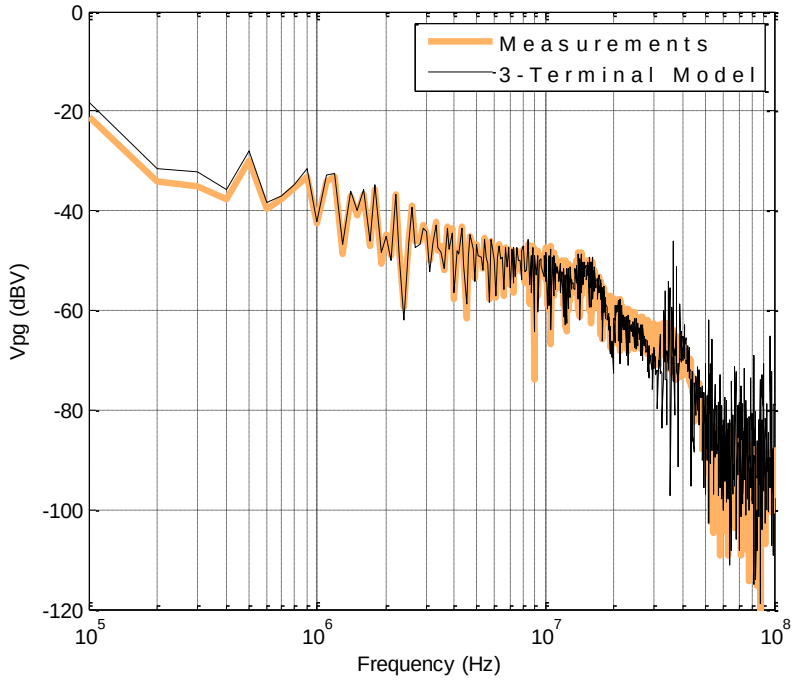

Fig. 3.30: Comparison of measured and predicted conducted emissions at the positive terminal (V_{PG}) of the LISN

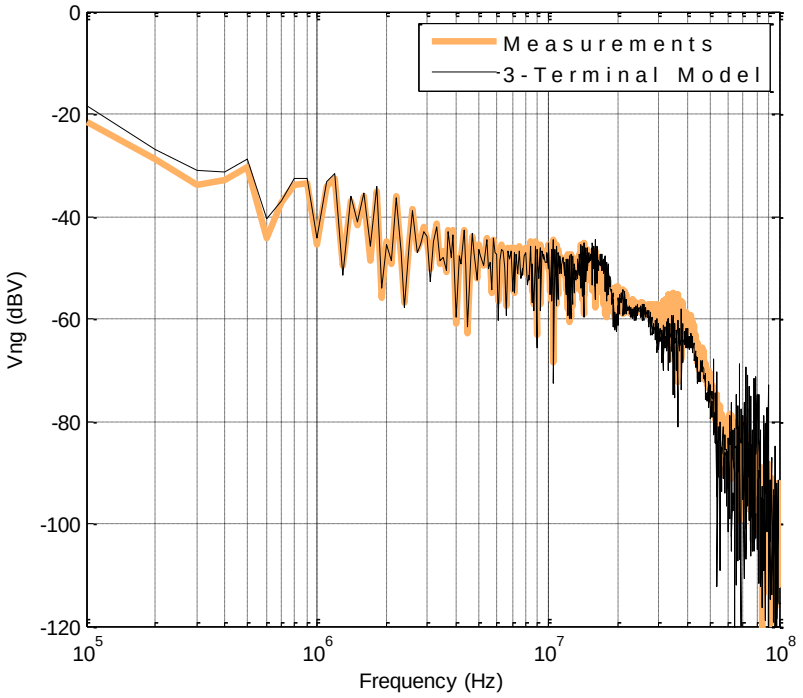

Fig. 3.31 Comparison of measured and predicted conducted emissions at the positive terminal (V_{NG}) of the LISN

In order to check the linearity of the model created from the 50 Ω LISN, the model was used to estimate the conducted emissions on a 1 kΩ LISN. The results obtained were compared with measured conducted emissions on the 1 kΩ LISN in Fig. 3.32. Comparison results for only the positive side of the LISN (V_{PG}) is shown here. The results for the negative side were similar. It is clear from Fig. 3.32 that the model created from the 50 Ω LISN failed to predict conducted emissions at low frequencies. The error in the predicted and measured result from 100 kHz to 1 MHz is about 10dB. The results from Fig. 3.30 and Fig. 3.32 indicate that the model created from the 1 kΩ LISN was more accurate than the model created from the 50 Ω LISN. The reasons for this are similar to the one explained in the subsection 3.2.3 for the buck converter.

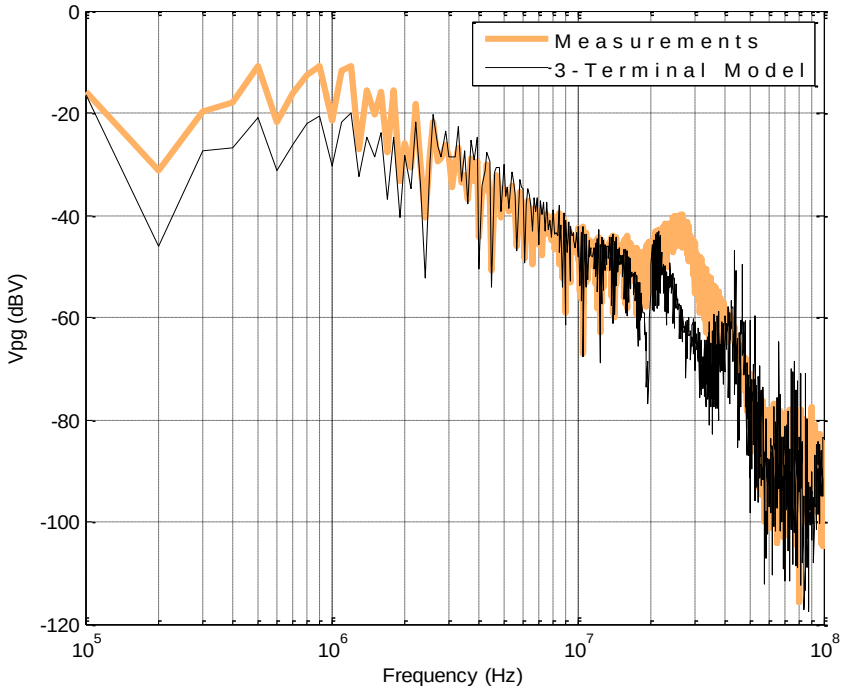

Fig. 3.32: Comparison of measured and predicted conducted emissions on a 1 kΩ LISN by a model created from a 50 Ω LISN

The range of frequencies for which the model was shown to work well covers the frequency range (150 kHz – 30 MHz) of conducted emissions compliance set by the standards. However in certain applications, like for the aerospace industry, power converters may switch at frequencies as low as 10 kHz. The proposed generalized behavioral modeling technique was tested for its accuracy in the extended frequency range from 10 kHz to 30 MHz. To carry out this test, the switching frequency of half-bridge inverter was set at 10 kHz instead of 100 kHz. The same

LISN was used for the extraction of the model. This LISN (Fig. 3.7) was designed for a frequency range of 70 kHz to 100 MHz. Below 70 kHz, the impedance of the 0.1µF capacitor starts to become significant. Thus the noise voltage received across the 50 Ω resistor is not the same as on the dc input bus. In order to correct this, transfer functions (V_2/V_1) were measured between the dc bus-ground and across the 50 Ω /1 k Ω as shown in Fig. 3.33. The set-up for measuring the transfer function is given in Fig. 3.34. The measured transfer functions are shown in Fig 3.35. It is evident that no compensation is needed for a 1 kΩ LISN, as V_2/V_1 is almost 0 dBV. In the case of the 50 Ω LISN, correction is definitely needed as the voltage attenuation at 10 kHz is -12 dBV. The transfer function of Fig. 3.35 was used to scale the voltage (V_{PG} and V_{NG}) measurements before model extraction.

Another issue was that of power supply immunity. For this LISN it rapidly degrades below 70 kHz. Immunity tests were conducted to find the amount of noise coming from the dc source into the DUT side of the LISN. It was found that the dc source used in the experiments had no significant interference in the interested range of frequencies.

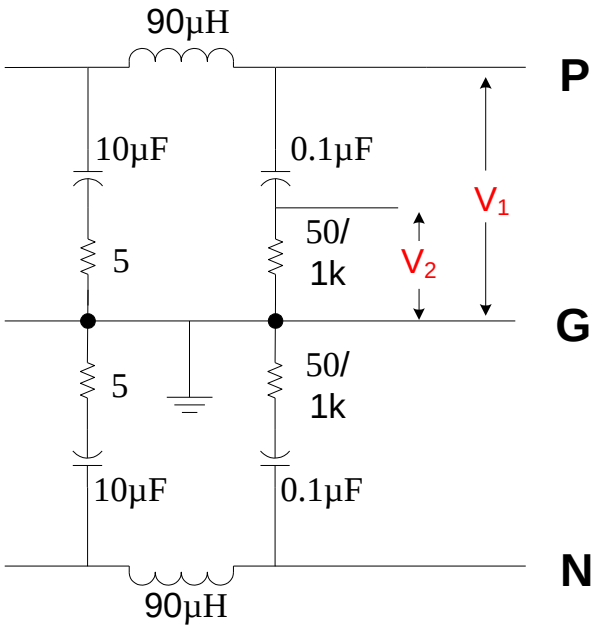

Fig. 3.33: Transfer function measurement between power-ground and 50 Ω /1 kΩ resistance

The modeling was carried out in exactly the same way as before. The three-terminal model was created from the 1 kΩ LISN and then used to estimate the conducted emissions received on

the 50 Ω LISN. The results are shown in Fig. 3.36 and Fig. 3.37. It is clear that the model performs well even at frequencies as low as 10 kHz. The error is about 6 dB at most frequencies from 10 kHz to 30 MHz.

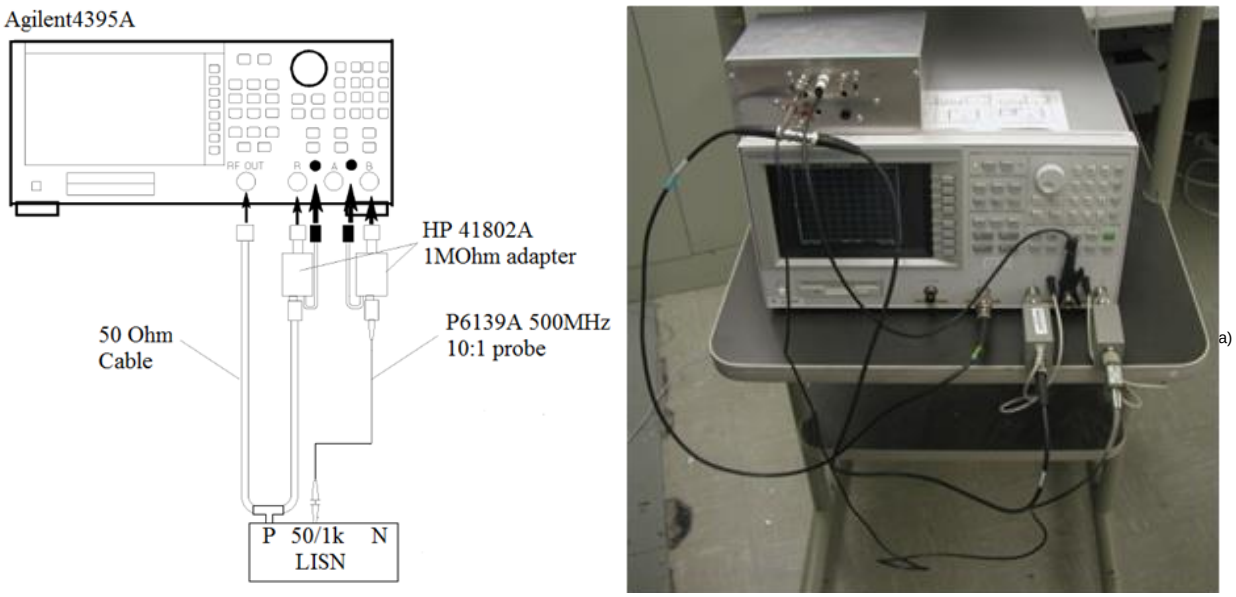

Fig. 3.34: Set-up for measuring the voltage transfer function

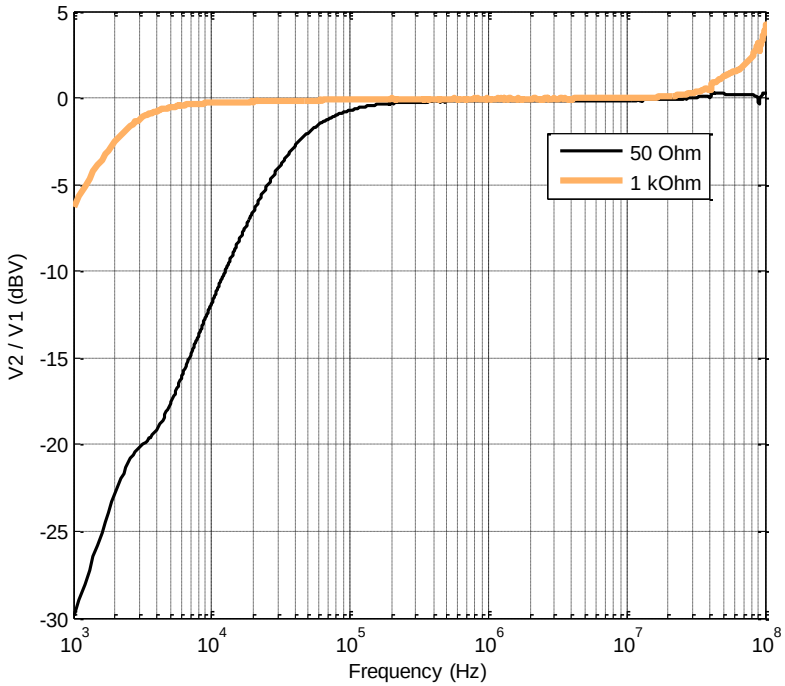

Fig. 3.35: Measured results of transfer function (V_2/V_1)

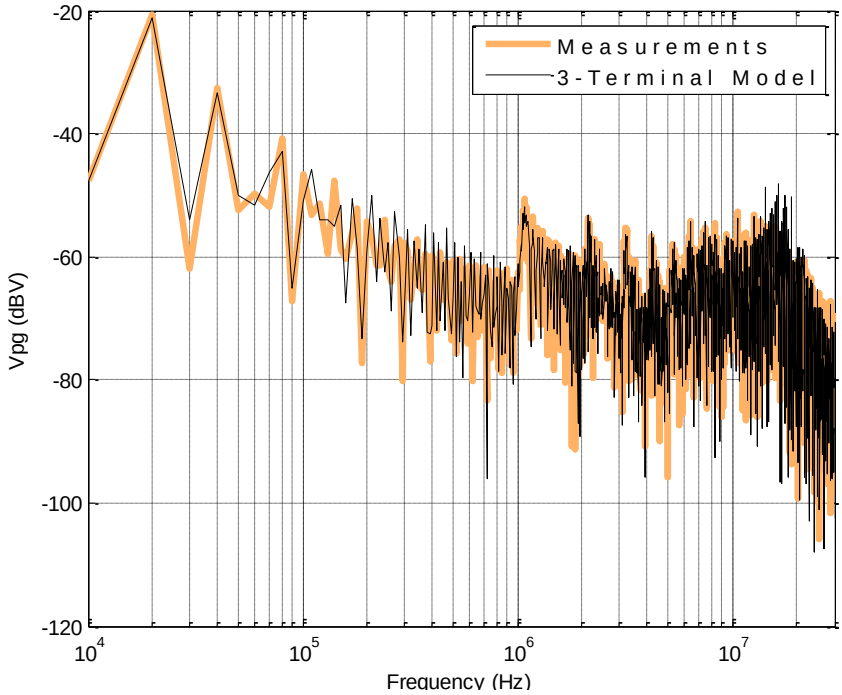

Fig. 3.36: Comparison of measured and predicted conducted emissions at the positive terminal (V_{PG}) of the LISN

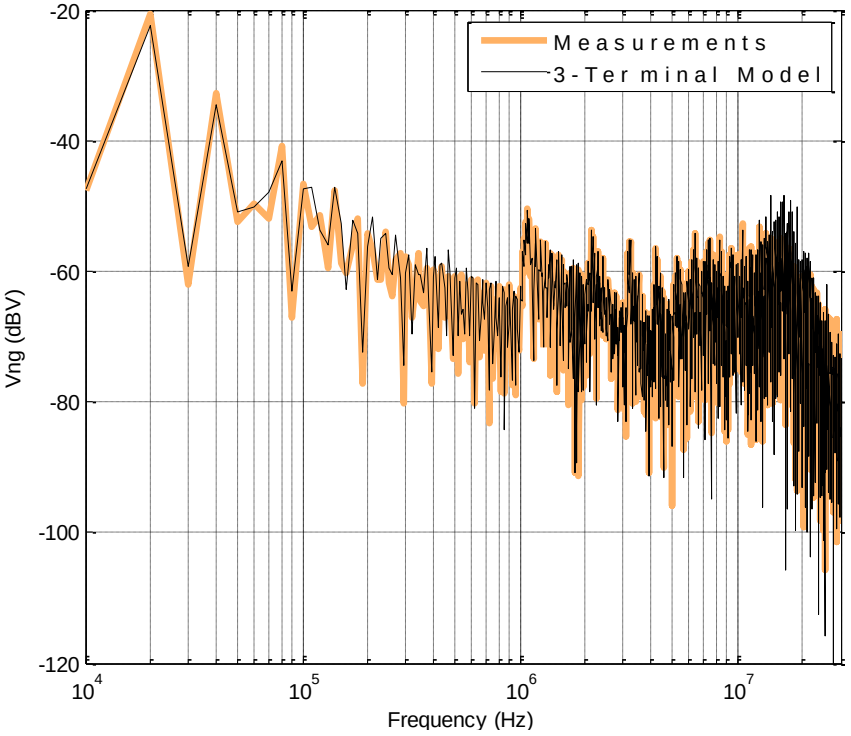

Fig. 3.37: Comparison of measured and predicted conducted emissions at the negative terminal (V_{NG}) of the LISN

3.4 THREE-PHASE INVERTER

The validation result for the modeling of half-bridge inverter shows that the GTM can be used for ac systems as well. As a final case, modeling of a three phase voltage source inverter (VSI) was attempted using GTM.

Fig. 3.38 shows the test set-up used and Fig 3.39 shows the picture of the laboratory set-up. The three-phase inverter used here has an IGBT module (Fuji 6MBP30RH060-50) and a resistive-inductive (R-L) load of 15 Ω and 600 µH respectively. A decoupling capacitor (film type) of 0.22 µF and a bulk capacitor (electrolytic) of 47 µF were placed at the input side of the VSI (C_{IN}). The switching frequency was set to 20 kHz and line frequency was 400 Hz. The converter was running at 1.2kW. The LISN used was the same as shown in Fig. 3.7. A high band width scope was used to record the waveforms for the entire line cycle with a time resolution of 5 nsec/point. Only validation results will be given here.

The predictions were carried out using a circuit model in (SABER® simulator) this time. The model was implemented as a look-up table with the information of all impedance and current sources listed frequency point by point. Another way is to fit a RLC circuit in the model impedances [49] with the sources implemented in time domain. A model created from 1 kΩ LISN was then used to predict EMI on a 50 Ω LISN. Fig. 3.40 shows these results. Again, a good matching of predicted and measured results can be seen at most frequencies between 20 kHz and 100 MHz.

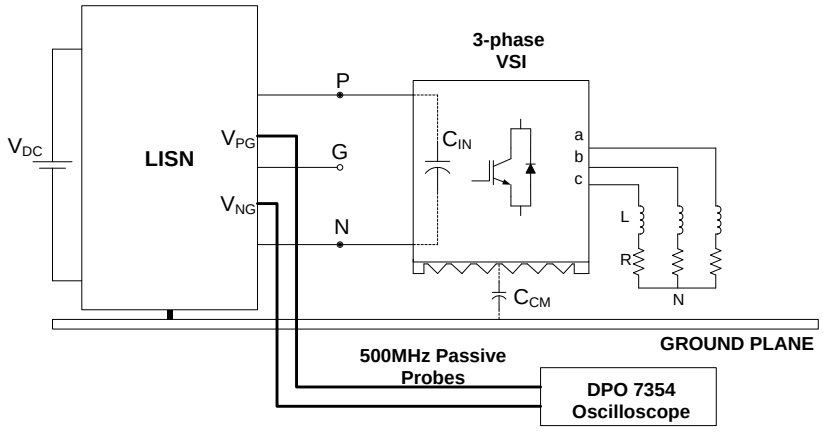

Fig. 3.38: Experimental setup for extraction of three-terminal model of a three-phase VSI.

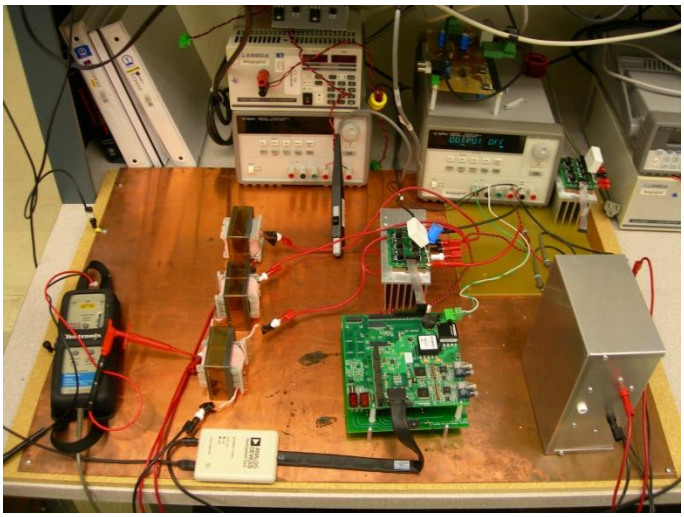

Fig. 3.39: Laboratory set-up for terminal model extraction of a three phase VSI

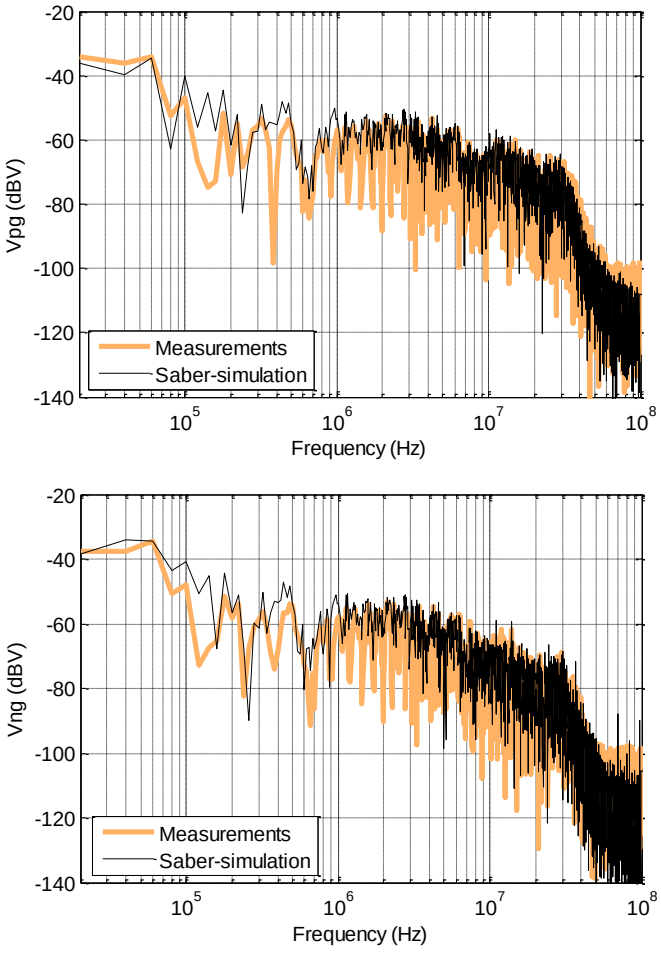

Fig. 3.40: Comparison of measured and predicted conducted emissions at the positive and the negative terminal (V_{PG} & V_{NG}) of 50 Ω LISN by a model created from 1 kΩ LISN for three-phase VSI.

3.5 CONCLUSIONS

The generalized terminal modeling technique of [55, 59] was successfully applied to a buck, half-bridge inverter and a three-phase inverter. It is clearly shown that this technique can be used to develop very accurate, highly compact and linear models of a wide variety of power converters. However, it is also shown here that the generalized terminal modeling method and other methods similar to it have a problem that the extracted model impedances often have negative real parts which is non-physical. This is something that has not been reported before. The extracted model impedances are also noisy and can be difficult to run in a circuit simulator. Hence there is need of a model whose parameters can be easily related to the physical attributes of the converter especially the impedances.

The terminal modeling techniques in general are still incapable of separating the load from the model and therefore such models are referred to as "*terminated EMI models*". This means that output side needs to be terminated with a fixed impedance if the model is to remain accurate. Changing the output side impedances will render the model invalid. In the next chapter an "*un-terminated EMI model*" is proposed to overcome this key limitation of the terminated EMI models.

4 UN-TERMINATED EMI BEHAVIORAL MODELING

The behavioral modeling technique discussed in chapter 3 was shown to model a power converter from the dc-input side. In all the cases discussed so far only dc-input converters were considered. This is because in an aircraft the primary source of power is usually an HVDC line. The dc-side terminal model has a fundamental limitation that it cannot predict or capture the effect of change at the load side on the EMI. The model is hence independent of the source conditions but not of load conditions. This problem can be worked around by modeling only the worst case loads from the EMI stand point. However, the restriction of "terminated terminal-models" is still viewed as a problem and needs further research. For example in aerospace applications, the DO-160 EMI standards limit the EMI on all power lines and cable bundles and most often the loads are connected via cables inside the aircraft. Thus, we need a model which addresses the load side as well. Here *"terminated behavioral model"* means that the load side of the power converter is fixed and re-modeling is necessary if a different load is used. An *"un-terminated behavioral model"* would then mean that the load can be changed without altering the model of the converter that is the terminal model of the converter is independent of the load or the source conditions.

In this chapter a 2kW motor-drive system, will be used to demonstrate the un-terminated EMI modeling technique. The CM emissions will be modeled first. This choice was made due to the fact that, above 10 MHz the EMI spectrum is mostly dominated by CM emissions. Observations suggest that DM noise on the AC and DC side are fairly decoupled but this not the case with CM noise [73, 76, 81]. Hence, developing an un-terminated model for CM should be given precedence. Moreover, the radiated EMI is mostly caused by CM emission and since a motor-drive system may have a harness on both input and output sides, restricting CM emission become even more important. Thus we address the problem of CM first.

Moreover, the idea of un-terminated behavioral model quickly complicates the procedure of model extraction. The addition of output side terminals would increase the order of the model and thus the number of equations necessary to solve for the model parameters. A study was done on how complicated the behavioral modeling gets with the increase in the number of terminals in the system [59]. For a 4-terminal network, we require four noise source and six impedances to completely describe the system. This brings the total number of unknowns to nine which would

require at least nine equations for obtaining a unique solution. Thus breaking the model into CM and DM can help to solve the above mentioned issue.

We will first develop the concept of CM modeling using detailed lumped circuit simulations and then validate the concept using experiments.

4.1 COMMON MODE

4.1.1 Model Definition

Fig. 4.1 shows a motor-drive system in a conducted EMI set-up. The power is supplied by a line impedance stabilization network (LISN) via two cables. No harness is used here from LISN to the converter, though this would not be the case when the system is installed in an aircraft. We start with this type of system configuration only for the purpose of demonstrating the concept. The length of the harness could be anywhere between 2-10 m

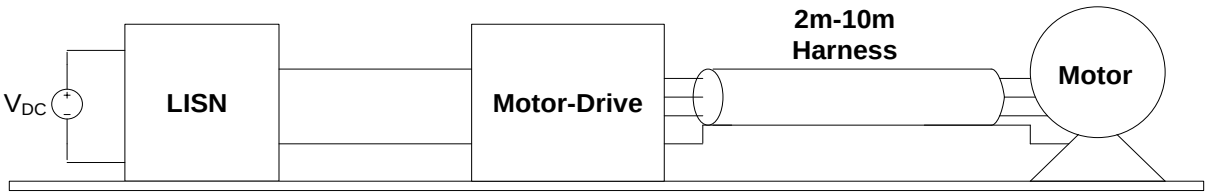

Fig. 4.1: Power train for motor-drive system

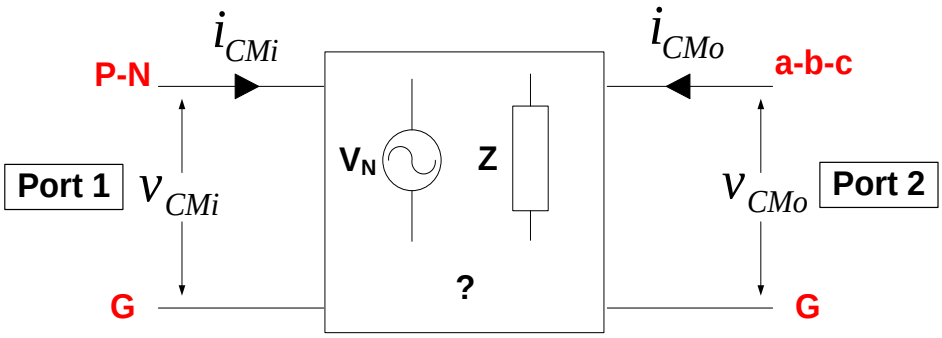

Fig. 4.2: Two port CM model for the motor-drive

The purpose of the modeling is to have a behavioral noise-model that has two ports, an input port where the LISN or the dc-network is supposed to be connected and an output port where the motor is connected. This idea is depicted in Fig. 4.2. The input port (port 1) is between positive

and negative short circuited and the ground and the output port (port 2) is formed between the three phases (phase-a, phase-b and phase-c) short circuit and the ground. The port currents are then directly the CM currents (i_{CMi} & i_{CMo}) on the input and output sides. The DO-160E standards are defined on the levels of these currents. The task is to find a suitable model to fit in the box of Fig. 4.2 so that it can be used to predict changes in EMI due to any change in the passive network on ac and dc sides.

The proposed model for the two port network of Fig. 4.2 is shown in Fig. 4.3. As it can be seen, the model is kept very simple. The impedances are defined by a two-port matrix and the noise sources are defined so as to comply with the Thevenin equivalent for a three-terminal network. Now a modeling procedure needs to be established for extraction of the noise-impedance matrix (model impedances) and the noise-sources (V_{N1} & V_{N2}). The equations that define the model of Fig. 4.3 model are simply given by:

$$\begin{bmatrix} v_{CMi} \\ v_{CMo} \end{bmatrix} = \begin{bmatrix} Z_{11} & Z_{12} \\ Z_{21} & Z_{22} \end{bmatrix} \begin{bmatrix} i_{CMi} \\ i_{CMo} \end{bmatrix} + \begin{bmatrix} v_{N1} \\ v_{N2} \end{bmatrix} \tag{1}$$

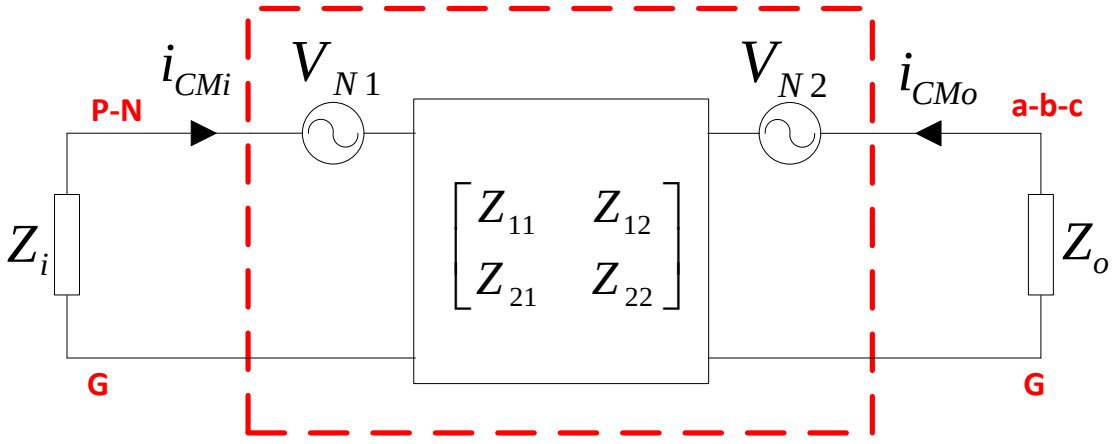

Fig. 4.3: Two port, three-terminal Thevenin noise-model of the motor-drive

4.1.2 Modeling Procedure

The modeling procedure should be generic and easily applicable. There are five model parameters that need to be identified. These include the two sources and the three elements in the

impedance matrix. The off-diagonal elements in the matrix should be the same for a linear and reciprocal network. Thus one needs to establish five conditions or at least five equations to extract all parameters uniquely. We accomplish this by applying shunt (with respect to ground) and series impedances at the input and the output of the motor-drive. Let's detail these conditions one by one.

In the first condition we put shunt impedances at both input and output sides of the motor-drive. At both input and output sides this is accomplished by connecting a RC impedance branch from each terminal to the ground. The choice of the values of these impedance was based on the error analysis conducted in [55, 59, 60]. Fig. 4.4 shows the input and the output side of the motor-drive after the implementation of the shunt impedances. In the CM model of Fig. 4.4, these impedances will appear in parallel and hence the model equations can be written as

$$\begin{bmatrix} -i_{CMi} \cdot Z_{SH-i} \\ -i_{CMo} \cdot Z_{SH-o} \end{bmatrix} = \begin{bmatrix} Z_{11} & Z_{12} \\ Z_{21} & Z_{22} \end{bmatrix} \begin{bmatrix} i_{CMi} \\ i_{CMo} \end{bmatrix} + \begin{bmatrix} v_{N1} \\ v_{N2} \end{bmatrix} \tag{2}$$

Where

$$Z_{SH-i} = \left(\frac{Z_{LISN}}{2} \parallel \frac{Z_{SHUNT-i}}{2} \right) \approx \frac{Z_{SHUNT-i}}{2} \tag{3}$$

$$Z_{SH-o} = \left(Z_{HAR-CM} \parallel \frac{Z_{SHUNT-o}}{3} \right) \approx \frac{Z_{SHUNT-o}}{3} \tag{4}$$

$Z_{SHUNT\text{-}i}$ and $Z_{SHUNT\text{-}o}$ are directly obtained from Fig. 4.4 and are shown in equations (5) and (6). Z_{LISN} is the impedance between positive to ground of the LISN and the LISN is assumed symmetric. If it's not then one needs to account for both positive to ground and negative to ground impedances in order to calculate the CM impedance of the LISN. $Z_{HAR\text{-}CM}$ is the CM impedance looking from the motor-drive output side and into the harness, at the end of which a motor is connected. Here a 2 m long harness will be used for model extraction. The motor impedance is then automatically included in $Z_{HAR\text{-}CM}$. Several parasitic inductances are also included in the shunt impedances to simulate a realistic condition. Thus (2) gives two equations and we need to find three more to solve for the parameters of the model. Once the impedances

are inserted the simulation is run for one line period in the steady state (one line period) and the input and output side CM currents (i_{CMi} & i_{CMo}) are recorded in the time-domain.

$$Z_{SHUNT-i} = 1 + j\omega 29e-9 - \frac{1}{j\omega 2e-6} \tag{5}$$

$$Z_{SHUNT-o} = 6 + j\omega 10e-9 - \frac{1}{j\omega 150e-12} + \frac{j\omega 50e-9}{3} \tag{6}$$

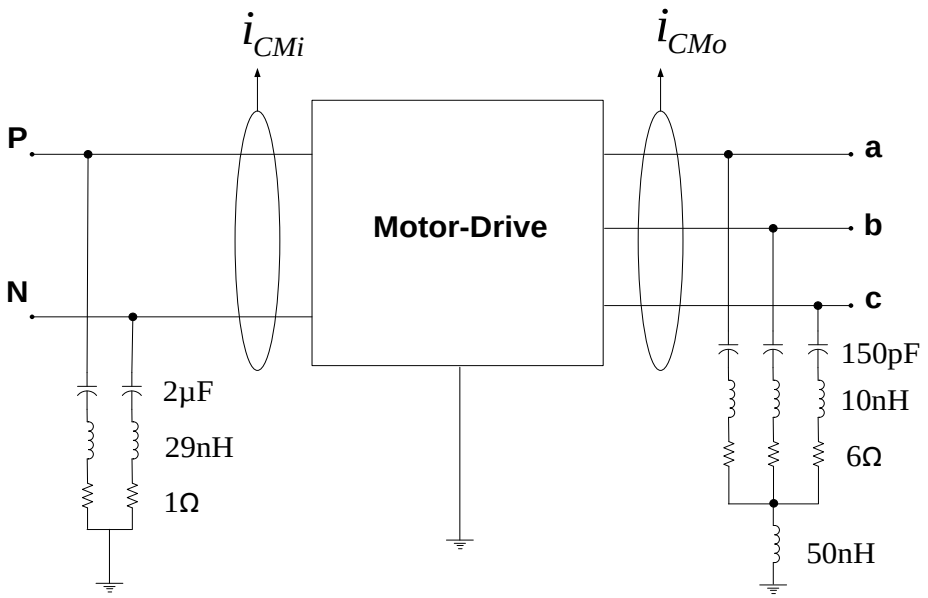

Fig. 4.4: Case 1: CM shunt impedances at the input and output of the motor-drive

The second condition can be created by inserting a CM choke on the input side. The output side is still connected to the shunt impedance as shown in Fig. 4.5. The choke implemented in SABER® includes 20pF of EPC and 10 kΩ of EPR also. These parasitic are not shown here for simplicity. Now the equations for the two port network can be written as:

$$\begin{bmatrix} -i'_{CMi} \cdot Z_{SR-i} \\ -i'_{CMo} \cdot Z_{SH-o} \end{bmatrix} = \begin{bmatrix} Z_{11} & Z_{12} \\ Z_{21} & Z_{22} \end{bmatrix} \begin{bmatrix} i'_{CMi} \\ i'_{CMo} \end{bmatrix} + \begin{bmatrix} v_{N1} \\ v_{N2} \end{bmatrix} \tag{7}$$

Where

$$Z_{SR-i} = \left(\frac{Z_{LISN}}{2} \parallel \frac{Z_{SHUNT-i}}{2} + Z_{Choke-i} \right) \approx Z_{Choke-i} \tag{8}$$

$$Z_{Choke-i} = j\omega 6e-3 \parallel \frac{-1}{j\omega 6e-3} \parallel 10k\Omega \tag{9}$$

Notice that the current terms in (7) are having a prime super-script. This indicates that the CM current will change when the choke is put on the input side. Another point to be noted is that, the shunt impedance on the input side can be removed too. However it was kept here because it does not make any significant difference as understood from (8). Equation (7) gives two more equations for the model extractions and thus only one more is needed to have five in total. With this configuration the simulation is run for one line period and the input and output side CM currents (i'_{CMi} & i'_{CMo}) are recorded.

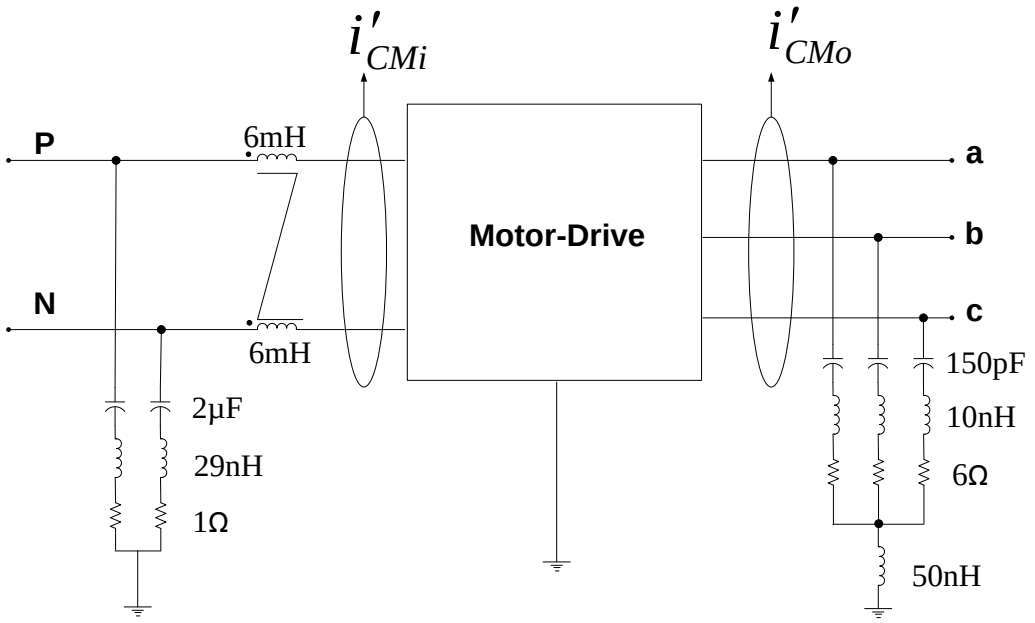

Fig. 4.5: Case 2: CM series and shunt impedance at the input and output of the motor-drive system

For the last equation, one can put a CM choke in the output side and the input side can remain connected to the shunt impedance. This is shown in Fig. 4.6. The equations for this configuration is given by

$$\begin{bmatrix} -i''_{CMi} \cdot Z_{SH-i} \\ -i''_{CMo} \cdot Z_{SR-o} \end{bmatrix} = \begin{bmatrix} Z_{11} & Z_{12} \\ Z_{21} & Z_{22} \end{bmatrix} \begin{bmatrix} i''_{CMi} \\ i''_{CMo} \end{bmatrix} + \begin{bmatrix} v_{N1} \\ v_{N2} \end{bmatrix} \tag{10}$$

Where

$$Z_{SR-o} = \left(Z_{HAR-CM} + Z_{Choke-o}\right) \approx Z_{Choke-o} \tag{11}$$

$$Z_{Choke-o} = j\omega 6e-3 \parallel \frac{-1}{j\omega 10e-12} \parallel 10k\Omega \tag{12}$$

Again some parasitic (EPC = 10pF and EPR = 10kΩ) were included in the CM choke (12). The input and output side CM currents (i''_{CMi} & i''_{CMo}) will change and are recorded after simulations. We now have two more equations from (10), though only one is required. The second equation is chosen here as it expresses the condition of series impedance in the output which was not used before. Equations must be kept distinct in order to avoid numerical ill-conditioning of the system of equations. Now we have five distinct equations given by (13)-(17) which can be solved for model parameters (Z_{11}, Z_{12}, Z_{22}, V_{N1} *and* V_{N2}) using a math tool. The solution is extracted in frequency domain and hence one needs to convert all the recorded CM currents into frequency domain by applying FFT. Notice that $Z_{12} = Z_{21}$, so it need not be treated as a separate variable.

$$-i_{CMi} \cdot Z_{SH-i} = Z_{11} \cdot i_{CMi} + Z_{12} \cdot i_{CMo} + v_{N1} \tag{13}$$

$$-i_{CMo} \cdot Z_{SH-o} = Z_{21} \cdot i_{CMi} + Z_{22} \cdot i_{CMo} + v_{N2} \tag{14}$$

$$-i'_{CMi} \cdot Z_{SR-i} = Z_{11} \cdot i'_{CMi} + Z_{12} \cdot i'_{CMo} + v_{N1} \tag{15}$$

$$-i'_{CMo} \cdot Z_{SH-o} = Z_{21} \cdot i'_{CMi} + Z_{22} \cdot i'_{CMo} + v_{N2} \tag{16}$$

$$-i''_{CMo} \cdot Z_{SR-o} = Z_{21} \cdot i''_{CMi} + Z_{12} \cdot i''_{CMo} + v_{N2} \tag{17}$$

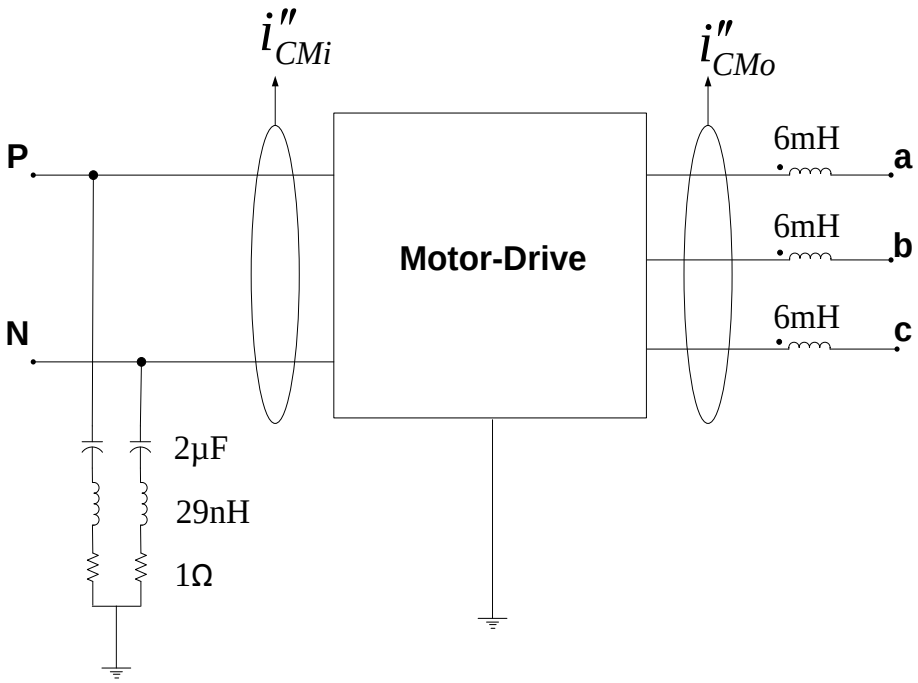

Fig. 4.6: Case 3: CM series and shunt impedance at the input and output of the motor-drive system

4.1.3 Model Verification Through Simulations

We start by defining the lumped circuit models of different parts of the motor-drive system (Fig. 4.1) that will be used in SABER simulations for extraction and validation of the model.

4.1.3.1 Motor-drive System

4.1.3.1.1 Motor-drive Model

The motor-drive was implemented by ideal switches in SABER®. The anti-parallel diodes however were physics based models of silicon carbide (SiC) diodes. This ensures some device capacitance and realistic dynamics of switches. It is possible to implement physics based models for IGBT as well, but then the simulations will become hard to converge and even if they do, it will take a long time. In fact this is the prime reason behind the research. The switches are controlled by center aligned space vectored modulation (SVM). Fig. 4.7 shows the model as implemented in SABER Schematic®. The motor-drive has an input bulk capacitor of 4 µF. This bulk capacitor and its parasitic can are included in the model. Realistic but arbitrary values of the bus bar inductance, interconnect inductance and CM capacitances to heat sink are included in the

model as well. From Fig. 4.7, it can be seen that the model is asymmetric from both the CM and DM stand point. The CM capacitor on the positive and negative rail are of different values and so are the interconnect inductances on the top and bottom switches.

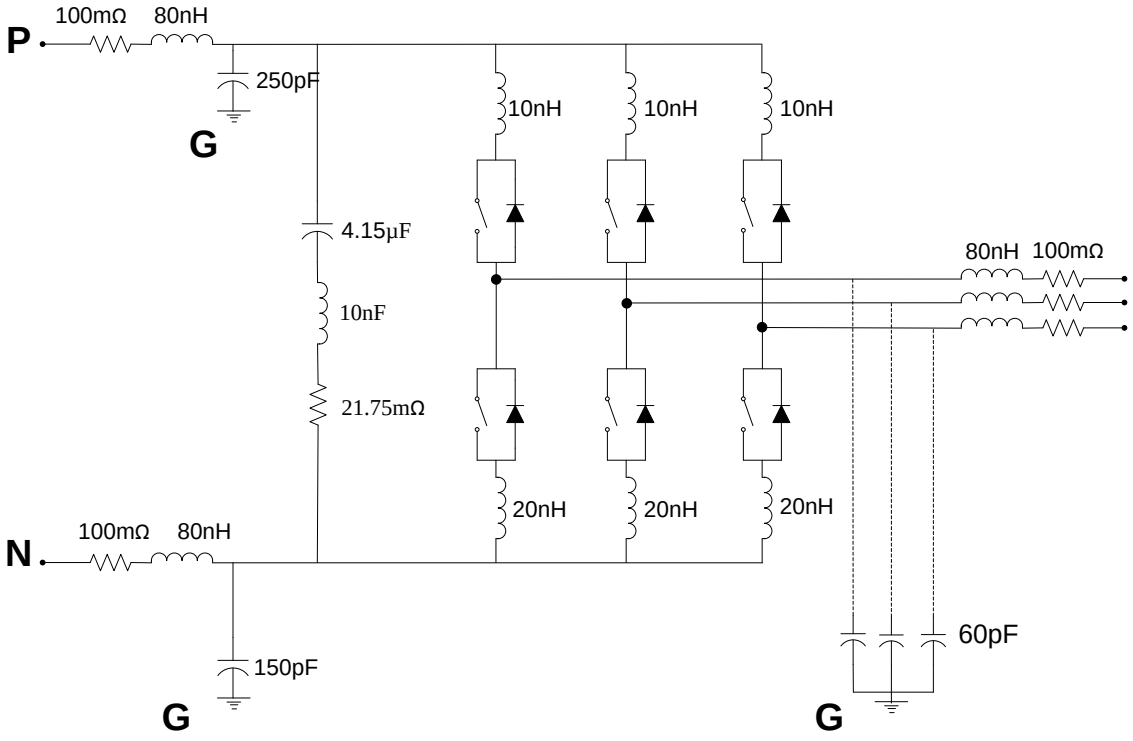

Fig. 4.7: SABER® model of three-phase motor-drive

4.1.3.1.2 Harness

A detailed lumped circuit model of the harness was used in SABER®. The per-unit length (20 cm) parameters are shown in Fig. 4.8. This model was provided by Hispano-Suiza (Safran Power). The harness is double-shielded with three wires. The model was developed through systematic measurements of DM and CM parameters of the harness. Notice the mutual coupling factors (M_{PH} and M_G) between self-inductances of the phases (L_{PH}) and also between phase & shield inductances (L_G). Shield here is denoted by the subscript G. In order to simulated a 2 m long cable 10 such sections are needed.

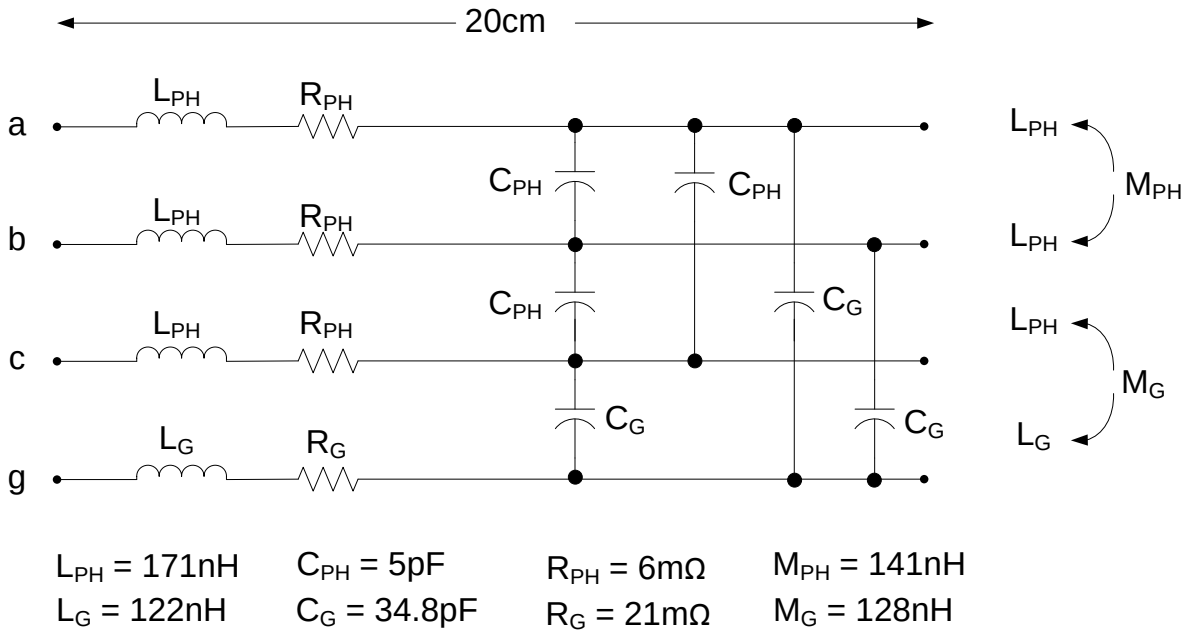

Fig. 4.8: Per-unit length (20 cm) parasitic model of the Harness

4.1.3.1.3 Permanent Magnet Motor

The motor is modeled using numerical curve fitting techniques and was again provided by Hispano-Suiza. Measurements were performed on the terminals of the motor and then a "pi" model was fitted to recover all the resonances up to 50 MHz for each winding. Details of this technique will not be discussed here and only a snapshot of the SABER® model for one winding is shown in Fig. 4.9. This model is made by numerical optimization in MATLAB® using several of RLC series and parallel circuits. The values of the RLCs in Fig. 4.9 are first guessed and then optimized by MATLAB® to best fit the impedance measurements conducted on the motor terminals.

4.1.3.1.4 Full Lumped Circuit Model

The full lumped circuit model of the motor-drive system is shown in Fig. 4.10 (as appearing in SABER® Schematics). The model is very complicated but realistic at the same time. The details of the SVM modulator and measurement probes for the input and output side CM currents will not be discussed here. Any modulations schemes like SPWM or SVM can be chosen here as the method should be independent of the type of modulation. The switching frequency is 20 kHz,

the line frequency is 100 Hz and the input voltage is 540V dc. The simulation is run in time domain, first for 50 msec with a time-step of 30 nsec (to reach a steady state) followed by another 10 msec (one line period) long simulation with 2 nsec time step to record the raw data for model extraction.

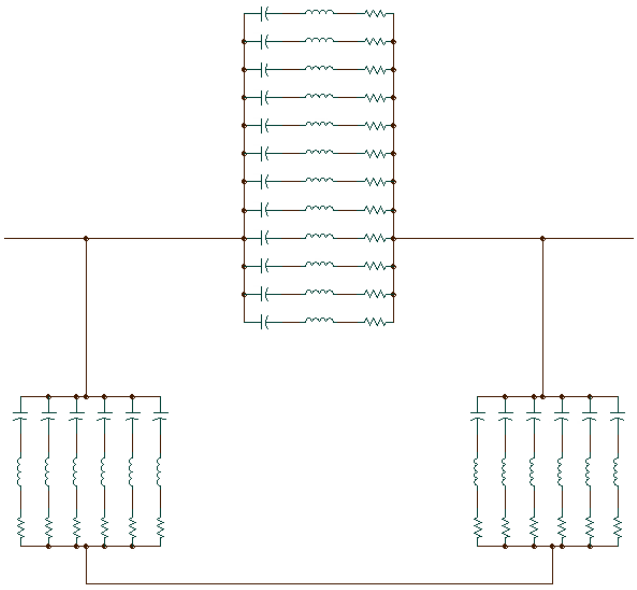

Fig. 4.9: Model Structure for the Permanent Magnet Motor

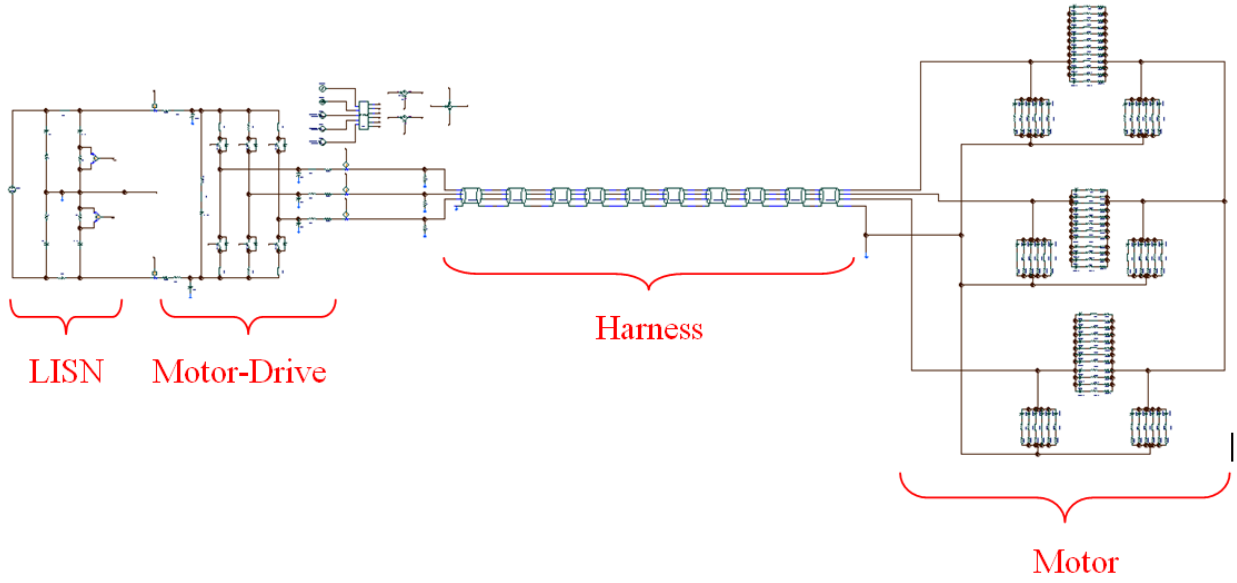

Fig. 4.10: Lumped circuit model of a single winding of the motor

4.1.3.2 Model Results

Once the equations are solved the model parameter results are obtained directly in frequency domain. Fig. 4.11 shows the two noise-voltage sources and Fig. 4.12 show the extracted noise-impedance matrix. The noise-impedance looks capacitive until 30 MHz which is expected as the model is only for CM. It can be observed that the noise-sources are different on the input and output side.

4.1.3.3 Model Discussions

It would be appropriate at this point to first understand the nature of the noise-impedances before proceeding for validation of the model. An approximate CM model of the converter can be made based on the observation of modeling results in Fig. 4.12 and is shown in Fig. 4.13. Here V_{N1} and V_{N2} are the noise sources (Fig. 4.12). The total CM capacitance on the input side is 400 pF and the total CM capacitance on the output side is 180 pF and hence is included in the model of Fig. 4.13. This model should be good only up to 30MHz as it does not include the parasitic inductances that cause resonances after 30 MHz (see Fig. 4.12).

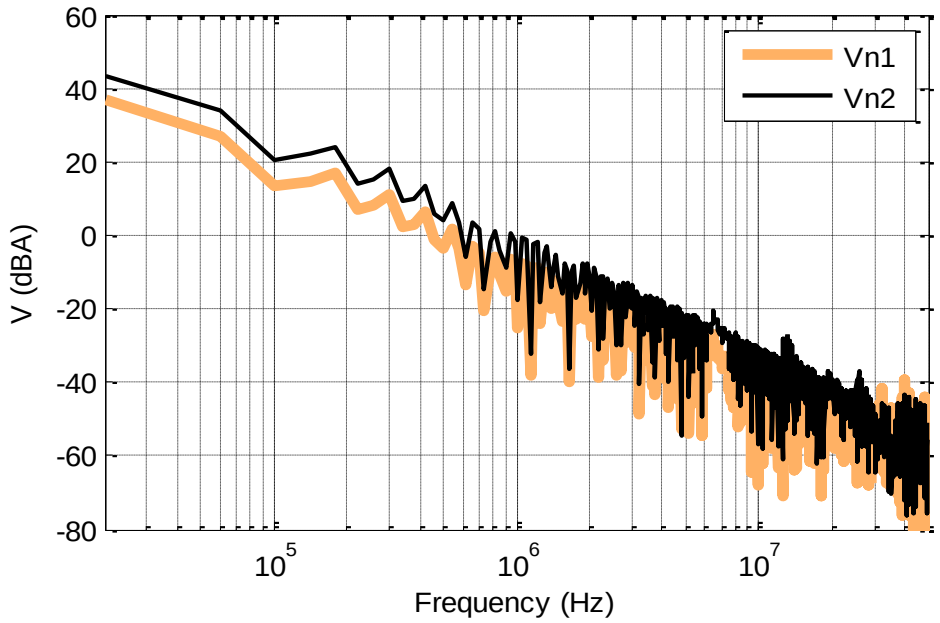

Fig. 4.11: CM noise-sources of Thevenin noise- model

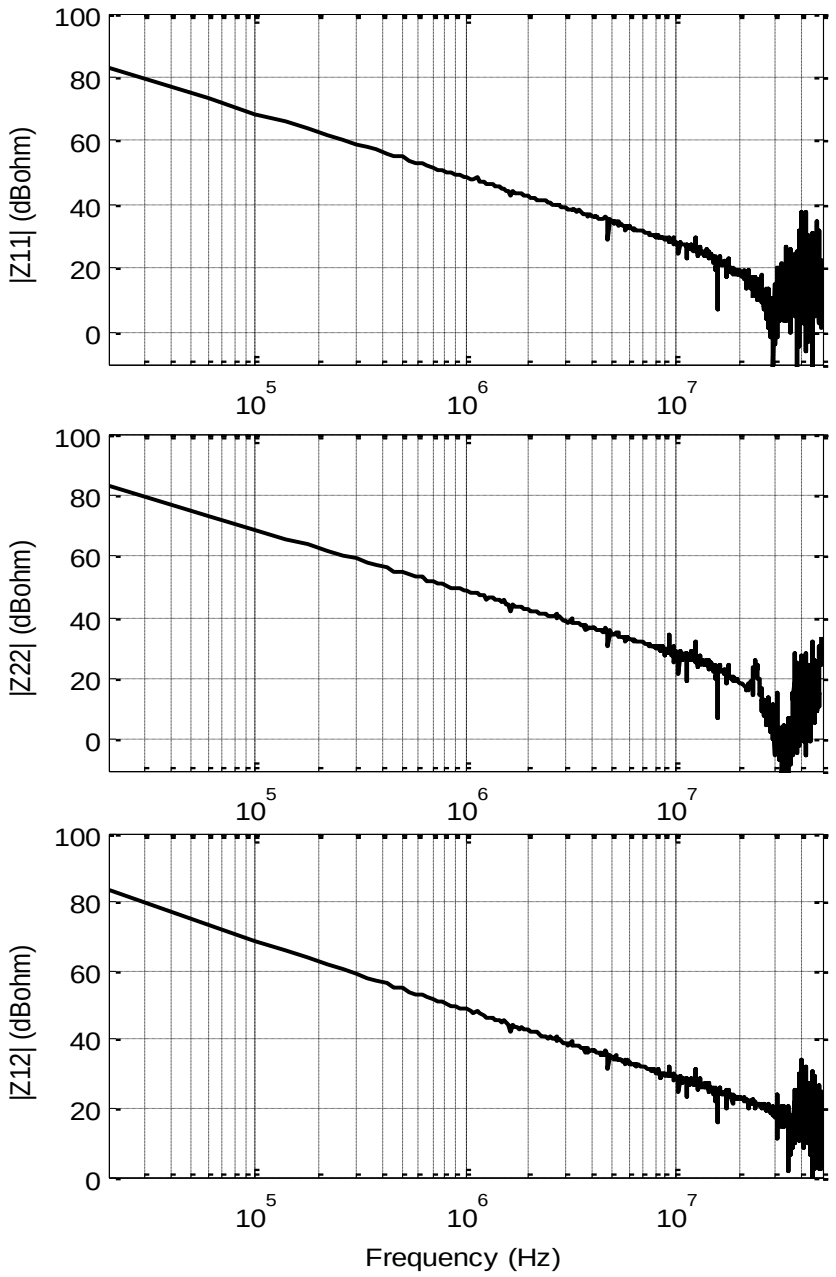

Fig. 4.12: CM noise-impedance of Thevenin noise-model

Some interesting facts can now be observed. First the transfer impedance (Z_{12}) is capacitive, so as one goes higher in frequency the interaction between the input and output of the converter actually decreases. Moreover from the model of Fig. 4.13 and the extracted impedances in Fig. 4.13, one can see that in the capacitive region (up to 30 MHz) all the noise-impedance (Z_{11}, Z_{12} and Z_{22}) are of the same value. The value of this capacitance was evaluated as 605 pF at

100 kHz. This is interesting because the sum of all CM impedances in Fig. 4.7 is 580 pF which is very close to the one extracted. This could be an indication that the motor-drive is almost acting as a short circuit between its two ports while it is switching, so whichever side one looks, the sum of only the CM capacitances is seen.

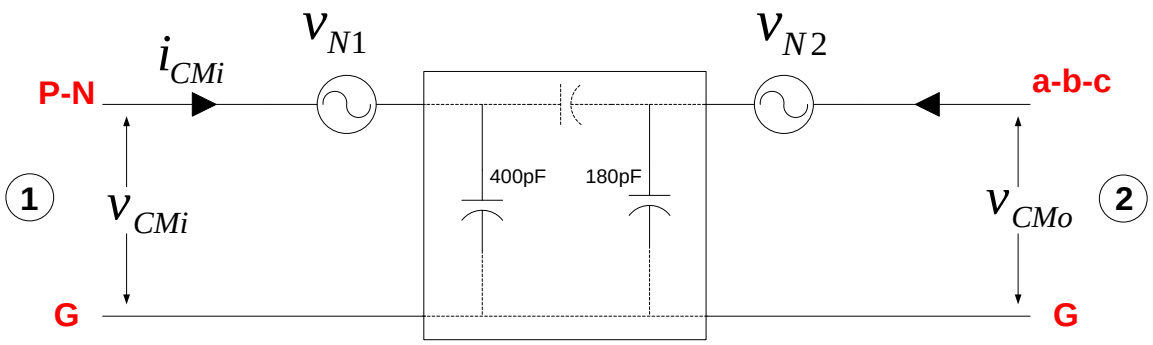

Fig. 4.13: Approximate CM model of the motor-drive based on the modeling results of Fig. 4.7

Linear impedances can in fact be directly measured using ac simulations or an impedance analyzer in the real. By doing this we avoid the noise that is seen above 30 MHz (see Fig. 4.12) which is mainly due to insufficient S/N in the high frequencies. Small signal ac simulations are done to extract the Z-matrix of the converter in the CM and under zero dc bias conditions and no switching. A zero dc bias condition is used in the ac simulations just as in the real system one would use an impedance analyzer that cannot be used at 540V dc voltage. The results are shown in Fig. 4.14. It can be observed that the direct measurement of the Z-matrix though small signal simulations matches well with that of the extracted Z-matrix by the behavioral modeling procedure. This may seem a little surprising at first since the device impedances change with the dc bias conditions and the small signal simulations were performed with zero dc bias. In contrast, the behavioral modeling procedure involves in-circuit tests the under nominal operating conditions. The result of Fig. 4.14 can be explained by considering the zero bias impedance of the diode. Diode impedance is mostly capacitive and is at least a couple of nF when there is no bias across the diode (0V). On the other hand, the CM capacitances are in the pF range and hence the device capacitance almost acts as a short circuit since it comes in series with the CM capacitances.

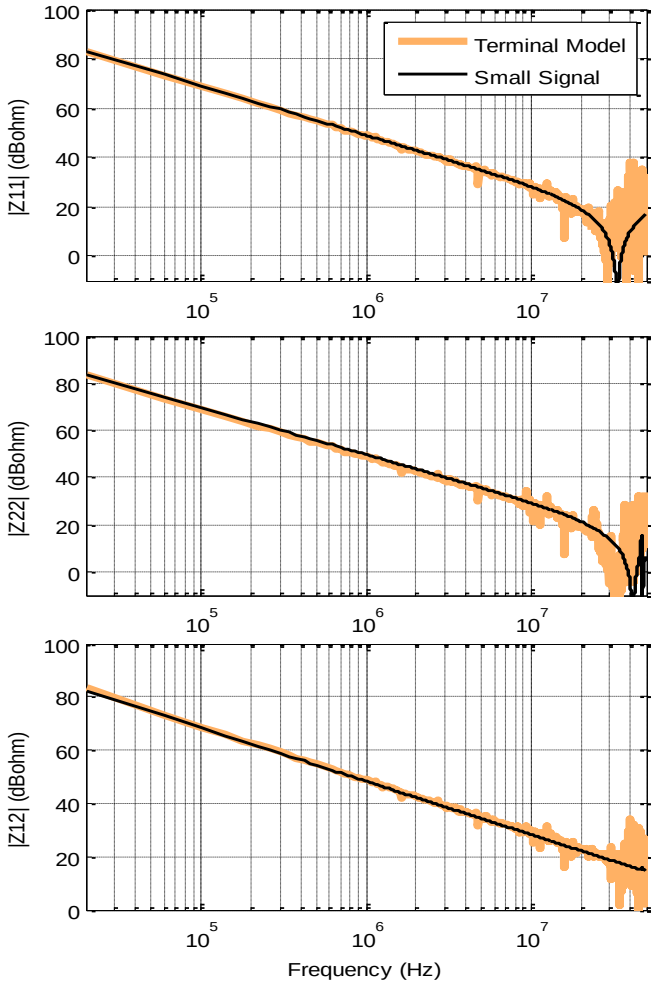

Fig. 4.14: Comparison of extracted Z-matrix of the noise model though direct measurements and through behavioral modeling procedure.

This can also be seen in form Fig. 4.13. The dashed capacitance inside the network is the total device capacitances as seen between port 1 and port 2. Let's say that the diode capacitance is about 2nF under zero dc bias condition, then between terminals "P-N" and "a-b-c" the net device capacitance would be 6x2 nF = 12 nF (because there are six switches) . Thus looking from port1 one would see a 400 pF capacitance in parallel with the series combinations of 12nF and 180 pF capacitance. This is equivalent to 400 pF in parallel to 180 pF, or 580 pF in total. Thus it is possible to extract the Z-matrix of the noise model by direct measurements and this not only simplifies the modeling process but also ensure more accuracy as now we can identify all

resonances in high frequency which otherwise would have been buried in the noise resulting from the poor S/N ratio at those frequencies.

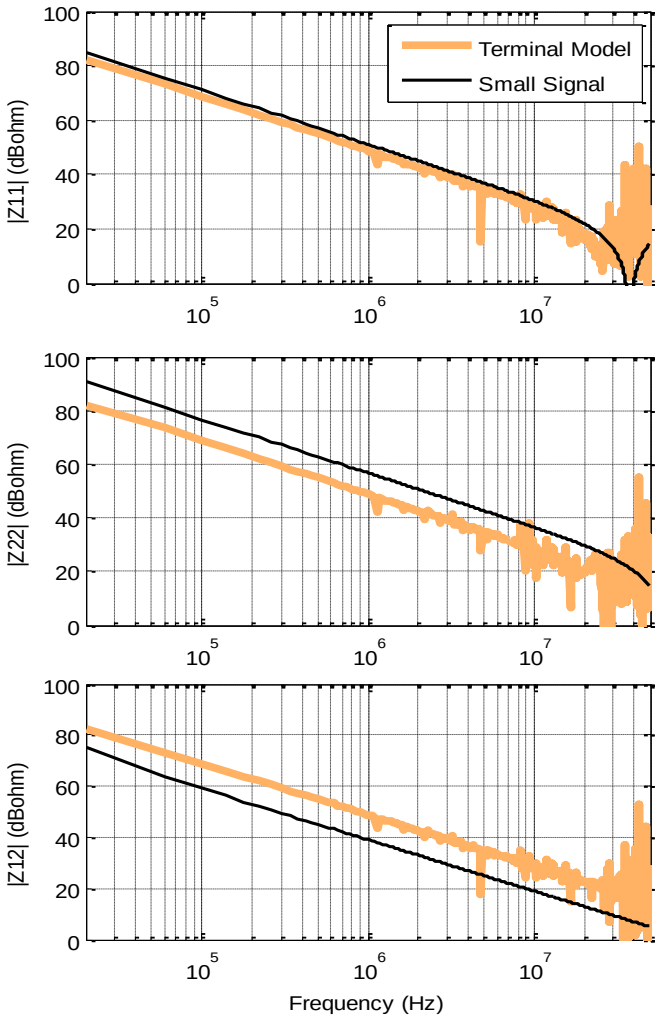

Fig. 4.15: Comparison of extracted Z-matrix of the noise model though direct measurements and through behavioral modeling procedure.

Last but not the least, it is wise to understand what would happen if the device capacitance was not high or if the devices were ideal. This condition will not exist in reality but can be created in simulations for the sake of a sanity check. The behavioral modeling procedure was repeated for the motor-drive system, only this time ideal diodes with only 10pF of external linear capacitance were used instead of power diode models. The result of the extracted noise-impedance matrix is shown in Fig. 4.15. It can be seen that this time the small signal simulations

could not match the extracted Z-matrix though the behavioral modeling procedure. This is because in small signal simulations the devices were acting as open circuit and hence different capacitances are observed when looking from either port, whereas in the behavioral modeling procedure reveals the Z-matrix when the converter was switching. In fact, there is no difference in the extracted Z-matrix though behavioral modeling procedure when Fig. 4.14 is compared to Fig. 4.15.

Thus one can conclude two things, first the terminal model is able to extract the true noise-impedance when the motor-drive is in operation, and second, because of the inherent high capacitance of the devices under zero bias condition, the model impedances can be measured directly using an impedance analyzer.

4.1.3.4 Model Validation

The validation will be carried out for several different input and output conditions that are usually seen in a motor-drive. The simulation circuit used for validation is shown in Fig. 4.16. The validation will be carried out step-by-step in order to show the versatility of the terminal model. Sections like the DM and CM filters will add one by one and the prediction of the change in the CM current spectrum will be shown. The final validation step will include all filters as shown in Fig. 4.17 and a 10 m long harness. These filters values are arbitrary chosen but are realistic. By doing so there is an element of uncertainty in the filter performance and we would like the terminal model to reveal it.

4.1.3.4.1 Validation with 10m harness

The first validation step is to predict the change in CM currents from motor-drive when the 2 m long harness is was replaced by a 10m long harness. Remember that the terminal model was developed with a 2 m long harness. The comparison results are shown in Fig. 4.17. It can be seen that the model is able to predict (see "predicted" in Fig. 4.18) the simulated CM currents (see "measured" in Fig. 4.17) on both dc and ac side within 6 dB of accuracy and up to at least 30 MHz. Beyond 30 MHz the model is performing well but the error is large at the resonant point for the harness. The plot of nominal (see “nominal” in Fig. 4.17) gives the CM current when a 2 m long harness is used. It can be seen that after 2 MHz there is a change in CM currents when the 2 m long harness is replaced by a 10 m long harness and the model is able to accurately predict this change.

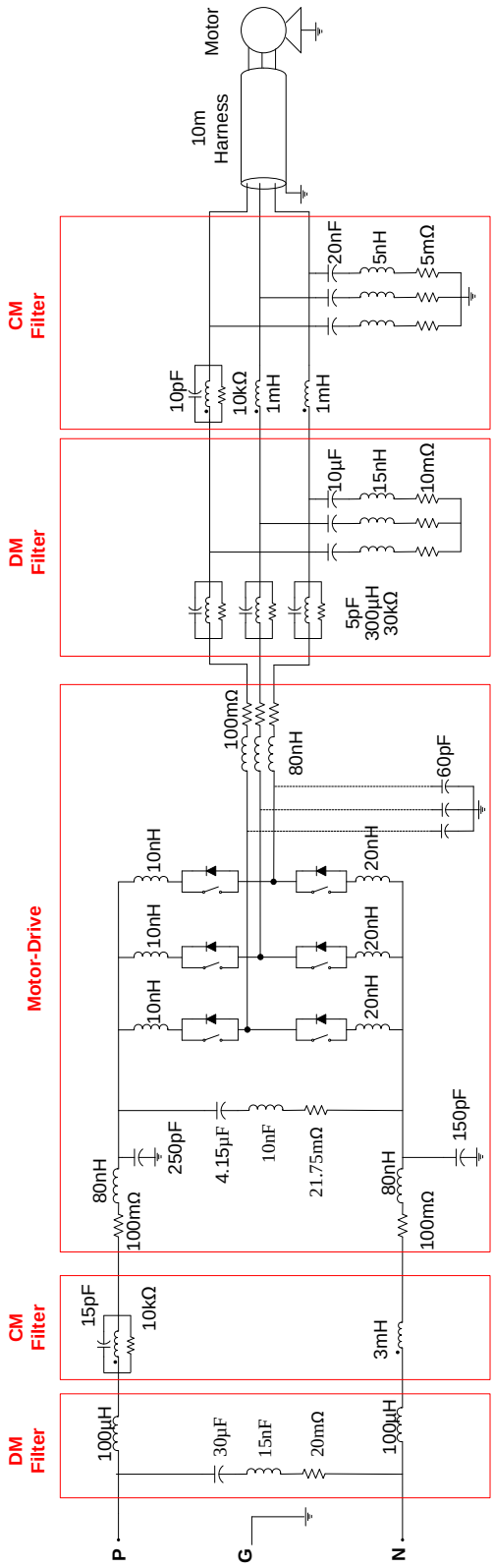

Fig. 4.16: Validation Model of motor-drive system with CM and DM filters on both ac and dc sides and a 10 m long harness

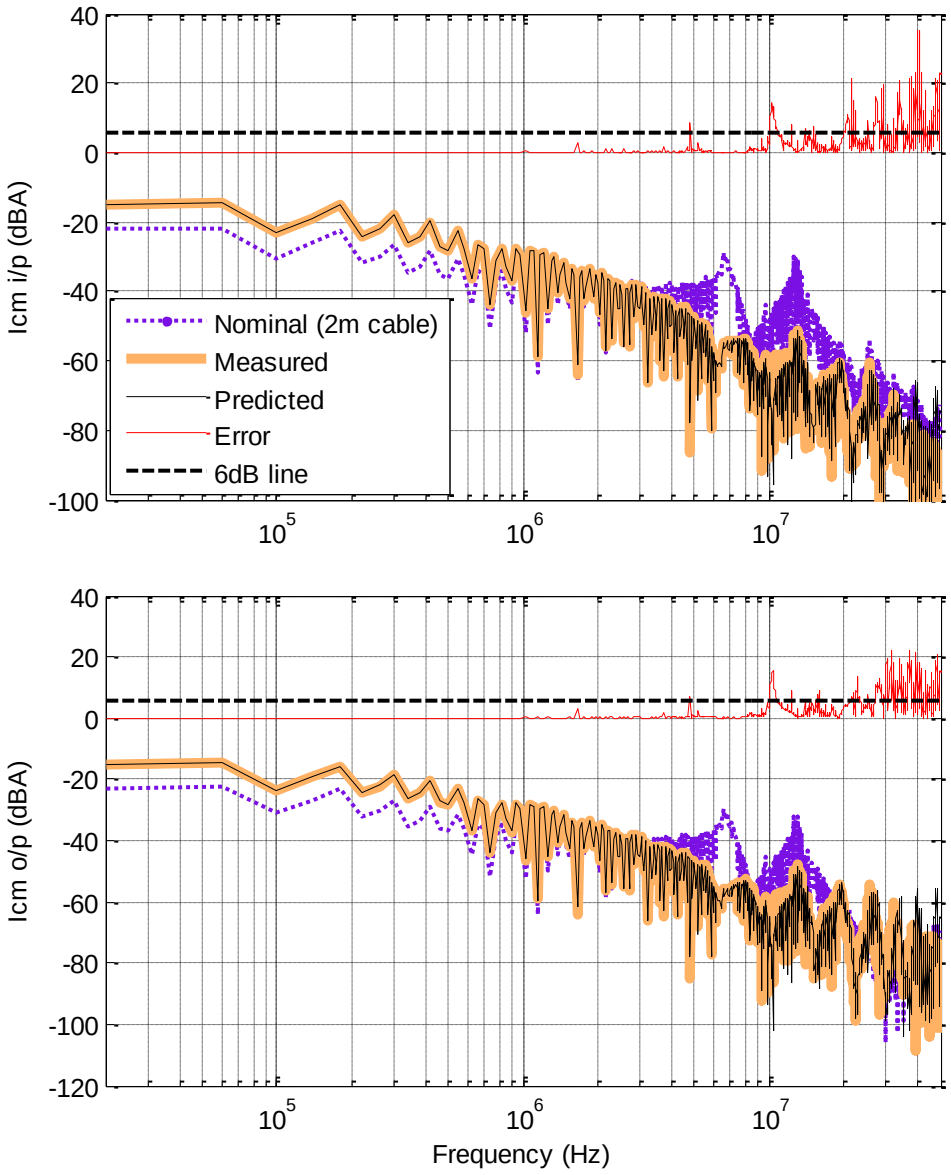

Fig. 4.17: Comparison of simulated and predicted CM current from motor-drive with a 10 m long harness

4.1.3.4.2 Validation with ac side DM filter

Fig. 4.18 gives the comparison of simulated and predicted, dc and ac side CM currents when a DM filter is inserted on the ac side. The 10 m long harness is kept as it is in the simulations. The topology of the filter is shown in Fig. 4.16. Again the predictions are found to be good up to 30 MHz. Comparing Fig. 4.17 and Fig. 4.18, we can see that the DM filter has significantly attenuated the CM noise above 1 MHz and the terminal model is able or accurately predict this change. In the low frequency the addition of the DM filter has led to an increase in the CM noise.

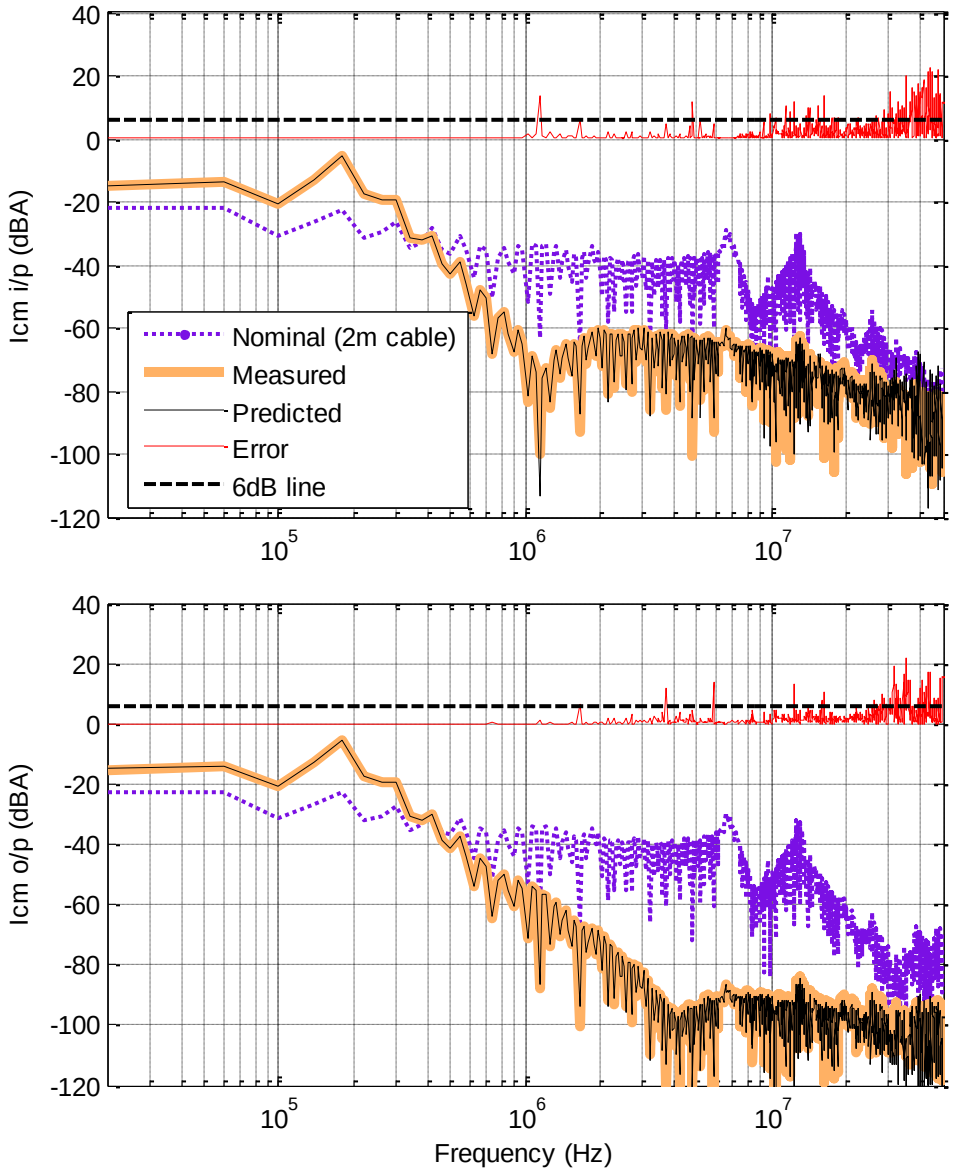

Fig. 4.18: Comparison of simulated and predicted CM current from motor-drive with a 10 m long harness and an ac side DM filter

4.1.3.4.3 Validation with ac side CM and DM filter

A CM filter was added in the ac side. The DM filter and the 10 m long harness was kept as it is in the simulations. Fig. 4.19 shows the validation results for the ac and dc side CM currents. The results match well up to 30 MHz. The topology of the ac side CM filter was shown in Fig. 4.16. It can be seen that the addition of the CM filter has further attenuated the CM noise

currents, especially from 100 kHz to 1 MHz. Thus by application of CM and DM filters in the ac side noise attenuation in the entire conducted emission spectrum is observed.

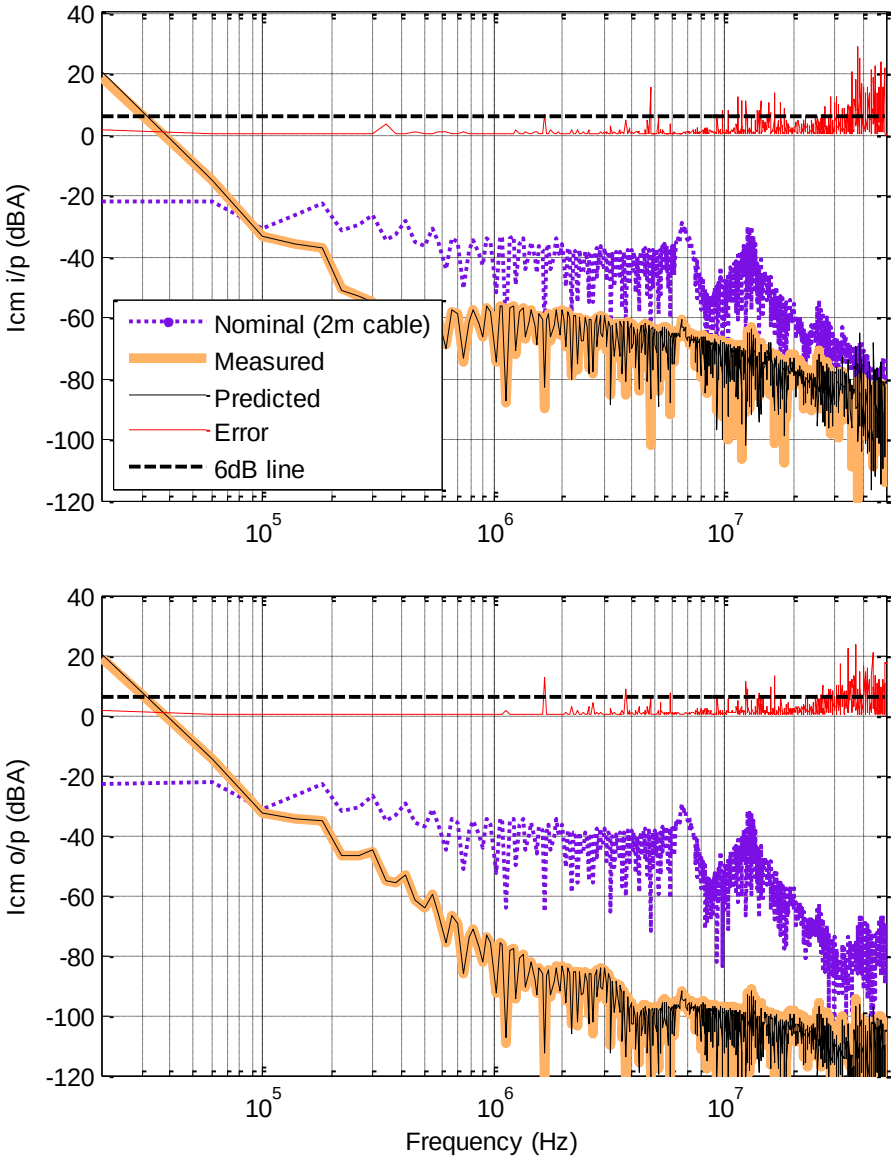

Fig. 4.19: Comparison of simulated and predicted CM current from motor-drive with a 10 m long harness and an ac side DM + CM filter

4.1.3.4.4 Validation with dc side DM filter

The ac side CM and DM filters are removed and instead a dc side DM filter is introduced. The results are shown in Fig. 4.20 and are again good up to 30 MHz. It is interesting to see that

when the ac side filters are removed the resonances due to the long harness are exposed and their effects are seen in CM currents on both sides. The dc side DM filter achieves good attenuations for dc side CM currents but does not make any significant contribution to ac side CM current.

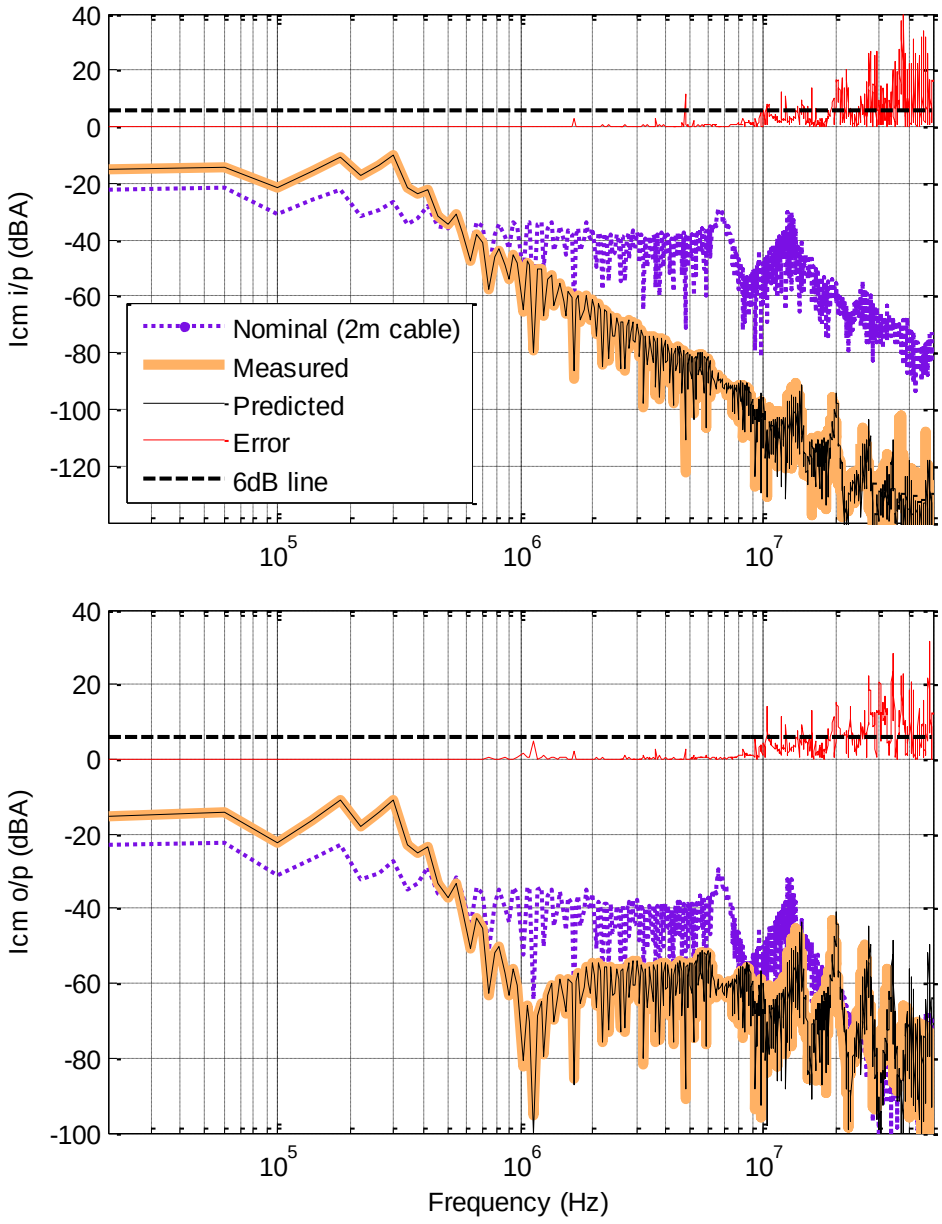

Fig. 4.20: Comparison of simulated and predicted CM current from motor-drive with a 10 m long harness and a dc side DM

4.1.3.4.5 Validation with dc side CM and DM filter

A CM filter is now inserted in the dc side. The DM filter was kept as is and the harness is still 10 m long. The topology of the dc side CM filter is shown in Fig. 4.16. Fig. 4.21 shows the validation results for this scenario. The prediction results are not as good as before though still acceptable until 30 MHz. It does not look like this CM filter is helping as it almost completely took out the effect of the dc side DM filter when compared to Fig. 4.20. Nevertheless, we were expecting some discrepancies since these filters were arbitrarily chosen.

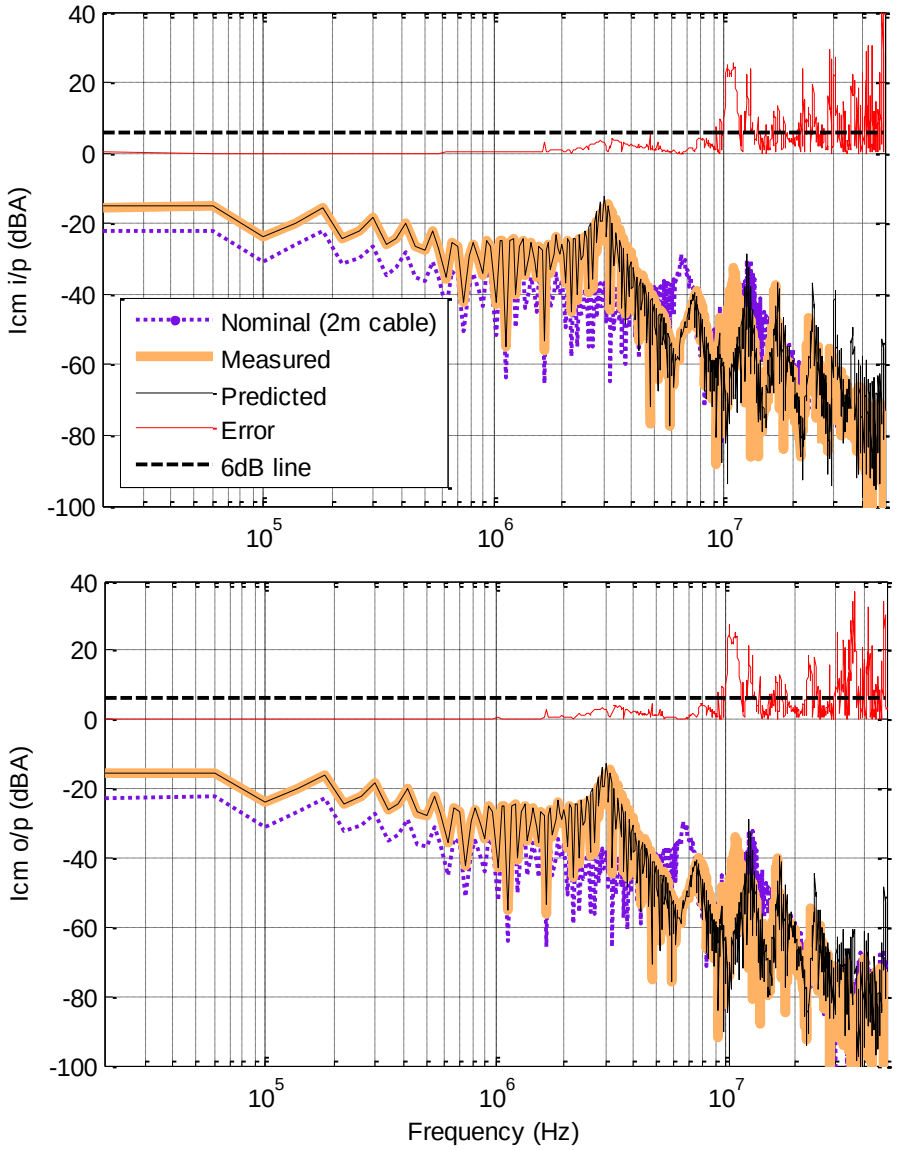

Fig. 4.21: Comparison of simulated and predicted CM current from motor-drive with a 10 m long harness and a dc side DM + CM filter

4.1.3.4.6 Validation with ac-dc side CM-DM filters

Let's put CM and DM filters on both the ac and dc side to see the overall effect of all filters. The schematic circuit now looks exactly like the one shown in Fig. 4.16. The results in general are good up to 30 MHz with less than 6 dB of error at most points. It can seen that the overall noise attenuation is good but there is a spike at about 31 MHz that appears when both CM and DM side filters are put. This spike was not observed before and is accurately predicted by the terminal model. Thus the unexpected peak can now be investigated to see its real cause. It may be happening due to interaction between the ac and dc side filters.

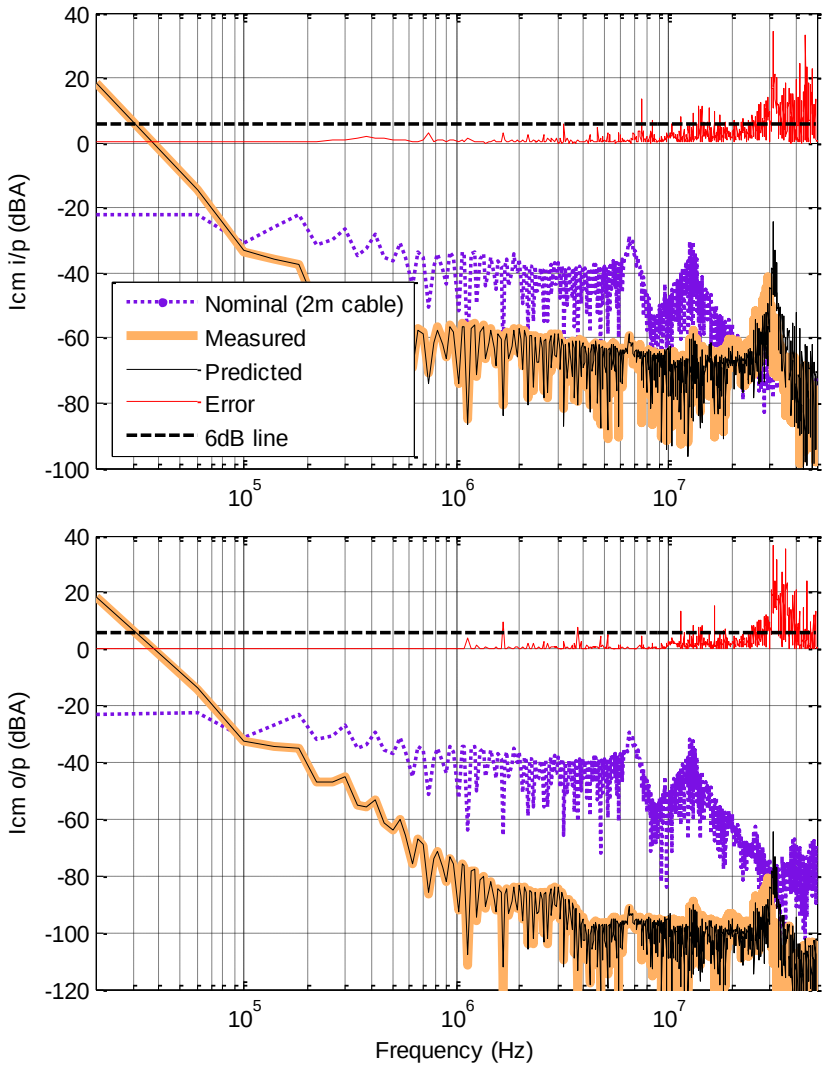

Fig. 4.22: Comparison of simulated and predicted CM current from motor-drive with a 10 m long harness and DM + CM filters on both ac and dc side.

4.1.3.4.7 Prediction for changes in input DC voltage

It would be interesting to know if the model can be scaled for changes in operating point or not. Though many things can lead to change in operating point like change in load of the motor, change in modulations index, change in the dc-input voltage etc., we will attempt to predict CM currents when the dc-input voltage changes. Simulations are carried out with a 10 m long harness but with only 100V dc input voltage as opposed to 540V. For these predictions the CM noise sources V_{N1} and V_{N2} (The model is still the old one created from simulations with 540V dc-supply) are scaled down by 5.4 times (540/100). The results for validation are shown in Fig. 4.24. The results show accurate prediction of CM current from the motor-drive up to 30 MHz. Thus changes in operating point due to a different dc voltage can be easily predicted by proportionally changing the noise sources of the terminal model.

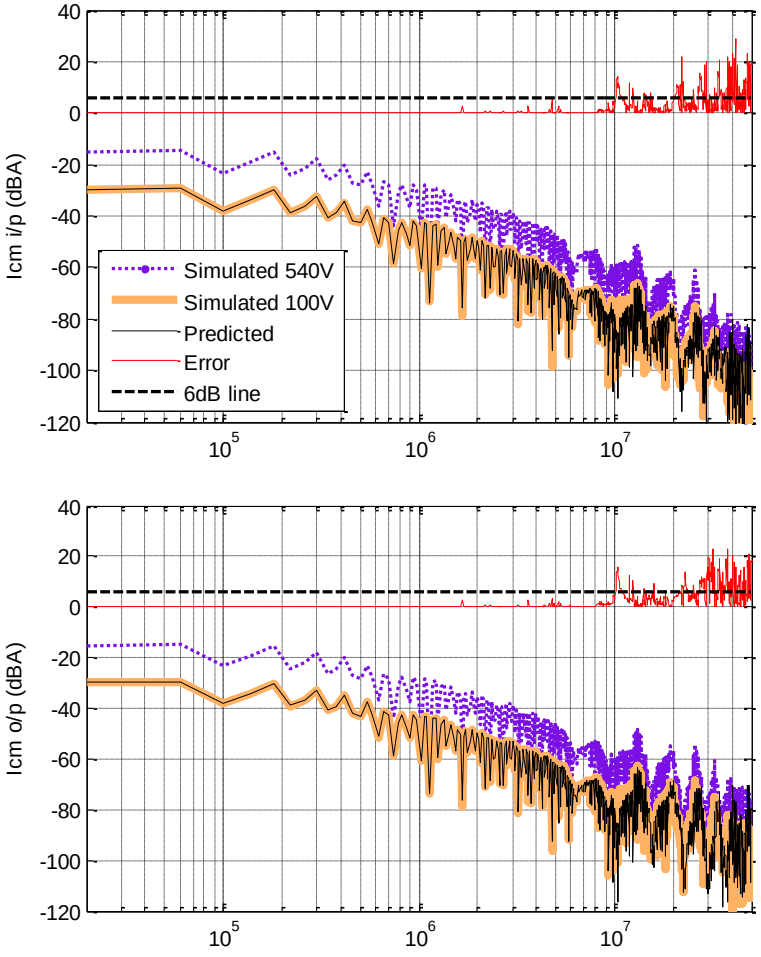

Fig. 4.23: Comparison of simulated and predicted CM current from motor-drive with a 10 m long harness and 100V dc input voltage

4.1.3.5 Conclusions

The validation results show that within the limits of the simulations the proposed terminal model for CM is working well. This verifies the proposed modeling procedure. Above all it verifies the concept and tells us that it is possible to extract a linear un-terminated equivalent of the motor-drive for the CM noise.

These simulations however, were not that easy. The extraction of the model itself was very slow, taking a couple of months. The simulations accuracy was also dependent on the time-step used. As mentioned before, all simulations are run for 50 ms simulation time with a 30 ns time-step until a steady state is achieved. This is followed by another 10 ms of simulations at 2 ns time-step to record time domain waveforms for the purposed of model extraction. Significant loss of accuracy was seen when simulation time-step of the last 10 ms is changed from 2 ns to 5 ns. The simulations are not robust either, a small change in the filter parameter can lead the simulation to crash and re-adjusting the simulation parameters can take up to a couple of hours.

4.1.4 Model Verification Through Experiments

In the previous work on behavioral modeling [60, 62, 64] the model extraction method was based on solving directly for the unknown parameters in the model. In fact the modeling procedure detailed in section 4.1.2 is also based on the same idea. Although from the simulations it is clear that an un-terminated model for CM modeling is possible in the case of motor-drives, there is a problem in directly using this strategy in actual experiments.

The behavioral modeling method has a very fundamental requirement that is the measurements made under different conditions must be time-synchronized to each other or in other words the phase shift between them is zero. This idea is described in Fig. 4.24. Here noise current measured at the same terminal is shown but in two different external conditions. By time-synchronization we mean that the delay between the noise spikes (t_{delay}) should be zero. To ensure this, the oscilloscope should be triggered using the PWM clock signals. However in the case of commercial power converters, the PWM signals are not accessible from outside and for ac converters the switching frequency is often not a perfect multiple of line (ac) frequency. Thus the PWM pattern and consequently the EMI do not repeat every line cycle. In other words, every time a line cycle is recorded, the noise pulses are found shifted in time. These measurements, if used directly lead to severe uncertainty in identification of model parameters.

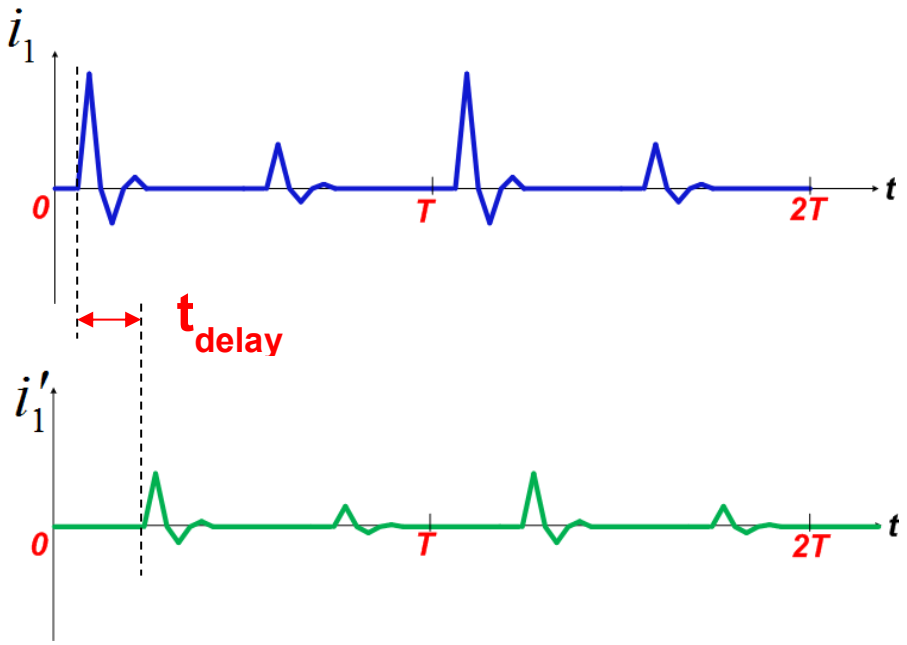

Fig. 4.24: Un-synchronized EMI noise pulses

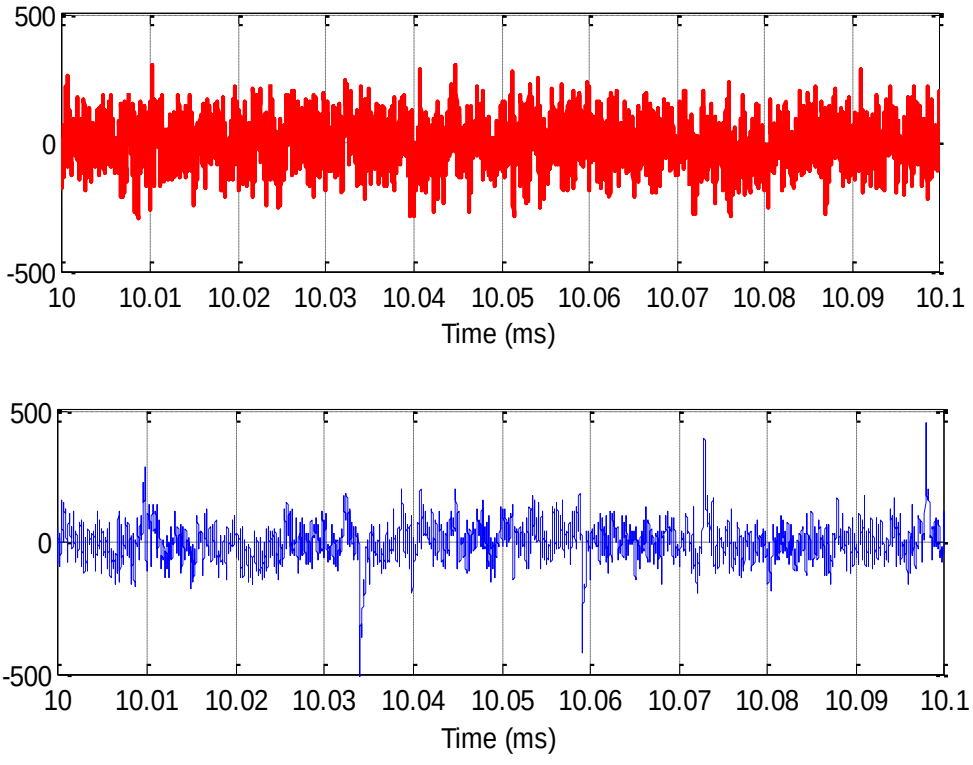

Fig. 4.25: Noise voltage source V_{N1} and V_{N2}

To demonstrate what happens if the issue of time-synchronization is ignored, the terminal model extraction procedure was implemented exactly like the way it was described in section 4.1.2. The results of the model extraction are shown in Fig. 4.25 and Fig. 4.26. It can be seen from the figures that there is no apparent switching observed in the voltage sources and the model impedances are extremely noisy. The model in fact makes no physical sense and hence cannot be used. Thus, the behavioral modeling procedure works only when there is perfect time synchronization. Contrary to these result it is evident the method worked in simulations. This is because all time-domain waveforms are recorded between the 50 ms to 60 ms simulation time which is the sixth cycle of the line frequency. Thus, automatically all PWM pulses and consequently the EMI noise signals were time-synchronized.

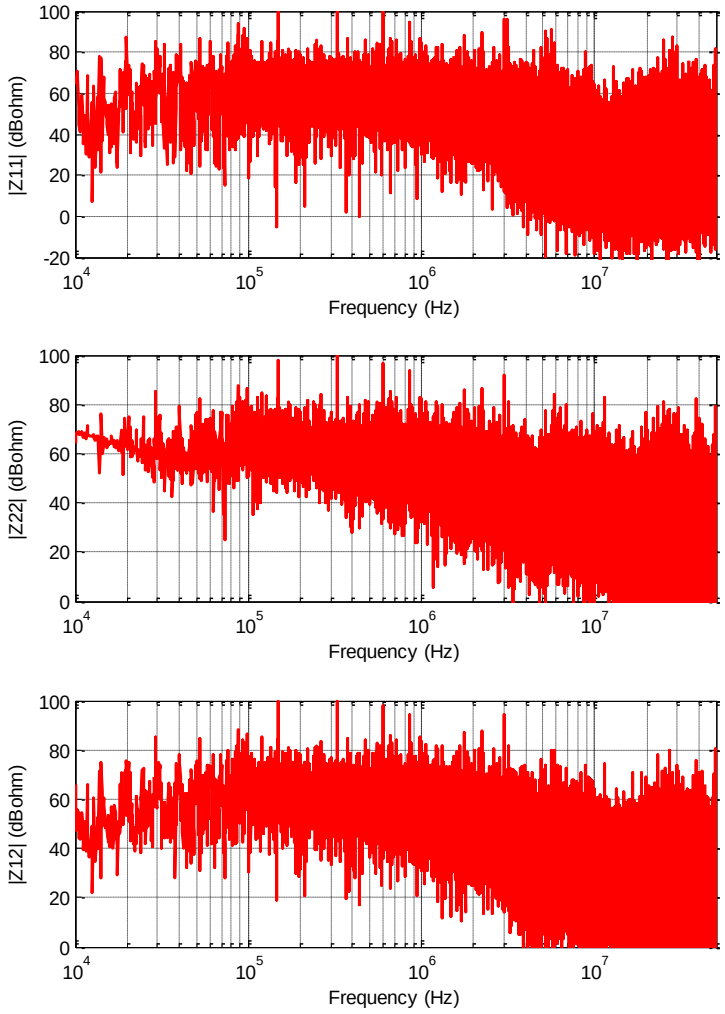

Fig. 4.26: Model Impedances Z_{11}, Z_{22} and Z_{12}

4.1.4.1 Alternate Modeling Procedure

An alternate model extraction method was developed to solve the problem associated with time-synchronization. The resulting procedure also simplifies the model extraction process and gives physically correct values of the model parameters.

4.1.4.1.1 Model Impedances

Fig. 4.27 shows the motor-drive in a conducted EMI set-up. For convenience, the proposed model of the motor-drive is given again in Fig. 4.28. The motor-drive of Fig. 4.27, enclosed within the dashed box is modeled using the noise model of Fig. 4.28. Again, it should be noted that the model of Fig. 4.28 represents the motor-drive only. The network equations for the model of Fig. 4.28 are given by:

$$\begin{bmatrix} -i_{CMi}Z_i \\ -i_{CMo}Z_o \end{bmatrix} = \begin{bmatrix} Z_{11} & Z_{12} \\ Z_{21} & Z_{22} \end{bmatrix} \begin{bmatrix} i_{CMi} \\ i_{CMo} \end{bmatrix} + \begin{bmatrix} V_{N1} \\ V_{N2} \end{bmatrix} \tag{18}$$

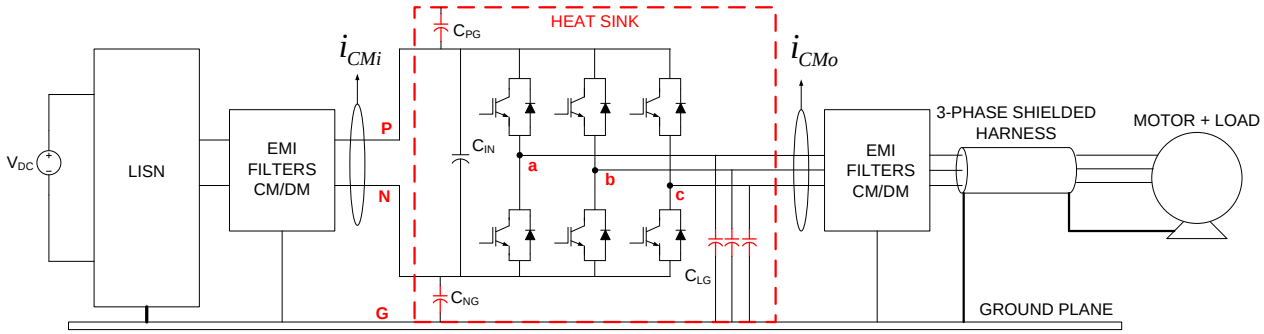

Fig. 4.27: Complete set-up of the motor-drive system

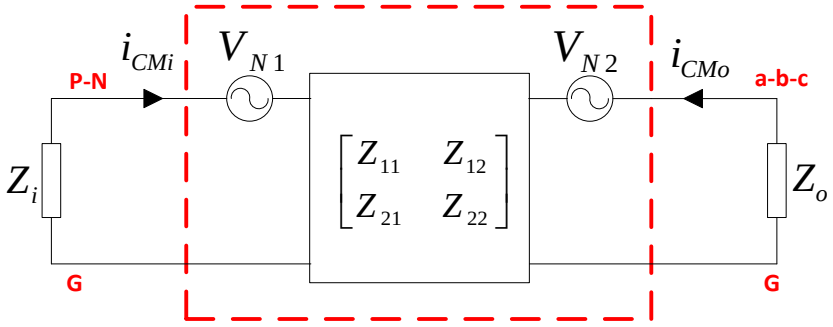

Fig. 4.28: Two-port model of the motor-drive

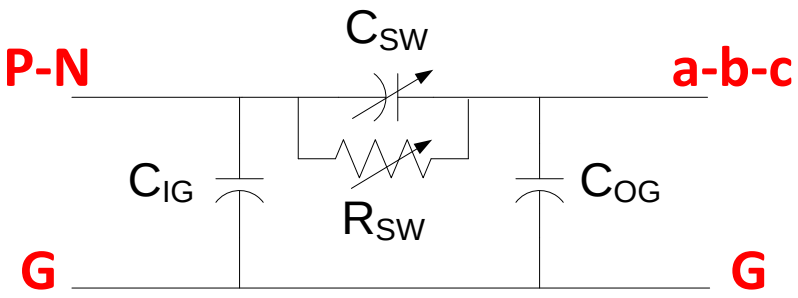

Fig. 4.29: Approximate CM equivalent circuit of motor-drive

In Fig. 4.27, C_{PG} and C_{NG} are parasitic CM capacitances from the dc-bus to the ground and C_{LG} is from each phase of the motor-drive to the ground. The parasitic CM capacitance from each phase to ground can be different but comparable and therefore for simplicity they are assumed equal here. Fig. 4.29 shows the low-frequency approximation of the motor-drive's impedance model in CM. From Fig. 4.27, the input-side parasitic capacitance to ground is equal to $C_{PG} + C_{NG}$ and is represented as C_{IG}. The output-side capacitance C_{OG} is equal to the sum of all capacitances from the three phases to ground (3 x C_{LG}). Also from Fig. 4.27, it can be seen that in CM all the semiconductor switches will appear in parallel and their net impedance (Z_{SW}) is represented by a time-variant RC branch in Fig. 4.29. Assuming $Z_{12} = Z_{21}$, the Z-matrix for the model in Fig. 4.29 is given by (19)-(21).

$$Z_{11} = \frac{Z_{C_{IG}}\left(Z_{C_{OG}} + Z_{C_{SW}}\right)}{Z_{C_{IG}} + Z_{C_{OG}} + Z_{C_{SW}}} \tag{19}$$

$$Z_{22} = \frac{Z_{C_{OG}}\left(Z_{C_{IG}} + Z_{C_{SW}}\right)}{Z_{C_{IG}} + Z_{C_{OG}} + Z_{C_{SW}}} \tag{20}$$

$$Z_{12} = \frac{Z_{C_{IG}} Z_{C_{OG}}}{Z_{C_{IG}} + Z_{C_{OG}} + Z_{C_{SW}}} \tag{21}$$

It can be seen form Fig. 4.29 that the model has a linear time-invariant part formed by the parasitic CM capacitances (C_{IG} and C_{OG}) in the system and a nonlinear time-variant part formed by the net impedance of the semiconductor switches. The impedance of semiconductor switches will change as per the switching function (PWM) when the drive is in operation. However, even during operation and under all possible states of the switches, the impedance of the time-variant

RC branch is expected to be much smaller in comparison to the impedances of the CM capacitances in system. Thus neglecting Z_{Csw}, (19)-(21) can be approximate as

$$Z_{11} \approx Z_{12} \approx Z_{22} \approx \frac{Z_{C_{IG}} Z_{C_{OG}}}{Z_{C_{IG}} + Z_{C_{OG}}} \tag{22}$$

From (22) it can be seen that the Z-matrix is dependent on only the linear part of the system. For simplicity the measurement of the Z-matrix can be conducted even in power-off condition. This is because in power-condition the impedance of the switches will be entirely capacitive and since under zeros bias (V_{DC} = 0) the output capacitance of the semiconductor switches is the largest, the approximation of (22) is still valid. Eq. (22) also shows that the parameters of the Z-matrix should be almost the same at lower frequencies. However, at higher frequencies the CM impedances are expected to be inductive due the stray inductances in the PCB traces and grounding paths which would render this approximation invalid. This is typically the case above 10 MHz.

4.1.4.1.2 Modeling Procedure

The following procedure is proposed to solve the problem of time-synchronized:

Step 1: Measure the Z-parameter matrix (Z_{11}*, Z_{22}* and Z_{12}*) with a VNA directly under power-off conditions. In [64, 74] it was shown that it is possible to measure the input-output impedances directly provided that the constant parasitic impedances in the converter dominate at the EMI frequencies. Here * means an approximate value.

Step 2: Implement input and output impedances Z_i and Z_o (Fig. 4.28) such that

$$Z_i >> Z_{11}^{*} \text{ and } Z_o >> Z_{22}^{*} \tag{23}$$

This is referred to as the "*series-condition*". The CM currents at both input side and output side are recorded simultaneously over one complete line cycle. Using (22) and (23) in (18), the noise voltage sources can be directly approximated as

$$v_{N1} \approx -i_{CMi} Z_i \tag{24}$$

$$v_{N2} \approx -i_{CMo} Z_o \tag{25}$$

Since Z_i and Z_o are passive and can be measured accurately with an impedance analyzer, the errors in the calculated noise voltage sources due to uncertainties in the Z-matrix measured in *Step 1* are reduced. Simultaneous measurements on two different channels of the oscilloscope will help in capturing the phase relationship between the noise sources.

Step 3: In principle the parameters of the proposed terminal model are now known. However as discussed before, the model impedance matrix obtained by direct measurement in power-off conditions is an approximation and hence needs to be optimized for better accuracy. To accomplish this, an opposite condition to (23) is created by selecting

$$Z_i << Z_{11}^{\ *} \text{ and } Z_o << Z_{22}^{\ *} \tag{26}$$

This is referred to as the "*shunt-condition*". The larger is the difference between the Z_i, Z_o pair used in the series and shunt-conditions, the large will be the range of input and output impedances that the model will become accurate after optimization. The input and output CM currents can be now estimated from (18) and are given by

$$i_{CMi}^{\ *} = \frac{v_{N2} Z_{12}^{\ *} - v_{N1}\left(Z_o + Z_{22}^{\ *}\right)}{\left(Z_i + Z_{11}^{\ *}\right)\left(Z_o + Z_{22}^{\ *}\right) - Z_{12}^{\ *} Z_{21}^{\ *}} \tag{27}$$

$$i_{CMo}^{\ *} = \frac{v_{N1} Z_{21}^{\ *} - v_{N2}\left(Z_i + Z_{11}^{\ *}\right)}{\left(Z_i + Z_{11}^{\ *}\right)\left(Z_o + Z_{22}^{\ *}\right) - Z_{12}^{\ *} Z_{21}^{\ *}} \tag{28}$$

Since the measured Z-matrix is approximate, the calculated currents in (27)-(28) are also approximate. Optimization of Z-matrix is now carried out to minimize the square of the error between the magnitudes of the estimated (i_{CMi}*) and measured (i_{CMi}) input CM current. Thus the objective function is:

$$\min_{(Z_{11}, Z_{12}, Z_{22})} \left(\left|i_{CMi}^{\ *}\right| - \left|i_{CMi-Meas}\right|\right)^2 + \left(\left|i_{CMo}^{\ *}\right| - \left|i_{CMo-Meas}\right|\right)^2 \tag{29}$$

Notice that in (29), error terms for both the input and output side CM current are used. The measured CM currents in ***Step 2*** and ***Step 3*** could be completely unsynchronized in time and thus in (29) only the magnitudes of CM currents are used. This method alleviates the problem of time synchronization discussed earlier. Also note that the objective function given in (29) can contain terms for other input/output conditions, but this only make the optimization process slow, so it has been avoided here to for simplicity. In principle the noise sources could also be optimized as

well, but the problem is that they have a very specific phase relationship between them and this phase relationship must be maintained for greater accuracy. Optimizing noise sources would mean optimizing the magnitude and phase of both noise sources under the constrained that the phase differences between them remains unchanged. This will definitely complicate the objective function of (29). Moreover it was found that the approximation in (23) is adequately accurate if the conditions are implemented correctly and therefore for simplicity the noise sources are not optimized here.

The optimization of impedances can be carried out on a frequency point by point basis, which makes the optimization fast but leads to uncertainty in the final results as all points get treated independently. When done this way, the final optimized results will have a lot of noise as the solver will have the freedom to change impedances at each frequency point independently. Forcing the impedances to have physical meaning can avoid this problem. Each parameter of the Z-matrix (Z_{11}, Z_{12}, Z_{22}) is thus approximated with an RLC equivalent circuit. The initial values of RLC can be obtained from the measured impedance in ***Step 1***. These RLC values are then optimized to minimize (29).

4.1.4.2 Laboratory Set-Up

The test set-up for experimental validations consists of a standard LISN terminated with 25 Ω resistance, a 2kW motor-drive, a three-phase shielded cable (32 feet), and a 5hp (3.73 kW) motor with a blower acting as a constant load. The entire set-up is kept on a copper sheet, except for the motor. The reason why motor and load assembly is not directly connected to the copper sheet is because of the space limitation on laboratory test bench. The only CM path from the motor chassis to the converter is through the shield of the output side harness. The input voltage to the drive is 300V (V_{DC}). The line frequency is set to 40 Hz and the switching frequency of the drive is 10 kHz. The set-up is based on Fig. 4.27 and is shown in Fig. 4.30.

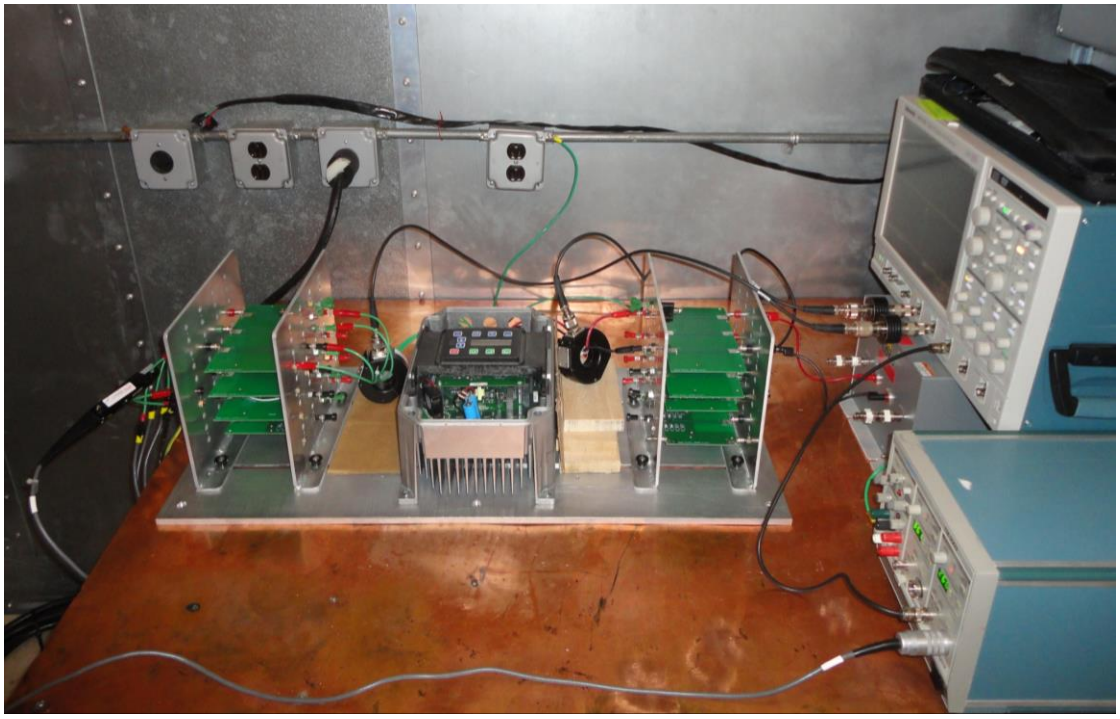

Fig. 4.30: Laboratory test set-up for un-terminated CM model extraction

Two current-monitoring probes (ETS-Lindgren 91550-1) with a bandwidth 10 kHz to 100 MHz are used for recording the input and output side CM currents. The oscilloscope was set to capture time domain data with a resolution of 2ns/point. CM noise is measured over one line cycle (25 ms) assuming that the magnitude of EMI spectrum remains same over every line cycle. All measurements are carefully calibrated to compensate for the transfer function of the current probes and the attenuators.

4.1.4.3 Model Results

The first step is to measure the model impedance matrix. The motor-drive was disconnected from the LISN and the harness. The terminals at the input side were short-circuited to form Port-1 and the output phases were short-circuited to form Port-2. A VNA is used to measure the full 2-port S-parameters with ground as the reference and then the S-parameters are converted into Z-parameters. Fig. 4.31 shows the measured model impedances. As discussed in Section 4.1.4.1.1, all impedances in the Z-matrix are almost the same and the condition in (22) is satisfied until about 5 MHz.

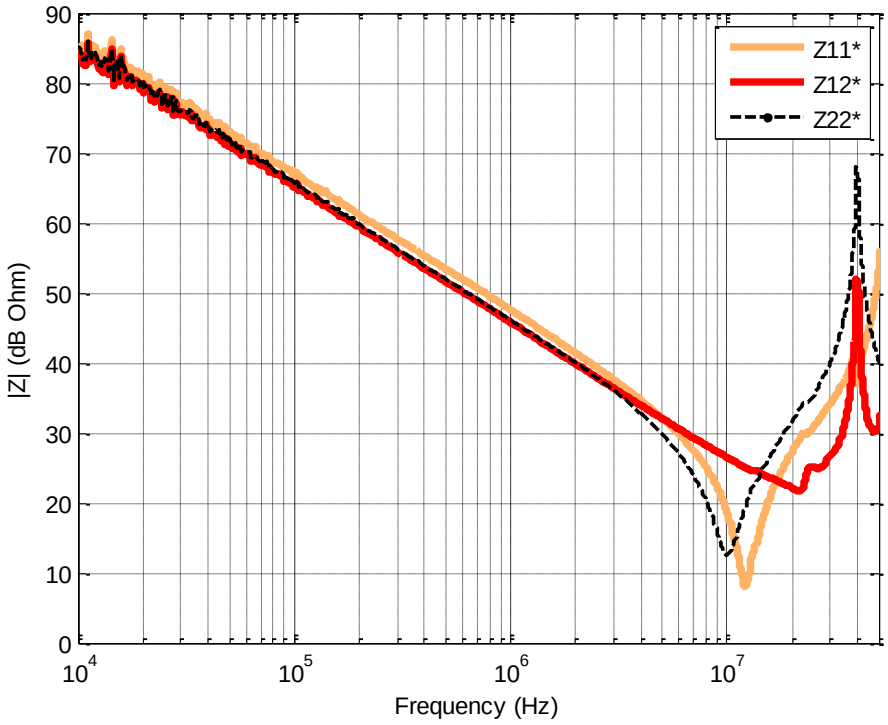

Fig. 4.31: Model impedances as measured by a VNA in power-off condition

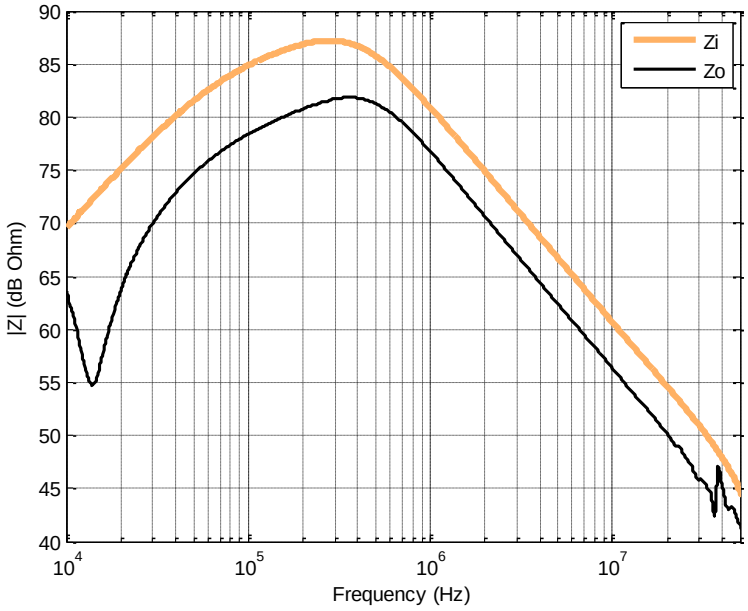

Fig. 4.32: External CM impedance after implementation of CM chokes

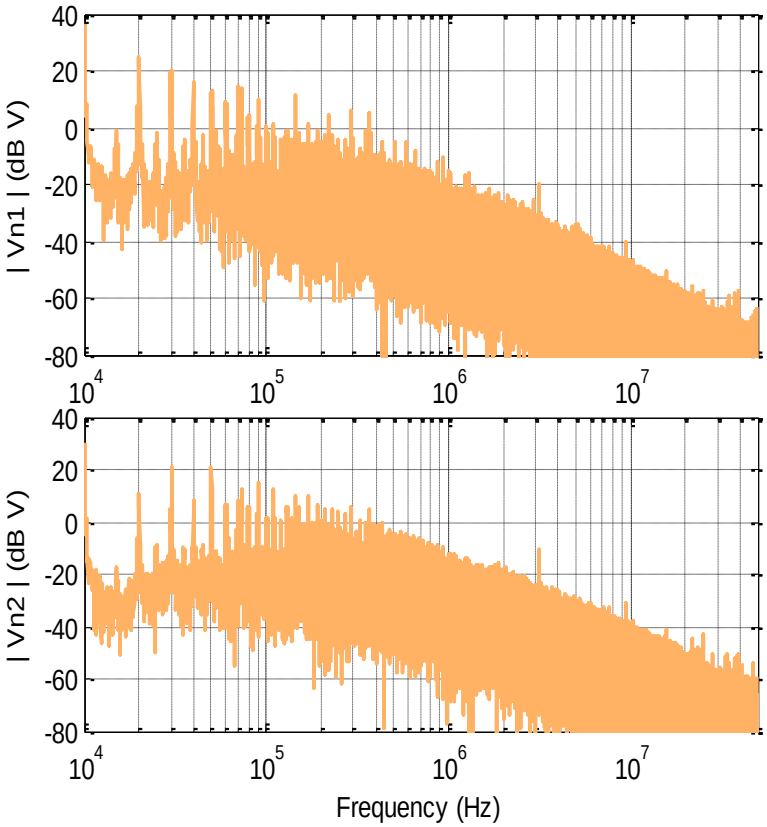

Fig. 4.33: Calculated noise voltage sources V_{N1} and V_{N2} in frequency domain

The second step is to calculate the noise voltage sources. Two CM chokes, one for the input side (40 mH) and the other for output side, (30 mH) were designed with a nano-crystaline core. After implementing these chokes, the terminal impedances (Z_i and Z_o) are shown in Fig. 4.32. These impedances were measured between all terminals short-circuited together and the ground. Comparing Fig. 4.31 and Fig. 4.32, it can be seen that impedances satisfy the condition in (22). In the EMI range (150 kHz - 30 MHz), the terminal impedances are about 20 dB higher than the measured input and output CM impedances (Z_{11}* and Z_{22}*) of the motor-drive. From Fig. 4.32, it is clear that after putting the CM chokes the impedance of LISN on the dc side and the resonances of the harness on the ac side are not visible to the motor-drive. Thus the motor-drive can be considered effectively decoupled (open-circuited) from the network at EMI frequencies. This is also the reason why disconnecting the motor's chassis from the ground plane will have no effect on the extracted model.

The motor-drive is then turned-on and the measurements are made of the input and output side CM currents on two different channels of the oscilloscope. Since both channels are recorded simultaneously, the measurements are automatically phase-correlated. The measured data was re-sampled with 5ns/point resolution and then converted into the frequency-domain by applying FFT. Then, the noise voltage sources (v_{N1} and v_{N2}) are calculated using (23) and (24). These are shown in Fig. 4.33 and Fig. 4.34 shows a snapshot of the noise voltage sources in time-domain.

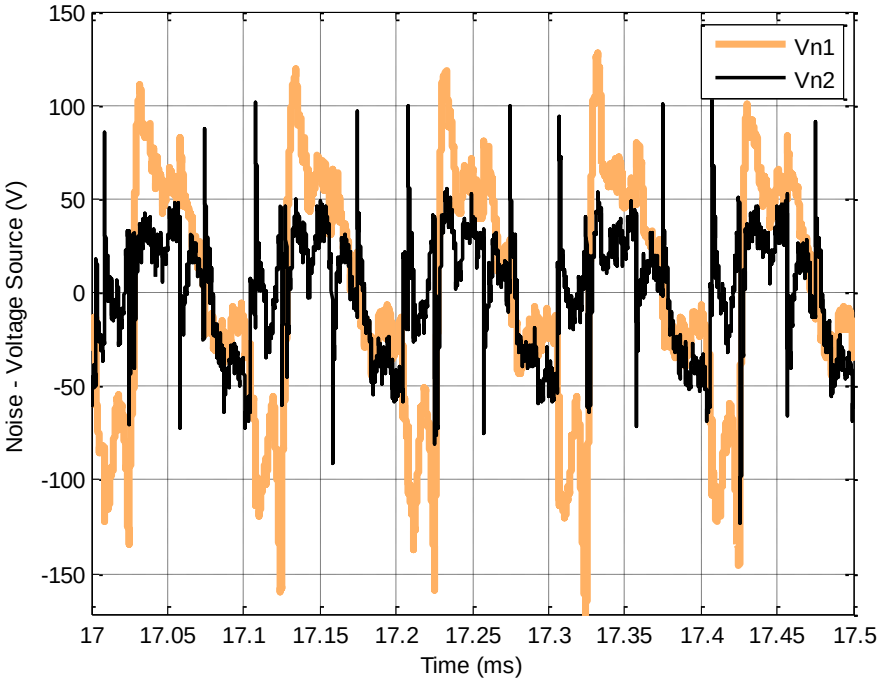

Fig. 4.34: Calculated noise voltage sources V_{N1} and V_{N2} in time-domain

The last step is to optimize the model impedances. Since it is expected that the measured model impedances in Fig. 4.31 are not far from the actual ones, each impedance (Z_{11}* , Z_{22}* and Z_{12}*) can be accurately modeled using a single RLC equivalent. Now to implement the condition in (26), the LISN was terminated with a 1 Ω resistance. At the output side of the motor-drive, each phase was terminated with a series RC branch (150 pF and 6 Ω) to ground. The goal here is to make the impedance of the input and output side network as small as possible. After implementation, the CM terminal impedances (Zi and Zo) are shown in Fig. 4.35. The CM impedance at the output side cannot have large capacitors as this is potentially dangerous due to the high dv/dt. This is the reason for which the size of shunt capacitances at the output side was

limited to only hundreds of pF. The 6 Ω resistance on each phase will come in paralleled and appear as a 2 Ω resistance in CM. Lowering the values of these resistances did not help much as the parasitic inductance of the shunt impedance dominates at higher frequencies. These resistances however do help in damping the resonances of the harness. It would have been ideal if the impedance of the output side network (Z_O) had no resonances and be smooth like the impedance at the input side this. However this difficult to achieve in practical conditions and the impedance at the output side is largely governed by the CM impedance of the harness itself. Comparing Fig. 4.31 and Fig. 4.35, the condition in (26) is clearly satisfied for the input side. For the output side the condition is satisfied except at frequencies around 10 MHz.

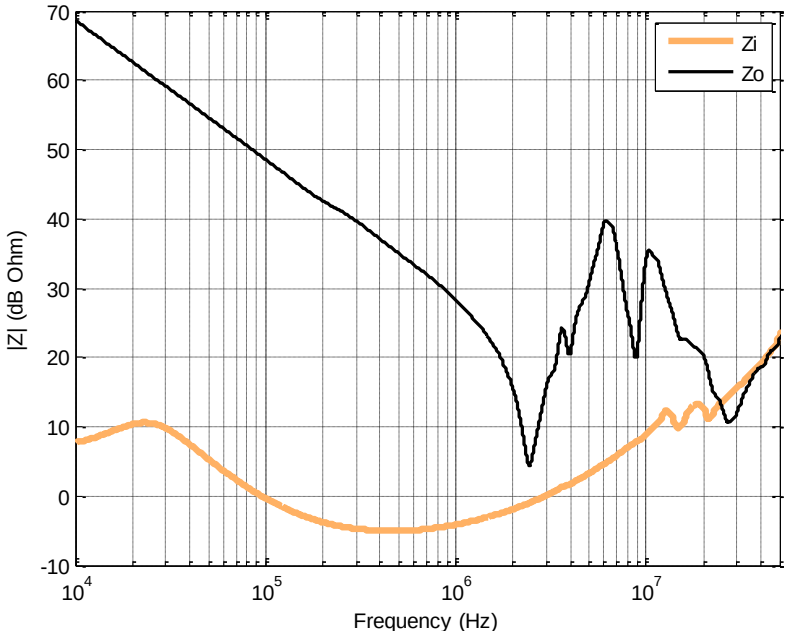

Fig. 4.35: External CM impedance after implementation of RC shunt

In order to show the significance of optimization step, let us first try to predict the input and output side CM currents in the conditions of Fig. 4.35 using (27) and (28). The model uses the un-optimized impedances shown in Fig. 4.31 and the noise voltage sources shown in Fig. 4.33. The prediction results are given in Fig. 4.36. It can be seen that the model is unable to predict the CM currents for the terminals conditions in Fig. 4.35. However, the difference is not too large and is systematic until 1MHz indicating that a slight tuning of the capacitive part of the model

impedances can fix the issue. It was found that the model is most sensitive to Z_{12}. However, all impedances are optimized here as they were measured in the power-off condition.

Optimization of model impedances is carried out to minimize the error between the measured CM current (i_{CMi}), and predicted CM current (i_{CMi}*) shown in Fig. 4.35. The model impedances after optimization are shown in Fig. 4.37. It can be seen that the difference between the measured and optimized impedance is very small. For instance, until 10 MHz the measured Z_{12} is about 820 pF and the optimized Z_{12} is 907 pF. Although the optimization here was carried out numerically, being such a small difference, it can be even done manually. With the optimized model impedances, the prediction of CM currents for the conditions in Fig. 4.35 was tried again, and the results are shown in Fig. 4.38. Unlike Fig. 4.36, now the model is able to successfully predict up to 20 MHz.

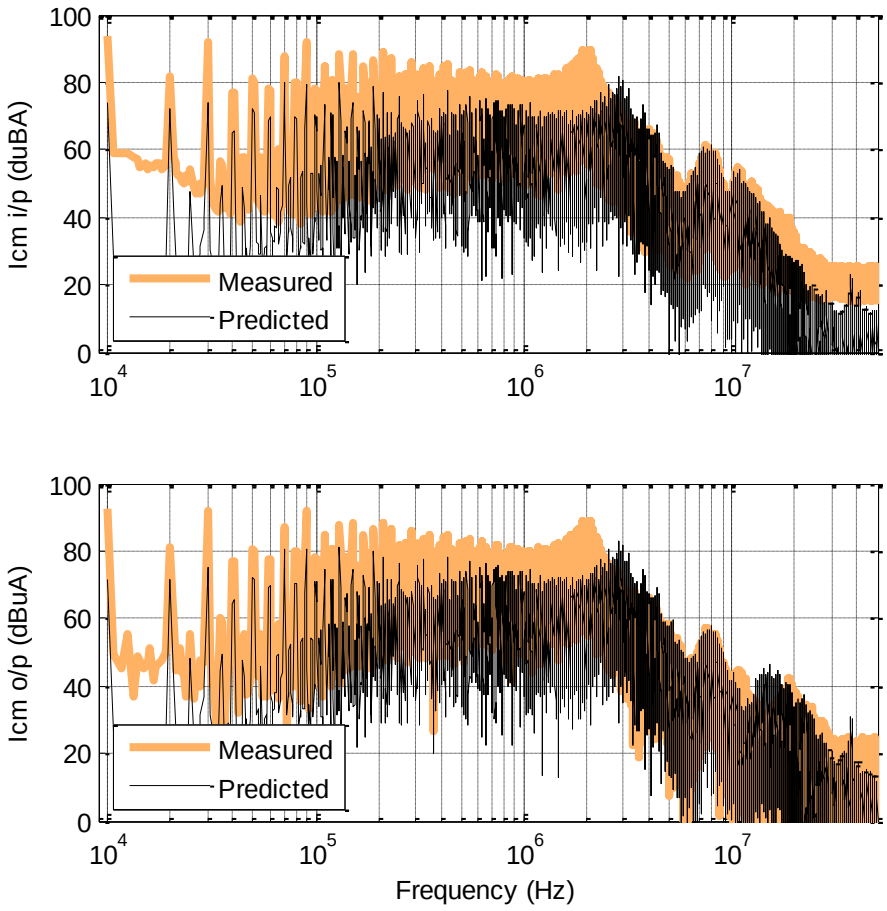

Fig. 4.36: Comparison of measured and predicted CM currents for terminal impedances shown in Fig. 4.35

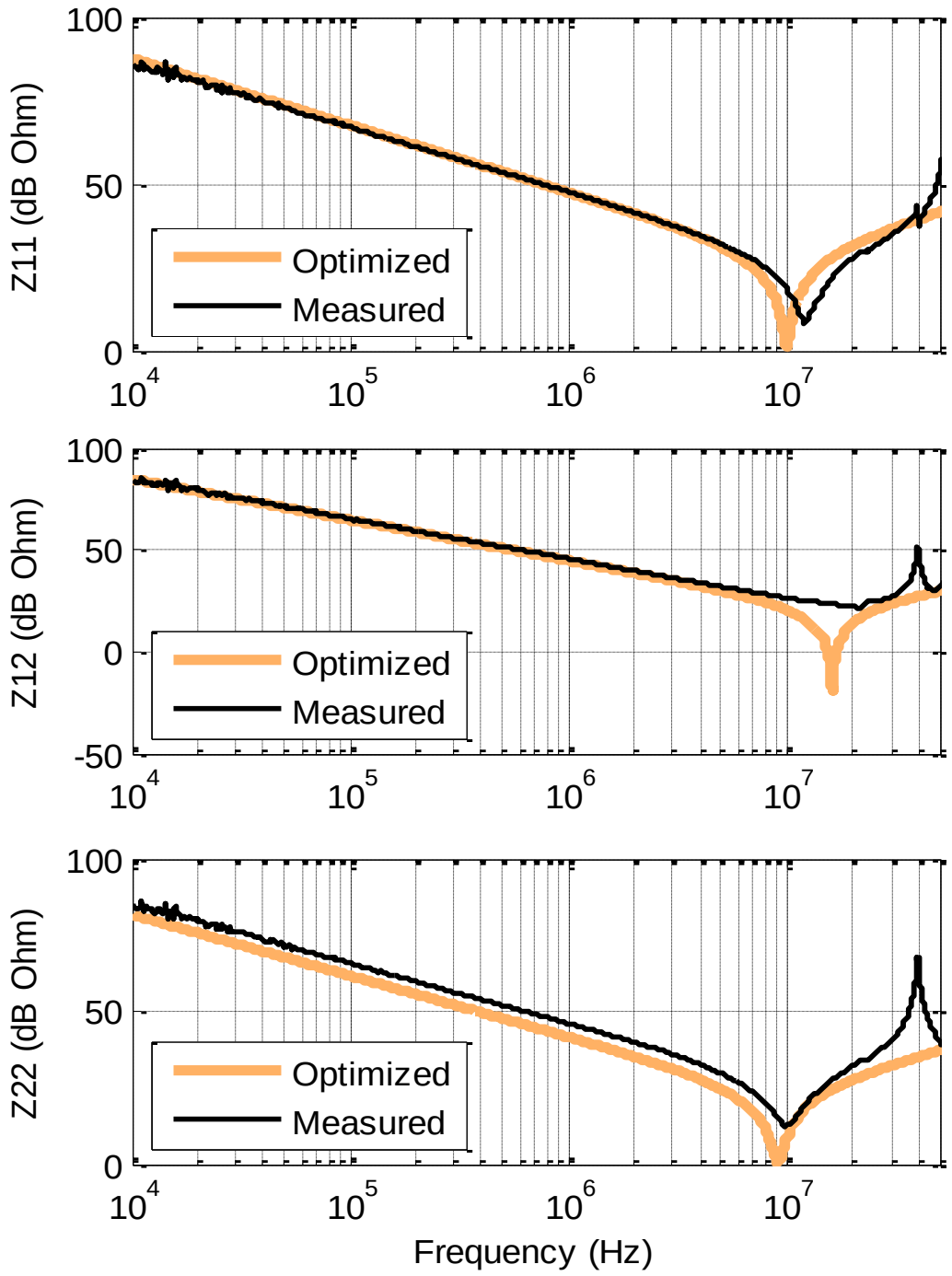

Fig. 4.37: Comparison of measured and optimized model impedances

Beyond 20 MHz the errors start to get larger due to several reasons, including difficulties in measuring impedances and the noise-floor of the oscilloscope. In Fig. 4.38 it can be seen that even with the best possible settings for the oscilloscope, the measured noise hits the noise floor

at around 30 MHz. For this reason, the optimization was carried out using data only up to 30 MHz. The total dynamic range of fitting is also quite large, about 100 dB. The problem of noise-floor also limits the number of poles (RLC equivalents) used to approximate the parameters in the model's impedance matrix. Since there is no measurable noise beyond 20 MHz, using more poles will not serve any purpose and thus only two poles (single RLC branch) have been used to show the validity of the method.

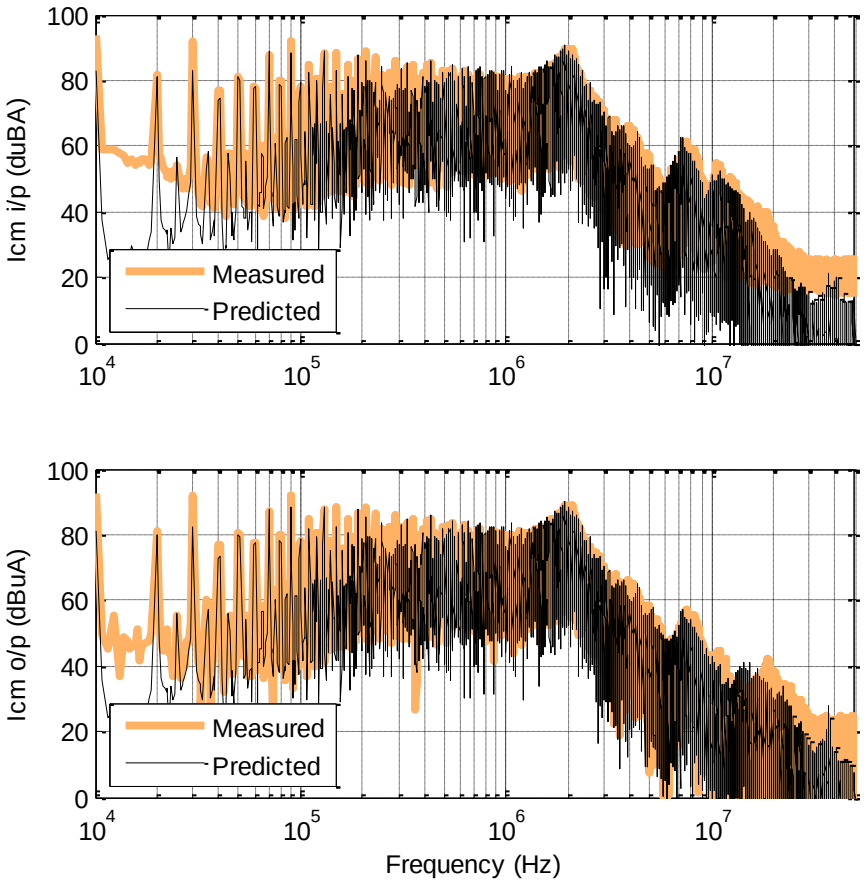

Fig. 4.38: Re-computation of CM currents for terminal impedances shown in Fig. 4.35 using the optimized model impedances

The optimization process is marginally sensitive to the choice of the shunt impedance and also to the EMI measurement conducted under this condition. A different shunt-condition may have resonances located at different frequencies and this could affect the error matrix of the objective function. Moreover, the optimization is carried out using a snap-shot of EMI taken arbitrarily in time. Thus EMI noise captured in two different snap-shots for the same input-

output condition may be slightly different and this can affect the final optimized impedance matrix. It was found however, that these technical issues do not significantly affect the accuracy of the final optimized model. A general frame work on model errors and sensitivity requires more investigation and is beyond the scope of work presented here.

4.1.4.4 Model Validation

The model is validated for several realistic input output conditions for the motor-drive. In the first validation case, the harness is changed from a 32 foot shielded harness to a 12 foot unshielded 4-wire harness. The input side of the motor-drive is terminated with a 50 Ω LISN. Thus both the input and output terminal impedances are different from those used for model extraction.

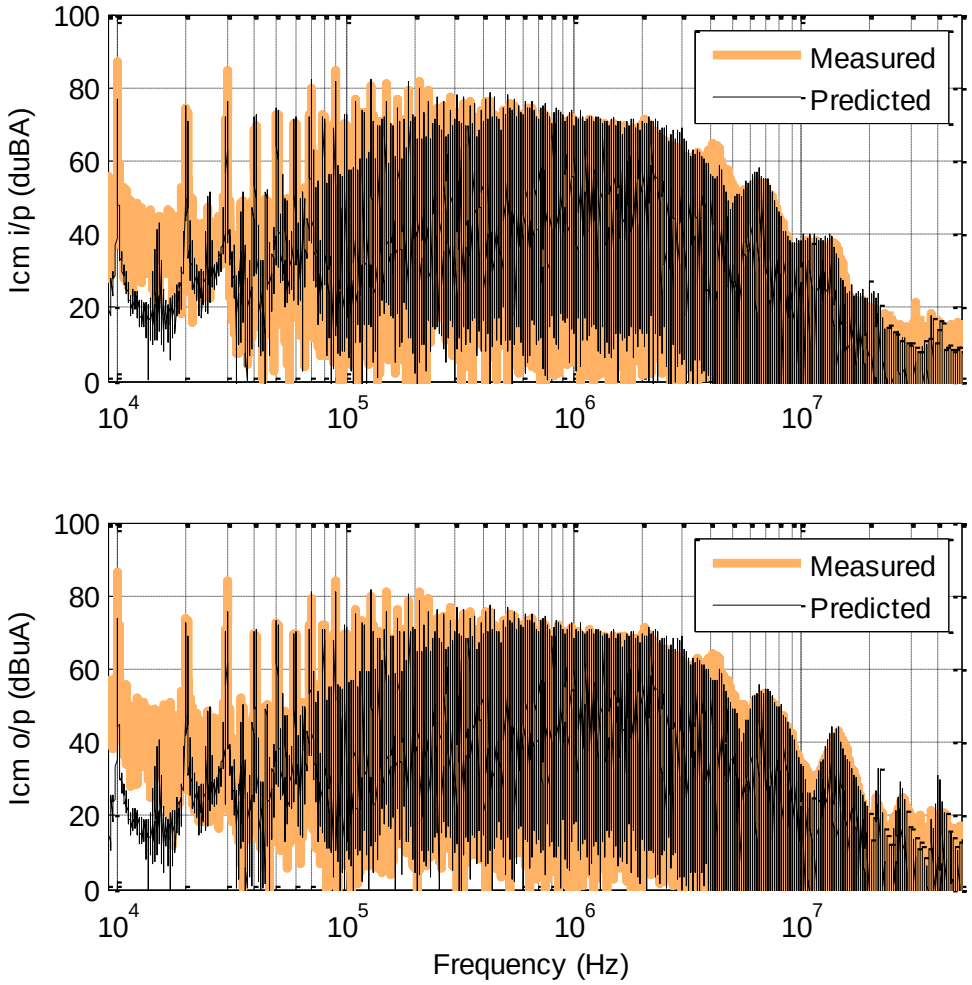

Fig. 4.39: Comparison of measured and predicted CM currents for change in the type and length of harness

For prediction of the input and output CM noise currents in this condition the CM impedance of the external network (Zi and Zo) at the input and output side is measured with an impedance analyzer. These measured impedances are used to terminate the input and output side of the CM model. Eq. (27) and (28) with optimized Z-matrix can be then used for calculating the resulting CM currents for the new input and output condition. Note that the goal here is to validate the model of the motor-drive only and hence there is no need of any complex models of the input and output side networks. The comparison of measured and predicted CM currents is shown in Fig. 4.39. It can be seen that the model is able to accurately predict the conducted emission up to 20 MHz.

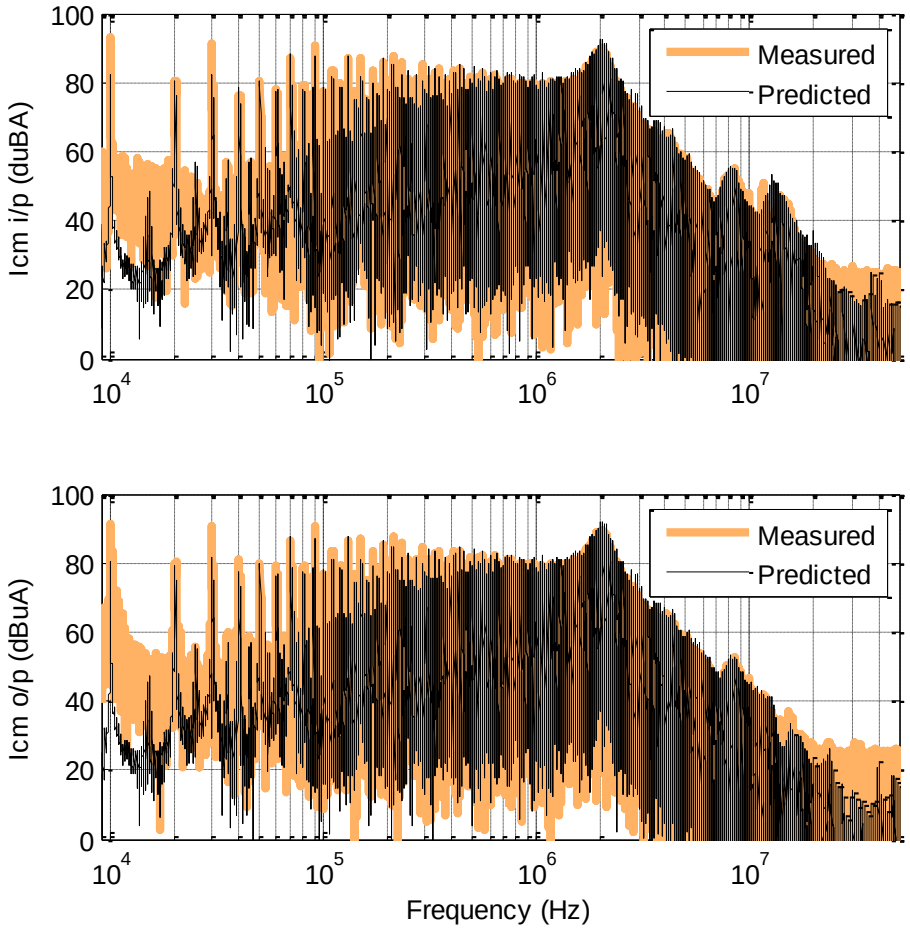

Fig. 4.40: Comparison of measured and predicted CM currents for CM-DM filter inserted at the input side of the motor drive

In the second validation case, the input side of the motor-drive is terminated with a dc-line EMI filter. This is a typical EMI filter with a CM choke and C_Y capacitors for CM filtering and a

C_X capacitor for DM filtering. The leakage inductance of the CM choke is used as the DM inductance. At the output side, a 32 foot shielded harness is used to connect the motor and the drive. Prediction results are shown in Fig. 4.40. Again, the results show good agreement between the measured and predicted CM currents.

The third validation case uses a LC DM filter on the output side of the motor-drive. The DM filter will also affect the CM noise. This filter is a LC filter with values of 160 µH for the inductors and 33 nF for the capacitors. The prediction results are shown in Fig. 4.41. The measured and predicted CM currents match well up to 30 MHz in this case.

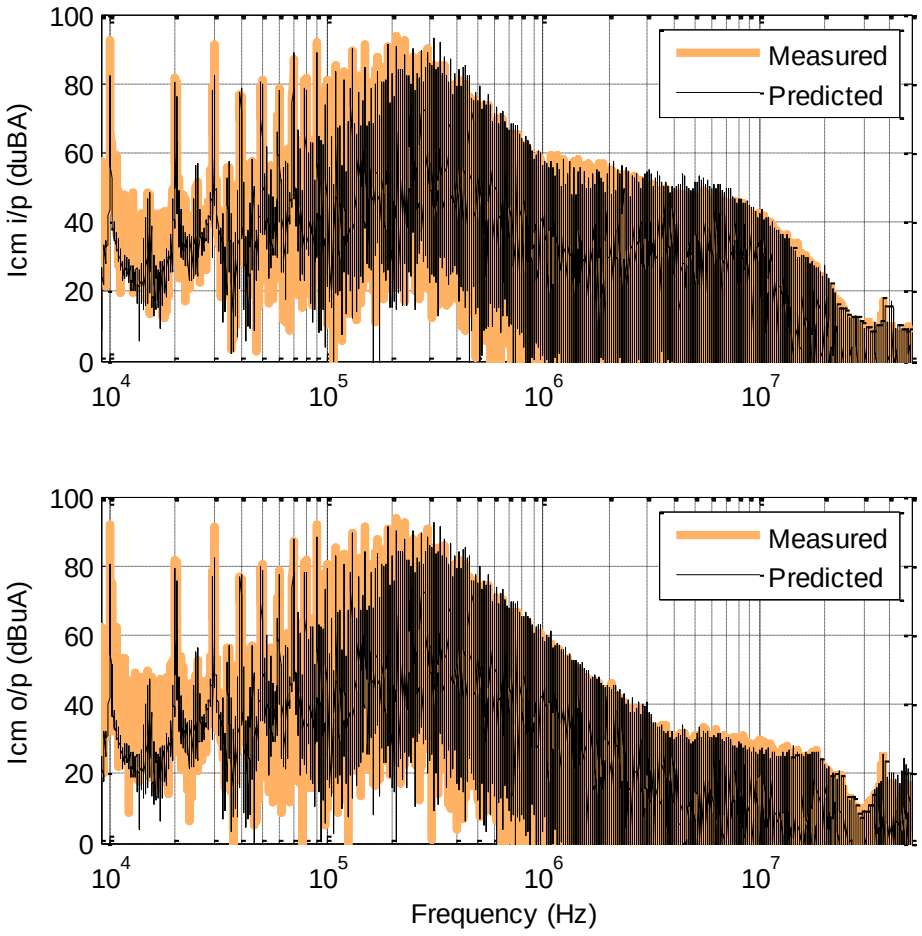

Fig. 4.41: Comparison of measured and predicted CM currents for DM EMI filter inserted in the output side of the motor-drive

As another validation case, we now put both the input and outside filter used previously. The comparison of measured and predicted results for this case is shown in Fig. 4.42. Again the predictions are good up to at least 30 MHz.

It was found that the CM noise does not change significantly with changes in operating frequency of the motor. Fig. 4.43 shows the measurement of CM noise at the output side of the motor-drive with different operating frequencies. It can be seen that in the EMI range (150 kHz to 30 MHz), there is very little difference in the CM currents. This measurement was taken directly with an EMC receiver. There is some difference seen at the switching frequency (10 kHz) and its first few harmonics. This happens because the closed loop control is changing the modulation index of the drive. However, these frequencies are below the EMI range.

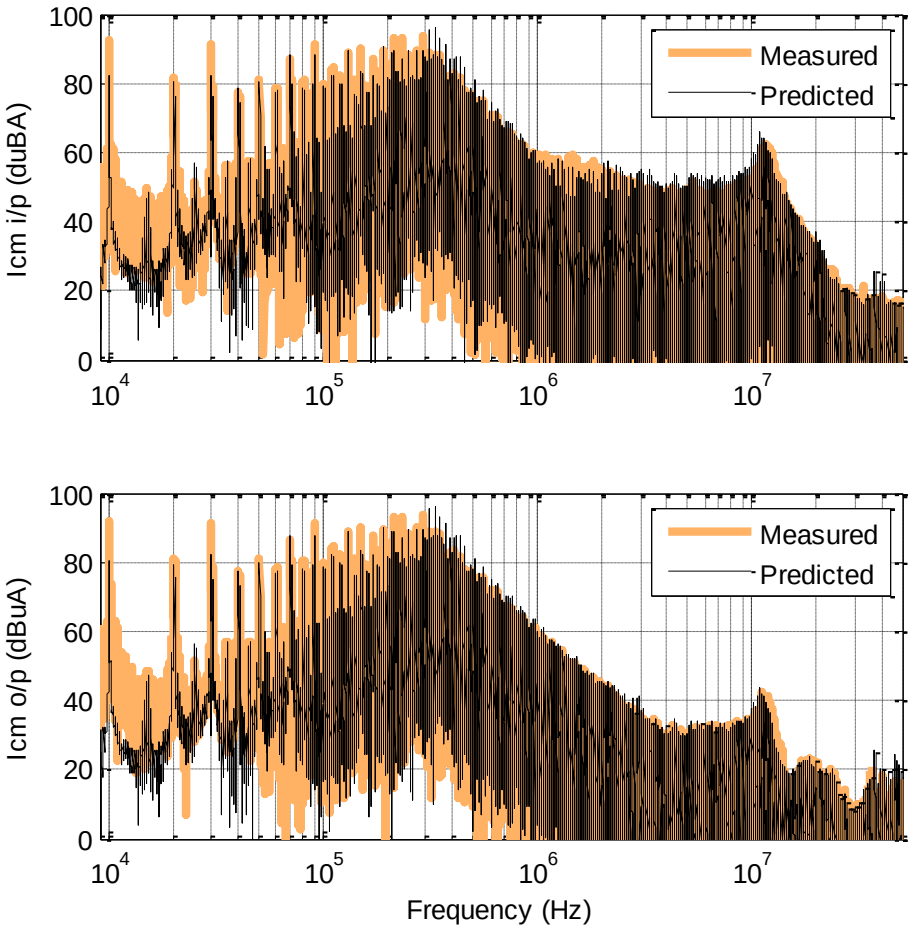

Fig. 4.42: Comparison of measured and predicted CM currents for CM-DM filter at the input side and a DM EMI filter at the output side

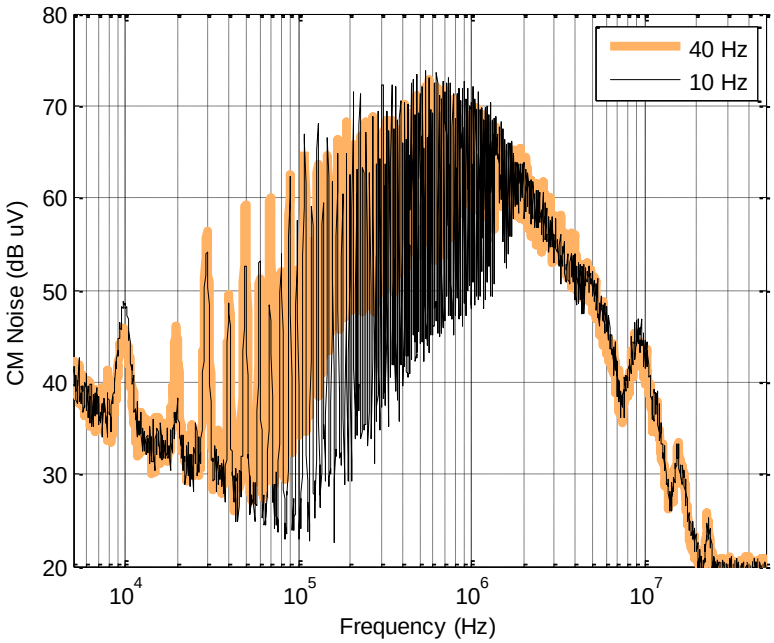

Fig. 4.43: Comparison of output side CM currents for different operating frequency of the motor-drive

As a last validation case the input dc voltage was changed from 300V to 250V. This slightly changes the operating point of the motor-drive. All frequency points of the two noise-sources in the model were scaled down by a constant factor of 250/300. The comparison of predicted and measured results is shown in Fig. 4.44 and good agreement can be seen. The dc voltage cannot be varied a lot since it is a commercial motor-drive and the internal protection trips beyond certain levels of input dc voltage. However it is possible to predict for change in input dc voltage by just scaling the voltage sources with a constant factor.

It should be noted that in most results, the prediction at the switching frequency (10 kHz) and the first couple of harmonics are not very accurate. When Fig. 4.31 and Fig. 4.32 are compared, it can be seen that condition given in (26) fails those frequency points. Thus the estimation of noise source voltage cannot be accurate there. This can be corrected manually, but was left here as it is to point out the problem.

Another thing to notice here is that the prediction of currents is done at the terminals of the motor. So these results do not directly indicate the attenuation achieved by the EMI filters. The results are only for the purpose of validating the proposed terminal model.

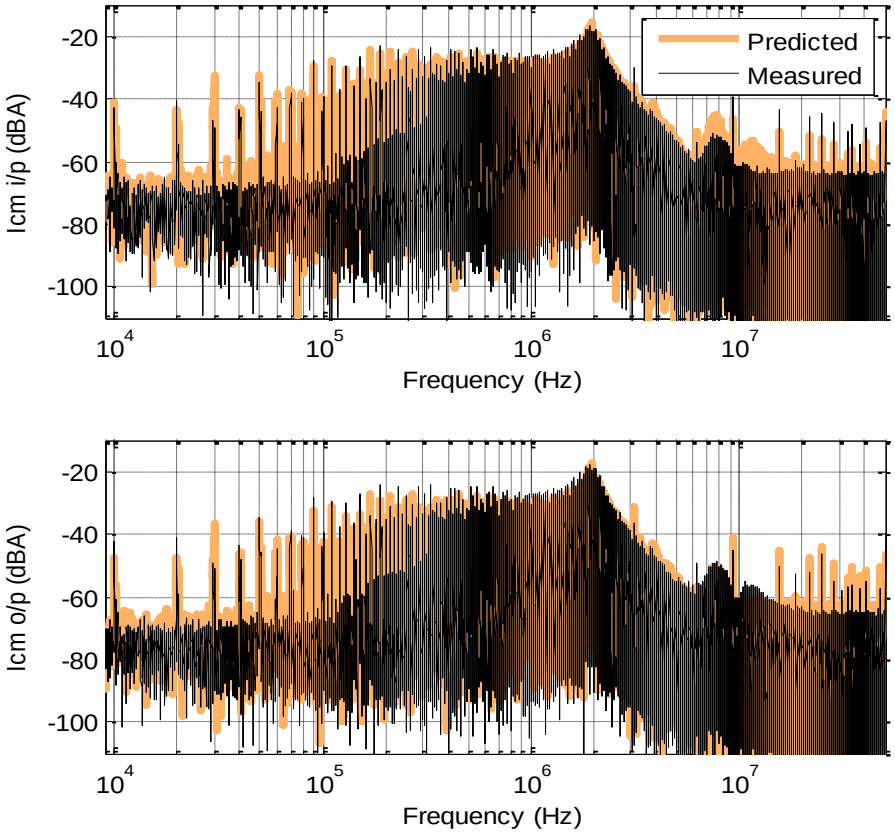

Fig. 4.44: Comparison of measured and predicted CM currents due change in the dc input voltage (V_{DC}) from 300V to 250V

4.1.5 Compliance Using EMC Analyzer

The measurement for electromagnetic compatibility (EMC) compliance testing is usually done with an EMC analyzer (or a spectrum analyzer). All the validation results shown till now are predicting measurements with an oscilloscope. Thus for EMC compliance, there is a need to predict the measurements taken by an EMC analyzer. In order to that, a resolution bandwidth (RBW) filter was implemented in MATLAB® [82]. The final predicted results were then post processed using this digital filter to get the predicted results for an EMC analyzer. The measurements were carried out using a 1 kHz RBW, as prescribed by the DO-160 standards, and only one sweep was taken in peak detection mode. The comparison of the measured and predicted EMC analyzer results for the case when both filters are present is shown in Fig. 4.45. The prediction is found to be good up to 20 MHz. Errors are seen at low frequency, below the

conducted emissions range. This is due to the issue of in accurate estimation of the noise-sources as mentioned before.

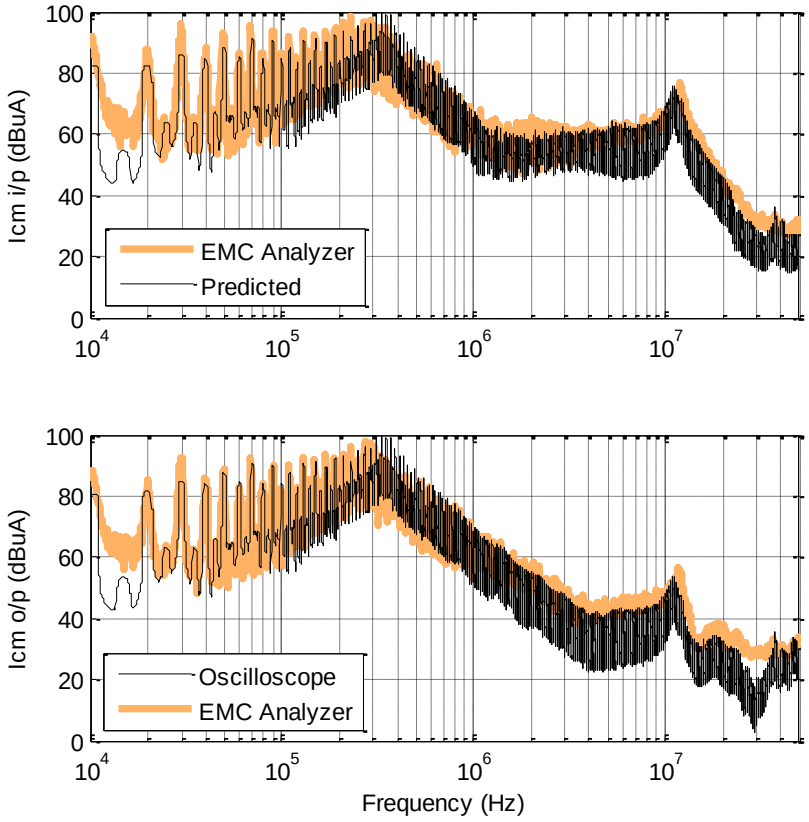

Fig. 4.45: Comparison of measured and predicted CM currents on an EMC analyzer for CM-DM filter at the input side and a DM EMI filter at the output side

4.2 DIFFERENTIAL MODE

4.2.1 Model Definition

The input side DM noise in a motor-drive system has been reported to be effectively decoupled from the output side noise, provided that the dc-link capacitor keeps the ac impedance between the dc rails low enough [42, 73]. Let's assume that this is true and let's also assume that due to the symmetry of the drive, there is no significant mixed-mode noise [8] present. Under these assumptions, unlike the CM model in [83, 84], there is no need of an un-terminated DM model for the motor-drive. Instead terminated EMI models can be extracted separately for

modeling the input (dc) and output (ac) side DM noise. This idea is shown in Fig 4.46. The motor-drive in consideration here is a dc-fed, three-phase drive. The input side model has the positive and negative as its terminals and owing to the symmetry the output side model can be approximated between any two phases.

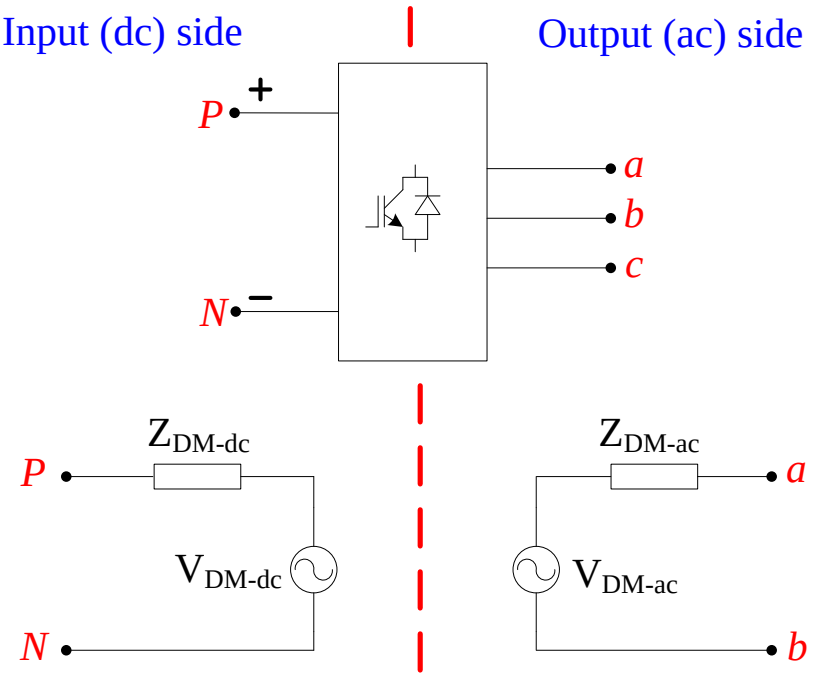

Fig. 4.46: DM noise models for a motor-drive system

The modeling procedure is similar for both input and output sides, so let's consider the input side to understand the model identification process. First, a near open-circuit condition at the terminals is created by using a large inductive filter. Fig 4.47 shows this configuration. This condition is referred to as the "series-condition". The DM noise current $i_{DM\text{-}SR}$ is then measured in time-domain using a clamp-on probe and a sampling oscilloscope.

The converter's input impedance $Z_{DM\text{-}dc}$ and the network impedance $Z_{DM\text{-}SR}$ are measured directly using an impedance analyzer. It should be noted that the probe of the impedance analyzer is often grounded and hence measuring DM impedance is difficult. Errors in the measured impedance can be minimized by either isolating the measured system from ground or by using an RF balun (unbalanced-to-balanced).

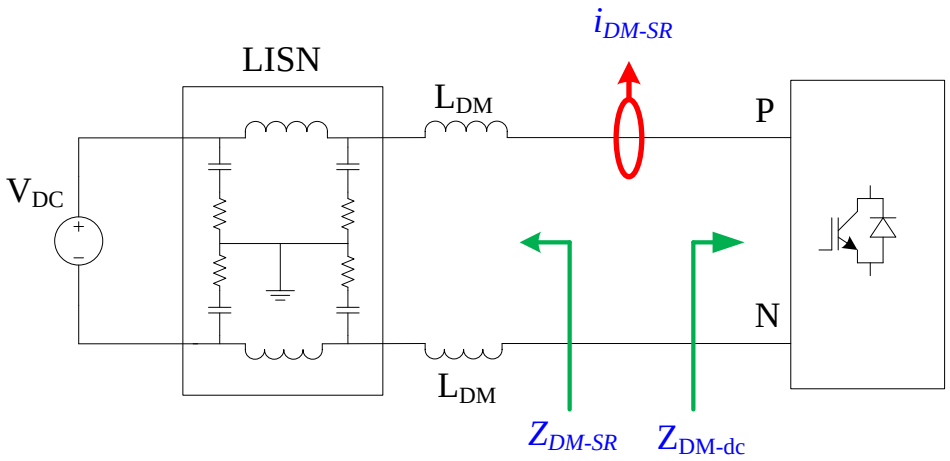

Fig. 4.47: Series-condition for input side DM model extraction

Fig. 4.48 shows the DM equivalent circuit for the input side of the motor-drive system. The noise source can be now extracted from the "series-condition" as:

$$V_{DM-dc} = i_{DM-SR} \cdot \left(Z_{DM-SR} + Z_{DM-dc}\right) \tag{30}$$

This completes the model extraction process for input side. Similarly the output side model can also be extracted. The only difference is that we need a three phase DM filters comprising of high value inductors to create the series condition. The assumptions of no significant input-output side coupling and no significant mixed-mode noise must be verified experimentally before applying this procedure.

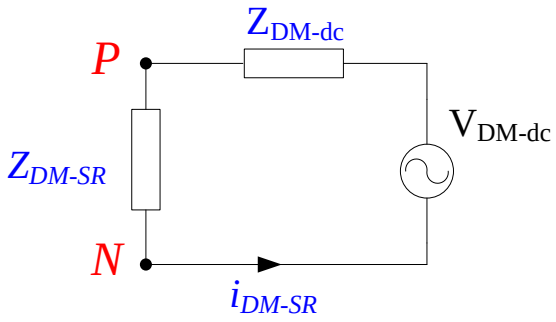

Fig. 4.48: Equivalent circuit at the input side in the series-condition

For the series inductors, a value is chosen such that it is much higher than the usual net DM inductance that the converter is likely to see in normal conditions. The measurement of DM current is done by using a clamped-on-probe, or a current-transformer. The correct use of probe

is shown in Fig. 4.49. The measured input and output DM currents should be divided by 2 and 3 respectively to get the correct magnitude of DM currents ($i_{DM\text{-}SR}$) in the system.

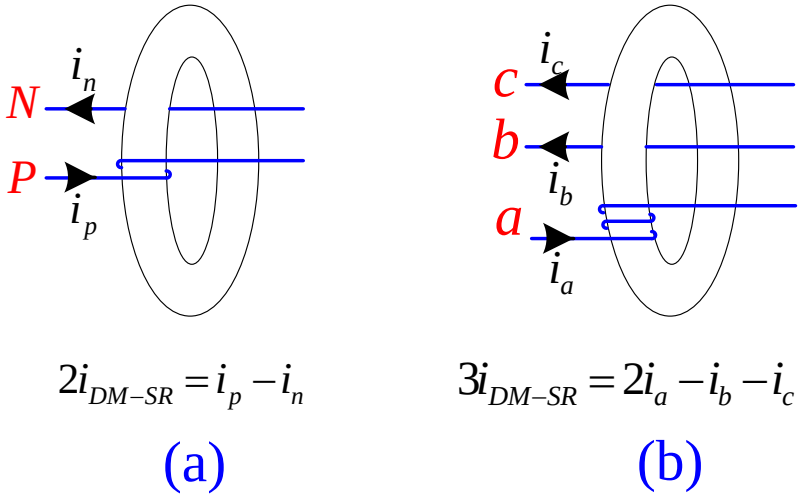

Fig. 4.49: Measurement of DM currents (a) input side (b) output side

4.2.2 Model Results

4.2.2.1 Differential Model Coupling

The extent of coupling between the input and output side DM noise was evaluated experimentally. The impedance seen by the converter at its output side was changed and the corresponding input side DM currents were measured using a spectrum analyzer. To change the impedance at the output, simple three-phase DM inductors (L-filters) were used. The results of this experiment are shown in Fig. 4.50. Note that between 10 kHz to 100 kHz, no difference is seen in the impedance as it is dominated by the winding inductance of the motor.

It can be seen that at most frequency points no significant change is observed in the input side DM noise. Change is seen only when the impedance at the output side comes close to the dc-link impedance which is dominate by the input dc-link capacitor. This in a way corroborates the assumptions made in [42, 73]. Thus the DM noise at the input and output side of a motor-drive is not entirely decoupled but can be considered decoupled as long as the input dc-link is adequate decoupled. This assumption however will lead to errors in the DM models but it was found that such errors can still be tolerable and therefore no further complications

were made to the proposed model. Note that this marginal coupling can be non-linear and in such cases cannot be captured effectively by linear-time-invariant (LTI) models. The coupling from output to input can be evaluated in the same way. The results were found to be similar and hence are not shown here.

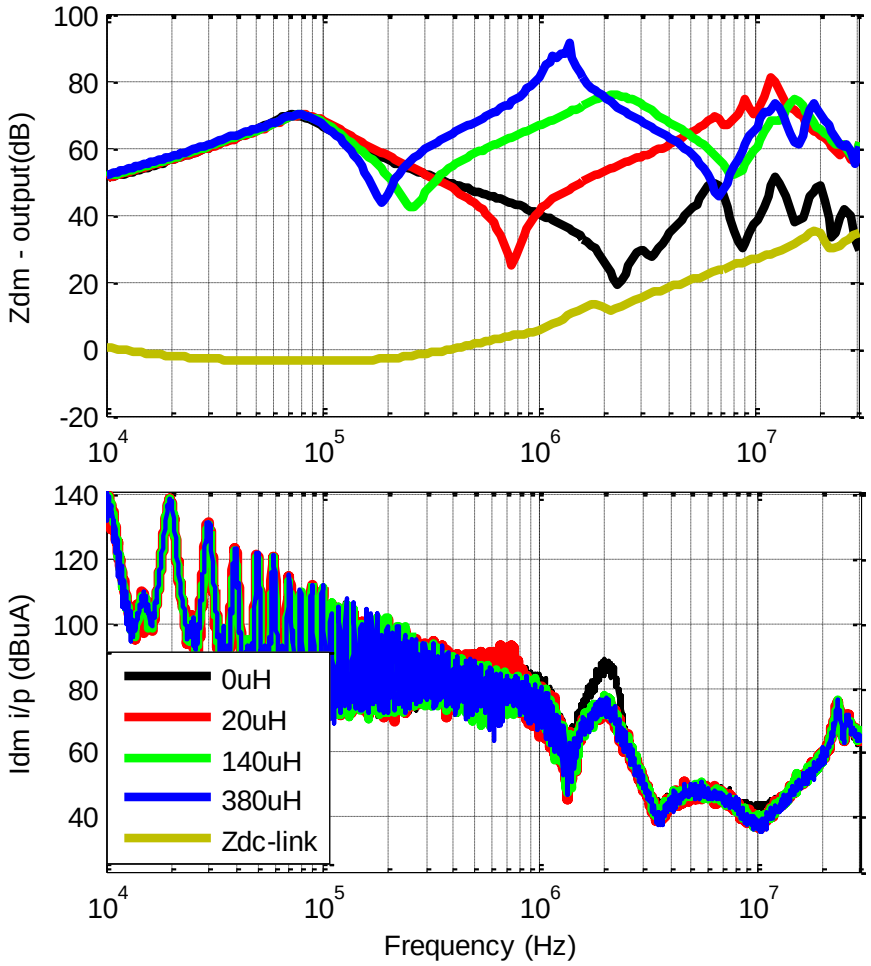

Fig. 4.50: Coupling from output side to input side of the motor-drive

4.2.2.2 Mixed-Mode Noise

The issue of mixed-mode noise is a complicated one. The presence of mixed-mode noise in the system will make the validity of the proposed method limited to only lower frequencies. Hence there is a need to check how sever the effects of mixed-mode noise are in the motor-drive system. The fact that the motor-drive is a very symmetric system should make the mixed-mode noise quite small. To verify this, the method given in [54] is adopted. For any given two-port

network with ground as a reference, an equivalent two-port network can be found where one of the port represent the CM noise and the other represents the DM noise flowing in the system.

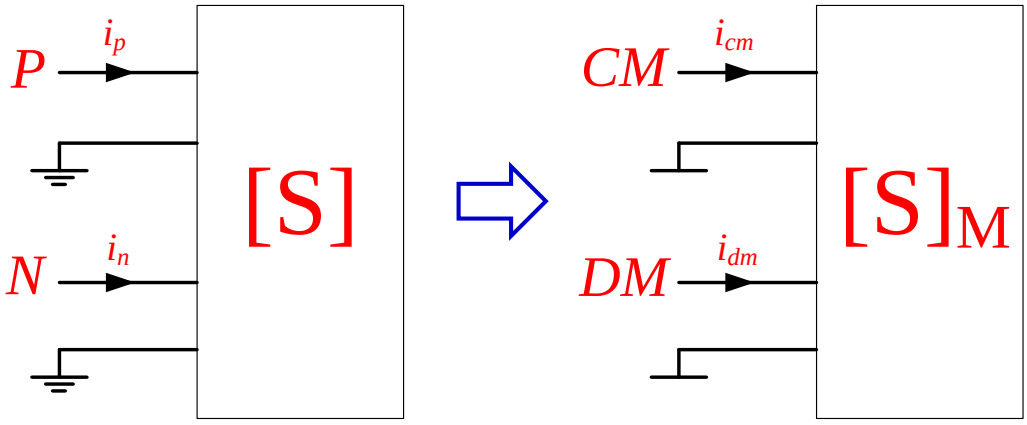

Fig. 4.51: An equivalent network based on modes of noise propagation

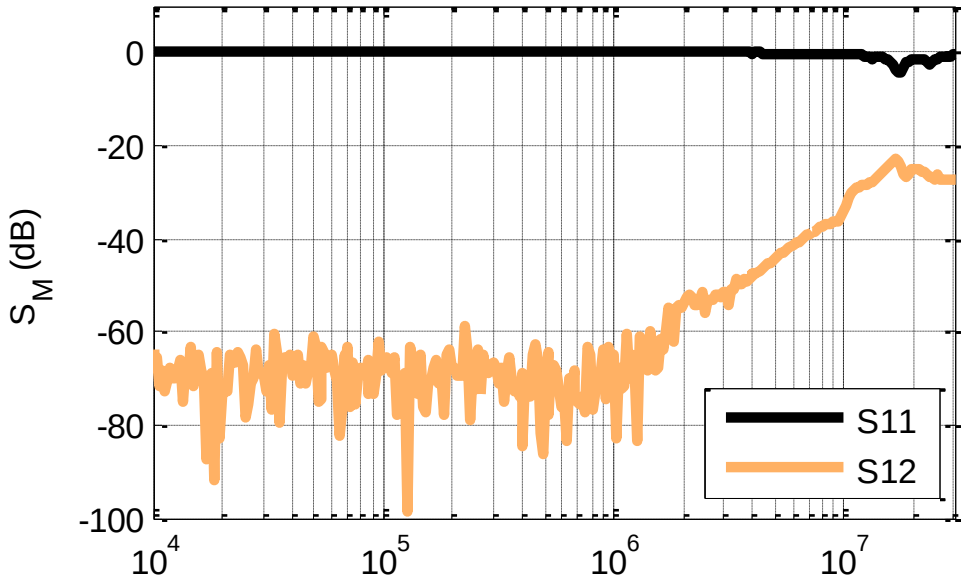

Fig. 4.52: Mode coupling at the input side of the motor-drive

This–is shown schematically in Fig. 4.51. For such an equivalent network the transfer parameters will give the coupling between the CM and DM noise. The S-parameters were measured using a network analyzer with positive and negative inputs of the motor-drive as the two ports. The motor-drive was in power-off condition. After the mathematical transformation

the S-parameters of the equivalent network $[S]_M$ were obtained and are shown in Fig. 4.52. It can be seen that the coupling factor S_{12} between CM and DM are at least 20 dB below S_{11} at all frequencies. The comparison between S_{21} and S_{22} was found to be same as well. Thus the DM noise can be measured even in the presence of CM noise. It also allows us to estimate the total as simply the sum of CM and DM noise.

The high magnitude of coupling in the high frequency range although can make the measurement of DM noise difficult in the high frequency range and hence for good measurements of DM noise it is best to isolate the set-up from the ground plane and also use the same CM chokes that were used for the extraction of CM noise-sources.

4.2.2.3 Model Impedance

The series condition at the input side is created with a DM filter comprising of two line inductors, 285 µH each. Fig. 4.53 shows the measured network impedance $Z_{DM\text{-}SR}$ and input impedance $Z_{DM\text{-}dc}$ of the motor-drive. These measurements were done using an impedance analyzer and in power-off condition. It can be seen that the input impedance of the motor-drive, which is dominated by the dc-link capacitor at lower frequencies and the dc-link parasitic inductance at higher frequencies, is at least 40 dB lower than the network impedance in the entire frequency range. This creates an adequate open-circuit condition at EMI frequencies.

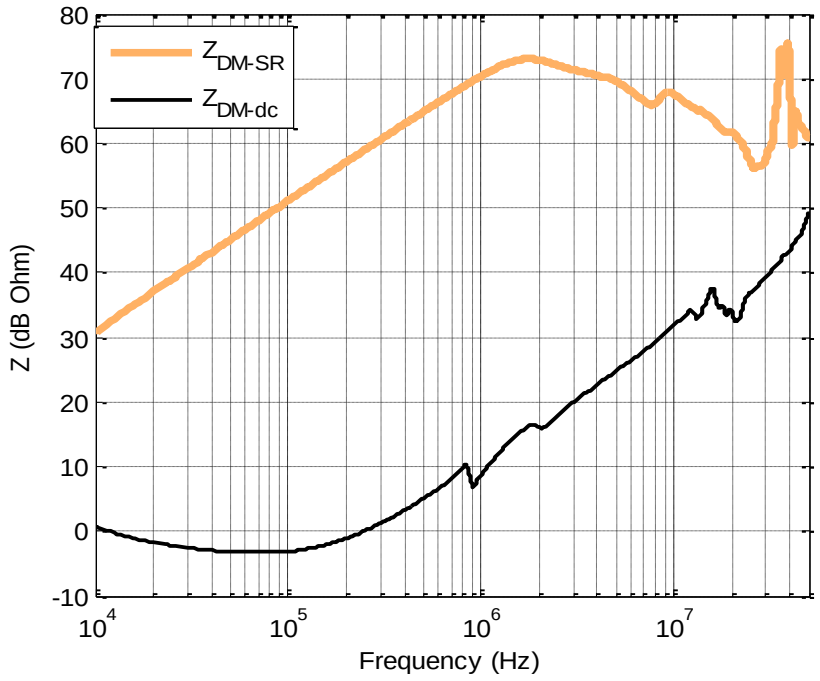

Fig. 4.53: Input DM impedance (Z_{DM-dc}) of the motor-drive and the DM impedance of the network (Z_{DM-SR}) at the input side

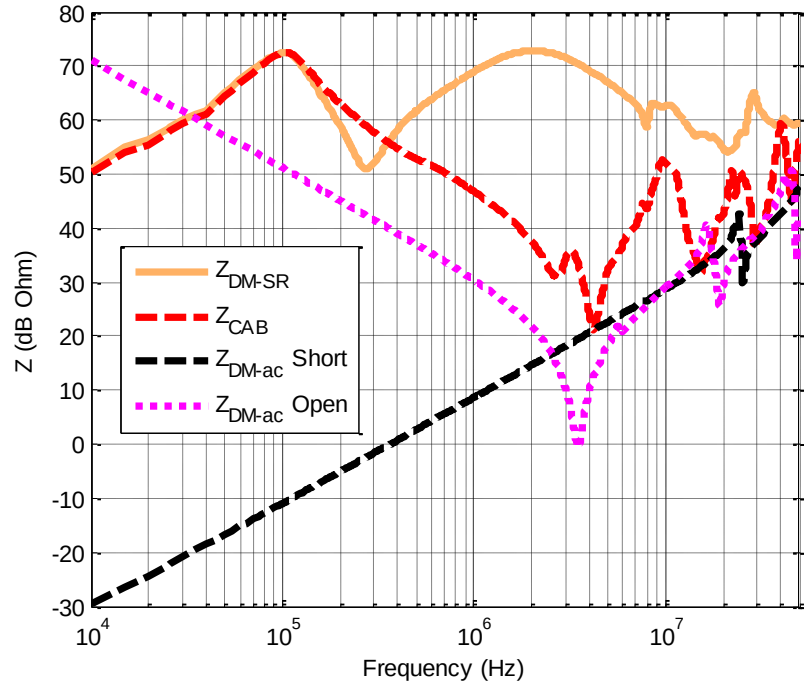

Fig. 4.54: Output DM impedance (Z_{DM-ac}) of the motor-drive and the DM impedance of the network (Z_{DM-SR}) at the output side

Note that for this application, 285 µH in each line (570 µH total) is a very high DM inductance. In real conditions, the total DM inductance that this drive is likely to see will be much lesser. Also notice that it is difficult to maintain constant high impedance beyond 10 MHz unless several inductance of different value are used in series. The sharp resonance at 40 MHz is a result of the calibration issue with the RF balun. It cannot be avoided and hence the model accuracy beyond 30 MHz is limited.

Similarly at the output side a three-phase DM filter with inductors of 250 µH each (a total of 500 µH between any two phases) is used to create the series condition. This is shown at $Z_{DM\text{-}SR}$ in Fig. 4.54. The output impedance ($Z_{DM\text{-}ac}$) of the motor-drive is in principle non-linear. While in operation, this impedance changes every switching cycle and hence the output impedance is time-variant. Thus, a simple approximation of $Z_{DM\text{-}ac}$ is required that works well for all output conditions. One way to approximat**e** the output impedance is to measure it directly between any two phases and in power-off conditions. This is shown in Fig. 4.54 as $Z_{DM\text{-}ac}$ *Open*. In this measurement the effect of output capacitance of the switches and the parasitic inductance of the interconnecting wires are included. Another way to approximate is to measure the same impedance with the two phases short-circuited, right at the power module. This is shown as $Z_{DM\text{-}ac}$ *Short* in Fig. 4.54. In this measurement only the parasitic inductance of interconnecting wires is seen.

It can be seen that the two approximations are very different in the low frequency region. However, the following points should be noted. At higher frequencies both measurements are similar because there the output impedance is dominated by the parasitic inductance of the interconnecting wires. At lower frequencies, between 30 kHz and 1 MHz, both impedances are smaller than the minimum impedance expected at the output side. This minimum impedance is shown as Z_{CAB} in Fig. 4.54 and is the DM impedance of the network without any EMI filter. Z_{CAB} is dominated by the winding impedance of the motor at low frequencies followed by the resonances of the harness used to connect the motor to the drive. Here Z_{CAB} can be considered as minimum impedance because the output EMI filters should never have capacitors facing the drive due to the high *dv/dt* at the output of drive. Thus Z_{CAB} being so small compared to other impedances in the output loop, neither of these approximations will create any significant difference in the calculated EMI between 30 kHz and 1 MHz. Below 30 kHz however, the approximation $Z_{DM\text{-}ac}$ *Open*, will create errors in the extracted model as the series condition fails

in this region. Moreover the impedance in the low frequency will change while the drive is in operation and hence $Z_{DM\text{-}ac}$ *Short* is chosen as the best approximation.

4.2.2.4 Model Sources

The motor-drive is then turned 'ON' and the input side DM noise current is recorded for two line-cycles (50 msec) with an oscilloscope (sampling period 5 nsec). At least one line cycle is needed to capture EMI behavior at all the operating points. The measurement is then converted into frequency-domain by using FFT. Using (1) the noise voltage source $V_{DM\text{-}dc}$ is calculated and shown in Fig. 4.55. Similarly the DM noise in the series condition at the output side is measured and the DM noise source $V_{DM\text{-}ac}$ is calculated. This is shown in Fig. 4.56.

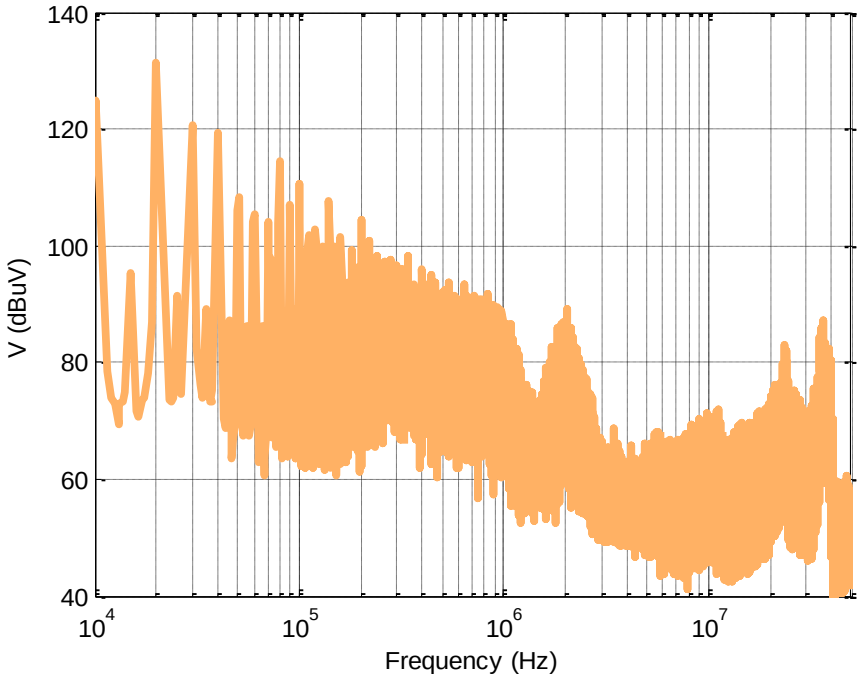

Fig. 4.55: Identified Noise voltage source ($V_{DM\text{-}dc}$) at the input side of the motor-drive

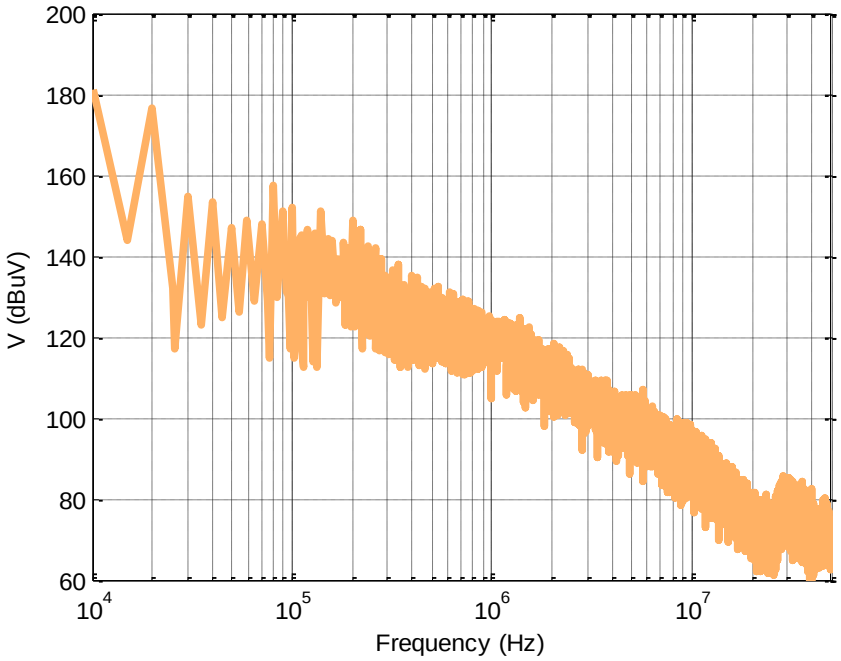

Fig. 4.56: Identified Noise voltage source ($V_{DM\text{-}ac}$) at the output side of the motor-drive

4.2.3 Model Validation

To validate the input DM model, a small LC filter is inserted at the input side of the motor-drive. The inductors were 4 µH each and the filtering capacitor was 5 nF as shown in Fig. 4.57. The resulting DM current can be simply computed as:

$$i_{DM-FL} = \frac{V_{DM-dc}}{Z_{DM-FL} + Z_{DM-dc}} \tag{30}$$

The comparison of predicted and measured DM currents at the input side is shown in Fig. 4.58. It can be seen that the prediction accuracy is good at most frequency points up to at least 30 MHz.

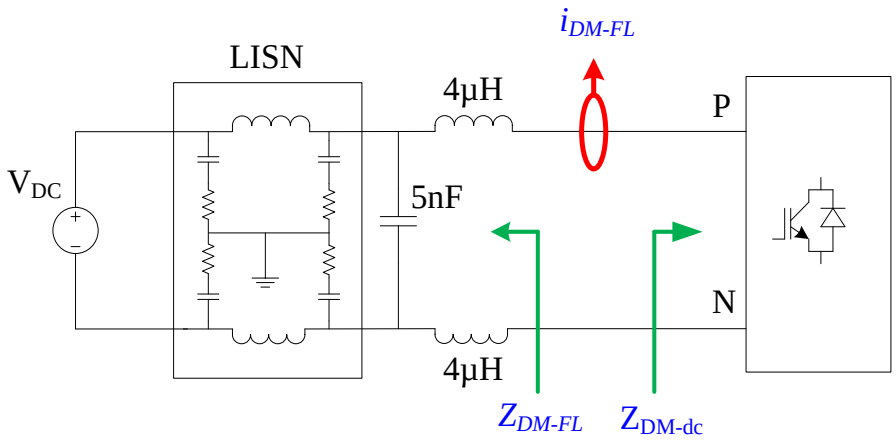

Fig. 4.57:Set-up for input side DM model validation

In a similar way the output side DM model is also validated. A three-phase DM LC-filter with 160 µH inductors and 33 nF capacitors is inserted at the output side of the drive. This is shown in Fig. 4.59. In another case the 33 nF capacitances were changed to 5 nF. Fig. 4.60 shows the resulting impedances ($Z_{DM\text{-}FL}$) of the output network in the two cases. The comparisons of predicted and measured DM currents for the two cases are shown in Fig. 4.61 and Fig. 4.62. Again it can be seen that the model predicts well up to 30 MHz in both cases. A slight over prediction at around 80 kHz is seen in Fig. 4.61. This is due to the nonlinearity in DM coupling between input/output mentioned in section 4.2.2. When the resonance at the output comes close to the input dc-link impedance the model is no longer linear. This problem is not seen in the other case as the resonance produced by it at 160 kHz is far from the dc-link impedance. Being an over prediction and outside the EMI range, the results are used at it is.

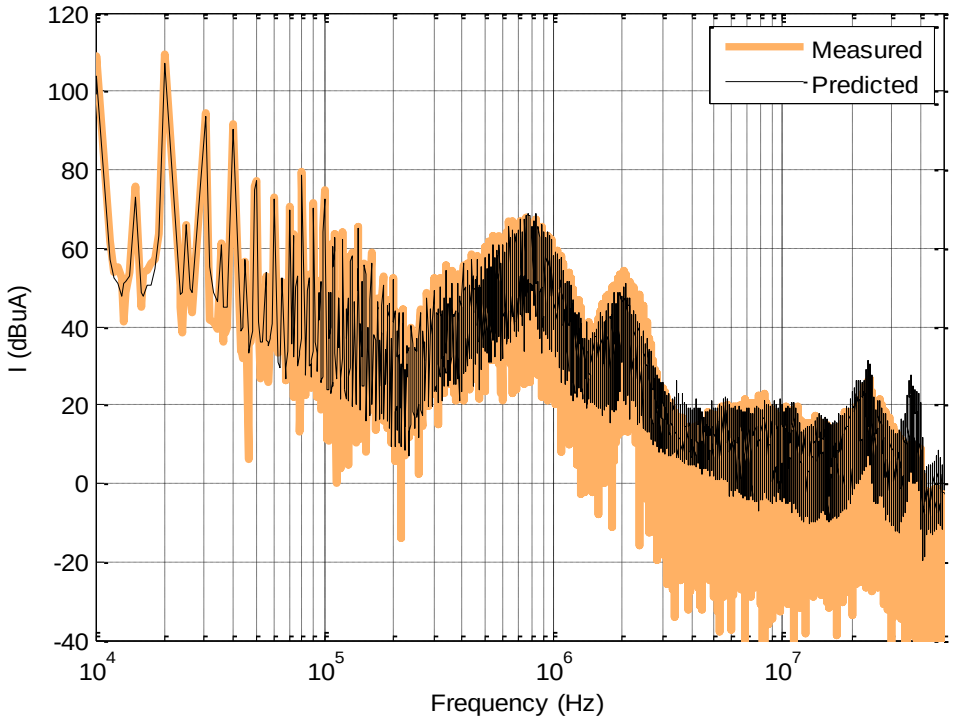

Fig. 4.58: Comparison of measured and predicted DM noise current for the case shown in Fig. 4.57

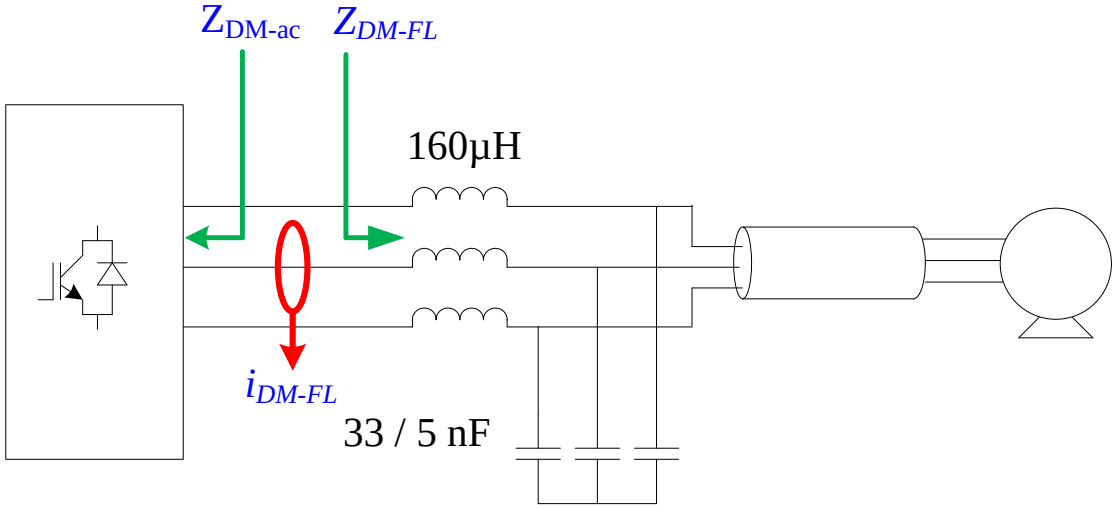

Fig. 4.59: Set-up for output side DM model validation

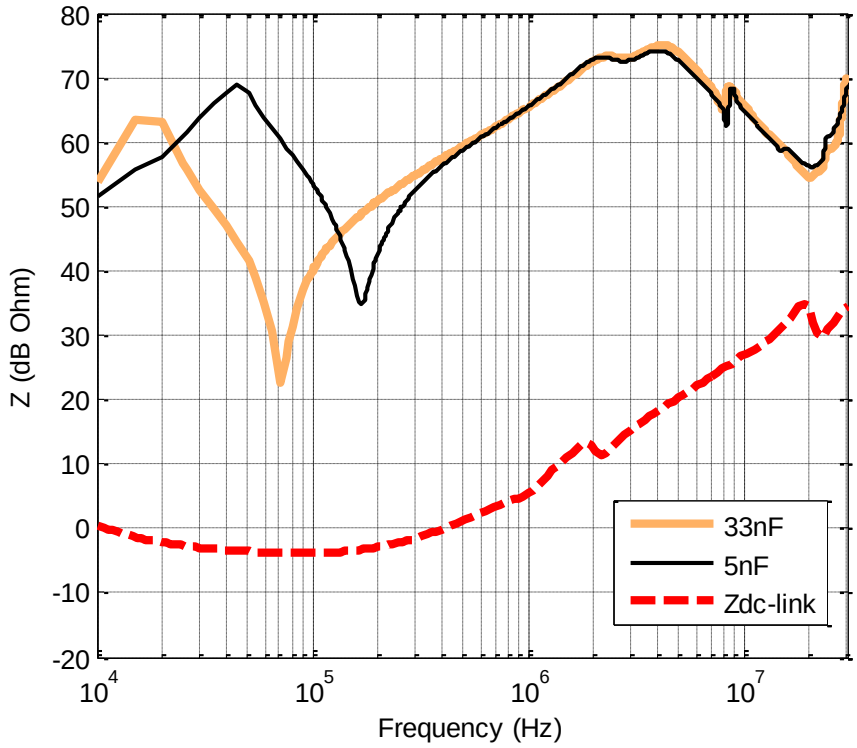

Fig. 4.60: Impedance at the output ($Z_{DM\text{-}FL}$ in Fig. 4.59) after the application of three-phase LC filter

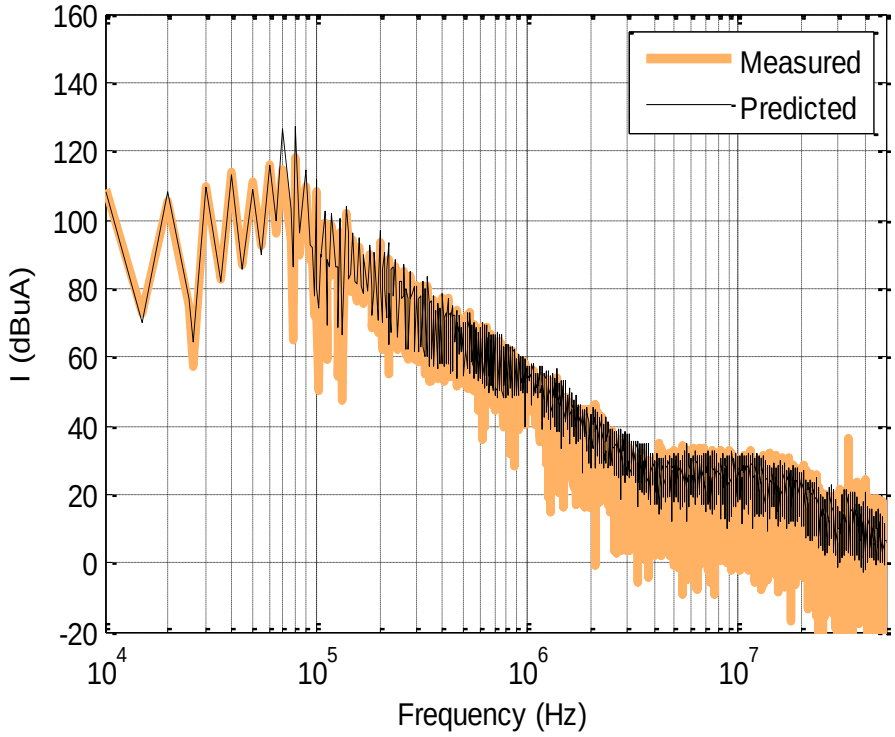

Fig. 4.61: Comparison of measured and predicted DM noise current for the case shown in Fig. 4.59 (33 nF)

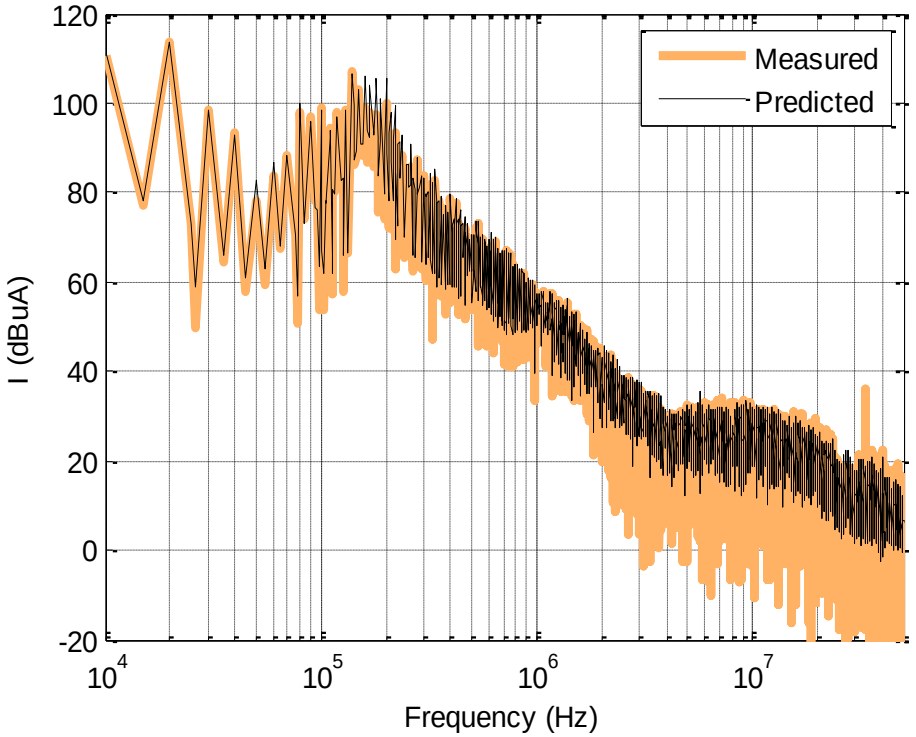

Fig. 4.62: Comparison of measured and predicted DM noise current for the case shown in Fig. 4.59 (5 nF)

4.2.4 Total Noise Prediction

To show the accuracy of the model in predicting the total noise in the system we take the case of Fig. 4.57 itself. The total noise is calculated by adding the magnitudes of predicted noise currents from the DM model and a CM model. In principal both magnitude and phase should be considered but the noise models are derived from different measurements and hence the recorded time-domain data is not synchronized in phase. Moreover, we have only a snapshot of the EMI in the time-domain, so it is impossible to align the recorded noise data unless time markers are used and the oscilloscope is triggered at exactly the same instant every time measurements are taken. Since this is a commercial motor-drive, it is not possible to use such a technique. In fact the situation confronted here depicts a real case of "black-box". Adding just the magnitudes however gives an estimation of the worst case total noise and this may be useful in designing EMI filters for the system.

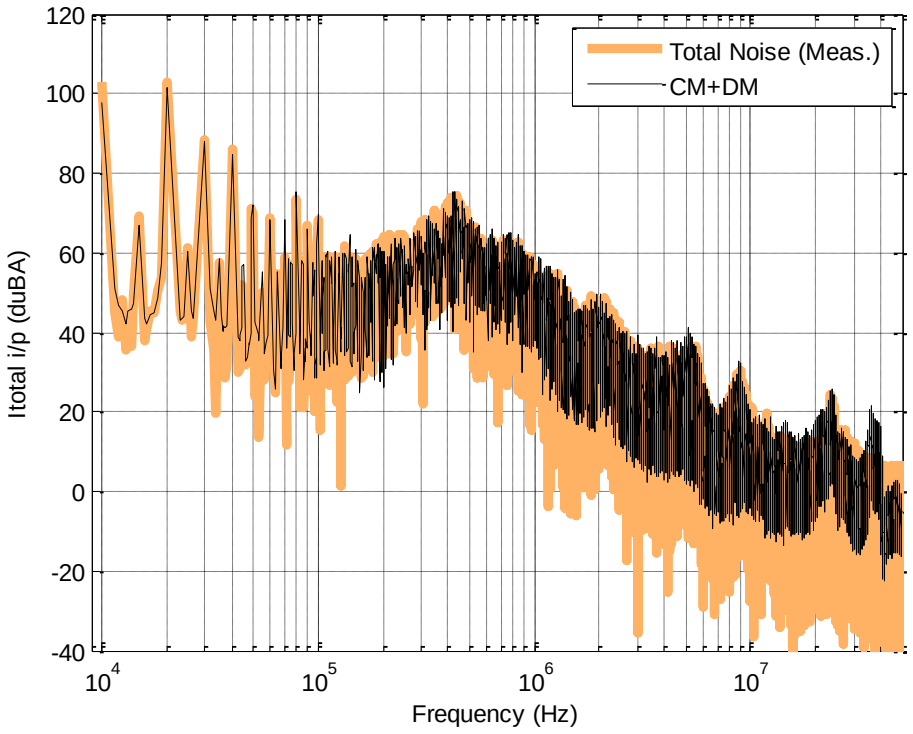

Fig. 4.63: Comparison of measured and predicted total input side noise current for the case shown in Fig. 4.57

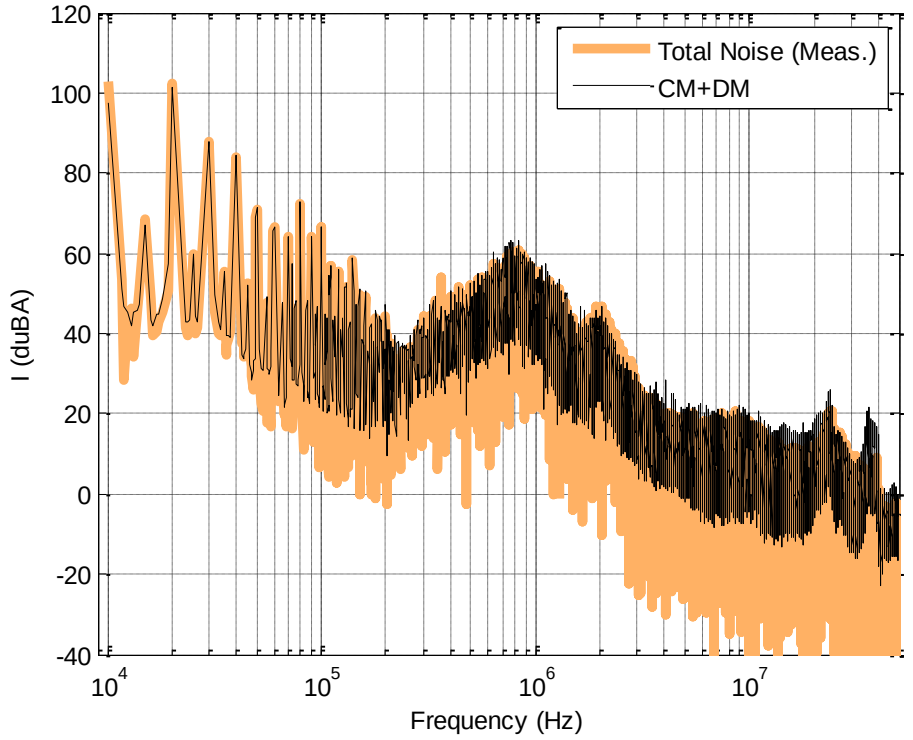

Fig. 4.64: Comparison of measured and predicted total input side noise current for the input DM filter of Fig. 4.57 and an output CM choke of 30mH.

The addition of CM and DM noise to calculate total noise is only valid for converters that are symmetrical with respect to ground. For other converters that are asymmetrical with respect to ground, like a buck or a boost converter, addition of CM and DM noise may not be accurate at higher frequencies due to the presence of mixed-mode noise. Fig. 4.63 shows the comparison of the predicted and measured total noise current at the input side of the motor-drive. It can be seen that the predicted total noise matches well with the measurements up to 30 MHz.

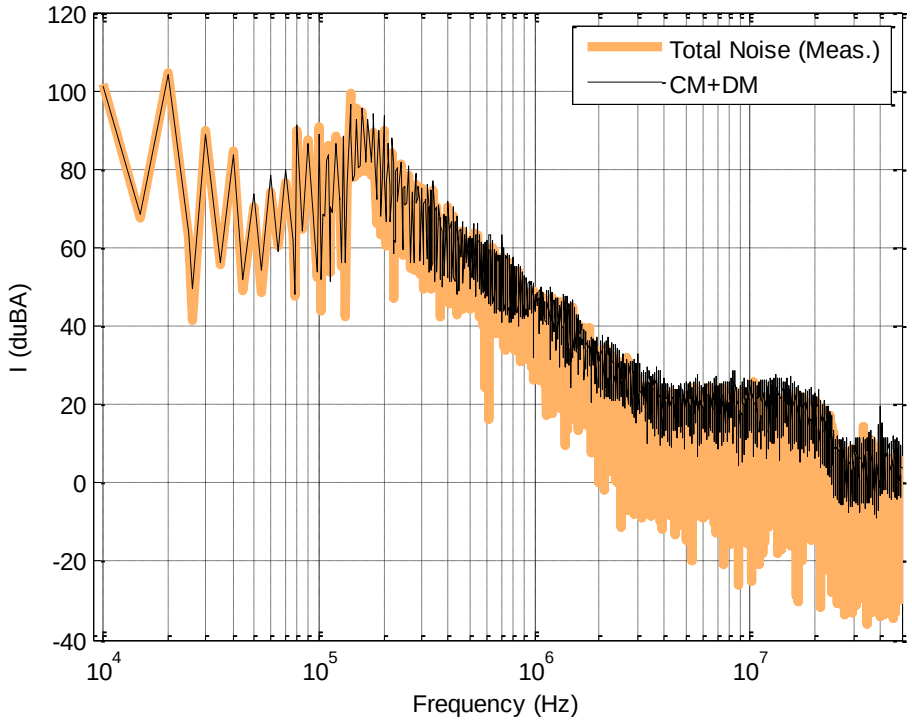

Fig. 4.65: Comparison of measured and predicted total input side noise current for the case shown in Fig. 4.59

To test the versatility of the method a small change was done in the set-up of Fig. 4.57. A huge CM choke of 30 mH was inserted. This choke reduces the CM noise circulating in the motor-drive system however its effect on DM noise should be negligible. The predicted DM noise will thus remain the same. However the predicted CM noise must be less. The total noise is again computed and is shown in Fig. 4.64. It can be seen that the total noise is different from Fig. 4.63 and again the models are able to predict with good accuracy.

As a last validation case the total noise at the output side is predicted for the 5 nF case shown in Fig. 4.59. This time the input side has not filters. The predictions from the output side DM models were used along with the CM currents predicted from the CM model. The comparison

results are shown in Fig. 4.65. It is again evident that the prediction matches well with the measurements, at least up to 30 MHz.

4.3 CONCLUSIONS

The work presented in this chapter shows the complete development of un-terminated behavioral EMI models for a motor-drive system. The modeling technique is "black-box" in nature and thus does not require internal details of the converter. The model is simple to simulate and yet remains accurate at higher frequencies. The results in general show that the model can predict EMI for most practical input and output conditions that a motor-drive is likely to be subjected too. It should also be noted that the un-terminated modeling method proposed here greatly simplifies the behavioral model extraction process when compared to the GTM (and MTB) modeling procedure discussed in chapter 3. Nevertheless, the models proposed here are still three-terminal models. The improved strategy of extracting three-terminal noise models should therefore be applicable to the type of models used in Chapter 3 as well.

The accuracy achieved in the prediction of total noise shows the usefulness of the model in predicting EMC compliance of the drive. This method can be potentially used to evaluate EMI and design at the system level where several converters may be used in a network. It can also be used to design EMI filters for EMC compliance and this application is the topic of discussion in the next chapter.

A brief guide to extracting CM un-terminated modeling procedure is given in APPENDIX A. This guide is like a manual that can help the readers understand how the proposed procedure of un-terminated CM model extraction was implemented in the lab. This guide should also help the readers identify the potential pitfalls that must be avoided for successful model extraction. The procedure of extracting DM models is similar to the CM model extraction and hence only the CM model extraction is discussed in APPENDIX A.

5 EMI FILTER DESIGN WITH BEHAVIORAL EMI MODELS

5.1 INTRODUCTION

Filter design is an art that has been perfected over decades. However, the fact remains that there are several possible solutions to reach the same goal. The question remains, which is the optimum solution, in terms of weight, volume, power loss etc. The issue with standard filter design techniques is that they usually start with certain assumptions regarding the impedances that the filter is going to see at its input and output. These assumptions work well when the systems are designed with certain standard input/output impedances, but in the case of power electronics the input and output impedances of the system are almost always non-standard. For example on the output side, the DM impedance of the motor-drive is switched in nature and both the CM and DM impedances of the load are a function of cable length, type and the motor used. Since these are all non-standard impedances, the process of finding an optimum solution becomes difficult and standard techniques may not apply or lead to a sub-optimal solution. In case the final conditions are not known, the design of the EMI filter should always be designed for the worst case conditions.

The goal of this chapter is to develop an automated process for designing EMI-filters that are optimized from a volume point of view. To accomplish this, existing methods for determining the filter elements behavior will be used. Improving the accuracy of estimating the various filter performance parameters like core-loss, temperature rise, high-frequency behavior is beyond the scope of this research. The goal here is to show the utility of the EMI terminal models developed in this dissertation. The design algorithm and the computer codes should be reconfigurable and therefore whenever better estimations of filter characteristics are available, equations/models can simply be replaced by the new ones.

5.2 FILTER HIGH-FREQUENCY BEHAVIOR

There are several important limitations in the practical design of EMI filters that push for a trial-and-error type process. The first of them is that the source impedance (impedance at the input of the filter) and the load impedance (impedance at the output of the filter) may not be accurately known. However with the terminal EMI models, better estimations of the source

impedances are now available. If the load impedance is known then the worst case should be used.

A major limitation is the difficulty in predicting how the parasitic will affect the high-frequency behavior of the EMI filter. In [85], it is shown that the prediction of the second order resonances of the inductors with an acceptable accuracy is possible. In [79, 86-88] analytical equations have been developed to estimate the second order resonance (or the self-resonance) or the equivalent parallel capacitance (EPC) of the inductors. These methods will be directly adopted here for fast estimation of the EPC, however there are obviously limitations as the EPC of the inductor is a sensitive function of the core's conductivity, turn-to-turn distance, turn radius and symmetry. The other parasitic that may affect the high-frequency behavior of the EMI-filters are the parasitic of the interconnects like PCB traces, wires and connectors. Lastly there is the issue of coupling between filter elements and parasitic. These effects have been analyzed, modeled and reported in [89-91] and are very important in determining the high frequency performance of the EMI filter. However since modeling of EMI filters is not in the scope of this research, effects have been neglected. Estimating the coupling between filter elements and estimation of parasitic will require FEM or PEEC analysis which is difficult and can be very time consuming. An integrated 3-D electromagnetic tools has been developed for EMI filters in power converter applications that uses a combination of PEEC and boundary element method [92]. This tool can run faster than the FEM and is shown to be very capable for designing EMI filters, but would still require time in developing the simulation models.

Another problem is the difficulty in predicting the loss in the magnetics. The loss in the magnetics will affect the quality factor (Q-factor) of the self-resonance and thus inaccuracies in core-loss estimation can lead to inaccurate estimation of Q-factor as well, which in turn will lead to inaccurate estimation in the peaks and valleys of the EMI noise. Most data sheets on magnetic cores give loss estimation at different frequencies of operation and also at different dc/ac bias points [93]. However all these losses are calculated for only sinusoidal excitations, which is seldom the case in power electronics. The most commonly used method of estimating the loss analytically is by using an empirical equation called the *Steinmetz's Equation*. However limitations have been reported in this equation and several improved versions of the equations have been developed [94], but they are all very complicated to use and hence will be dropped here. For the work presented here, two different types of cores are used. Iron-powdered cores for

DM filter inductors and nano-crystalline cores for CM chokes. For iron-powdered cores the estimation of core loss will be done on the basis of Oliver's model given in [95] and for the nano-crystalline core, the ordinary Steinmetz equation will be used. The Steinmetz parameters for nano-crystalline cores can be found in [96, 97]. For modeling the high-frequency behavior of the nano-crystalline core the methods in [97-99] are used. The data for permeability of nano-crystalline core can be found in the catalog [100].

Lastly, filter damping may be required to limit the EMI noise at lower frequencies (<150 kHz). An unwanted resonance near the switching frequency can lead to amplification of noise in the low frequency region. This can cause the magnetics to saturate, as the power at the switching frequency and its first few harmonics is higher compared to the power in the high frequency part of the spectrum. So even though there are no EMI standards that go so low in the frequency, low frequency noise mitigation is an important aspect of the EMI filter design as it may interfere with the other systems and can cause the EMI filters to fail in the high frequency. Several methods of damping have been developed which includes RC-parallel damping, RL-parallel damping and the RL-series damping [101-104]. However from the volume point of view the RC-parallel damping seems to provide the best solution and hence will be used here.

5.3 DIFFERENTIAL-MODE FILTER DESIGN

The filter design procedure explained in this section is built around the terminated terminal models developed earlier in chapter 4 for DM noise from the motor-drive. The procedure assumes a topology of the EMI filters and is developed only for a single-stage. The topology chosen for the DM filter is an LC filter with the L facing the motor-drive on both the input and output side. This arrangement is chosen to produce a maximum impedance mismatch at the terminals of the motor-drive. That is if the input impedance of the system (for which filters are to be designed) is small then large impedance must be chosen to terminate the input port for maximum impedance mismatch. Since the DM input impedance for input is dominated by the dc-link capacitor and the DM output impedance is dominated by the parasitic inductance of the interconnects, they are both very small and hence inductors are put first, facing the drive. This topology is shown in Fig. 5.1. The method developed in this section can be easily extended to other topologies as well.

Fig. 5.1 also shows the parasitic of the EMI filter. These parasitic must take into account if the high frequency behavior of the filter needs to be accurately predicted. The next section will show the method of determining the values of EMI filter elements and achieving minimum volume.

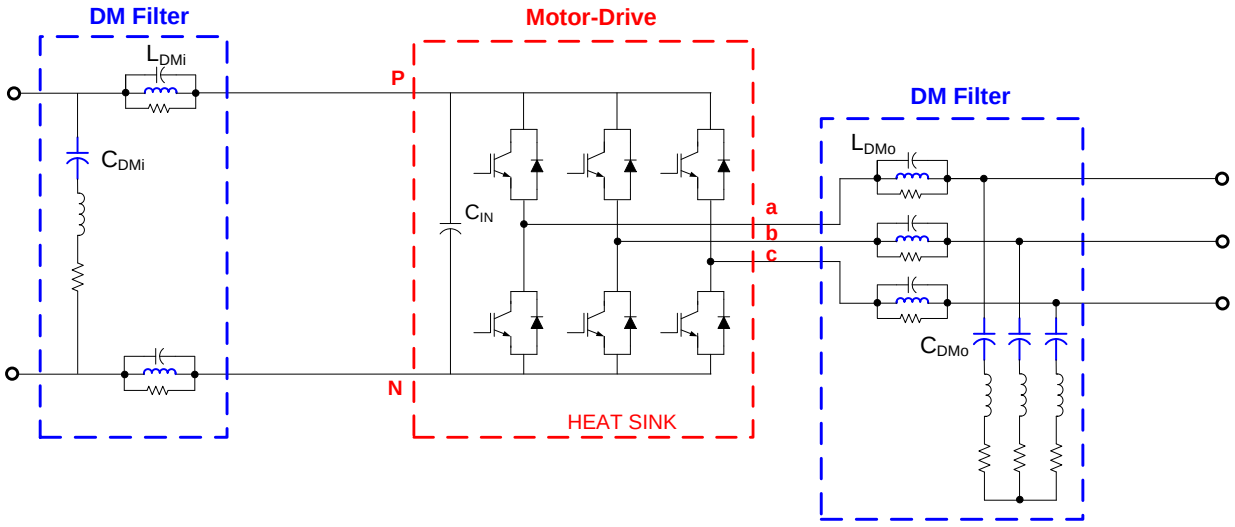

Fig. 5.1: LC filter topologies selected for the input and output side DM filters

5.3.1 Filter Design Procedure

The filter design procedure is developed to use components that are easily available or are available off-the-shelf. The filter design starts with picking up the smallest capacitor in the list of the available capacitors. For this capacitor, a minimum inductance is then found so as to satisfy the EMC standards with a small design margin. The method assumes that the minimum possible inductance is directly proportional to the minimum possible volume of the magnetics. Once the inductance is found, a formal inductor design procedure is followed and the smallest core is found that can be used to implement the inductance without getting saturated or heated excessively. This procedure is shown in Fig. 5.2.

We start by making a catalog of available capacitors with their dimensions, value, parasitic inductance (ESL) and parasitic resistance (ESR). The ESL and ESR are measured using an impedance analyzer (Agilent 4394A) and are in the catalogue. This is an important step towards estimating the high frequency behavior of the filters. Most engineers would simply neglect the parasitic, but this can lead to several design iterations. However, the goal here is to avoid design iterations. The capacitors in the catalog are arranged in increasing order of their volume.

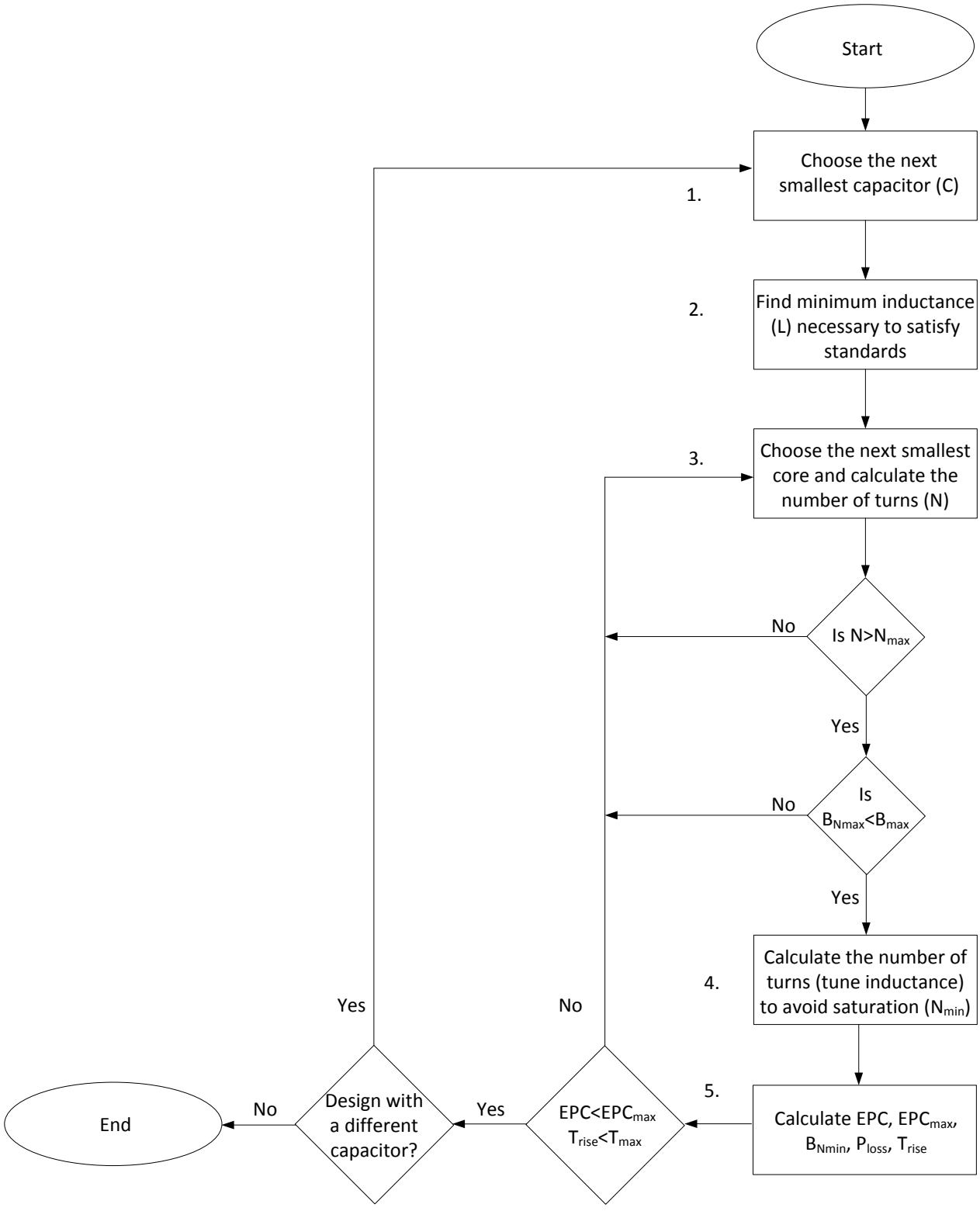

Fig. 5.2: General design procedure of EMI filters

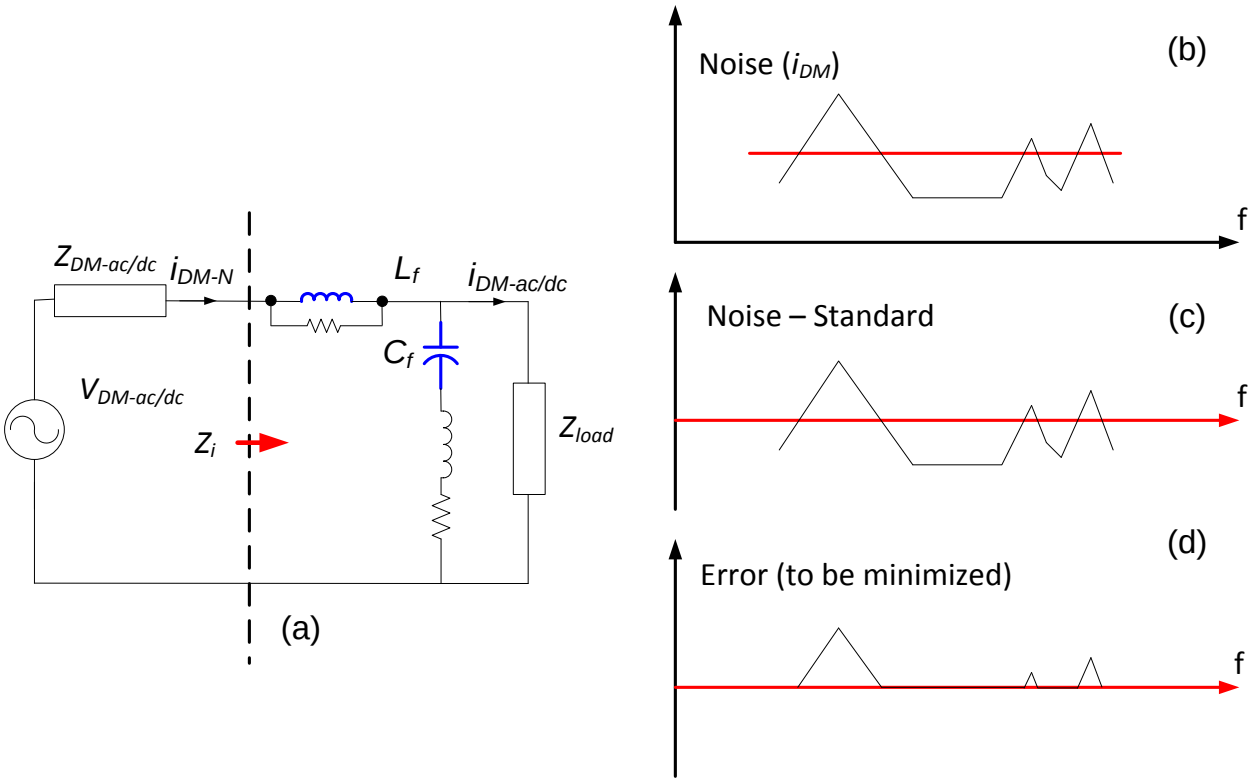

Fig. 5.3: Filter inductance Optimization Process

To find the minimum inductance a simple optimization process is introduced. This optimization process (2. In Fig. 5.2) starts with first assuming a very small value of inductance (initial solution). This inductance is then optimized until all the peaks in the spectrum of filtered noise are below the EMI standards. Fig. 5.3 illustrates the optimization process in a simple way. First the filtered current ($i_{DM\text{-}ac/dc}$) is calculated using the terminal model, the chosen capacitance and the initial estimation of filter inductance. To calculate this we use the DM terminal model consisting of a source ($V_{DM\text{-}ac/dc}$) and impedance ($Z_{DM\text{-}ac/dc}$) as shown in Fig. 5.3 (a). Then the filtered current for an LC filter can be calculated from (1), where $Z^*_{Lf} = 2\pi f L^*$. Note that '*' denotes an approximated value. Z_{load} is the DM impedance of the LISN.

$$i^*_{DM-ac/dc} = V_{DM-ac/dc} \frac{Z_{Cf}}{Z_{load}Z_{Cf} + \left(Z_{load} + Z_{Cf}\right)\left(Z_{DM-ac/dc} + Z^*_{Lf}\right)} \quad (1)$$

Let us suppose that the spectrum of the calculated filtered current from (1) looks like the one shown in Fig. 5.3 (b) and the EMC standard to be met is shown in red. The offset is then removed by subtracting the standards from the noise spectrum. This is shown in Fig. 5.3 (c). Since the only concern is that the peaks do not cross the standards, the negative side spectrum is zeroed and the final objective function (error) is shown in Fig. 5.3 (d) and is calculated from (2).

$$e^{+} = \left| i^{*}_{DM-ac/dc} - i_{stad} - i_{mar} \right| \quad \text{and} \quad e^{-} = 0 \tag{2}$$

The square of this error will be minimized with inductance 'L' as the variable to obtain the tightest design possible for the chosen capacitor. Notice that, here the EPC of the filter inductor is not considered as we have no idea about the physical dimensions of the inductor at this stage. A worst case value of EPR (equivalent parallel resistance) based on experience is however used but can be neglected as well.

Instead of optimizing the inductance value, the volume can be optimized directly. In that way one can avoid going through all the possible combinations of capacitors and instead arrive at the optimum combination directly. However there is a problem in doing that. The volume of the capacitor can be written as a function of capacitance by curve fitting techniques [85] but the volume of the inductor is the function of many variables and not just the inductance. This includes core saturation and power loss (or temperature rise). In other words, a small inductance might have to be wound on a big core just because the power at lower frequencies is large enough, which can cause the smaller cores to saturate but also cause excessive power loss (or temperature rise). Thus, there is no clear way of relating the inductance to the volume of the available cores and hence building an objective function like (2) is difficult. Therefore, the assumption made here is that the minimum inductance will lead to minimum volume of the core.

This procedure is then repeated for all other capacitors (or a few) and then finally the best possible combination with respect to volume or weight can be chosen. If at all possible combinations are looked into, and then global minima can easily be found. The number of possible combinations is not too many since usually the type and value of capacitance are restricted by safety standards and application area. Thus, in the end there is only a small range of capacitances that need to be tried and the computer can do this quick enough. This procedure will become clearer with the following examples.

5.3.2 Example: Input DM Filter Design

The input side DM filter is designed without any additional damping as the input dc-link capacitor attenuated most of the low frequency harmonics. The capacitors were selected to be metal-film type as they have a longer life and are preferred for aerospace applications. There are no bounds on the value of the capacitances so a reasonable range is chosen from 0.022µF to 10µF from the EPCOS® catalog for X2 type 305V EMI suppression capacitors [105]. In all 11 different values of capacitances are available in this range. The data for these 11 capacitors including the volume, measured ESL and ESR is shown in Fig. 5.4.

Epcos_type_X2_305V_capacitors.xlsx

	A	B	C	D	E	F	G	H	I	J
1	Sr.	EPCOS	C	W	H	L	A	V	ESL	ESR
2	No.	Part Number	uF	mm	mm	mm	cm2	cm3	nH	mΩ
3	1	B32921C3223	0.022	4	9	13	4.1	0.47	8.23	190.4
4	2	B32921C3333	0.033	4.00	9.00	13.00	4.10	0.47	8.23	190.4
5	3	B32921C3473	0.047	5.00	11.00	13.00	5.26	0.72	7.49	147
6	4	B32922C3104	0.100	5.00	10.50	18.00	6.63	0.95	6.58	63.23
7	5	B32922C3224	0.220	7.00	12.50	18.00	8.77	1.58	6.03	47.27
8	6	B32922C3334M	0.330	8.00	14.00	18.00	10.16	2.02	6.8	39
9	7	B32922C3474	0.470	9.00	17.50	18.00	12.69	2.84	11.2	54
10	8	B32923C3105	1.000	11.00	20.50	26.50	21.21	5.98	9.857	22.3
11	9	B32923E3225M	2.200	12.00	22.00	26.50	23.30	7.00	16.66	33.8
12	10	B32924E3475M	4.700	18.00	27.50	31.50	38.57	15.59	16.7	16.28
13	11	B32926E3106	10.000	20.00	39.50	42.00	65.78	33.18	29.68	10.6

Sheet1 Sheet2 Sheet3

Fig. 5.4: Catalog of available capacitors for DM filter design

For the cores in DM filters, powdered-iron cores from Micrometals® are used. The choice is restricted to only Type-26 material [93] cores which is very popular for line-filter application. In all 12 different cores are chosen from the catalogue to demonstrate the EMI filter design process. Powdered cores provide a distributed air-gap and hence help with avoiding saturation of the inductor. The 12 cores were chosen to make sure that they have different volumes, sizes and are easily available off-the-shelf. The data for the selected cores including the surface area and the volume is shown in Fig. 5.5.

Micrometal_type_26_cores.xlsx

	A	B	C	D	E	F	G	H	I
1	Sr.	MicroMetals	Al	OD	ID	H	l	A	V
2	No.	Part Number	nH/N2	mm	mm	mm	cm	cm2	cm3
3	1	T50-26	33	12.7	7.7	4.83	3.19	0.112	0.358
4	2	T80-26	46	20.2	12.6	6.35	5.14	0.231	1.19
5	3	T94-26	60	23.9	14.2	7.92	5.97	0.362	2.16
6	4	T80-26D	92	20.2	12.6	12.7	5.14	0.453	2.33
7	5	T106-26	93	26.9	14.5	11.1	6.49	0.659	4.28
8	6	T106-26B	124	26.9	14.5	14.6	6.49	0.858	5.57
9	7	T130-26	81	33	19.8	11.1	8.28	0.698	5.78
10	8	T175-26	105	44.5	27.2	16.5	11.2	1.34	15
11	9	T200-26	92	50.8	31.8	14	13	1.27	16.4
12	10	T225-26	98	57.2	35.7	14	14.6	1.42	20.7
13	11	T184-26	169	46.7	24.1	18	11.2	1.88	21
14	12	T201-26	224	50.8	24.1	22.2	11.8	2.81	33.2

Sheet1 Sheet2 Sheet3

Fig. 5.5: Catalog of available Type-26 cores for DM inductor design

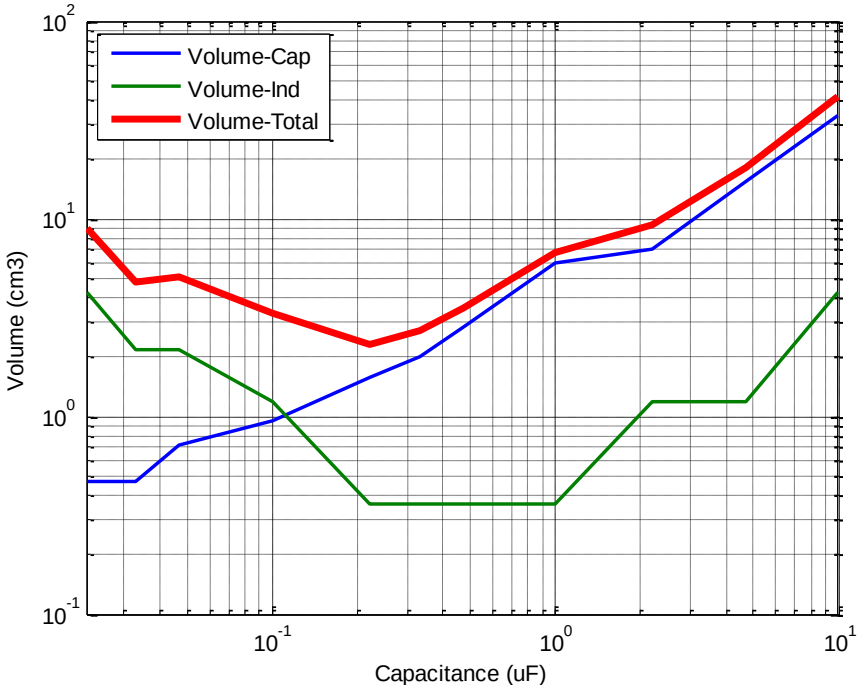

Fig. 5.6: Filter volume comparison for different choice of capacitors

The design procedure shown in Fig. 5.2 is then written in a MTALAB script and the process is then run for all the 11 capacitors and the final volume is recorded for all combinations. This is shown in Fig. 5.6. It can be seen that the volume plots are not smooth because we have only discrete sizes of the capacitances and cores available to us. The design details for all possible combinations are shown in Fig. 5.7.

DM_ip_filter_design.csv

	A	B	C	D	E	F	G	H	I
1	Cap	Core	i/p Cap(uF)	i/p Ind(uH)	i/p Turns	i/p EPC(pF)	i/p Bmax(T)	i/p Tmax(C)	Vol(cubic cm)
2	1	5	0.022	237.5868	51	4.2533	0.30215	29.2776	9.03
3	2	3	0.033	153.4257	51	3.2587	0.3316	32.152	4.79
4	3	3	0.047	102.3559	42	3.1909	0.27545	27.3945	5.04
5	4	2	0.1	33.7942	28	2.5567	0.21995	22.776	3.33
6	5	1	0.22	18.9724	24	1.9823	0.31573	31.5167	2.296
7	6	1	0.33	12.3905	20	1.9523	0.28604	28.6644	2.736
8	7	1	0.47	8.5312	17	1.9327	0.255	25.8619	3.556
9	8	1	1	3.8209	11	1.8974	0.25888	32.1689	6.696
10	9	2	2.2	1.53	6	2.4483	0.13584	20.4663	9.38
11	10	2	4.7	0.49361	4	2.4353	0.16017	31.2848	17.97
12	11	5	10	0.35186	2	3.9025	0.10758	27.7993	41.74

DM_ip_filter_design

Fig. 5.7: Filter options possible for input side DM filter with the available capacitors and cores

Fig. 5.7 is a snap shot of the output file generated by a MATLAB® script. In Fig. 5.7, the first two columns are the serial numbers of capacitors and magnetic cores respectively. These serial numbers can be traced back to Fig. 5.4 and Fig. 5.5 to find the corresponding capacitor and the core. Additionally the output file shows the value of the filter capacitance, the optimized value of the filter inductance, the number of turns to put on the core, the estimated EPC of the final inductor using analytical methods, the maximum expected flux density in the core, the temperature rise and the total volume of the filter. It can be seen that increasing the size of the capacitor decreases the inductance required for designing the filter but does not necessarily decrease the size of the inductor core as large capacitors can cause large flux swings in the inductors causing them to saturate.

The last column in Fig. 5.7 shows the smallest total volume is given by a capacitance of 0.22 µF and inductance of 18.9 µH wound on a T50-26 core. However in the design, the 0.1 µF capacitance option is used instead because a smaller capacitor will require a larger inductor (corner-frequency of the filter being the same for all combinations) thus giving better performance in terms of temperature rise (see column H in Fig. 5.7). Moreover since the calculation of temperature rise is approximate and it can have significant error, it is wise to make a conservative choice. So the T80-26 core and 0.1 µF capacitor is chosen for the design of the input side DM filter.

The DM filter is designed and is shown in Fig. 5.8. This filter was put together on a general purpose printed circuit board and hence it has not been optimized for parasitic. However, since

the aim is to show utility of the EMI terminal models in quick design of EMI filter, this serves as an ideal example. The accuracy of design and filter performance is discussed next.

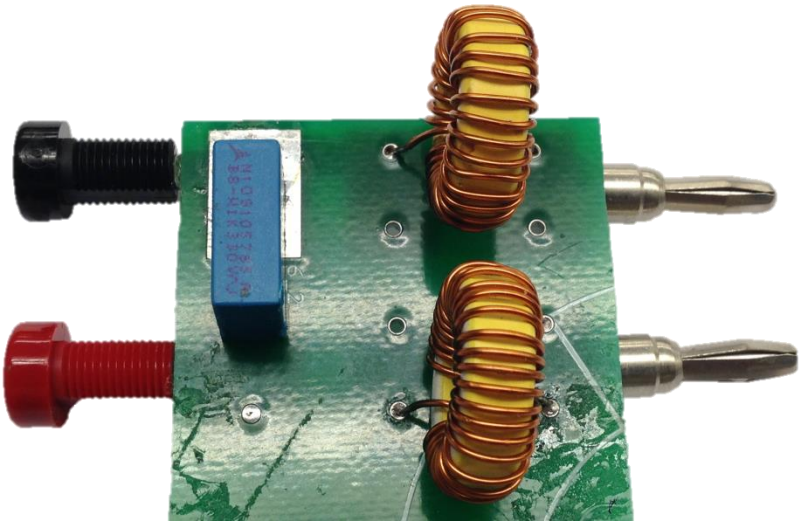

Fig. 5.8: Input DM filter design based the best possible combination from Fig. 5.7.

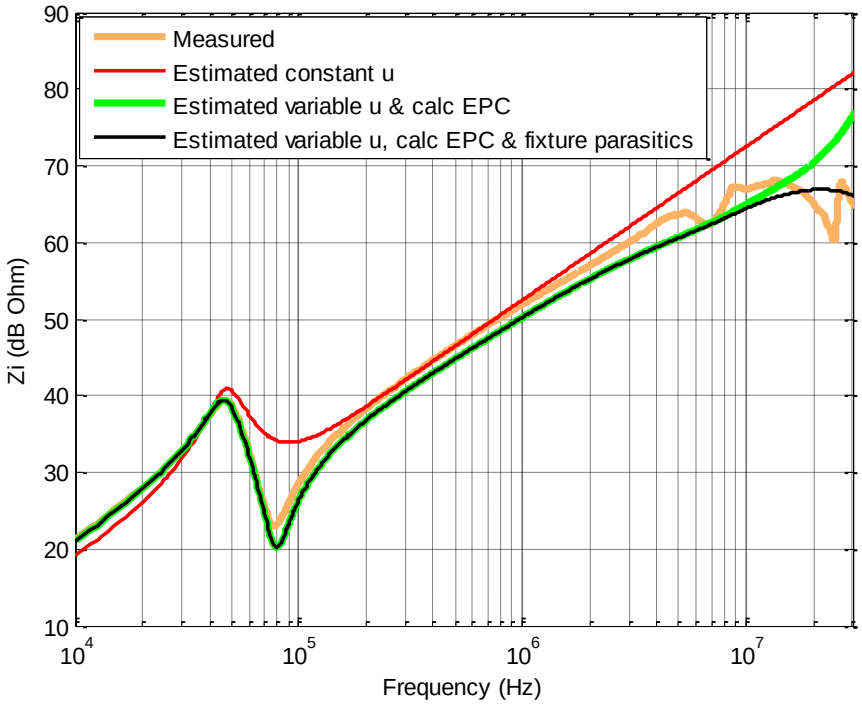

Fig. 5.9: Comparison of estimated and measured input impedance of the input side DM filter

Fig. 5.9 shows the comparison of the estimated input impedance (Z_i in Fig. 5.3) of the filter with the measured input impedance. Note that in order to be accurate at higher frequencies, the

variation of permeability (μ) with respect to frequency must be taken into consideration and this can be found in the datasheet of the magnetic cores. The red plot shows the estimated input impedance of the filter if the inductors are assumed ideal. Their impedance is calculated using a constant (initial) permeability (μ = 75 for Type -26 material) and zero EPC. It can be seen that at both low and high frequencies this estimation is far from the measured one. The green plot shows the estimated input impedance where the impedance of the inductor is calculated with a variable permeability (non-linear) and an EPC is calculated from analytical equations. The inclusion of the change in permeability with respect to frequency and EPC improves the low frequency accuracy of the estimated input impedance. Finally it was found that there is small parasitic capacitance of (~ 2-3 pF) between the positive and negative terminals of the filter at both input and output side. This capacitance comes from the fixture in which the banana connectors of the filter are inserted and once this parasitic capacitor is included in the filter model, the final estimation of (black plot) input impedance is obtained. It can be seen that now the estimated input impedance matches well with the measured one at both low and high frequencies. Fig. 5.9 shows that parasitic are very important in the filter's performance and neglecting them could cause inaccuracy in estimation of both low and high frequency performance, hence leading to several design iterations.

Let us now see the comparison of estimated and measured output to input transfer function ($I_{DM\text{-}ac/dc} / V_{DM\text{-}ac/dc}$ in Fig. 5.3) of the filter. The measurements were done using a vector-network-analyzer (VNA) with the RF-baluns on both ports. This helps in isolating the DUT from the ground or reference of the VNA, a must for making DM measurements. The VNA is then calibrated with the RF-baluns for maximum accuracy. The comparison of measured and simulated transfer function is shown in Fig. 5.10. In the low frequency the simulated transfer function matches well with the measurements but in the high frequency a huge discrepancy is seen. This discrepancy is due to the mutual coupling between the filter components and it's parasitic [89-91].

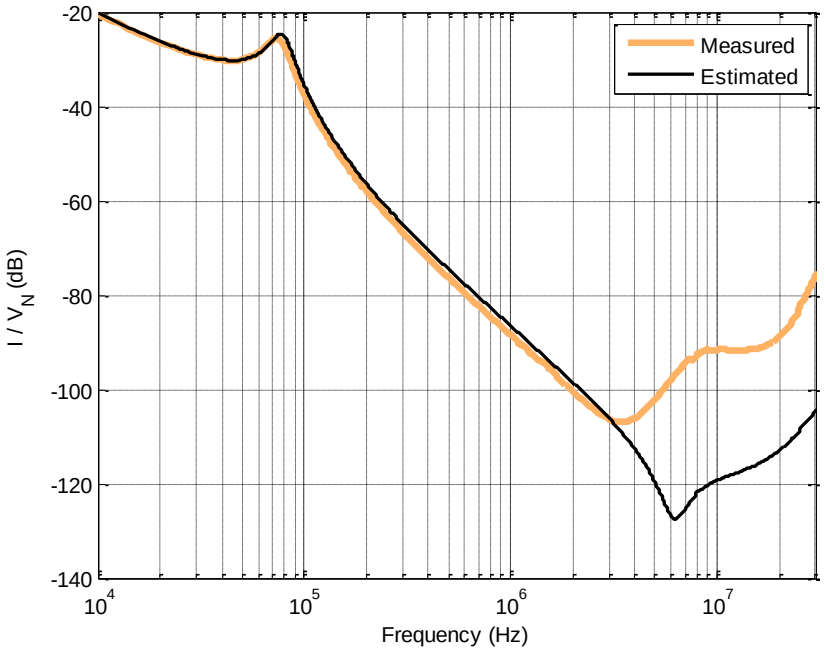

Fig. 5.10: Comparison of estimated and measured transfer-function of the input side DM filter

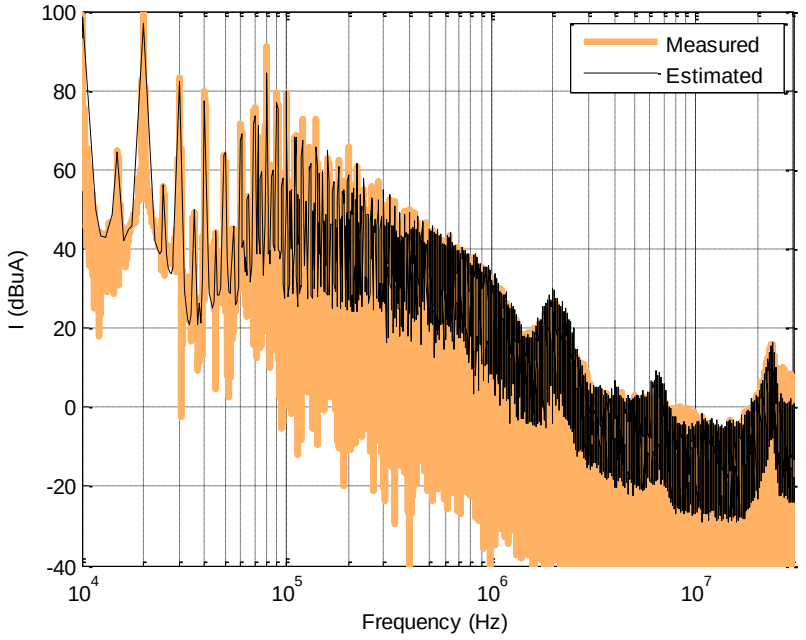

Fig. 5.11: Comparison of estimated and measured input noise current of the input side DM filter

It is now possible to use the estimated input impedance and the transfer-function to calculate the input ($i_{DM\text{-}N}$ in Fig. 5.3) and output ($i_{DM\text{-}ac/dc}$ in Fig. 5.3) side noise current of the filter. The

comparison of estimated and measured input side noise current is shown in Fig. 5.11 and the comparison of estimated and measured output side noise current is shown in Fig. 5.12. It can be seen from Fig. 5.11 that the estimated input EMI noise matches well with the measurements, except at around 80 kHz. This mismatch results from the mismatch at around 80 kHz in the estimated input impedance shown earlier in Fig. 5.9. In Fig. 5.12, the estimated output noise current matches well with the measurements up to 1 MHz, but after that the noise floor of the oscilloscope is hit and it becomes difficult to verify the accuracy of the estimation. Nevertheless it is difficult to get accurate after 2 MHz anyway because of the inaccuracy in the estimation of filter's transfer-function shown earlier in Fig. 5.10. Note that the design was made with a 6 dB margin. Since the noise in DM is so small in the high frequency and the EMI standards are met, no further investigation was found necessary here.

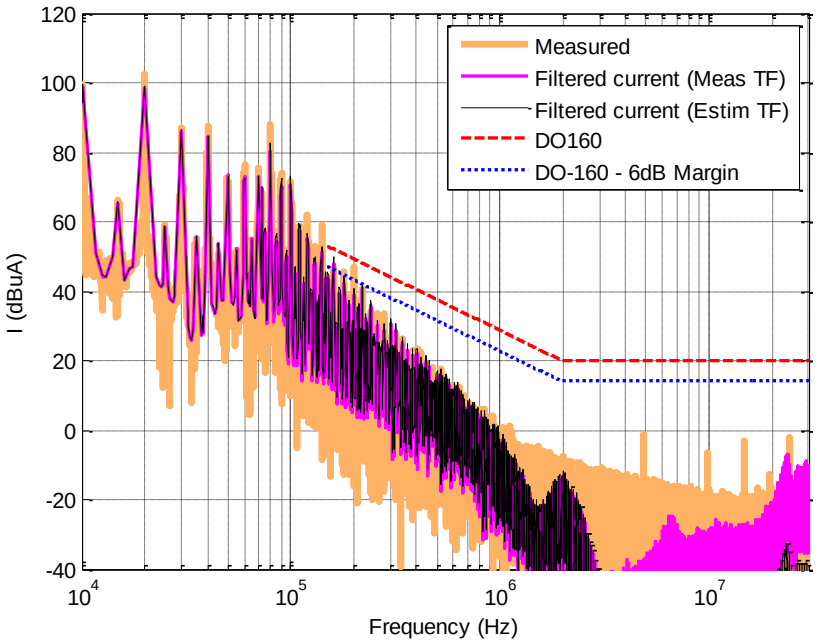

Fig. 5.12: Comparison of estimated and measured output noise current of the input side DM filter

5.3.3 Example: Output DM Filter Design

The design of output side DM EMI filter is done in a very similar way as the input side DM filter and hence the detailed analysis as shown in the latter case will be skipped here. The major difference between input and output side DM filter is the addition of a low frequency damping network in order to limit the flux in the DM inductors which may cause them to saturate. The RC

parallel-damping is used here as this gives the lowest volume amongst all the commonly used damping techniques. The filter damping structure along with the filter topology is shown Fig. 5.13. Note that the damping capacitor is chosen to be of the same value as that of the filter capacitor. Fig. 5.14 shows the snapshot of the file that shows all the possible filter design options as calculated from a MATLAB®. It can be seen that the number of options are fewer as increasing the size of the capacitor was found to increase the flux swing in the core forcing the algorithm to pick bigger cores. Thus it is best to use the smallest capacitor available and that is 0.022 µF. The output file also gives the value of the damping resistor which in this case is 201.2174 Ω or approximately 200 Ω.

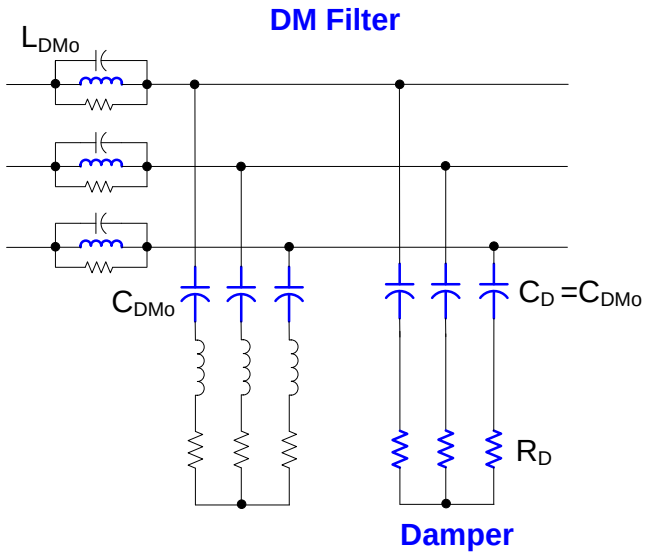

Fig. 5.13: Complete output side three-phase DM filter with a damper

DM_op_filter_design.csv

	A	B	C	D	E	F	G	H	I	J	K
1	Cap	Core	o/p Cap(uF)	Cd (uF)	Rd (Ohm)	o/p Ind(uH)	o/p Turns	o/p EPC(pF)	o/p Bmax(T)	o/p Tmax(C)	Vol(cubic cm)
2	1	8	0.022	0.022	201.2174	222.6864	47	6.7332	0.43665	65.8145	46.41
3	2	8	0.033	0.033	135.9839	152.556	39	6.6791	0.42277	92.1212	46.41
4	3	10	0.047	0.047	96.2831	108.9277	34	6.4984	0.33525	93.2333	64.26

DM_op_filter_design

Fig. 5.14: Filter options possible for output side DM filter with the available capacitors and cores

The filter is then built on a general purpose PCB. The input impedance of this filter was measured and compared to that of the estimated one and is shown in Fig. 5.15. It can be seen that

unlike the input side DM filter, there is a mismatch in the high frequency between the estimated and measured input impedance. This is due to the fact that the output side DM inductor is much bigger than that of the input side DM filter resulting in multiple resonances in the high frequency. However, in the inductor model only second order effects are included and because of this the second resonance cannot be matched. There is only one way to estimate the third and fourth order effects and that is by conducting a detailed FEM or PEEC modeling.

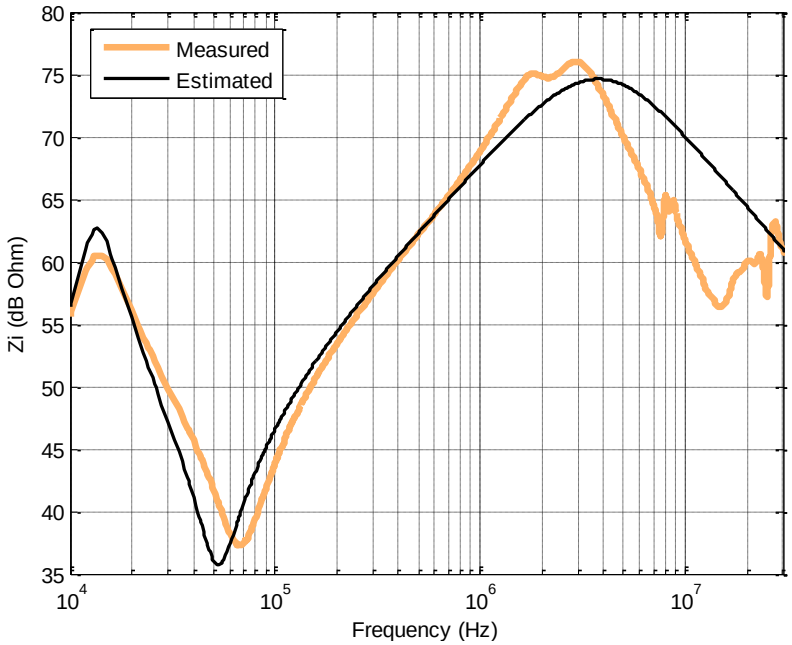

Fig. 5.15: Comparison of estimated and measured input impedance of the input side DM filter

Fig. 5.16 shows the comparison of estimated and measured input and output side noise currents. From Fig. 5.16, it is expected that there is a mismatch at the high frequency because of the inaccuracy in the estimated input impedance seen in Fig. 5.15. Fig. 5.17 is the comparison of measured and estimated output current noise current of the filter. Again as seen in the input side of the DM filter, there is always difficulty in estimating the correct output side noise currents as filter coupling is not included in the models. Note that again a margin of 6 dB was left out to account for design tolerances.

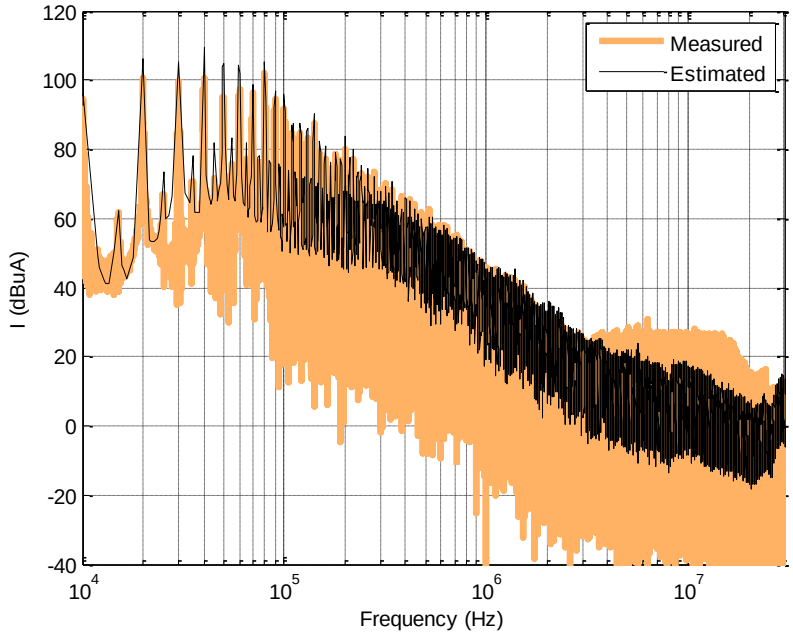

Fig. 5.16: Comparison of estimated and measured input noise current of the input side DM filter

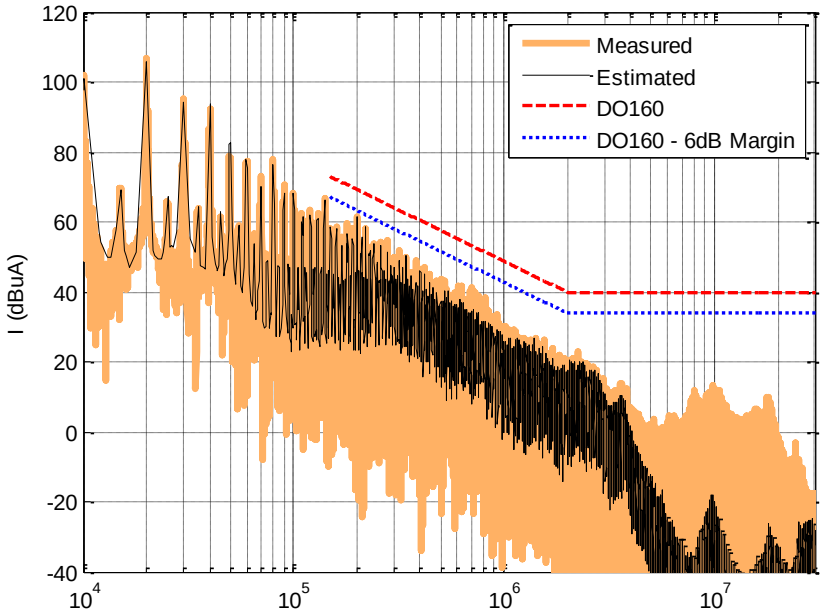

Fig. 5.17: Comparison of estimated and measured output noise current of the input side DM filter

5.4 COMMON-MODEL FILTER DESIGN

The design of CM filter is a little complicated when compared to the DM filter. This is because the CM model of the motor-drive is un-terminated and hence the selection of filter components on one side of the motor drive will affect the CM noise and selection of components on the other side as well. The next sections will describe the method for designing CM filters for motor-drives with an example to validate the proposed method.

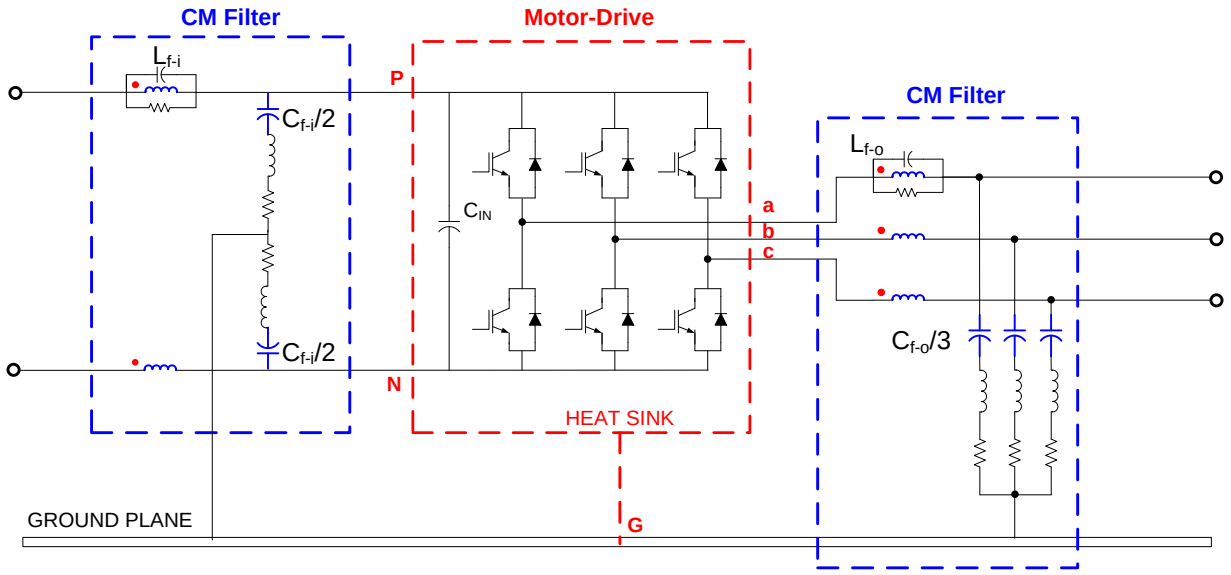

Fig. 5.18: LC filter topologies selected for the input and output side CM filter

5.4.1 Filter Design Procedure

The basic design philosophy remains the same as was shown in the algorithm of Fig. 5.2. The goal is to accommodate the simultaneous design of the input and output side CM filter in the optimization process. Again for simplicity it is assumed that the smallest inductance will give the smallest volume for the magnetics. We start by first selecting a topology for the CM filters as shown in Fig. 5.18. The topology is again restricted to LC filter only. However, unlike the input side DM filter, the input side CM filter has the capacitor facing the motor-drive. This configuration is chosen because the input impedance of the motor drive is very high as it is equal to the impedance of the parasitic capacitance from terminals to ground, which is usually very small. Thus to obtain maximum impedance mismatch, capacitors are chosen to face the drive.

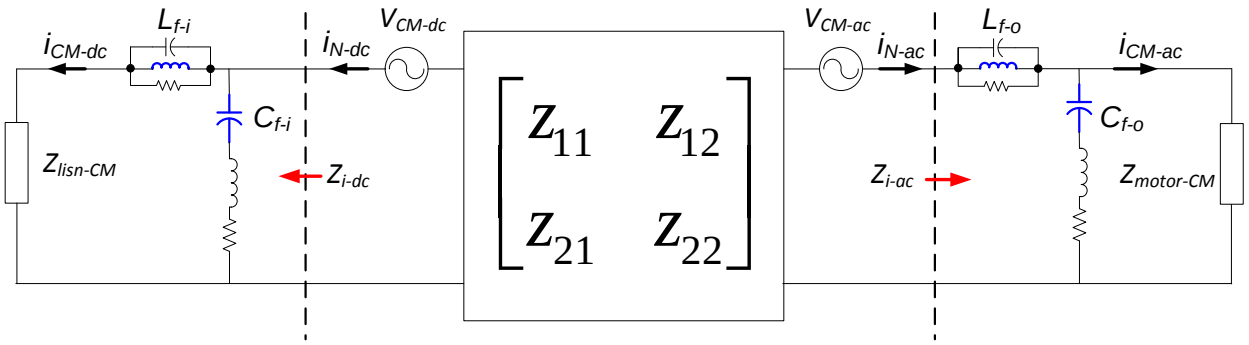

Fig. 5.19: Equivalent circuit model in CM with models of motor-drives and CM filter elements

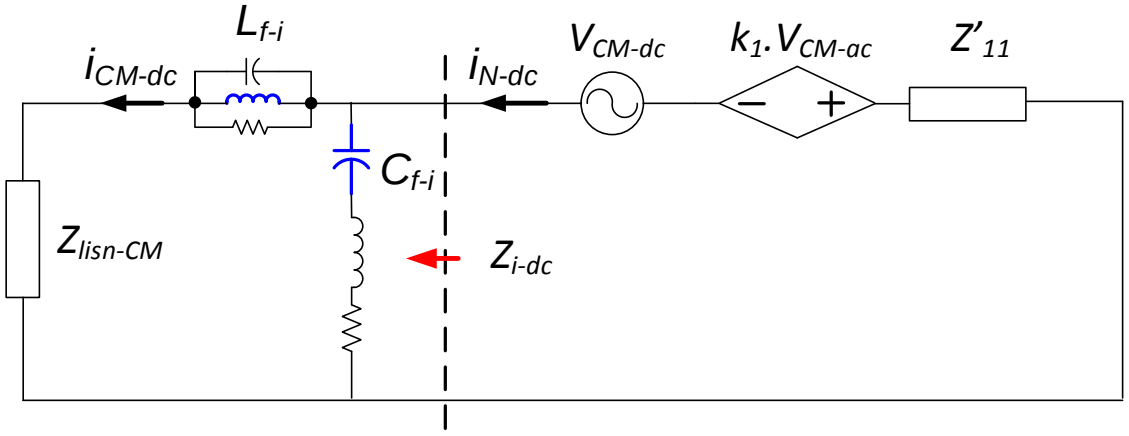

(a)

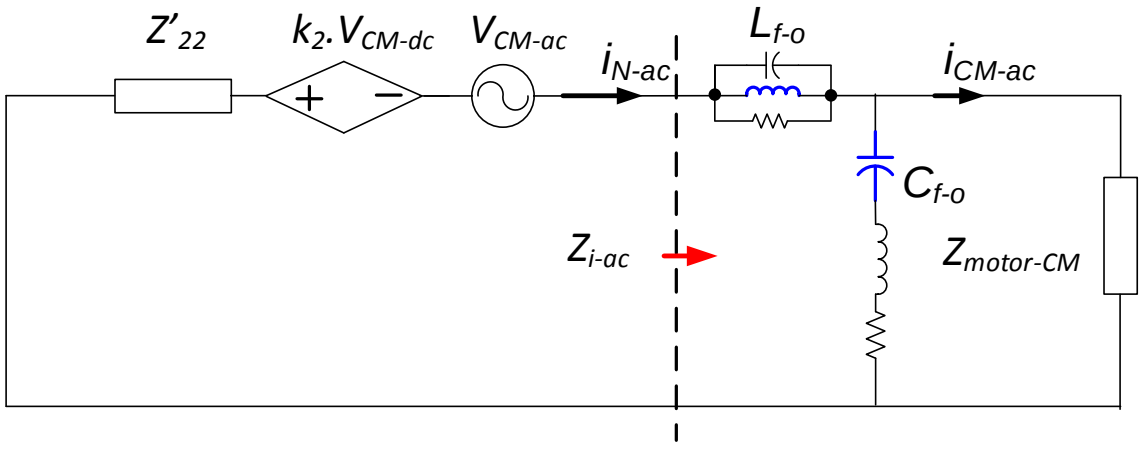

(b)

Fig. 5.20: Coupled terminated CM models obtained from Fig. 5.19. (a) Equivalent CM model for the input side (b) Equivalent CM model for the output side

The output impedance of the motor-drive is large as well but because of high dv/dt there, it is unsafe to have the CM capacitors facing the drive on the output side. Fig. 5.19 shows the equivalent circuit model of the motor-drive and the filters where the motor-drive has been replaced with its un-terminated CM model. Now the model of Fig. 5.19 is divided into two terminated EMI models as shown in Fig. 5.20. The parameters in Fig. 5.20 can be calculated using (3)-(8).

$$k_1 = \frac{z_{12}}{Z_{motor-CM} \parallel Z_{Cf-o} + Z_{Lf-o} + z_{22}} \tag{3}$$

$$k_2 = \frac{z_{21}}{\left(Z_{lisn-CM} + Z_{Lf-i}\right) \parallel Z_{Cf-i} + z_{11}} \tag{4}$$

$$Z'_{11} = z_{11} - \frac{z_{12} \cdot z_{21}}{Z_{motor-CM} + z_{22}} \tag{5}$$

$$Z'_{22} = z_{22} - \frac{z_{12} \cdot z_{21}}{Z_{lisn-CM} + z_{11}} \tag{6}$$

$$i^*_{CM-dc} = \left(v_{N-dc} - k_1 v_{N-ac}\right) \frac{Z_{Cf-i}}{Z'_{11} Z_{Cf-i} + \left(Z'_{11} + Z_{Cf-i}\right)\left(Z_{lisn-CM} + Z^*_{Lf-i}\right)} \tag{7}$$

$$i^*_{CM-ac} = \left(v_{N-ac} - k_2 v_{N-dc}\right) \frac{Z_{Cf-o}}{Z_{motor-CM} Z_{Cf-o} + \left(Z_{motor-CM} + Z_{Cf-o}\right)\left(Z'_{22} + Z^*_{Lf-o}\right)} \tag{8}$$

Following the filter design procedure of Fig. 5.2, a capacitor is chosen for both input and output side. Then using optimization, the minimum inductance is found that will just meet the EMC standards with some margin for design tolerances. The key difference between the DM filter design and the CM filter design is that the objective function must include error in both input ($i_{CM\text{-}dc}$) and output ($i_{CM\text{-}ac}$) side filtered current. This is given in (9)-(11). The error in (11) is what needs to be optimized with $L_{f\text{-}i}$ and $L_{f\text{-}o}$ being the variables in the optimization. The initial solution of the inductance is chosen to be a very small value which would almost always fail the EMC standards. Also note that the EMC standards on the input and output side are different, the

input side being subjected to power line standards and the output side being subjected to cable bundles (See Fig. 1.4).

$$e_{dc}^{+} = \left| i_{CM-dc}^{*} - i_{stad-dc} - i_{mar} \right| \quad \text{and} \quad e_{dc}^{-} = 0 \tag{9}$$

$$e_{ac}^{+} = \left| i_{CM-ac}^{*} - i_{stad-ac} - i_{mar} \right| \quad \text{and} \quad e_{ac}^{-} = 0 \tag{10}$$

$$e = \left(e_{\backslash dc}\right)^2 + \left(e_{ac}\right)^2 \tag{11}$$

Epcos_type_Y2_300V_capacitors.xlsx

	B	C	D	E	F	G	H	I	J	K
1	Sr.	Epcos	C	W	H	L	A	V	ESL	ESR
2	No.	Part Number	uF	mm	mm	mm	cm2	cm3	nH	mΩ
3	1	No Capacitor	0	0	0	0	0	0	0	0
4	2	B32021A3472	0.0047	5.00	11.00	13.00	5.26	0.72	7.2	103.6
5	3	B32022A3103	0.0100	5.00	10.50	18.00	6.63	0.95	7.77	94.16
6	4	B32022A3223	0.0220	6.00	12.00	18.00	7.92	1.30	6.98	65.57
7	5	B32022A3333	0.0330	8.00	14.00	18.00	10.16	2.02	6.38	49.87
8	6	B32022A3473	0.0470	8.50	14.50	18.00	10.75	2.22	5.2	55.17
9	7	B32022A3683	0.0680	9.00	17.50	18.00	12.69	2.84	6.5	46
10	8	B32024A3154	0.1500	11.00	19.00	31.50	23.08	6.58	13.25	49.88
11	9	B32023A3224	0.2200	12.00	22.00	26.50	23.30	7.00	10.27	41.35
12	10	B32024A3334	0.3300	13.50	23.00	31.50	29.21	9.78	14.3	39.1

Sheet1 Sheet2 Sheet3

Fig. 5.21: Catalog of available capacitors for CM filter design

Finemet_type_nanocrystalline_cores.xls [Compatibility Mode]

	A	B	C	D	E	F	G	H	I	J	K	L
1	Sr.	FineMet Cores		OD ± 0.7	H ± 0.7	ID ± 0.7	Volume	Ae	Lm	Weight	AL @ 10KHz	AL @ 100KHz
2	No.	Product code	P/N	(mm)	(mm)	(mm)	(mm^3)	(mm^2)	(mm)	(g)	(μH/N^2)	(μH/N^2)
3	1	F1AH0538	FT-3KM K1208A	13	7.1	6	741.2755	7.7	30.3	2.9	18.2	5.8
4	2	F1AH0692	FT-3KM K1208C	13.5	12.5	6.8	1334.598	13.3	31.7	4.5	24	8.8
5	3	F1AH0654	FT-3KM K1812A	20.2	8.1	10.3	1919.949	11.3	47.1	5.8	14.7	5.3
6	4	F1AH0693	FT-3KM K1912C	21.1	13.3	10	3604.165	24.4	48.9	13	28.2	10.6
7	5	F1AH0971	FT-3KL V1912C	21.1	13.3	10	3604.165	25.4	48.9	13	10.5	11.1
8	6	F1AH0695	FT-3KM K2214B	24.2	10.6	12	3674.886	22.2	56.5	13	22.2	8.1
9	7	F1AH0694	FT-3KM K2313D	25.2	15.1	11.5	5959.821	43.9	57.3	23	41.6	15.3
10	8	F1AH0696	FT-3KM K2515D	27.2	15.6	13	6990.507	46.3	62.8	26	41.6	15.3
11	9	F1AH0702	FT-3KM N2515D	27.6	16	12.6	7573.68	46.9	62.8	28	41.6	15.3
12	10	F1AH0697	FT-3KM K2818E	30.4	18	15.8	9530.968	55.5	72.3	37	43.4	15.9
13	11	F1AH0703	FT-3KM N3320E	35.6	19	17.4	14387.01	73.1	73.3	56	49.7	19.9
14	12	F1AH0699	FT-3KM K3819D	40.4	15.5	16.8	16425.15	87.9	89.5	68	55.5	20.4
15	13	F1AH0700	FT-3KM K3824G	40.6	23	21.4	21492.67	105	97.4	87	61	24.4
16	14	F1AH0704	FT-3KM N4225E	46	19	21	24982.63	95.6	105.2	95	51.4	20.6
17	15	F1AH0705	FT-3KM N5034E	54	19	30	30068.64	90	131.9	110	38.6	15.4
18	16	F1AH0701	FT-3KM K5328E	56.4	19	24.6	38418.06	127.5	114.7	155	62.5	25
19	17	F1AH0706	FT-3KM N6442E	68	19	38	47429.7	123.8	166.5	184	42	16.8
20	18	F1AH0708	FT-3KM N5434G	58	25	30	48356	150	138	210	61.4	24.5

CM_Core_Data_1phase

Fig. 5.22: Catalog of available no-crystalline cores for CM filter design

Like in the case of the DM filter design, a catalog is created for the capacitors and inductors. The capacitors are of the type Y2 300V metal-film capacitors from EPCOS [105]. The cores for designing CM chokes are nano-crystalline cores from Hitachi-metals [100]. The snapshot of the selected capacitors and cores is shown in Fig. 5.21 and Fig. 5.22 respectively. Note that in the capacitors catalog, the first choice is no capacitor. This is done to include just an L filter as a design option as well. Also note that, just like in case DM filter design, the second order effects are taken into consideration for CM filters as well. Now let's look at an example for CM filter design using the proposed method.

5.4.2 Example: Input-Output CM filter Design

The design equations in the previous section are written in a MATLAB script and the procedure is run for a few values of the capacitor. Note that since we have 10 options for the capacitances the total combinations are 100 accounting for both the input and output side. This makes the calculation algorithm slow so calculations were only conducted for a only small range of capacitances. The capacitors to ground are almost always restricted to smaller sizes because of the associated safety issues, thus the algorithm is run only for the two options of input capacitor (0.0047 µF and 0.01 µF), three options of output capacitors (0.0 µF, 0.0047 µF and 0.01 µF) and one option for the nano-crystalline core (Sr. No. 13 in Fig. 5.22). The final design results are shown in Fig. 5.23. From Fig. 5.23, it can be seen that by selecting the 0.0047 µF capacitor on the input side and no capacitor on the output side, the smallest volume can be obtained within the possible combinations.

CM_filter_design.csv

	A	B	C	D	E	F	G	H	I	J	K	L	M
1	Cap-i	Cap-o	Core-i	Core-o	i/p Cap(uF)	o/p Cap(uF)	i/p Ind(uH)	o/p Ind(uH)	i/p Turns	o/p Turns	i/p Tmax(C)	o/p Tmax(C)	Vol(cubic cm)
2	2	1	13	13	0.0047	0	4941	4941	9	9	48.3922	66.9227	44.4253
3	2	2	13	13	0.0047	0.0047	26901	4941	21	9	63.1266	22.7886	46.5853
4	2	3	13	13	0.0047	0.01	32269	4941	23	9	65.9597	30.024	47.2753
5	3	1	13	13	0.01	0	1525	4941	5	9	51.2248	47.1204	44.8853
6	3	2	13	13	0.01	0.0047	15616	4941	16	9	66.5542	15.457	47.0453
7	3	3	13	13	0.01	0.01	19764	4941	18	9	57.6086	21.9655	47.7353

CM_filter_design

Fig. 5.23: Filter options possible for CM filter with the available capacitors and cores

The design performance is then evaluated by putting the filter together and testing it in the experimental standards. The comparison of estimated and measured input noise currents ($i_{N\text{-}dc}$ & $i_{N\text{-}ac}$) on the input and output side of the motor-drive are shown in Fig. 5.24 and Fig. 5.25

respectively. The comparison of estimated and measured filtered currents on the input and output side of the motor-drive are shown in Fig. 5.26 and Fig. 5.27 respectively.

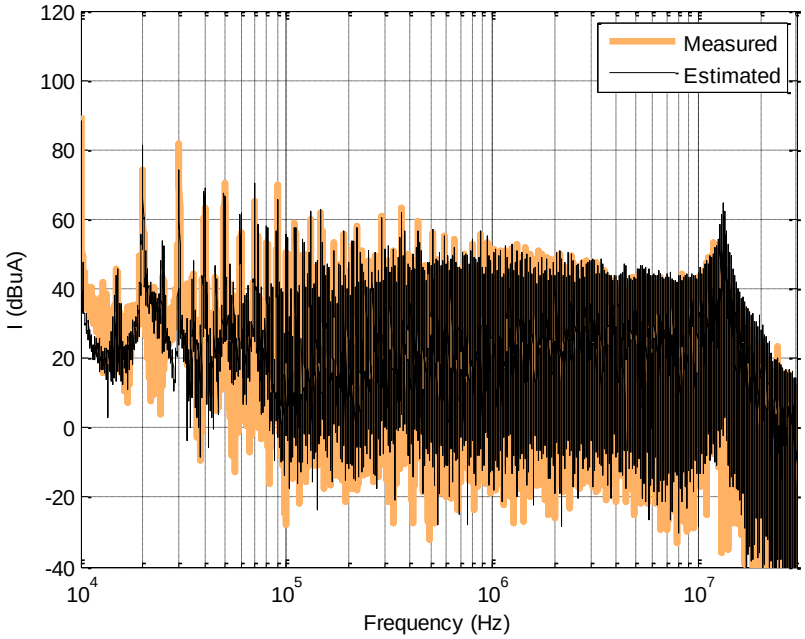

Fig. 5.24: Comparison of estimated and measured input noise current of the input side CM filter

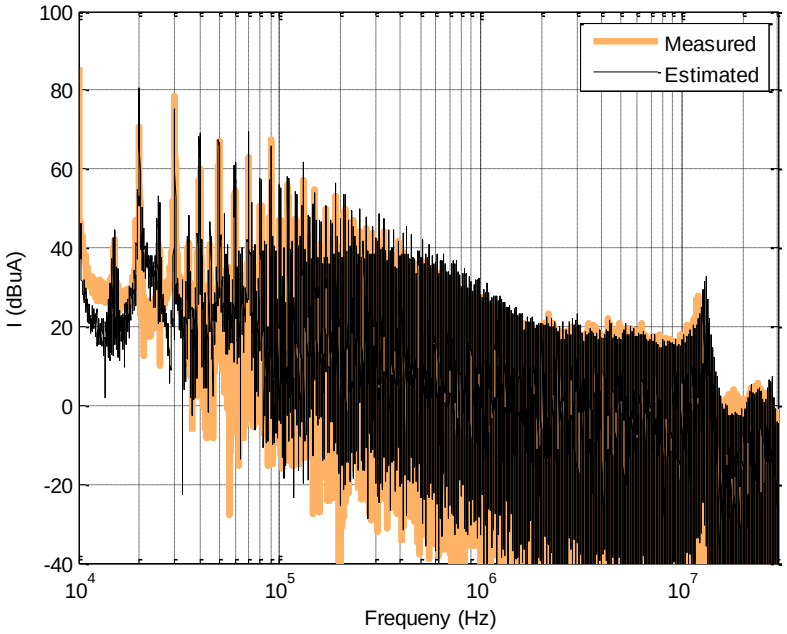

Fig. 5.25: Comparison of estimated and measured input noise current of the output side CM filter

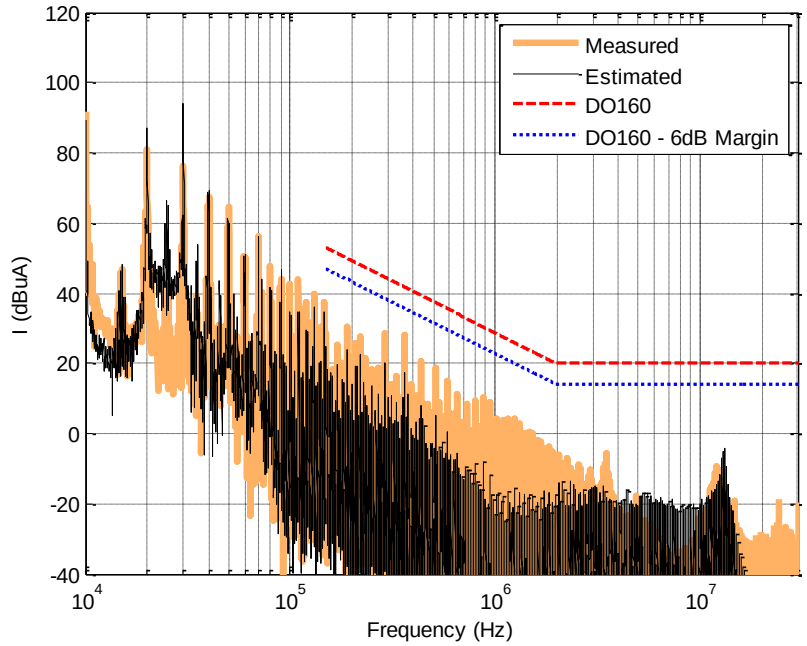

Fig. 5.26: Comparison of estimated and measured filtered noise current of the input side CM filter

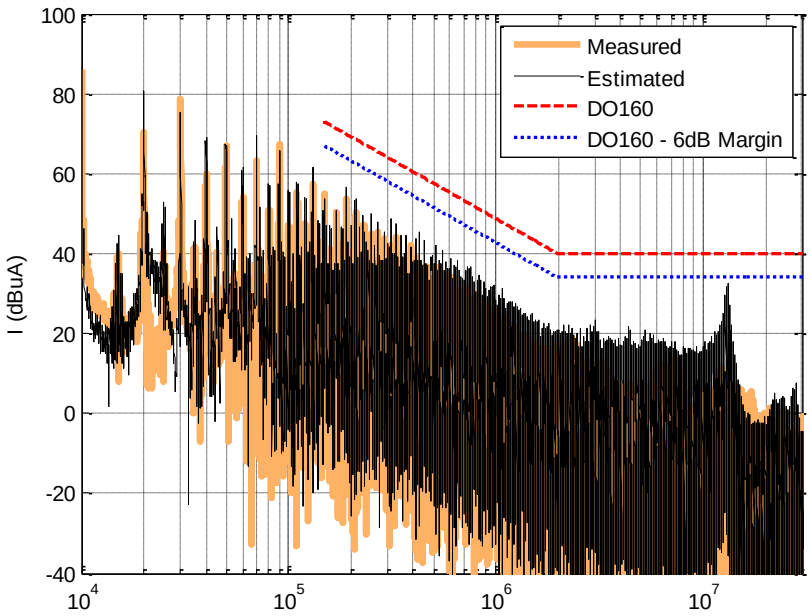

Fig. 5.27: Comparison of estimated and measured filtered noise current of the output side CM filter

The accuracy of estimation for the input noise currents is quite good in the entire EMI range. However from Fig. 5.256 and Fig. 5.27, it can be seen that the estimation accuracy is not so good

and this again comes from the limitation in the filter's model itself. It is evident from Fig. 5.27 that the algorithm is very versatile in designing EMI filters as the estimation shows a strong resonance at around 12 MHz and the algorithm adjusted the values of the inductances to make sure that this resonances stay below the standards with a 6dB margin. The over-estimation of this resonance however did lead to a slight overdesign of the CM chokes but since only one choice for the inductor core was included this design is accepted as it.

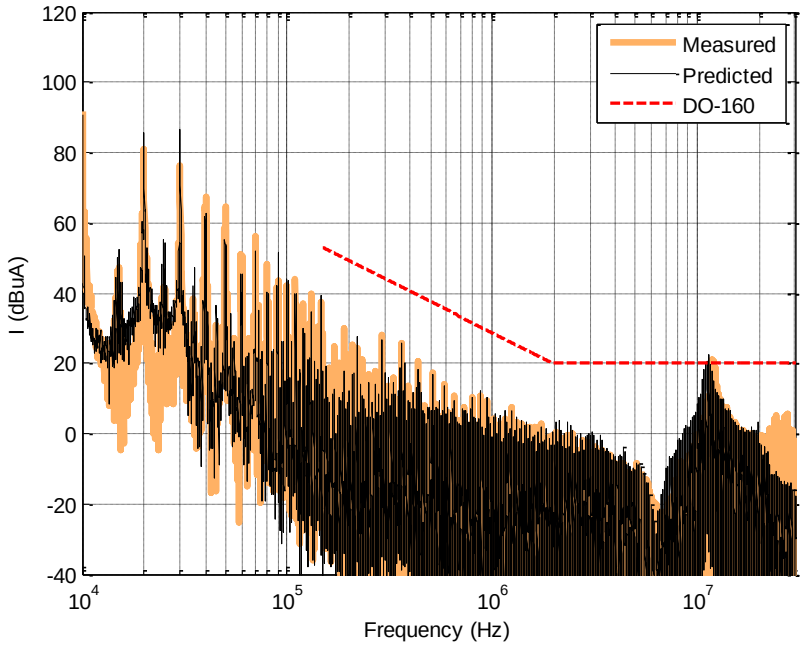

Fig. 5.28: Comparison of measured and estimated filtered noise current of the input side CM filter after using the measured transfer-function

5.4.3 Prediction Accuracy

The design examples shown earlier may raise suspicion that the inaccuracy in the prediction of the filtered current can also be coming from the terminal models and not just from the limitations of the filter models. In order to show that the poor accuracy in some results is only due to poor estimation of the filter model, it was decided to measure the transfer function and use that to predict the filtered current. Since one such example has already been covered in the case of the DM filter, this section shows the prediction accuracy of the CM un-terminated EMI models if an accurate transfer function of the filter was available for use. Let's take the input side CM filter that was designed in the previous section. In order to make sure that the high frequency

noise stays above the noise floor of the oscilloscope, an extra 47 pF capacitors were put in parallel with each winding of the input side CM choke. This will reduce the attenuation at a higher frequency leading to an amplification of EMI noise. Fig. 5.28 shows the comparison of measured and predicted filtered noise ($i_{CM\text{-}dc}$) from the measured transfer function. It can be seen that the un-terminated model is able to predict the noise well up to 20 MHz if an accurate transfer function of the filter is available. This conclusively proves that the terminal models are very accurate but the filter models can limit the accuracy of prediction of filtered currents.

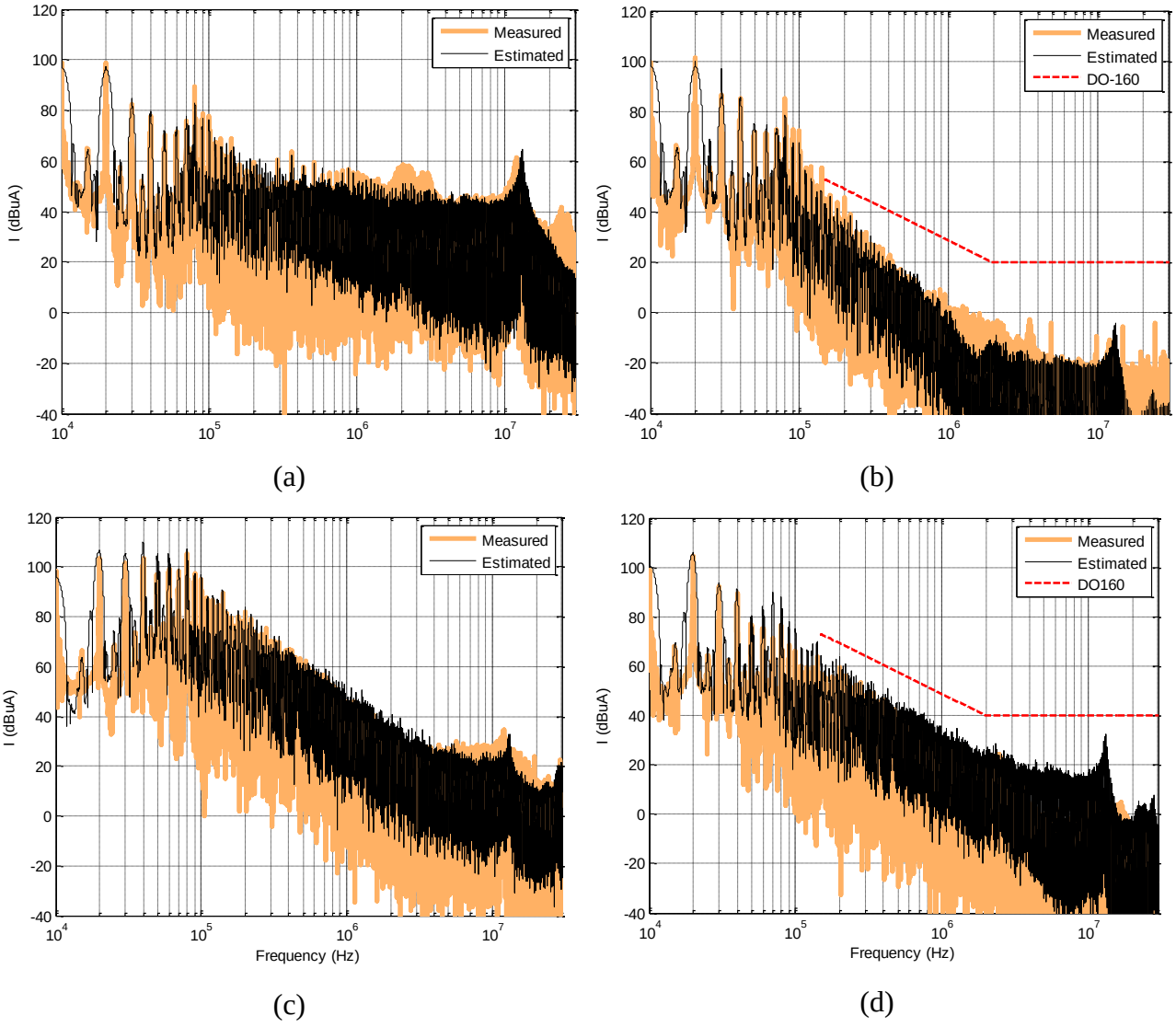

Fig. 5.29: Comparison of estimated and measured total noise current with both DM and CM filters. (a) Input noise currents at the input side. (b) Filtered noise currents at the input side. (c) Input noise currents at the output side. (d) Filtered noise currents at the output side.

5.5 COMPLETE INPUT-OUTPUT FILTER

With the design of both DM and CM filters complete, they can all be put together to see their impact on the total noise. The EMC standards of DO-160 are based on total noise and hence for meeting EMC compliance both DM and CM filters are necessary. Fig. 5.29 shows the comparison of estimated and measured total noise at both the input and output side of the motor drive. From Fig. 5.29 (b) and (d), it can be seen that when all the filters are put together, the total EMI noise will meet the DO-160 standards. This completes the filter design process.

5.6 IMPORTANCE OF ACHIEVING HIGH FREQUENCY ACCURACY

With the codes working for the EMI filters, it is now possible to understand the importance of a good high frequency EMI model of the power converter. Many engineers design EMI filters by considering only the low frequency requirements, the argument being that the size of the EMI filter is determined by the spectrum near the switching frequency, so why look in the high frequency at all? We now use an example to show the potential pitfalls of using only the low frequency approximations for designing EMI filters.

Let's design a LC DM filter for the input side, similar to the one designed in section 5.3.2, where the filter capacitance is 10 μF. Now like in [77], the LISN impedance is assumed to be 100 Ω and the DM converter (source) impedance is assumed to be very small or 0 Ω. With these approximations, the algorithm for the design of DM filter is run with C_f = 10 μF and a 6 dB margin. The resulting filter inductance was found to be 622.5 μH and the total filter volume was found to be 44.32 cm^3. The predicted filtered DM current is shown in Fig. 5.30.

For the same filter capacitance, the actual impedance of the LISN and the source is used and the filter design procedure is run again with a 6 dB margin. This time the algorithm narrows down on a filter inductance of value 351.9 μH and a volume of 41.74 cm^3 (see last column in Fig. 5.7). The predicted filtered DM current for this filter is also shown in Fig. 5.30.

It can be seen that both designs clearly satisfy the DO-160 margin, but the filter design with actual load and source impedances is smaller than the one designed with ideal load and source impedance. Thus it is important to consider the actual load and source impedance for the entire EMI range rather than approximations when it comes to design of EMI filters. The size difference is not large but the merits of using an accurate high frequency model of the power converter such as the behavioral EMI model are readily apparent. Such models can help in

designing very precise EMI filters and evaluating their performance up to 30 MHz, thereby avoiding design iterations.

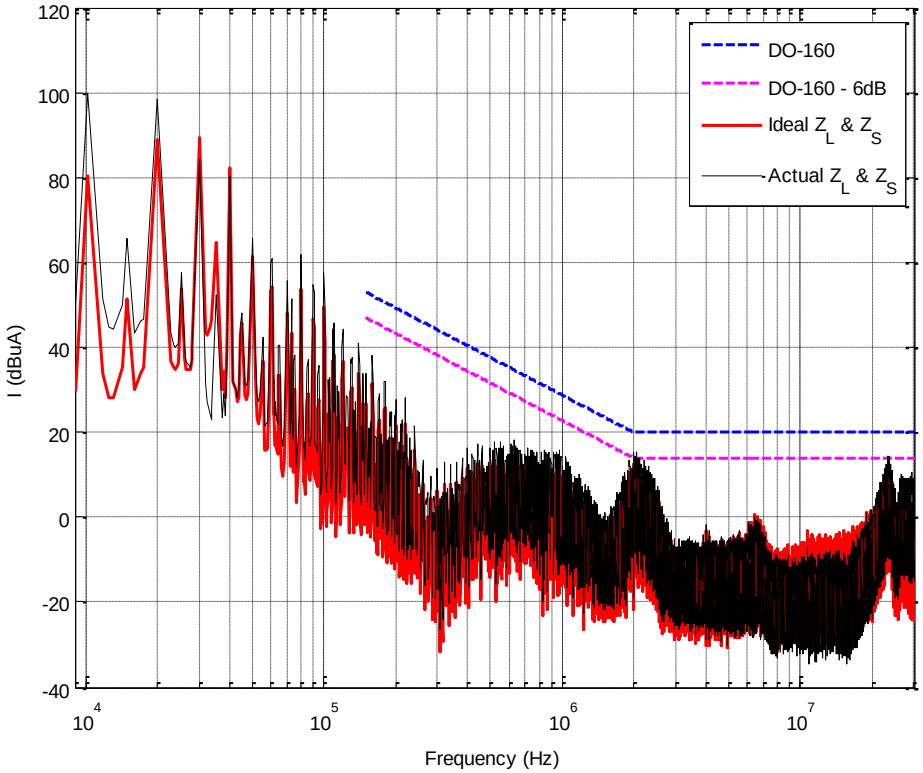

Fig. 5.30: Predicted filtered DM current for two input DM filters designed using ideal and actual load and source impedance

5.7 CONCLUSIONS

This chapter showed an application of EMI terminal models. The experimental validations provided here proves that the EMI terminal models can be very useful in testing EMC compliance of the motor-drive and can be used to design EMI filters with relatively good accuracy and no design iterations. The inaccuracy in estimating the filter's parasitic and coupling can limit the validity of the design but the procedure described here can still be used for a good first design. The algorithms themselves are reconfigurable, that is if better estimations of filter models are available. They can simply be included in the transfer-function and its ready to go. The process of finding the correct filter components is quite versatile and the optimization procedure introduced here can take care of all the peaks seen the EMI range simultaneously.

Most importantly, this design procedure gives the tightest design possible for a give source and load impedance and it inherently imposes the adequate impedance mismatch in the entire EMI range.

6 SUMMARY & FUTURE WORK

The work presented in this dissertation in general shows the wide applicability of behavioral modeling techniques for modeling EMI in power converters. It has been shown, both using simulations and experiments that behavioral EMI models can accurately capture the high frequency behavior of the power converters and are easy to simulate when compared to the lumped-circuit models. Such models can facilitate faster simulations and rapid iterations of EMI design at the system level.

6.1 SUMMARY

This dissertation has made significant improvements over the existing behavioral EMI modeling techniques. The following are the specific contributions of this dissertation:

- The "*terminated*" EMI-behavioral-modeling technique developed in [59, 60] was tested experimentally for several different power converters and in both dc and ac operations to show the generality of its application. The issue of negative real parts of the model impedances was reported and investigated in detail.
- It was shown using simulations of simplified switched-resistance topologies that the behavioral modeling technique will in general fail for time-variant circuits but can give something usable as long as the internal switched-resistance is insignificant compared to all other impedances in the system.
- An "*un-terminated*" behavioral EMI modeling technique was developed for CM noise in a motor-drive system using a two-port linear network and two noise-sources. The model was validated extensively using experiments and was shown to be accurate up to 30 MHz at most frequencies. This contribution is the most important extension made over the previous work.
- The limitation of the previous work involving frequency-domain noise in the identified model impedances was solved by first making an initial estimate using high-S/N impedance measurements, followed by numerical optimization. This gives physical meaning (no negative real parts) to the impedances and makes it possible to simulate them in a circuit simulator.

- The limitation of the previous work that required phase-synchronized measurements was overcome as well. It was shown that using numerical optimization, snapshots of EMI taken arbitrary in time and under different conditions can be combined to correctly identify both magnitude and phase of the model parameters.
- An EMI-filter design technique was developed using the behavioral EMI models and example filters were built for both input and output side of the motor-drive to show the effectiveness of the proposed technique. The filters were experimentally shown to satisfy the DO-160 conducted emissions standards.
- Numerical optimization was used again to ensure that the filter design technique is not limited to specific load or source conditions. This effort also led to identification of limitations involving prediction of electromagnetic behavior of the filter components.

The work helped in the identification of several directions for future research and also some limitations. These will be discussed in the following sections.

6.2 LIMITATION

An important limitation of the un-terminated modeling can be its application to asymmetric topologies. This limitation is in fact quite fundamental in nature. If the topologies are asymmetric, there is a chance that it will appear time-variant at its terminals. It has already been shown in chapter 2 that for time-variant circuits, the technique of terminal modeling in general fails. Let us try to work out an example using simulations to see if how does the un-terminated modeling technique fair when applied to asymmetric topologies.

The simulation model chosen was of the half-bridge inverter in Chapter 3, Fig. 3.7. The bottom dc-link capacitor was short circuit and modulation was changed for it to behave like a buck-converter. The A procedure, which is very similar to the one developed in section 4.1 was used here and the noise-model is so that the CM will stay exactly the same. This is obvious as the two-port linear model chosen for the CM is very generic and independent of the topology of the converter. The shunt impedance used on the input side was a 2 Ω resistance with a 2uF capacitor to the ground and at the output side a 1 Ω resistance with 2uF capacitor to ground. The series impedance used on both the input and output side was a 30 mH choke. Three cases were run, series impedances on both sides, shunt impedances on both sides and shunt and series impedance

on input and output side respectively. Since in simulations there is no issue of synchronized measurements, the equations of the system under three different conditions can be directly solved simultaneously to extract the model parameters. Fig. 6.1 shows the extracted model impedances and Fig. 6.2 shows the model noise sources for the buck converter.

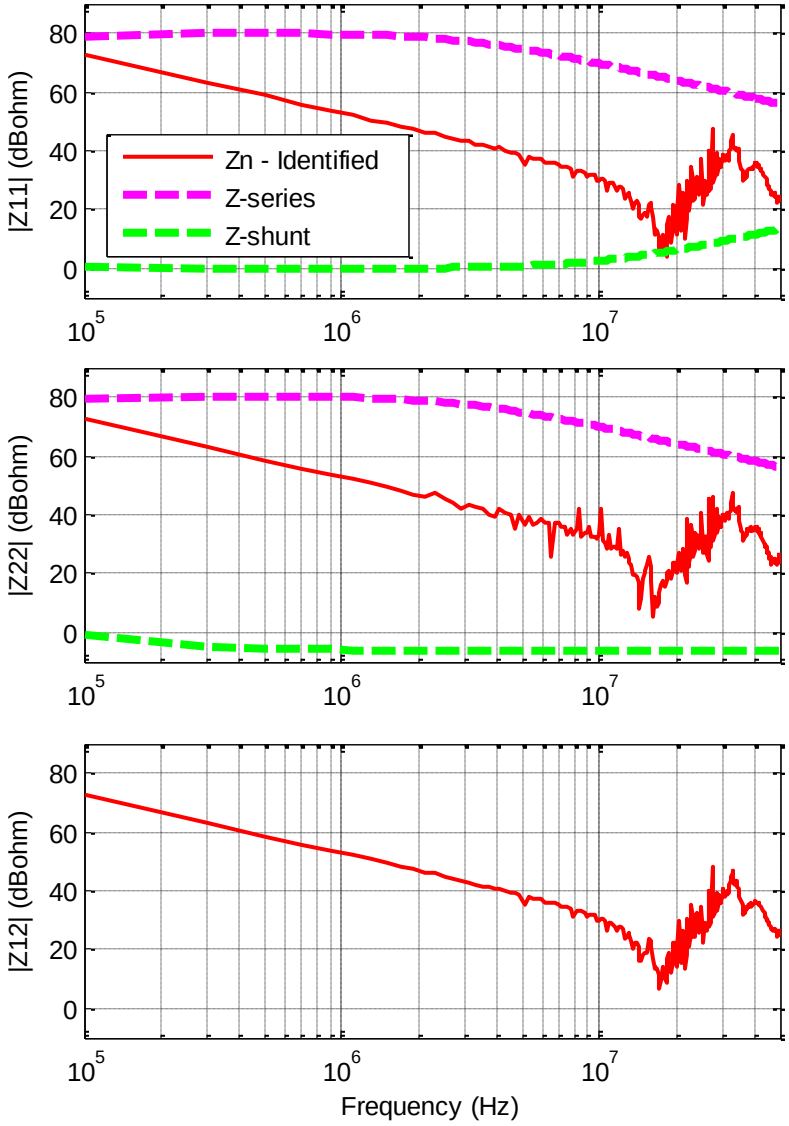

Fig. 6.1: Identified impedance of the un-terminated CM model of the buck converter

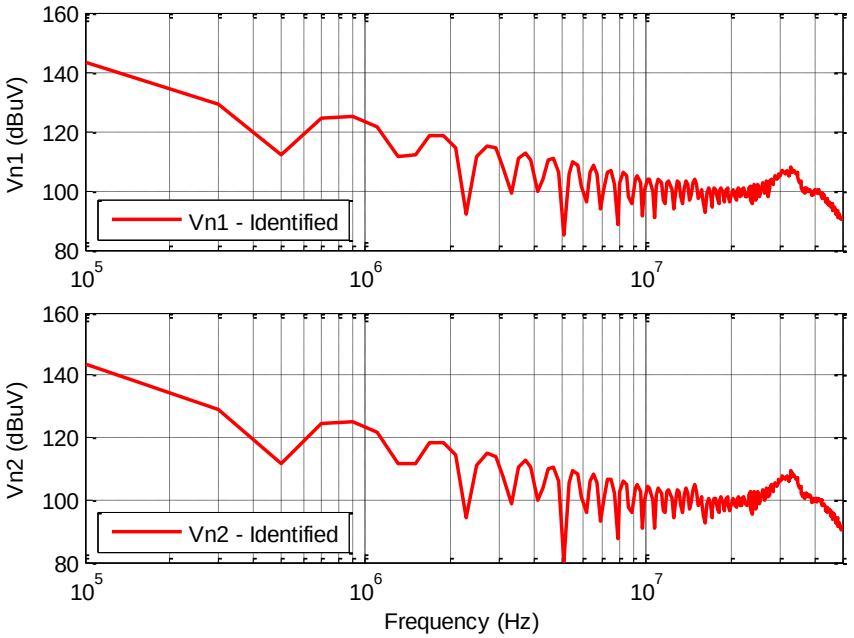

Fig. 6.2: Identified noise-voltage sources for un-terminated CM model of buck converter

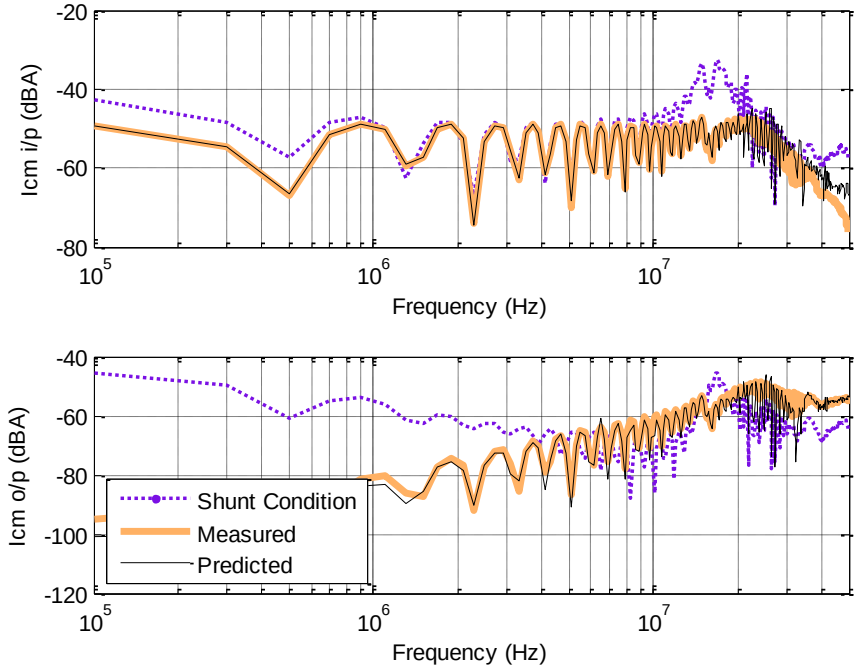

Fig. 6.3: Validation of un-terminated CM model of the buck converter in the nominal condition

From Fig. 6.1, the CM capacitances from the heat sink to the ground in the simulation model can be clearly seen in the impedance matrix of the un-terminated model Fig. 6.1. The model was

now validated for the nominal condition, which is a 50 Ω LISN on the input side and a 50 Ω load on the output side. The comparison of simulated results for nominal condition and predicted results from the un-terminated EMI model are shown in Fig. 6.3.

It can be seen from Fig. 6.3 that until 20 MHz, the model is able to correctly predict the input and output side CM noise currents. Beyond that there is a mismatch in the simulated and predicted results. Note that the issue of S/N ratio is not so significant here as there are no real measurements involved and everything is simulated. Let's look at the transfer impedance (Z_{12}) in the two states of the buck converter. The first state is when the switch is "ON" and the Diode is "OFF" and the second state is when the switch is "OFF" and the diode is "ON". The Z_{12} is calculated by first replacing the IGBT and the diode with an equivalent RC model that represents their impedance in any given state. The goal here is to identify the possible issue and hence this approximation should give enough insight. The simulated Z_{12} in the two states are shown in Fig. 6.4.

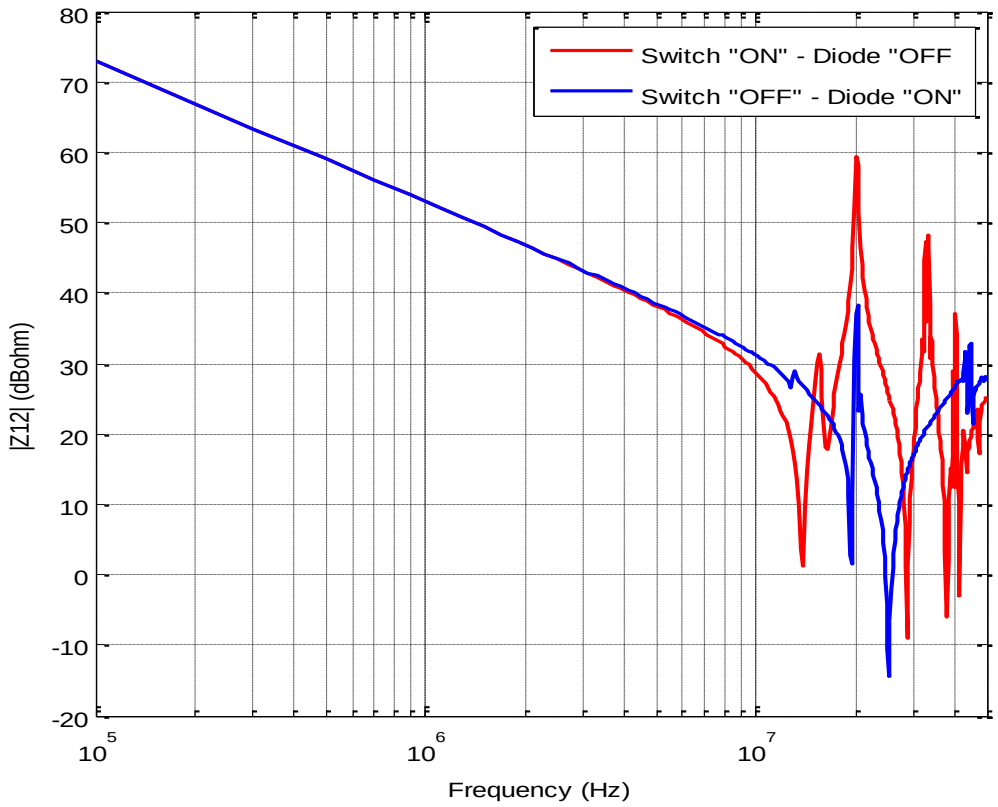

Fig. 6.4: Approximated transfer impedance of the buck converter in the CM for the two states of the switches

It can be seen here that at high frequency multiple resonances are seen and they occur at different frequencies in the two cases. Comparing Fig. 6.4 and Fig. 6.1 is can be seen that the resonances in the extracted model impedance do not match with any of two cases. Thus there is a possibility that the system is appearing time-variant at high frequencies and hence the model is not able to predict the correct CM noise in the nominal conditions. It is difficult to comment upon what is the true impedance of the system while the system is switching from one state to another. This third state is not discussed here and the analysis was made only on the basis of two distinct states that exist before and after the switching has taken place.

6.3 FUTURE WORK

The following provides some direction for future research that can be pursued:

6.3.1 System-Level EMI Modeling

The behavioral modeling technique is mature enough to be tried for predicting EMI when multiple power converters are connected in parallel or cascade within a power distribution network. No standards exist currently for system level EMI but it could be very useful for system level design engineers to conduct global optimization of EMI solutions. The research can begin by looking at two simple power converters connected in parallel to the same dc-bus and then their terminated behavioral models are used to predict the worst case conducted EMI on the bus. Another side direction that could be pursued is to combine the behavioral EMI models developed here with the EMI models based on double-Fourier integrals [76]. The double-Fourier integral method gives better accuracy at switching frequencies and its first few harmonics that are easily influenced by the operation point or the modulation index. However such models are only accurate up to a couple of MHz, so finding a way to combine them with behavioral EMI models can lead to a unified model that is not only accurate at higher frequencies but can also predict the low frequency noise due to changes in the operating point.

6.3.2 Filter-Design with Improved Models

It was shown in chapter 5 that although a systematic algorithm for EMI filter design can be made, the limitations in the filter model due to difficulty in estimating the coupling between filter elements and lack of methods to estimate high frequency resonances of the inductors, limits the design accuracy of the filter. Inaccurate estimation of resonances may lead to design iteration.

Thus simplified “predictive” models of the EMI filters that are adequately accurate for designing EMI filters are needed. Note that being predictive is the key because once the filter is built, the user can simply measure its parameters and if the filter fails then design iterations will be needed regardless, which is what we were trying to avoid in the first place.

6.3.3 EMI Models for Asymmetric Topologies

As discussed in section 6.2 of this chapter, there is a need to further investigate the applicability of behavioral modeling techniques to asymmetric converter topologies. This research can help in creating more generalized understanding of the applicability of the method itself. Although dc-dc converters for point-of-load-applications may not even require an un-terminated model, they can be taken as the first test case to research this further. The issue of mixed-mode noise also needs to be investigated, as for asymmetric converters the prediction of total noise by adding the magnitude of CM and DM noise may not be accurate at higher frequencies.

REFERENCES

[1] M. A. Briere. (2008) GaN Based Power Devices: Cost-Effective Revolutionary Performance. *Power Electronics Europe*. Available: http://www.power-mag.com/pdf/issuearchive/16.pdf

[2] H. W. Ott, *Electromagnetic Compatibility Engineering*, 1 ed.: John Wiley & Sons, 2009.

[3] A. A. AbdElhafez and A. J. Forsyth, "A Review of More-Electric Aircraft," presented at the 13th International Conference on Aerospace Sciences & Aviation Technology, ASAT- 13, Cairo, Egypt, 2009.

[4] *Boeing 787 from the Ground Up, Quaterly review 2006: Aeromagzine*. Available: http://www.boeing.com/commercial/aeromagazine/articles/qtr_4_06/AERO_Q406.pdf

[5] *Electrical Thrust Reverser Actuation System (ETRAS®), A World First*. Available: http://www.hispano-suiza-sa.com/IMG/pdf/BROCHURE_VUS_FINAL-2.pdf

[6] X. Roboam, "New trends and challenges of electrical networks embedded in "more electrical aircraft"," in *Industrial Electronics (ISIE), 2011 IEEE International Symposium on*, 2011, pp. 26-31.

[7] C. R. Paul, *Introduction to Electromagnetic Compatibility*, 2 ed. New York,NY: John Wiley & Sons, 2006.

[8] Z. Dongbing, C. Dan, and D. Sable, "Non-intrinsic differential mode noise caused by ground current in an off-line power supply," in *Proc. IEEE Power Electron. Spec. Conf.*, 1998, pp. 1131-1133 vol.2.

[9] J. Meng and W. Ma, "A new technique for modeling and analysis of mixed-mode conducted EMI noise," *IEEE Trans. Power Electron.*, vol. 19, pp. 1679-1687, 2004.

[10] J. R. Regue, M. Ribo, D. Duran, D. Badia, and A. Perez, "Common and differential mode characterization of EMI power-line filters from S-parameters measurements," in *Proc. IEEE Int. Symp. Electromagn. Compat.*, 2004, pp. 610-615 vol.2.

[11] G. Ting, D. Y. Chen, and F. C. Lee, "Separation of the common-mode- and differential-mode-conducted EMI noise," *IEEE Trans. Power Electron.*, vol. 11, pp. 480-488, 1996.

[12] CISPR22, *Information technology equipment – Radio disturbance characteristics – Limits and methods of measurement*, 6 ed.: International Electrotechnical Commission, 2008-09.

[13] MIL-STD-461F, *Requirement for the Control of Electromagnetic Interference Characteristics of Subsystems and Equipment*, 6 ed.: US Department of Defense, 2007.

[14] DO-160G, *Environmental Conditions and Test Procedures for Airborne Equipment*, 7 ed.: Radio Technical Commission for Aeronautics, 2010.

[15] J. Roudet, E. Clavel, and J. L. Schanen, "A very useful CAD tool for designing packaging of integrated power converter," in *Integrated Power Packaging, 1998. IWIPP. Proceedings., IEEE International Workshop on*, 1998, pp. 18-22.

[16] A. C. Baisden, D. Boroyevich, and J. D. van Wyk, "High Frequency Modeling of a Converter with an RF-EMI Filter," in *Industry Applications Conference, 2006. 41st IAS Annual Meeting. Conference Record of the 2006 IEEE*, 2006, pp. 2290-2295.

[17] Z. Huibin, L. Jih-Sheng, A. R. Hefner, Jr., T. Yuqing, and C. Chingchi, "Analysis of conducted EMI emissions from PWM inverter based on empirical models and comparative experiments," in *Proc. IEEE Power Electron. Spec. Conf.*, 1999, pp. 861-867 vol.2.

[18] M. Moreau, N. Idir, and P. Le Moigne, "Modeling of Conducted EMI in Adjustable Speed Drives," *IEEE Trans. Electromagn. Compat.*, vol. 51, pp. 665-672, 2009.

[19] L. Qian, "Modular Approach for Characterizing and Modeling Conducted EMI Emissions in Power Converters " PhD Dissertation, Electrical and Computer Engineering, Virginia Tech, Blacksburg, 2005.

[20] L. Ran, S. Gokani, J. Clare, K. J. Bradley, and C. Christopoulos, "Conducted electromagnetic emissions in induction motor-drive systems. I. Time domain analysis and identification of dominant modes," *IEEE Trans. Power Electron.*, vol. 13, pp. 757-767, 1998.

[21] L. Ran, S. Gokani, J. Clare, K. J. Bradley, and C. Christopoulos, "Conducted electromagnetic emissions in induction motor-drive systems. II. Frequency domain models," *IEEE Trans. Power Electron.*, vol. 13, pp. 768-776, 1998.

[22] P. Xuejun, Z. Kai, K. Yong, and C. Jian, "Analytical estimation of common mode conducted EMI in PWM inverter," in *Conf. Rec. IEEE IAS Annu. Meeting*, 2004, pp. 2651-2656 vol.4.

[23] F. Giezendanner, J. Biela, J. W. Kolar, and S. Zudrell-Koch, "EMI Noise Prediction for Electronic Ballasts," *IEEE Trans. Power Electron.*, vol. 25, pp. 2133-2141, 2010.

[24] E. Hoene, W. John, M. Michel, and H. Reichl, "Evaluation and Prediction of Conducted Electromagnetic Interference Generated by High Power Density Inverters," in *Power Electronics and Applications (EPE 2001), Proceedings of the 9th European Conference on*, Graz, Austria, 2001, pp. P.1-P.9.

[25] M. Moreau, N. Idir, P. Le Moigne, and J. J. Franchaud, "Utilization of a behavioural model of motor-drive systems to predict the conducted emissions," in *Power Electronics Specialists Conference, 2008. PESC 2008. IEEE*, 2008, pp. 4387-4391.

[26] D. Labrousse, B. Revol, and F. Costa, "Common-Mode Modeling of the Association of N -Switching Cells: Application to an Electric-Vehicle-Drive System," *IEEE Trans. Power Electron.*, vol. 25, pp. 2852-2859, 2010.

[27] J. Kotny and N. Idir, "Time domain models of the EMI sources in the variable speed drives," in *Energy Conversion Congress and Exposition (ECCE), 2010 IEEE*, 2010, pp. 1355-1360.

[28] B. Revol, J. Roudet, J. L. Schanen, and P. Loizelet, "EMI Study of Three-Phase Inverter-Fed Motor-drives," *IEEE Trans. Ind. Appl.*, vol. 47, pp. 223-231, 2011.

[29] J. Meng and W. Ma, "Power Converter EMI Analysis Including IGBT Nonlinear Switching Transient Model," *IEEE Trans. Ind. Electron.*, vol. 53, pp. 1577-1583, 2006.

[30] Q. Tao, J. Graham, and S. Jian, "Characterization of IGBT modules for system EMI simulation," in *IEEE Appl. Power Electron. Conf. Expo.*, 2010, pp. 2220-2225.

[31] X. Lei, F. Feng, and S. Jian, "Behavioral modeling methods for motor-drive system EMI design optimization," in *Proc. IEEE ECCE*, 2010, pp. 947-954.

[32] C. Henglin, F. Limin, C. Wei, and Q. Zhaoming, "Modeling and measurement of the impedance of common mode noise source of switching converters," in *IEEE Appl. Power Electron. Conf. Expo.*, 2006, p. 4 pp.

[33] Y. Koyama, M. Tanaka, and H. Akagi, "Modeling and Analysis for Simulation of Common-Mode Noises Produced by an Inverter-Driven Air Conditioner," *IEEE Trans. Ind. Appl.*, vol. 47, pp. 2166-2174, 2011.

[34] B. Toure, J. L. Schanen, L. Gerbaud, T. Meynard, and J. P. Carayon, "EMC modeling of drives for aircraft applications: Modeling process, EMI filter optimization and

technological choice," in *Energy Conversion Congress and Exposition (ECCE), 2011 IEEE*, 2011, pp. 1909-1916.

[35] H. A. Haus, W. R. Atkinson, G. M. Branch, W. B. Davenport, W. H. Fonger, W. A. Harris, *et al.*, "Representation of Noise in Linear Twoports," *Proc. IRE,* vol. 48, pp. 69-74, 1960.

[36] M. F. Moad, "Two-port networks with independent sources," *Proc. IEEE,* vol. 54, pp. 1008-1009, 1966.

[37] M. Hosoya. (2000) The Simplest Equivalent Circuit of a Multi-Terminal Network. *Bulletin of the College of Science - Univ. Ryukyus*. 1-10.

[38] M. Hosoya. (2001) The Straightforward Expansion of Helmholtz-Thevenin Theorem to Multi-Terminal Networks. *Bulletin of the College of Science - Univ. Ryukyus*. 39-45.

[39] F. F. Judd and P. M. Chirlian, "The Application of the Compensation Theorem in the Proof of Thevenin's and Norton's Theorems," *IEEE Trans. Educ.,* vol. 13, pp. 87-88, 1970.

[40] M. F. Moad, "On Thevenin's and Norton's Equivalent Circuits," *IEEE Trans. Educ.,* vol. 25, pp. 99-102, 1982.

[41] L. Ran, J. C. Clare, K. J. Bradley, and C. Christopoulos, "Measurement of conducted electromagnetic emissions in PWM motor-drive systems without the need for an LISN," *IEEE Trans. Electromagn. Compat.,* vol. 41, pp. 50-55, 1999.

[42] F. Costa, C. Vollaire, and R. Meuret, "Modeling of conducted common mode perturbations in variable-speed drive systems," *IEEE Trans. Electromagn. Compat.,* vol. 47, pp. 1012-1021, 2005.

[43] C. Jettanasen, F. Costa, and C. Vollaire, "Common-Mode Emissions Measurements and Simulation in Variable-Speed Drive Systems," *IEEE Trans. Power Electron.,* vol. 24, pp. 2456-2464, 2009.

[44] L. M. Schneider, "Noise Source Equivalent Circuit Model of Off-line Converters and Use in Input Filter Design," in *Proc. POWERCON*, 1982.

[45] Q. Liu, W. Shen, F. Wang, D. Boroyevich, V. Stefanovic, and M. Arpilliere, "Experimental evaluation of IGBTs for characterizing and modeling conducted EMI emission in PWM inverters," in *Power Electronics Specialist Conference, 2003. PESC '03. 2003 IEEE 34th Annual*, 2003, pp. 1951-1956 vol.4.

[46] J. Meng, W. Ma, and L. Zhang, "Determination of noise source and impedance for conducted EMI prediction of power converters by lumped circuit models," in *Proc. IEEE Power Electron. Spec. Conf.*, 2004, pp. 3028-3033 Vol.4.

[47] Q. Liu, F. Wang, and D. Boroyevich, "Model conducted EMI emission of switching modules for converter system EMI characterization and prediction," in *Industry Applications Conference, 2004. 39th IAS Annual Meeting. Conference Record of the 2004 IEEE*, 2004, pp. 1817-1823 vol.3.

[48] Q. Liu, F. Wang, and D. Boroyevich, "Frequency-domain EMI noise emission characterization of switching power modules in converter systems," in *IEEE Appl. Power Electron. Conf. Expo.*, 2005, pp. 787-792 Vol. 2.

[49] M. Jin, M. Weiming, P. Qijun, Z. Zhihua, and Z. Lei, "Noise Source Lumped Circuit Modeling and Identification for Power Converters," *IEEE Trans. Ind. Electron.,* vol. 53, pp. 1853-1861, 2006.

[50] L. Qian, W. Fei, and D. Boroyevich, "Modular-Terminal-Behavioral (MTB) Model for Characterizing Switching Module Conducted EMI Generation in Converter Systems," *IEEE Trans. Power Electron.*, vol. 21, pp. 1804-1814, 2006.

[51] A. Perez, J. R. Regue, M. Ribo, A. M. Sanchez, F. J. Pajares, and D. Badia, "Circuital Characterization of an Electronic Equipment for Narrow-Band Conducted Emissions," in *Proc. EMC Europe Int. Symp.*, Barcelona, Spain, 2006, pp. 1035–1040.

[52] L. Qian, F. Wang, and D. Boroyevich, "Conducted EMI Noise Prediction and Characterization for Multi-phase-leg Converters Based on Modular-Terminal-Behavioral (MTB) Equivalent EMI Noise Source Model," in *Power Electronics Specialists Conference, 2006. PESC '06. 37th IEEE*, 2006, pp. 1-7.

[53] L. Qian, F. Wang, and D. Boroyevich, "Conducted-EMI Prediction for AC Converter Systems Using an Equivalent Modular Terminal Behavioral (MTB) Source Model," *IEEE Trans. Ind. Appl.*, vol. 43, pp. 1360-1370, 2007.

[54] A. Perez, A. M. Sanchez, J. R. Regue, M. Ribo, P. Rodriguez-Cepeda, and F. J. Pajares, "Characterization of Power-Line Filters and Electronic Equipment for Prediction of Conducted Emissions," *IEEE Trans. Electromagn. Compat.*, vol. 50, pp. 577-585, 2008.

[55] A. C. Baisden, D. Boroyevich, and F. Wang, "EMI Terminal Modeling," in *Conf. Rec. IEEE IAS Annu. Meeting*, 2008, pp. 1-8.

[56] H. M. Rebholz and S. Tenbohlen, "Efficient characterization of RF sources for the design of noise suppression filters," in *Antennas, Propagation and EM Theory, 2008. ISAPE 2008. 8th International Symposium on*, 2008, pp. 929-932.

[57] M. Foissac, J. L. Schanen, and C. Vollaire, ""Black box" EMC model for power electronics converter," in *Proc. IEEE ECCE*, 2009, pp. 3609-3615.

[58] H. M. Rebholz, S. Tenbohlen, and W. Kohler, "Time-Domain Characterization of RF Sources for the Design of Noise Suppression Filters," *IEEE Trans. Electromagn. Compat.*, vol. 51, pp. 945-952, 2009.

[59] A. C. Baisden, "Generalized Terminal Modeling of Electro-Magnetic Interference," PhD Dissertation, Electrical Engineering, Virginia Tech, Blacksburg, VA, 2010.

[60] A. C. Baisden, D. Boroyevich, and W. Fei, "Generalized Terminal Modeling of Electromagnetic Interference," *IEEE Trans. Ind. Appl.*, vol. 46, pp. 2068-2079, 2010.

[61] H. Bishnoi, A. C. Baisden, P. Mattavelli, and D. Boroyevich, "EMI Modeling of Buck Converter using a Generalized Terminal Model," in *Proc. GCMS*, 2010, pp. 158-164.

[62] H. Bishnoi, A. C. Baisden, P. Mattavelli, and D. Boroyevich, "EMI modeling of half-bridge inverter using a generalized terminal model," in *IEEE Appl. Power Electron. Conf. Expo.*, 2011, pp. 468-474.

[63] M. Foissac, J. Schanen, G. Frantz, D. Frey, and C. Vollaire, "System simulation for EMC network analysis," in *IEEE Appl. Power Electron. Conf. Expo.*, 2011, pp. 457-462.

[64] H. Bishnoi, A. C. Baisden, P. Mattavelli, and D. Boroyevich, "Analysis of EMI Terminal Modeling of Switched Power Converters," *IEEE Trans. Power Electron.*, vol. 27, pp. 3924-3933, 2012.

[65] S. Kye Yak and D. Junhong, "Measurement of noise source impedance of SMPS using a two probes approach," *IEEE Trans. Power Electron.*, vol. 19, pp. 862-868, 2004.

[66] J. R. Regue, M. Ribo, D. Duran, D. Badia, and A. Perez, "Measurement and modeling of noise source impedance of electronic equipment," in *Proc. EMC Europe Int. Symp.*, Eindhoven, Netherlands, 2004, pp. 150-154.

[67] A. M. Sanchez, A. Perez, J. R. Regue, M. Ribo, P. Rodrıguez-Cepeda, and F. J. Pajares, "Optimization of the Scattering Parameter Measurement of Electronic Equipment with Conducted Emissions," in *EMC Europe Workshop 2007*, Paris, France, 2007.

[68] K. Kiatgamjorn, P. Boonma, and W. Khan-ngern, "The study of input impedance of switched mode power supply," in *Proc. ECTI-CON*, 2008, pp. 1049-1052.

[69] V. Tarateeraseth, H. Bo, S. Kye Yak, and F. G. Canavero, "Accurate Extraction of Noise Source Impedance of an SMPS Under Operating Conditions," *IEEE Trans. Power Electron.*, vol. 25, pp. 111-117, 2010.

[70] B. Zhao, M. Zhao, Z. Feng, L. Shui, and M. Yao, "An improved dual-probe approach to measure noise source impedance," in *Proc. APEMC*, 2010, pp. 214-217.

[71] W. Yan, Y. Zhao, X.-q. Lu, Y.-h. Dong, and W. Feng, "A modified EMI noise source impedance modeling by employing two resistances calibration and Levenberg-Marquardt's method," in *Proc. ICMMT*, 2010, pp. 2021-2024.

[72] V. Tarateeraseth, S. Kye Yak, F. G. Canavero, and R. W. Chang, "Systematic Electromagnetic Interference Filter Design Based on Information From In-Circuit Impedance Measurements," *IEEE Trans. Electromagn. Compat.*, vol. 52, pp. 588-598, 2010.

[73] L. Fang, Z. Xuning, D. Boroyevich, P. Mattevelli, X. Jing, F. Wang, *et al.*, "On discussion of AC and DC side EMI filters design for conducted noise suppression in DC-fed three phase motor-drive system," in *IEEE Appl. Power Electron. Conf. Expo.*, 2011, pp. 667-672.

[74] W. Ruxi, H. F. Blanchette, D. Boroyevich, and P. Mattavelli, "EMI noise attenuation prediction with mask impedance in motor-drive system," in *IEEE Appl. Power Electron. Conf. Expo.*, 2012, pp. 2279-2284.

[75] L. Fang, D. Boroyevich, and P. Mattavelli, "Improving EMI filter design with in circuit impedance mismatching," in *IEEE Appl. Power Electron. Conf. Expo.*, 2012, pp. 1652-1658.

[76] Z. Xuning, L. Fang, D. Dong, P. Mattavelli, and D. Boroyevich, "CM noise containment in a DC-fed motor-drive system using DM filter," in *IEEE Appl. Power Electron. Conf. Expo.*, 2012, pp. 1808-1813.

[77] S. Fu-Yuan, D. Y. Chen, W. Yan-Pei, and C. Yie-Tone, "A procedure for designing EMI filters for AC line applications," *IEEE Trans. Power Electron.*, vol. 11, pp. 170-181, 1996.

[78] Y. Maillet, L. Rixin, W. Shuo, F. Wang, R. Burgos, and D. Boroyevich, "High-Density EMI Filter Design for Dc-Fed Motor-drives," in *IEEE Appl. Power Electron. Conf. Expo.*, 2009, pp. 1998-2005.

[79] W. Ruxi, D. Boroyevich, H. F. Blanchette, and P. Mattavelli, "High power density EMI filter design with consideration of self-parasitic," in *IEEE Appl. Power Electron. Conf. Expo.*, 2012, pp. 2285-2289.

[80] M. Ali, Laboure, X, E., F. Costa, and B. Revol, "Design of a Hybrid Integrated EMC Filter for a DC-DC Power Converter," *IEEE Trans. Power Electron.*, vol. 27, pp. 4380-4390, 2012.

[81] Z. Xuning, D. Boroyevich, P. Mattavelli, and F. Wang, "Filter design oriented EMI prediction model for DC-fed motor-drive system using double fourier integral transformation method," in *Power Electronics and Motion Control Conference (IPEMC), 2012 7th International*, 2012, pp. 1060-1064.

[82] M. Rahkala, T. Suntio, and K. Kalliomaki, "Effects of switching frequency modulation on EMI performance of a converter using spread spectrum approach," in *IEEE Appl. Power Electron. Conf. Expo.*, 2002, pp. 93-99 vol.1.

[83] H. Bishnoi, A. C. Baisden, P. Mattavelli, and D. Boroyevich, "Un-terminated Common-Mode EMI Model of DC-Fed Motor-drives," in *Power Electronics and Motion Control Conference (EPE-PEMC 2012), Proceedings of the 2012-15th International Conference on*, Novi-Sad, Serbia, 2012, pp. 1-8.

[84] H. Bishnoi, P. Mattavelli, and D. Boroyevich, "EMI Terminal Modelling of DC-Fed Motor-drives I: Common Mode Noise," in *CPES Annual Conference*, Blacksburg, VA, USA, 2013.

[85] W. Ruxi, "High Power Density and High Temperature Converter Design for Transportation Applications," PhD Dissertation, Electrical Engineering, Virginia Tech, Blacksburg, VA, 2012.

[86] L. Dalessandro, F. da Silveira Cavalcante, and J. W. Kolar, "Self-Capacitance of High-Voltage Transformers," *IEEE Trans. Power Electron.*, vol. 22, pp. 2081-2092, 2007.

[87] A. Massarini and M. K. Kazimierczuk, "Self-capacitance of inductors," *IEEE Trans. Power Electron.*, vol. 12, pp. 671-676, 1997.

[88] G. Grandi, M. K. Kazimierczuk, A. Massarini, and U. Reggiani, "Stray capacitances of single-layer solenoid air-core inductors," *IEEE Trans. Ind. Appl.*, vol. 35, pp. 1162-1168, 1999.

[89] W. Shuo, F. C. Lee, D. Y. Chen, and W. G. Odendaal, "Effects of parasitic parameters on EMI filter performance," *IEEE Trans. Power Electron.*, vol. 19, pp. 869-877, 2004.

[90] W. Shuo, F. C. Lee, and W. G. Odendaal, "Characterization and parasitic extraction of EMI filters using scattering parameters," *IEEE Trans. Power Electron.*, vol. 20, pp. 502-510, 2005.

[91] T. Wenhua, C. Cuellar, X. Margueron, and N. Idir, "A High Frequency Equivalent Circuit and Parameter Extraction Procedure for Common Mode Choke in the EMI Filter," *IEEE Trans. Power Electron.*, vol. 28, pp. 1157-1166, 2013.

[92] I. F. Kovacevic, T. Friedli, A. M. Muesing, and J. W. Kolar, "3-D Electromagnetic Modeling of EMI Input Filters," *IEEE Trans. Ind. Electron.*, vol. 61, pp. 231-242, 2014.

[93] Micrometals. (2007). *Power Conversion & Line Filter Applications*. Available: http://www.micrometals.com/pcparts/PC_L.pdf

[94] K. Venkatachalam, C. R. Sullivan, T. Abdallah, and H. Tacca, "Accurate prediction of ferrite core loss with nonsinusoidal waveforms using only Steinmetz parameters," in *Computers in Power Electronics, 2002. Proceedings. 2002 IEEE Workshop on*, 2002, pp. 36-41.

[95] C. Oliver. (2002). *A New Core Loss Model - Micrometals*. Available: http://www.micrometals.com/appnotes/appnotedownloads/corelossupdate.pdf

[96] S. Wei, W. Fei, D. Boroyevich, and C. W. Tipton, "Loss Characterization and Calculation of Nanocrystalline Cores for High-Frequency Magnetics Applications," *IEEE Trans. Power Electron.*, vol. 23, pp. 475-484, 2008.

[97] M. L. Heldwein, L. Dalessandro, and J. W. Kolar, "The Three-Phase Common-Mode Inductor: Modeling and Design Issues," *IEEE Trans. Ind. Electron.*, vol. 58, pp. 3264-3274, 2011.

[98] Y. Qin, T. W. Holmes, and K. Naishadham, "RF equivalent circuit modeling of ferrite-core inductors and characterization of core materials," *IEEE Trans. Electromagn. Compat.*, vol. 44, pp. 258-262, 2002.

[99] M. Bartoli, A. Reatti, and M. K. Kazimierczuk, "Modelling iron-powder inductors at high frequencies," in *Industry Applications Society Annual Meeting, 1994., Conference Record of the 1994 IEEE*, 1994, pp. 1225-1232 vol.2.

[100] Hitachi-Metals. (2007). *FINEMET® EMC Components*. Available: http://www.hitachi-metals.co.jp/e/products/elec/tel/pdf/hl-fm4-f.pdf

[101] R. W. Erickson, "Optimal single resistors damping of input filters," in *Applied Power Electronics Conference and Exposition, 1999. APEC '99. Fourteenth Annual*, 1999, pp. 1073-1079 vol.2.

[102] X. Lei, F. Feng, and S. Jian, "Optimal Damping of EMI Filter Input Impedance," *IEEE Trans. Ind. Appl.*, vol. 47, pp. 1432-1440, 2011.

[103] X. Lei and S. Jian, "Optimal Damping of Multistage EMI Filters," *IEEE Trans. Power Electron.*, vol. 27, pp. 1220-1227, 2012.

[104] X. Jing, F. Wang, Z. Xuning, D. Boroyevich, and P. Mattavelli, "Design of output passive EMI filter in DC-fed motor-drive," in *Applied Power Electronics Conference and Exposition (APEC), 2012 Twenty-Seventh Annual IEEE*, 2012, pp. 634-640.

[105] EPCOS, "Film Capacitors - EMI Suppression Capacitors (MKP)," ed, 2009.

APPENDIX A: A GUIDE TO CM MODEL EXTRACTION IN EXPERIMENTS

A.1 INTRODUCTION

The drive's input and output are isolated by board stack-up as shown in Fig. A.1. This stack-up will be used for both model extraction/validation purpose and also for design and testing of EMI filters. The following points should be noted about the stack-up:

1. There are exposed metallic banana connectors at the boards. These are dangerous if touched directly and hence turn off-the power supply before touching anything in the system 
2. The board stack-up is placed a little far from the inverter itself. The boards are places within two L-shaped metallic plates that connected to the main ground at their on the chassis. These L-shaped planes are called vertical plates. There are four such panels (L1 – L4).
3. The vertical plates facing the inverter (L1 and L2) are the calibration planes and the model extracted within these inner vertical planes will be the model of the entire drive. The other vertical planes, L3 and L4 are facing the dc and ac side external network respectively.
4. In reality the position of these vertical calibration planes should be exactly where the filters are intended to be placed but here that would require more careful design of the fixture. For demonstration of the proposed modelling method, the set-up of Fig. A.1 should be sufficient.

A.2 UN-TERMINATED MODEL EXTRACTION PROCEDURE

Step 1: Record the CM impedances of the network

In order to measure the common-mode (CM) impedances of the network, the phases (Input side: positive & negative and Output side: phase a, b and c) have to short circuited with a connection that is as small as possible. This is shown in Fig. A.1. The measurements have to be

made from the left side of L1 and the right side L2, that is looking towards the external network. Insert the appropriate network impedance (like the series and shunt impedances) or a through connection before making the measurement. The nearest ground connection is used to measure the impedance between the short-circuited phases (Point A in Fig. A.2) and the ground. The ground pin is usually taken on the vertical plane itself. Always be aware of the current paths. The current will return though the least inductive path and for a system that is spread out on the ground plane, it raises an ambiguity about the definition of ground. Thus the nearest ground is selected. The parasitic inductance of the short implemented here is definitely going to affect the measurement but since a motor-drive is not an RF system, it is almost impossible to avoid errors due to connection inductances.

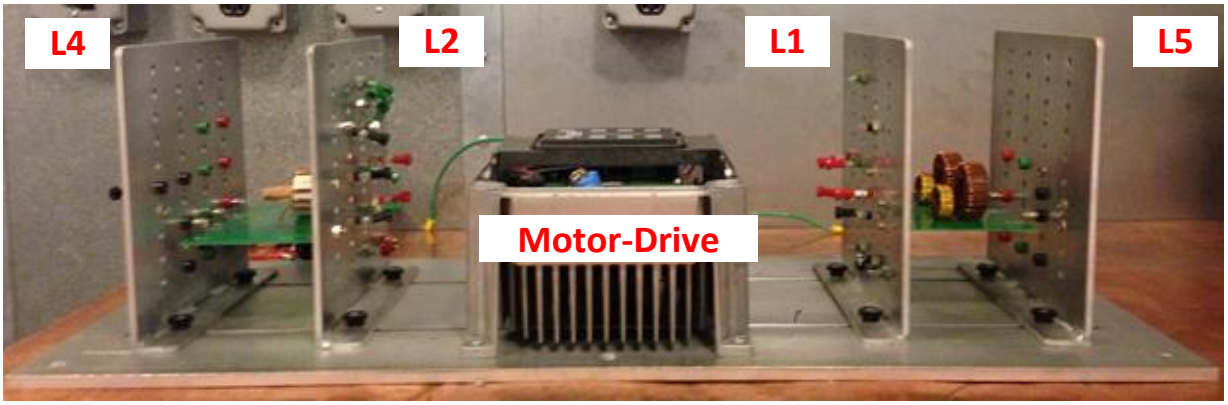

Fig. A.1 : Model extraction set-up

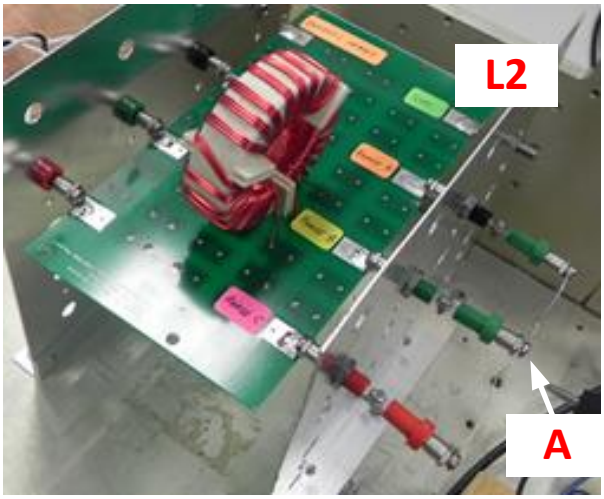

Fig. A.2: Impedance measurement point

Sanity Check: Note that once the series and shunt boards are inserted, the network will not be able to affect the impedance measurements. These boards are designed to have impedances that are either too large or too small and hence the network is invisible to the converter at EMI frequencies once these boards are in place. For the input side, this can be checked by changing the terminations on the LISN. Changing the impedance of the LISN from 1 kΩ to 50Ω should not change the impedance looking into the dc network, both for the series and shunt conditions. For the output side some change is expected in the shunt case as the harness resonances are difficult to mask with shunt impedances. So if the harness is changed the impedance seen into the network will change slightly but should still remain very low. For the series condition at the output side the change in of harness should not affect the impedance seen in the ac network.

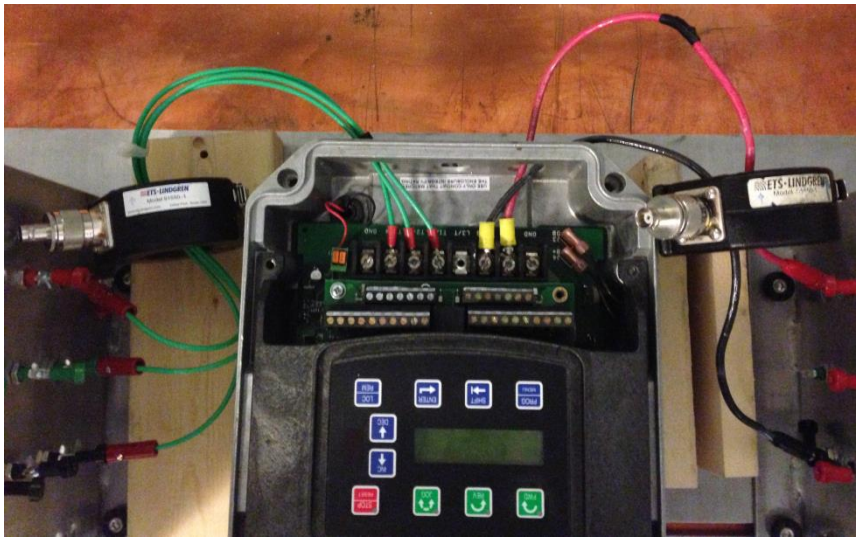

Fig. A.3: Clamp on current probes, position and orientation

Step 2: Record the input and output impedance of the drive

In order to measure the input and output CM impedances of the drive, the same procedure as given in Step 1 is to be repeated, except that the impedance measurement are now to be conducted looking towards the drive rather than towards the external network. In Fig. A.1, Port 1 is define at L1, looking from the right side of L1 and towards the drive. Port 2 is defined at L2, looking from the left side of L2 and towards the drive. The Z_{11} and Z_{22} can be measured using an impedance analyzer. The other critical piece of the Z-matrix is the Z_{12}. If there is a network

analyzer (VNA) available, then this can be measured along with Z_{11} and Z_{22}. But if a VNA is not available, then at least for a motor-drive a good approximation of Z_{12} can made by keeping $Z_{12} = Z_{11}$ or $Z_{12} = Z_{22}$. The optimization program can help a bit in removing any discrepancies in the initial estimation of Z_{12}. Also remember, when measuring Z_{11} using an impedance analyzer, the port-2 which in this case are the three output phases must be disconnected from the network, or kept open circuited. The same goes for port 1 when Z_{22} is measured using an impedance analyzer.

Step 3: Make noise measurements:

In order to make the noise measurements, put clamp-on probes on either side of the drive as shown in Fig. A.3. Notice that the clamp-on probe is inside the calibration plane as our target is to identify the model of the motor-drive. Connect the series impedance boards and turn on the drive and select 40 Hz line frequency. Set the oscilloscope for 2 line cycles (5ms/div) and acquisition of 10nsec/point. Also change the acquisition type from sample (default) to Hi-Res. This will offer some averaging of the noise although averaging over time is not possible because of unstable triggering of the scope while measuring PWM noise over the line cycle. Change the port termination of the scope from 1MΩ to 50Ω. Make a "snapshot" (single) measurement of both input and output noise simultaneously on two different channels of the oscilloscope. Record the measurements as text files indicating the measurement place, that is whether it is input or output side and which impedances were connected on the input and output side. A typical file name looks like "*ip_dc_srs_ac_srs.txt*". This means that this is the input side CM noise measurement when both input and output sides of the drive were terminated with series impedances.

Repeat the measurements with shunt impedance on both sides.

Step 4: Extract model using MATLAB:

There should be 7 impedance files and 4 noise measurement files before extraction of model can begin. The 7 impedance files include:

Impedance measurements: (7 files)

1. Series impedances looking into the external network, dc and ac side (2 files)

- *Z_srs_ip.txt*
- *Z_srs_op.txt*

2. Shunt impedances looking into the external network, dc and ac side (2 files)
   - *Z_shs_ip.txt*
   - *Z_shs_op_cab_10m.txt*

   Note that for the shunt impedance at the output side, the harness used to connect the motor-drive and the motor is also mentioned in the name. This is because it is not possible to mask the resonance of the cable with a shunt impedance and hence if the cable is changed the shunt impedance of the ac network will change.

3. Z-parameters, Z_{11}, Z_{22} and Z_{12} for the drive (3 files)

Noise Measurements: (4 files)

1. Noise with series impedance both side, input and output side noise (2 files)
   - *ip_dc_srs_ac_srs.txt*
   - *op_dc_srs_ac_srs.txt*
2. Noise with shunt impedance both side, input and output side noise (2 files)
   - *ip_dc_shs_ac_shs.txt*
   - *op_dc_shs_ac_shs.txt*

Probe Calibration Data (2 files)

The probes used in the experiments her were two ETS-Lindgren 91550-1 current probes. The calibration data usually come with the new probe. However, it is recommended that calibration be done in-house to avoid errors and regardless it's a good practice. For the experiments shown in this dissertation, the probe calibration was done using a special calibration jig from A.H. Systems CPF-530. The calibration revealed that there is a slight difference between the two probes. The old probe's transfer function was little off in the low frequency range from the one given in the data sheet. The new probe's transfer function exactly matched the data sheet. That is why calibration prior to measurements is so important. Note that the direction of current must be taken in to the consideration. High frequency probes may not come with positive direction of current indicated on them. The best way to avoid error is to at least be consistent with the way (sense) the probes are put in the system. Fig. A.3 shows the correct orientation of the current probes. Use the same BNC cables while calibrating the probes as would be used for measuring the noise using the oscilloscope. This will help in calibrating out the error of the BNC cables as

well. In the end just because of the discrepancy noticed with the transfer function of the older probe, two calibration files are needed:

- *91550NEW.txt*
- *91550OLD.txt*

After everything is measured and recorded, keep the files in the same folder as the MATLAB code for extracting CM model. Check that the file names in the code are changed to the ones that you have used. Then run the code.